

# Strongly Interacting Quantum Mixtures of Ultracold Atoms

by

Cheng-Hsun Wu

Department of Physics,  
National Taiwan University (2006)

Submitted to the Department of Physics  
in partial fulfillment of the requirements for the degree of  
Doctor of Philosophy

at the

MASSACHUSETTS INSTITUTE OF TECHNOLOGY

February 2013

© Massachusetts Institute of Technology 2013. All rights reserved.

Author .....  
Department of Physics  
January 31, 2013

Certified by .....  
Martin W. Zwiernlein  
Silverman Family Career Development Associate Professor of Physics  
Thesis Supervisor

Accepted by .....  
John Belcher  
Professor of Physics, Associate Department Head for Education

# Strongly Interacting Quantum Mixtures of Ultracold Atoms

by

Cheng-Hsun Wu

Submitted to the Department of Physics  
on January 31, 2013, in partial fulfillment of the  
requirements for the degree of  
Doctor of Philosophy

## Abstract

This thesis describes the construction of a new apparatus for ultracold quantum gases as well as the scientific results this machine has produced so far. This new apparatus is capable of simultaneously cooling and trapping lithium, sodium, and potassium. It therefore provides a platform to study a large variety of quantum mixtures.

Three main experimental results are presented. Firstly, the direct cooling of  $^{41}\text{K}$  to Bose-Einstein condensation is presented. Then the  $^{41}\text{K}$  atoms provide the coolant for  $^6\text{Li}$  and  $^{40}\text{K}$ , achieving a triply degenerate gas of  $^6\text{Li}$  -  $^{40}\text{K}$  -  $^{41}\text{K}$ . In particular, a broad interspecies Feshbach resonance between  $^{40}\text{K}$  -  $^{41}\text{K}$  is observed, opening a new pathway to study a strongly interacting isotopic Bose-Fermi mixture of  $^{40}\text{K}$  -  $^{41}\text{K}$ .

Secondly, a new Bose-Fermi mixture of  $^{23}\text{Na}$  -  $^{40}\text{K}$  is introduced. We show that  $^{23}\text{Na}$  is a very efficient coolant for  $^{40}\text{K}$  by sympathetically cooling  $^{40}\text{K}$  to quantum degeneracy with the help of a  $^{23}\text{Na}$  condensate. Moreover, over thirty interspecies Feshbach resonances are identified, paving the way to study strongly interacting Bose-Fermi problems, in particular the Bose polaron problem.

Thirdly, we report on the first formation of ultracold fermionic Feshbach molecules of  $^{23}\text{Na}^{40}\text{K}$  by radio-frequency association. The lifetime of the nearly degenerate molecular gas exceeds 100 ms in the vicinity of the Feshbach resonance. The NaK molecule features chemical stability in its ground state in contrast to the case of the KRb molecule. Therefore, our work opens up the prospect of creating chemically stable, fermionic ground state molecules of  $^{23}\text{Na}^{40}\text{K}$  where strong, long-range dipolar interactions will set the dominant energy scale.

Finally, the thesis concludes with an outlook on future topics in polaron physics and quantum dipolar gases, which can be studied using the new apparatus.

Thesis Supervisor: Martin W. Zwierlein

Title: Silverman Family Career Development Associate Professor of Physics

*To my parents,  
Keng-Liang Wu and Ching-Jong Liu  
and my sister, Pin-Hsuan Wu*

# Acknowledgements

The time at MIT was one of the most fruitful periods of my life. It was the first time I was surrounded by so many bright people. However, what deeply surprises me is the fact that these people are not only the smartest people in the world but also the kindest. The words in this acknowledgement can not show my gratitude to them. After all those years, they turned from strangers to my best friends, even like my families.

First I would like to express my highest gratitude to my thesis committee members, Prof. Martin Zwierlein, Prof. Wolfgang Ketterle, and Prof. Leonid Levitov, for their kind supervision, comments and suggestions.

I remember vividly the first time I met my advisor, Prof. Martin Zwierlein in the hallway of building 26. He welcomed me with his firm handshake and warm smile. It was the handshake that took me to a new journey, a new scientific adventure. We obtained the first potassium-40 MOT together, we designed and constructed one of the most complicate ultracold atom machines together, and we observed the first potassium-41 BEC in Fermi I together. Each achievement was followed by Martin's excited shouting "Djyeah". It was the sound that announced a new era of Fermi I. Martin is not only a great mentor but also a very good friend. He is like a brother whom I always want to look up to. I have learned so many things from him but his knowledge never ends. Once, we were trying to figure out a quantum collision problem. We studied a book together from sunset to midnight. His passion on sharing knowledge with others always warms my heart. I am so grateful to be one of his students.

Actually, I was admitted to MIT before Martin joined MIT as a faulty member. During that time, Prof. Wolfgang Ketterle kindly allowed me to attend his group meetings with the old BEC I members. I felt extremely lucky that my first contact with atomic physics was provided by the master of the field. Wolfgang has the magic

to describe complicated physics concepts in a very simple way. I deeply respect him not only because of his great achievements in science but also his extremely kind and gentle personality.

Prof. Vladan Vuletic, who is my academic advisor, always encouraged me in the registration meeting. I was fully charged every time after talking to him in the beginning of each semester.

Dr. Peyman Ahamdi joined Fermi I as a postdoc in 2008. Without him, the construction of the Fermi I machine would not have been possible. Working with him lets me realize one thing: the best way of teaching is to be patient and to be considerate. He always puts himself in the learner's position and he tried to understand how we thought. He taught me how to make something from nothing, how to create an ultra-high vacuum environment from the air, and how to cool atoms from room temperature to quantum degeneracy. His warm and kind attitude made my time at MIT so memorable and cherishable.

The interaction between Dr. Sebastian Will and me was limited to the last year and half of my PhD. I wish we could have had more time to pursue scientific goals together. I look up to his careful attitude in explaining data and organized ways in looking for new phenomena in physics. He always seeks truth from facts and he provided Peter and me with bright suggestions while we were wandering in the dark.

Christian Schunck and I were officemates for about two years. I am very grateful to have had such a knowledgeable person sitting behind me during the early time of my PhD. He introduced me to the concepts of superfluidity and many-body pairing. His life is an integration of science and art. I found out very late that he was a master in playing harp. We went to the Boston Symphony Orchestra once. He let a complete outsider of classical music like me have a memorable night.

Andre Schirotzek is the coolest scientist I have ever met. I remember clearly that the first time that I entered the BEC I lab, I saw Andre wearing a cool goggle and

a no-sleeve shirt. First I was stunned by his enormous muscles. I even murmured to myself: Who is this guy? Life is non-predictable! Afterwards, we turned out to be very good friends and I also found out that inside his muscular body, Andre has a very considerate personality which guides him to the great achievements in science.

Ibon Santiago is a very special friend of mine; we share a lot in common. He is like a live book of science and art history. So many times the stories he told made my day. I cherish a lot those moments that we walked together to the Thailand Cafe talking about our lives, the research, and the future. He always ordered the pork with bamboo and I always ordered the beef noodle. He built not only the best water cooling system in the Fermi I machine but also the finest emotional flow in my life at MIT.

I would like describe Jee Woo Peter Park with an old Chinese slang: “blue comes from indigo, and yet wins over indigo”. He is such an intelligent and humble learner. I am so grateful to have had him around while running the machine and taking data. His intelligence can always guide me through hurdles and his humor can always provide me energy during late night experiment. I would like to apologize to him that I shocked him so many times by intentionally entering the lab quietly. He is like a little shy brother to me and I am the bullying one. Right now he is the master of the Fermi I machine. As I always say: Peter is the best part of my thesis.

I would like to thank our kind neighbor, the BEC I members, in particular Ariel Sommer who participated in the early stage of building the Fermi I machine. He helped us put the main chamber together and also designed and built the lithium laser system. He is such a gentleman and sometimes he is too gentle to say no to your request. His great passion in science together with his cleverness lead him to all the fantastic results he has achieved in BEC I. Another kind member of BEC I, Mark Ku, once invited me to his house. That was the first time I realized that he knew by heart not only the equation of state of a two-component degenerate Fermi

gas but also the equation of state of the most delicious food. He is a wonderful cook in both quantum soups and real soups. The other kind member of BEC I, Lawrence Cheuk, is always interested in almost everything. He has great interests in all aspects of physics and I believe that this intrinsic curiosity will ensure him a great success in the future. With his assistance, I was able to refine my calculations of the Zeeman energy levels. Thank you, Lawrence!

There are two members in the BEC II experiment whom I need to show my great respect to - Christian Sanner and Aviv Keshet. Christian's knowledge of instruments always surprised me. He was not only the owner of the "Walmart" but also the creator. Without Aviv, we would have been probably still stuck in the stone age. He automatized the whole data taking process. He is the savior of many hours of our time.

Sara Campbell, Caroline Figgatt, Jacob Sharpe, Kevin Fischer and Vinay Ramasesh devoted their fun college time to the Fermi I machine. They made every scientific result produced in Fermi I possible. In particular, I would like to thank Sara. We once burned the midnight oil together to tighten the main chamber flanges. It was a great memory working with her. She is such a positive and happy person.

Christoph Clausen and I were the first two students working in the Fermi I experiment. He taught me how to align and construct a laser system from the ground up. Unfortunately, we cannot harvest the fruit from Fermi I together. But I believe that his great achievements in quantum optics at the Université de Genève will lead him to a bright and successful future.

I deeply appreciate having the opportunity to do research at MIT. Being a PhD student at MIT was beyond the scope of my childhood dream. But my parents, Keng-Liang Wu and Ching-Jong Liu, have believed in me and supported me unconditionally. They represent my physical shelter, my spiritual pillar, and my real home. The big hug from my little sister, Pin-Hsuan Wu, warmed me every time when I went back home. She is a little angel who knows how to cheer me up whenever I am tired or

exhausted.

Finally, I would like to thank my dear wife, Chun-Hui Tseng. In many cold evenings, by the time I went home she was already asleep. However, she never complained. I deeply appreciate her understanding. Her unconditional support and her big warm smile make everything I have done at MIT possible.

# Contents

<b>1</b>	<b>Introduction</b>	<b>18</b>
1.1	Bosons and Fermions . . . . .	19
1.2	Entering the quantum regime: degenerate gases . . . . .	21
1.3	Feshbach resonances . . . . .	23
1.4	The Fermi I machine . . . . .	24
1.5	Overview of this thesis . . . . .	25
<b>2</b>	<b>A Multi-Species Machine : Fermi-I</b>	<b>26</b>
2.1	Overview . . . . .	26
2.2	Vacuum chamber design . . . . .	28
2.2.1	Atomic ovens . . . . .	32
2.2.2	Vacuum Pumps . . . . .	35
2.3	Zeeman slowers . . . . .	39
2.3.1	The potassium Zeeman slower . . . . .	41
2.3.2	The lithium-sodium Zeeman slower . . . . .	41
2.3.3	Getting the slowers to work . . . . .	44
2.4	Magneto-optical traps (MOT) . . . . .	47
2.4.1	Configuration of the MOT beams . . . . .	47
2.4.2	MOT coils . . . . .	50
2.4.3	Parameters for the MOTs . . . . .	51

2.5	Optically plugged magnetic trap . . . . .	56
2.6	RF coils . . . . .	59
2.7	Crossed optical dipole trap . . . . .	59
2.8	The Feshbach field . . . . .	60
2.8.1	Stabilizing the Feshbach field . . . . .	61
2.9	Water cooling systems . . . . .	63
2.10	Optics . . . . .	65
2.10.1	The potassium laser systems . . . . .	65
2.10.2	The lithium laser system . . . . .	66
2.10.3	The sodium laser system . . . . .	66
<b>3</b>	<b>Strongly Interacting Isotopic Bose-Fermi Mixture Immersed in a Fermi Sea</b>	<b>68</b>
3.1	Introduction . . . . .	69
3.2	A new coolant for fermionic alkali species: $^{41}\text{K}$ . . . . .	70
3.2.1	Why $^{41}\text{K}$ ? . . . . .	70
3.2.2	Making $^{41}\text{K}$ Bose-Einstein condensates . . . . .	71
3.3	A new quantum degenerate Bose-Fermi-Fermi mixture: $^{41}\text{K}$ - $^6\text{Li}$ - $^{40}\text{K}$ . . . . .	75
3.4	Observation of interspecies Feshbach resonances: towards strongly inter- acting Bose-Fermi mixtures: . . . . .	86
3.5	Conclusion . . . . .	89
<b>4</b>	<b>A New Ultracold Quantum Mixture of <math>^{23}\text{Na}</math> - <math>^{40}\text{K}</math></b>	<b>91</b>
4.1	Introduction . . . . .	91
4.2	A new coolant for $^{40}\text{K}$ : $^{23}\text{Na}$ . . . . .	92
4.2.1	Making the $^{23}\text{Na}$ Bose-Einstein condensate . . . . .	93
4.2.2	Two stage MOT loading technique . . . . .	95
4.2.3	Obtaining double degeneracy . . . . .	99

4.3	Feshbach resonances between $^{23}\text{Na}$ and $^{40}\text{K}$ . . . . .	103
4.3.1	Spin state preparation . . . . .	103
4.3.2	Feshbach loss spectroscopy . . . . .	105
4.3.3	$p$ -wave multiplets . . . . .	105
4.3.4	Understanding the NaK Feshbach resonances . . . . .	110
4.4	Conclusion . . . . .	111
<b>5</b>	<b>Ultracold Fermionic Feshbach Molecules of <math>^{23}\text{Na}^{40}\text{K}</math></b>	<b>112</b>
5.1	Introduction . . . . .	112
5.2	Formation of fermionic NaK Feshbach molecules . . . . .	114
5.2.1	Magnetic field control . . . . .	115
5.2.2	The first molecular signal . . . . .	120
5.2.3	Radio frequency association of NaK molecules . . . . .	122
5.3	The singlet admixture of molecules . . . . .	128
5.4	The kinetic energy of molecules . . . . .	130
5.5	The lifetime of molecules . . . . .	132
5.6	Conclusion . . . . .	137
<b>6</b>	<b>Conclusion and Outlook</b>	<b>138</b>
6.1	Bose polarons . . . . .	139
6.1.1	The Bose polaron Hamiltonian . . . . .	140
6.1.2	Simulated radio-frequency spectra . . . . .	142
6.2	Quantum dipolar gases . . . . .	146
6.2.1	Dipole-dipole interaction . . . . .	147
6.2.2	Fermionic dipolar quantum gases . . . . .	147
<b>A</b>	<b>Schematics of the Fermi I vacuum chamber</b>	<b>155</b>
<b>B</b>	<b>Vapor pressure curves of different elements</b>	<b>166</b>

C Schematics of the Fermi I laser systems	168
D Published journal articles	175

# List of Figures

1-1	Behavior of bosons and fermions in a harmonic trap. . . . .	20
2-1	Overview of the Fermi-I laboratory. . . . .	27
2-2	$^{40}\text{K}$ MOT fluorescence vs. nozzle temperature. . . . .	28
2-3	3D schematic of the Fermi-I vacuum system. . . . .	29
2-4	Top and side view schematics of the Fermi-I main chamber. . . . .	30
2-5	Exploded view of the potassium oven. . . . .	33
2-6	$^{39}\text{K}$ MOT fluorescence vs. oven cup temperature. . . . .	34
2-7	3D schematic of the cold cup assembly. . . . .	36
2-8	Picture of the micro-channel nozzle. . . . .	37
2-9	TiZrV coating assembly. . . . .	38
2-10	Graphical representation of possible detuning conflicts. . . . .	42
2-11	Winding profile of the potassium slower. . . . .	43
2-12	Potassium decreasing part slower magnetic field profiles. . . . .	43
2-13	Potassium increasing part slower magnetic profiles . . . . .	44
2-14	Winding profile of the lithium-sodium slower. . . . .	45
2-15	Lithium-sodium decreasing part slower magnetic profiles. . . . .	45
2-16	Lithium-sodium increasing part slower magnetic profiles. . . . .	46
2-17	Schematic of the MOT beams setup on the experimental table. . . . .	48
2-18	Configuration of the MOT, magnetic trap, and Feshbach coils. . . . .	49

2-19	Measurement of the magnetic field as a function of the distance to the coil center in the Helmholtz configuration. . . . .	50
2-20	Pictures of the trap coils. . . . .	51
2-21	Potassium energy level scheme. . . . .	52
2-22	Experimental sequence for loading the $^{39}\text{K}$ MOT. . . . .	53
2-23	Experimental sequence for loading the $^{40}\text{K}$ MOT. . . . .	54
2-24	Experimental sequence for loading the $^{41}\text{K}$ MOT. . . . .	55
2-25	$^{40}\text{K}$ fluorescence image in the magnetic trap. . . . .	56
2-26	Side view of the main chamber. . . . .	57
2-27	Picture of the inner RF antenna. . . . .	58
2-28	Circuit schematic of the magnetic trap and the Feshbach magnetic fields. . . . .	61
2-29	Schematic of the detection and stabilization circuits for the Feshbach magnetic field. . . . .	62
2-30	Overview of the Fermi-I water cooling system. . . . .	64
3-1	The temperature of $^{39}\text{K}$ vs. the final RF knife frequency. . . . .	71
3-2	Absorption image of the $^{41}\text{K}$ atoms in the optically plugged quadrupole magnetic trap towards the end of evaporation. . . . .	72
3-3	Simulated potential of the biased optically plugged magnetic trap for $^{41}\text{K}$ in three different directions. . . . .	73
3-4	Optimized profiles of the magnetic field gradient and the RF knife frequency for cooling $^{41}\text{K}$ atoms towards Bose-Einstein condensation. . . . .	74
3-5	Absorption image of the first $^{41}\text{K}$ BEC in the Fermi-I machine. . . . .	75
3-6	$^{41}\text{K}$ BEC emerges from a thermal cloud. . . . .	76
3-7	Illustration of the gravity assisted spin purification scheme. . . . .	77
3-8	Effect of the $^6\text{Li}$ spin purification scheme. . . . .	79
3-9	Extracting the trapping frequency of the biased optically plugged magnetic trap from condensate fraction. . . . .	81

3-10	Phase space density as a function of the atom numbers of three different species ( $^6\text{Li}$ , $^{40}\text{K}$ , and $^{41}\text{K}$ ).	83
3-11	Triply degenerate quantum gases of $^{41}\text{K}$ , $^{40}\text{K}$ and $^6\text{Li}$ .	84
3-12	Observation of Pauli pressure and Bose condensation in a triply degenerate quantum mixture.	85
3-13	Observation of a wide Feshbach resonance in the isotopic Bose-Fermi mixture of $^{41}\text{K}$ - $^{40}\text{K}$ .	87
3-14	Bose and Fermi clouds after short time of flight.	89
3-15	The Bose-Fermi lifetime and the evolution of temperature in the strongly interacting regime.	90
4-1	Absorption image of the $^{23}\text{Na}$ Bose-Einstein condensate.	93
4-2	$^{23}\text{Na}$ atom number as a function of the purification field gradient.	95
4-3	Lifetime curves of $^{40}\text{K}$ in the magnetic trap.	96
4-4	Illustration of the two stage MOT loading technique.	97
4-5	Fluorescence images of $^{40}\text{K}$ in the magnetic trap.	98
4-6	Experimental sequence of the two stage MOT loading technique and the RF evaporation.	99
4-7	In-trap images of $^{23}\text{Na}$ and $^{40}\text{K}$ .	100
4-8	Simultaneous quantum degeneracy of $^{23}\text{Na}$ and $^{40}\text{K}$ atoms.	101
4-9	Evolution of the phase space density (PSD) as a function of the atom number ( $N$ ) of $^{23}\text{Na}$ and $^{40}\text{K}$ .	102
4-10	Stern-Gerlach experiment for identifying the spin states of $^{40}\text{K}$ .	104
4-11	Feshbach resonances in $^{23}\text{Na}$ - $^{40}\text{K}$ .	107
4-12	Triplet structure of the $p$ -wave resonance.	108
5-1	Experimental sequence for preparing $^{40}\text{K}$ atoms in the $ 9/2, -3/2\rangle$ state at high field.	116

5-2	Rabi oscillation measurements in two different field stability regimes.	117
5-3	RF spectra taken between the $^{40}\text{K}$ $ 9/2, -3/2\rangle$ and $ 9/2, -5/2\rangle$ states at 130 G.	119
5-4	The first signal of NaK molecules.	120
5-5	Molecular loss spectroscopy as a function of the magnetic fields.	121
5-6	Association and dissociation spectra of fermionic Feshbach molecules.	123
5-7	Molecular conversion efficiency as a function of the RF pulse time.	124
5-8	A fit to the molecular association spectrum.	126
5-9	(a) Binding energy of NaK Feshbach molecules as a function of magnetic field. (b) Open-channel fraction and singlet admixture of the molecular state.	129
5-10	Time-of-flight expansion of leftover $^{40}\text{K}$ atoms and associated molecules.	131
5-11	Lifetime of fermionic Feshbach molecules.	133
5-12	Gravitational sag of different species in the ODT.	134
5-13	Schematic of the experimental sequence for removing sodium atoms from the ODT.	135
5-14	Lifetime of NaK molecules as a function of scattering length.	136
6-1	Real and imaginary parts of the function $C(\tilde{t})/\beta$ .	144
6-2	Simulated Bose polaron RF spectra.	145
6-3	Effect of the dipolar interaction on the centrifugal barrier.	149
6-4	Pairing gap $\Delta$ of fermionic dipolar molecules as a function of the angle $\theta$ between the Fermi momentum and the dipoles.	152
6-5	Induced electric dipole moments of NaK and KRb molecules as a function of external electric fields.	153
A-1	Schematic of the 4" recessed viewport from UKAEA.	156
A-2	Schematic of the 2.5" recessed viewport from UKAEA.	156

B-1	Vapor pressure curves of different elements. . . . .	167
C-1	Schematic of the potassium FM spectroscopy setup. . . . .	169
C-2	Schematic of the potassium imaging and optical pumping system. . .	170
C-3	Schematic of the $^{40}\text{K}$ laser system. . . . .	171
C-4	Schematic of the $^{41}\text{K}$ laser system. . . . .	172
C-5	Schematic of the $^6\text{Li}$ laser system. . . . .	173
C-6	Schematic of the Raman fiber amplifier. . . . .	174

# Chapter 1

## Introduction

The first experimental realization of Bose-Einstein condensation (BEC) [1, 2] in dilute atomic gases in 1995 opened an exciting new field which has successfully integrated atomic physics, many-body condensed matter physics, and optics. Ultracold quantum gases can be considered as artificial condensed matter systems where interactions can be tuned via Feshbach resonances [3], densities can be changed with trapping potentials, and temperatures can be controlled through cooling schemes (in condensed matter systems, the sample can only be tuned by pressure and by doping). The major impact of ultracold quantum gases on the present-day physics is their extraordinary degree of control. Therefore they allow us to investigate fundamental behavior of quantum matter in pristine fashion. Not only can quantum behavior within single atomic species be studied, ultracold quantum mixtures have opened the door to problems which can not be easily addressed in traditional condensed matter systems such as the BEC-BCS crossover [4, 5, 6, 7], polaron physics [8, 9, 10], quantum dipolar gases [11, 12], and Efimov physics [13, 14], just to name a few.

A unique feature of ultracold quantum gases is their dilute densities which prevents the gas from crystallization before entering quantum degeneracy. A typical BEC has a density of  $10^{14}/\text{cm}^3$  which is almost one million times thinner than air. For such

a dilute gas to enter quantum degeneracy, it needs to be cooled to extremely low temperature, typically a few hundreds of nanokelvin. Ultracold quantum gases are generally produced by laser cooling [15] and subsequent evaporative cooling [16]. Laser cooling can bring the atoms from room temperature to a few hundreds of microkelvin. After laser cooling, evaporative cooling is then performed in a magnetic trap where the trap forms a conservative potential as opposed to the trap during the laser cooling stage. Using radio frequency (RF) to force energetic atoms to leave the trap has been proven to be one of the most efficient ways to cool atoms to quantum degeneracy. When the system is close to quantum degeneracy, different atoms behave differently according to their quantum statistics - bosons or fermions - that is determined by their total spin (nuclear spin + electronic spin).

## 1.1 Bosons and Fermions

Atoms with integer spin are bosons and those with half-integer spin are fermions. In our experiment, we have used  $^{23}\text{Na}$  ( $I = 1/2, S = 1/2$ ),  $^6\text{Li}$  ( $I = 1, S = 1/2$ ),  $^{39}\text{K}$  ( $I = 1/2, S = 1/2$ ),  $^{40}\text{K}$  ( $I = 4, S = 1/2$ ), and  $^{41}\text{K}$  ( $I = 1/2, S = 1/2$ ) atoms. Therefore, from the total spin, we know that only  $^6\text{Li}$  and  $^{40}\text{K}$  are fermions and the others are bosons. The knowledge of quantum statistics plays an extremely important role when analyzing physical quantities of trapped atomic gases close to quantum degeneracy, in particular the density distributions. Figure 1-1 illustrates the behavior of bosons and fermions in a harmonic trap. Before the system reaches the degeneracy temperature, both bosons and fermions behave like a classical gas and follow the Maxwell-Boltzmann distribution. As the system is close to the degeneracy temperature, bosons and fermions start to behave differently. This is the point when the atomic waves begin to overlap - the spacing between atoms,  $d = n^{-1/3}$ , becomes equal to their de Broglie wavelength,  $\lambda_{dB} = \sqrt{\frac{h}{2\pi M k_B T}}$  or in other words, when the phase

space density  $\rho = n\lambda_{dB}^3$  is of order unity. The mass of the atom is denoted by  $M$ ,  $T$  is the temperature of the system,  $n$  is the gas density, and  $h$  and  $k_B$  are Planck and Boltzmann constants, respectively. Below the degeneracy temperature, bosons start to condense in the ground state of the harmonic trap - the onset of Bose condensation; however, fermions, due to the Pauli exclusion principle, can not condense. Instead, they are forced to occupy different energy states of the harmonic trap and form a Fermi sea. These distinct properties of bosons and fermions are the basic concepts for understanding quantum degenerate gases. Detailed descriptions of the effect of quantum statistics on interesting physical quantities can be found in Ref. [17] for bosons and Ref. [5] for fermions.

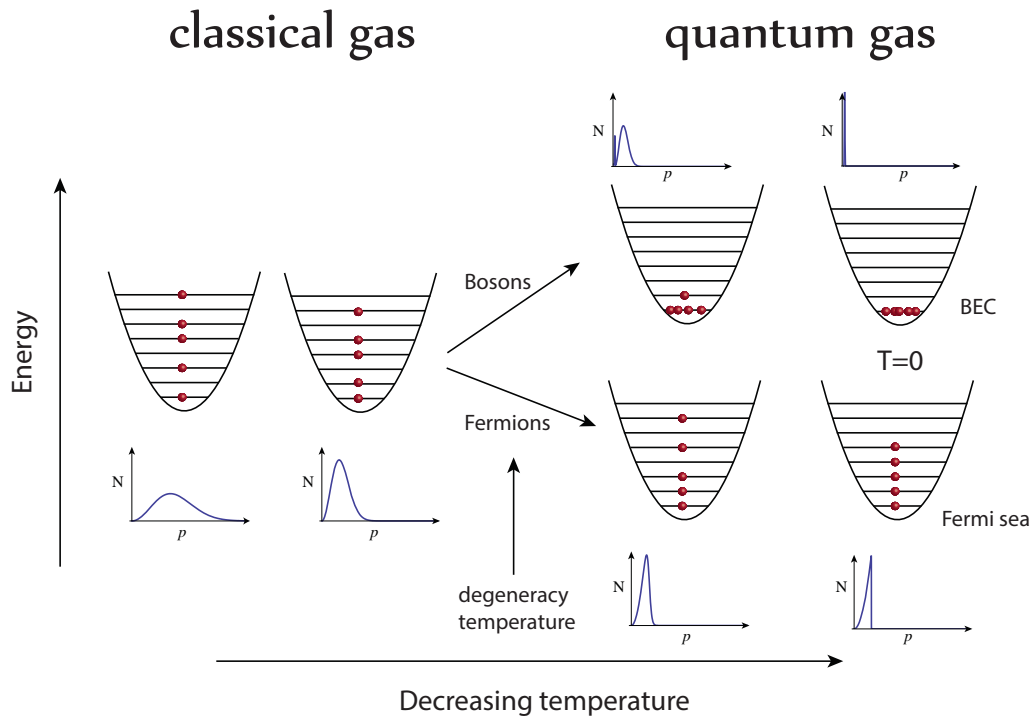


Figure 1-1: The behavior of bosons and fermions in a harmonic trap. When the system is above the degeneracy temperature, both bosons and fermions behave classically. Below the degeneracy temperature, bosons start to condense in the ground state of the harmonic trap; however, fermions are forced to occupy different energy states of the harmonic trap due to the Pauli exclusion principle. The momentum distributions of atoms at different temperatures are shown next to the harmonic traps.

## 1.2 Entering the quantum regime: degenerate gases

Below the degeneracy temperature, the behavior of atomic gases needs to be explained by quantum mechanics. Although in 1924-25, a new state of matter (BEC) was first predicted in papers by Satyendra Nath Bose [18] and Albert Einstein [19], only since the late 70's, have the efforts to create BEC in spin-polarized hydrogen been started [20]. However, it was only in 1998 that BEC in hydrogen was first realized at MIT [21]. The study of spin-polarized hydrogen was superseded by another approach with the advent laser cooling and trapping of alkali atoms and with further cooling of them in a magnetic trap using forced RF evaporation. Since the first discovery of BEC in 1995, the study of dilute alkali gases has become the most popular approach of ultracold atom experiments.

The journey of understanding BECs started with the exploration of their quantum coherent [22, 17] and collective [23, 24] properties. Then the first realization of Feshbach resonances in a  $^{23}\text{Na}$  condensate in 1998 introduced a new “knob” to the field [25]- a knob that can tune the interaction strength between atoms [3]. A year later, the study of fermionic alkali atoms manifested itself by the creation of a degenerate Fermi gas of  $^{40}\text{K}$  [26]. Since then, the study of degenerate Fermi gases has become a rising star of the field. In late 2003, three groups reported on the achievement of molecular Bose-Einstein condensation using Feshbach resonances, the MIT group ( $^6\text{Li}$ ) [27], the JILA group ( $^{40}\text{K}$ ) [28], and the Innsbruck group ( $^6\text{Li}$ ) [29]. Early in 2004, the MIT group [30] and the JILA group [31] demonstrated pair condensation in strongly interacting Fermi gases with resonant interactions which is beyond the BEC regime. These experiments demonstrated a new macroscopic quantum state of ultracold matter beyond well-established BEC physics, which has stimulated an enormous interest in the field and opened a new chapter of quantum many-body physics - the BEC-BCS crossover [4, 5]. Finally, in 2005, the MIT group proved the superfluidity in a strongly interacting Fermi gas of  $^6\text{Li}$  by observing vortices in various

interaction regimes [32], 35 years after the discovery of superfluidity in  $^3\text{He}$ .

Moreover, the study of ultracold atoms in the optical lattice has had a profound impact in the condensed matter physics since the first realization of quantum phase transition from a superfluid to a Mott insulator in an optical lattice [33]. This experiment demonstrated the power of quantum simulation in an ultracold atomic system.

The discussion above focuses on a single species experiment. However, meanwhile the study of ultracold quantum mixtures has paved a new avenue in this field. First, it had been shown that the bosonic species could be used as a sympathetic coolant for the fermionic species providing a new and efficient method to cool fermions [34, 35, 36, 37]. Second, Interspecies Feshbach resonance was first discovered in the  $^6\text{Li}$  -  $^{23}\text{Na}$  [38] and  $^{87}\text{Rb}$  -  $^{40}\text{K}$  [39] systems, and later in  $^{85}\text{Rb}$  -  $^{87}\text{Rb}$  [40],  $^6\text{Li}$  -  $^{40}\text{K}$  [41],  $^6\text{Li}$  -  $^{87}\text{Rb}$  [42],  $^{39}\text{K}$  -  $^{87}\text{Rb}$  [43],  $^{41}\text{K}$  -  $^{87}\text{Rb}$  [44],  $^7\text{Li}$  -  $^{87}\text{Rb}$  [45],  $^{40}\text{K}$  -  $^{41}\text{K}$  [46],  $^6\text{Li}$  -  $^{41}\text{K}$  [46], and  $^{23}\text{Na}$  -  $^{40}\text{K}$  [47] systems (in chronological order). These discoveries allow the study of strongly interacting Bose-Fermi mixtures [48, 49, 46] as well as a strongly interacting Fermi-Fermi mixture of  $^6\text{Li}$  -  $^{40}\text{K}$  [50]. Third, thanks to the large mass imbalance in some of these systems, heteronuclear molecules in the absolute ground state possess a large dipole moment (from one tenth to a few Debye) in the presence of an external electric field, allowing the study of dipolar quantum gases [11, 12] (which will be elaborated more in Chapter 6). In particular, the successful formation of ultracold fermionic Feshbach molecules of  $^{23}\text{Na}^{40}\text{K}$ , the first fermionic molecule that is chemically stable in its ground state, provides us with the hope of studying a stable molecular Fermi gas with strong dipolar interactions.

A unique feature of ultracold quantum mixtures is that different atomic species can be addressed with different laser frequencies, opening up the possibility of new experiments, such as studying Anderson localization in a species-dependent optical lattice in which one species becomes immobile while the other species remains mobile [51] and exploring new phases in a bilayer Fermi gas [52].

Furthermore, with the newly discovered broad Feshbach resonances in the  $^{40}\text{K}$  -  $^{41}\text{K}$  and  $^{23}\text{Na}$  -  $^{40}\text{K}$  systems [46, 47], we are in a unique position to study the Bose polaron problem [53, 54, 55, 56, 57] (a single impurity swimming in a Bose condensate) - a direct analogy to the electron-phonon interaction - which will also be elaborated in Chapter 6.

But without Feshbach resonances all of these studies would not have been possible. In the next section, we will briefly discuss the concept of Feshbach resonances.

### 1.3 Feshbach resonances

A great advantage of ultracold atomic systems is the potential to tune the interaction strength between atoms via Feshbach resonances [3]. This tunability does not exist in traditional condensed matter experiments where the electron interactions are “cast in stone” by the material properties. Feshbach resonances were first introduced by Herman Feshbach in 1958 [58, 59] to study interactions between nuclei. The realization of Feshbach resonances in ultracold atomic systems was suggested first in a spin-polarized hydrogen by Stwalley in 1976 [60] and later in ultracold cesium atoms by Tiesinga *et al.* [61] in 1993. Eventually, the first Feshbach resonance in ultracold atomic systems was realized in a sodium BEC in 1998 by Inouye *et al.* at MIT [25]. For Feshbach resonances to happen, the scattering process requires at least two different scattering channels. Due to the coupling between these two channels, as the energy of a scattering state of one channel coincides with the energy of a real bound state of the other channel, a Feshbach resonance occurs. A channel is energetically open (closed) when the total energy of the two-atom system is above (below) the dissociation threshold energy of the incoming channel. In the case of alkali atoms, the open and closed channels are usually associated with different spin configurations and have different magnetic moments. Therefore, the energy difference between the

open and closed channels can be tuned by changing the external magnetic field. This means that the energy of a scattering state in the open channel can be shifted to match the energy of a bound state in the closed channel, giving rise to a Feshbach resonance. The  $s$ -wave scattering length in the vicinity of a Feshbach resonance can be tuned via the magnetic field according to [3]:

$$a = a_{bg} \left( 1 - \frac{\Delta_{res}}{B - B_{res}} \right), \quad (1.1)$$

where  $a_{bg}$  is the background scattering length defined at zero magnetic field,  $\Delta_{res}$  is the width of the resonance which depends on the coupling strength between the open and closed channels, and  $B_{res}$  is the resonance position. The  $s$ -wave scattering length  $a$  can, therefore, be tuned from positive to negative values through infinity, and the effective interaction changes accordingly from repulsive ( $a > 0$ ) to attractive ( $a < 0$ ). Right on top of the resonance, the two atoms are in a superposition state of two free atoms and a bound molecule, and the scattering length diverges. Therefore, the interparticle distance becomes the only relevant length scale and the interaction between atoms is as strong as quantum mechanics allows - the so-called universal regime.

## 1.4 The Fermi I machine

Along this line of research, we designed and constructed a new generation ultracold atom apparatus, the Fermi I machine, which is capable of cooling and trapping three different atomic species simultaneously - lithium, sodium, and potassium. It is the most versatile quantum simulator to date. It allows us to study Bose-Bose (e.g.,  $^{23}\text{Na}$  -  $^{39}\text{K}$ ,  $^{23}\text{Na}$  -  $^{41}\text{K}$ , and  $^{39}\text{K}$  -  $^{41}\text{K}$ ), Bose-Fermi (e.g.,  $^{23}\text{Na}$  -  $^6\text{Li}$ ,  $^{23}\text{Na}$  -  $^{40}\text{K}$ ,  $^{39}\text{K}$  -  $^6\text{Li}$ ,  $^{39}\text{K}$  -  $^{40}\text{K}$ ,  $^{41}\text{K}$  -  $^6\text{Li}$ , and  $^{41}\text{K}$  -  $^{40}\text{K}$ ), and Ferm-Fermi (e.g.,  $^6\text{Li}$  -  $^{40}\text{K}$ ) mixtures. We even have successfully created a triply degenerate quantum Bose-Ferm-Fermi mixture

of  $^{41}\text{K}$  -  $^6\text{Li}$  -  $^{40}\text{K}$  [46]. Right now, this machine is adjusted to create the ground state molecule of  $^{23}\text{Na}^{40}\text{K}$ , which is the most promising candidate to study quantum dipolar gases. With the power of cooling and trapping three different atomic species, the Fermi I machine is like a smaller version of the Large Hadron Collider which was designed to study all aspects of high energy physics. The Fermi I machine provides a platform to study a large variety of ultracold quantum gases in a bulk or potentially in optical lattices with a unique handle of atomic species. The detailed description of the machine is in Chapter 2.

## 1.5 Overview of this thesis

This thesis summarizes the research I have done during my PhD at MIT. The first chapter provides an overview and prospects of the field. The second chapter describes the nuts and bolts for constructing the Fermi I machine. The third chapter demonstrates a new efficient coolant -  $^{41}\text{K}$  - for the fermionic alkali species and shows that a quantum mixture of  $^{40}\text{K}$  and  $^{41}\text{K}$  could be an ideal system to study polaron physics with the observed broad interspecies Feshbach resonance. The fourth chapter introduces another new quantum mixture of  $^{23}\text{Na}$  and  $^{40}\text{K}$ . More than thirty Feshbach resonances are identified in this mixture. Motivated by the fact that NaK ground state molecules are stable against chemical reactions in contrast to KRb molecules, in the fifth chapter, we demonstrate the first formation of ultracold fermionic NaK Feshbach molecules. The properties of these newly born ultracold molecules such as lifetime and kinetic energy are also studied. The last chapter concludes this thesis and also provides an outlook on quantum dipolar gases and polaron physics which can be studied in the Fermi I machine in the future.

# Chapter 2

## A Multi-Species Machine : Fermi-I

*In this chapter, I am going to introduce a new apparatus for ultracold quantum gases constructed from the ground up by my colleagues and myself. It is capable of cooling and trapping three different alkali species (lithium, sodium, and potassium) simultaneously. It has produced all the science I am going to discuss in this thesis. The main vacuum chamber arrived from Sharon Vacuum in December 2008. After several months of intense construction, we obtained the first  $^{41}\text{K}$  BEC in October 2009, marking the beginning of the Fermi-I era.*

### 2.1 Overview

The design philosophy of the Fermi-I machine is to construct an apparatus which will allow us to study a large variety of quantum mixtures of alkali atoms. It inherits the design from BEC-III [62] with significant modifications which will be elaborated in this chapter. Atoms are first captured and trapped in a Magneto-Optical Trap (MOT) [63] and then loaded into an optically plugged magnetic trap where RF evaporation cools atoms down to a few tens of microkelvin [16]. Afterwards, atoms are transferred into an optical dipole trap (ODT) [64]. Eventually, when atoms are all in the ODT, a uniform magnetic field is switched on to bring atoms close to Feshbach resonances. All

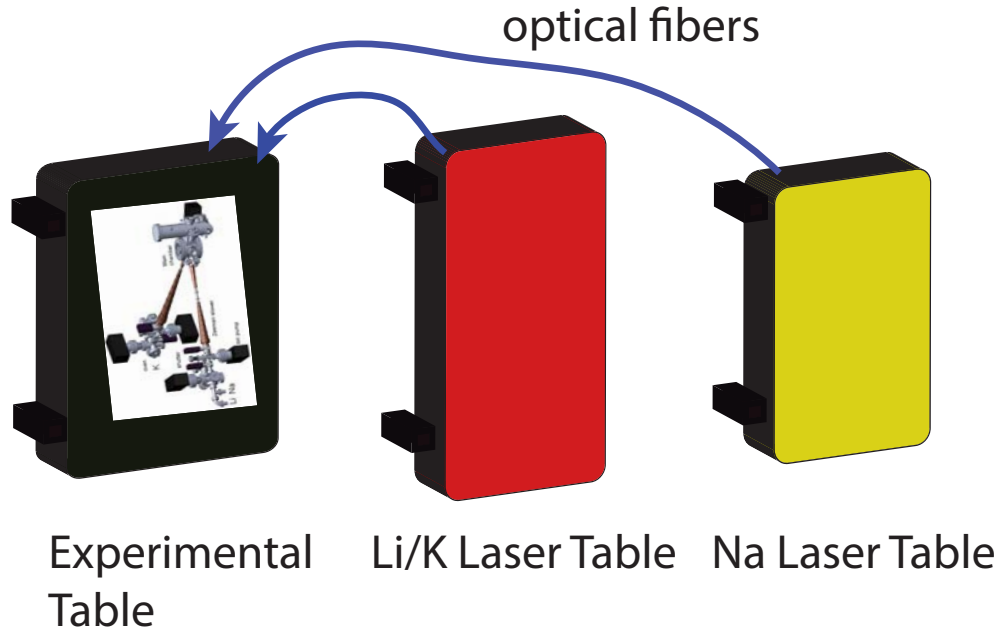


Figure 2-1: Overview of the Fermi-I laboratory. The potassium and lithium laser systems sit on the same optical table while the sodium laser system sits on an independent optical table. Laser light generated from the laser table is transmitted through optical fibers to the experimental table.

of these procedures sound straightforward; however below certain temperature (when the kinetic energy of atoms can no longer overcome the  $p$ -wave potential barrier) bosons can only collide through  $s$ -wave scattering and the collisions between identical fermions stop due to the Pauli blocking [65]. Therefore, it is usually required to make use of another species [66, 67, 37] or another spin state [26, 68] to sympathetically cool fermions into quantum degeneracy. Studies in Prof. Ketterle's group have shown that  $^{23}\text{Na}$  is a very efficient sympathetic coolant for  $^6\text{Li}$  [37]. Hence, in order to study a Fermi gas of  $^6\text{Li}$ , we decided to include  $^{23}\text{Na}$  in our system.

For the  $^{40}\text{K}$  source, Peter Zarth who was a Diploma student in Prof. Ketterle's group demonstrated that a significant number of  $^{40}\text{K}$  atoms ( $5 \times 10^7$ ) can be slowed and trapped in the MOT using a slower [69] that is operated with a natural potassium source which only contains 0.01%  $^{40}\text{K}$  [70]. Despite the fact that a reasonable atom

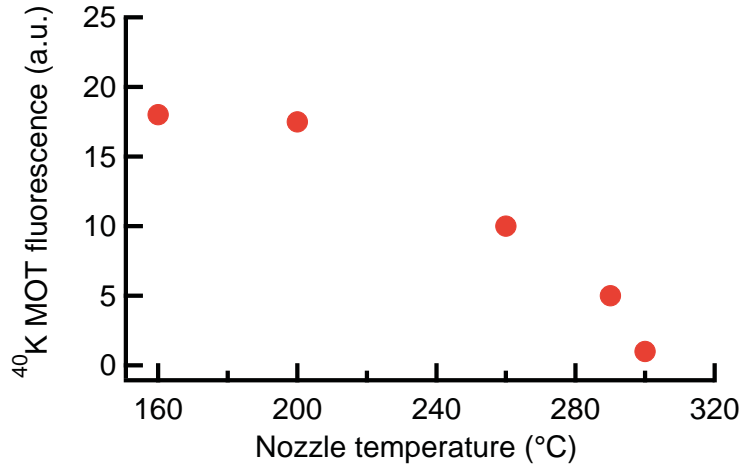


Figure 2-2: <sup>40</sup>K MOT fluorescence as a function of the nozzle temperature.

number of <sup>40</sup>K can be obtained by a slower, we still did not know if it could be extended from a double species oven designed by Claudiu Stan [71, 72] to a triple species oven (Li, Na, and K). To check the possibility of having a single slower for all three alkali species, we first needed to know if potassium could survive at a high nozzle temperature of 450 °C used in a double species oven due to the high melting point of lithium (180 °C). We monitored the <sup>40</sup>K MOT fluorescence signal as a function of the nozzle temperature and we observed that at a temperature of 450 °C, the <sup>40</sup>K MOT completely vanished due to the depletion of slow potassium atoms. Fig. 2-2 shows the <sup>40</sup>K MOT fluorescence signal as a function of the nozzle temperature. As a result, we realized that in order to cool and trap all three atomic species simultaneously, it is required to have an independent slower for potassium. Fig. 2-1 shows an overview of the Fermi-I laboratory and Fig. 2-3 shows a 3D schematic of the Fermi-I chamber.

## 2.2 Vacuum chamber design

Two main modifications are made in the Fermi-I vacuum chamber as compared to the BEC-III vacuum chamber [62]. First, because of the choice of the magnetic trap

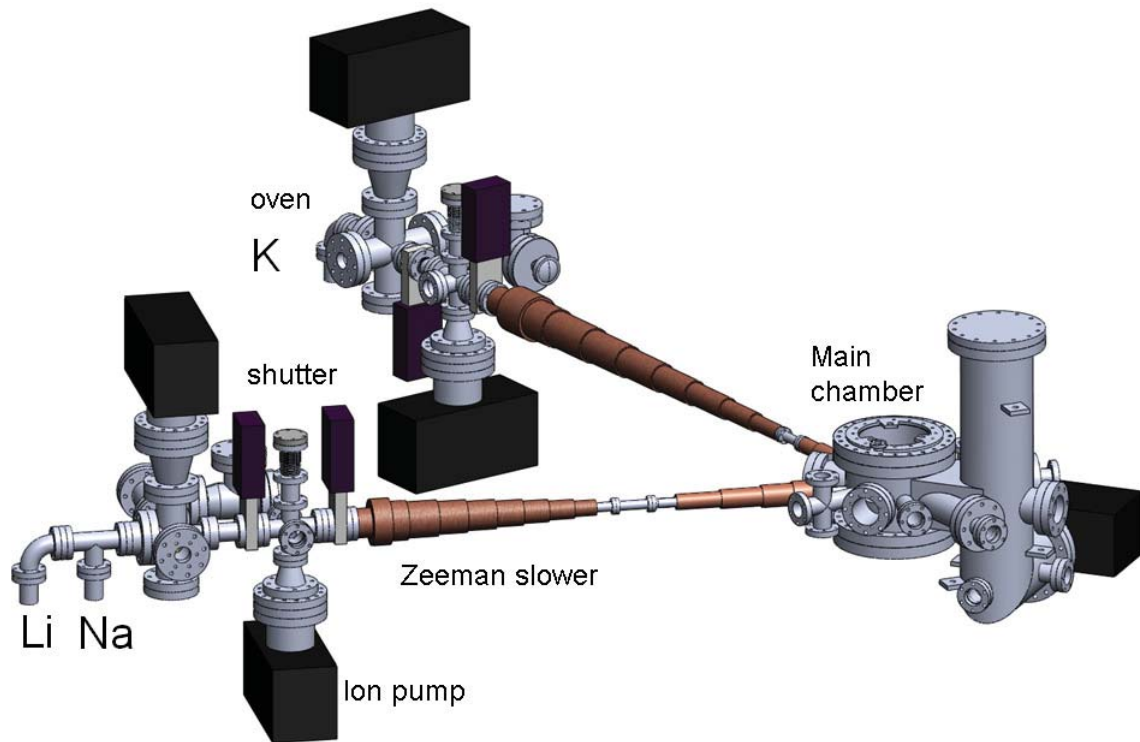


Figure 2-3: 3D schematic of the Fermi-I vacuum system. Two independent slowers for lithium/sodium and potassium, allowing us to simultaneously load large samples of each atomic species directly into a UHV chamber. Atoms are cooled, trapped and imaged in the main chamber.



configuration (we use an optically plugged quadrupole trap as opposed to an Ioffe-Pritchard trap in BEC-III), the Fermi-I chamber is allowed to have better optical access in the direction parallel to the trap symmetry axis (the vertical direction in our case, ports #5 and #6 in Fig. 2-4) than the BEC-III chamber. Without the complex cloverleaf coils which provide the radial confinement in a Ioffe-Pritchard trap, we are able to accommodate two  $\sim 4''$  diameter recessed viewports (the top and bottom bucket windows), as shown in Fig. A-1. The glasses on the viewports are made of fused silica which can stand higher temperature during baking and has better homogeneity (less birefringent) than quartz. The viewport assemblies were manufactured by UKAEA with a specified flatness of  $\lambda/5$  over the whole glass. In addition to the two  $4''$  recessed viewports, UKAEA also provided us three small recessed viewports (Fig. A-2) which were installed on the horizontal plane of the main chamber (ports #7, 9 and 10 in Fig. 2-4). Second, in order to accommodate one more slower, we had to sacrifice two viewports from the original BEC-III chamber (one for atomic beam and the other one for the slower laser beam). We chose the symmetric side from the BEC-III slower as our second slower ports. This choice was based on minimizing the interference between the two slower and maximizing optical accesses. Fig. 2-4 shows the schematics of the top and side views of our main chamber where atoms are trapped and cooled at the center, as illustrated by the red dots. MOT beams are sent in from the ports #1 to #6. Two imaging paths on the horizontal plane go through the ports #7  $\rightarrow$  #8 and #9  $\rightarrow$  #10 which are also used for two beams of the crossed ODT. The optical plug beam (18 W, 532 nm, and  $1/e^2$  beam waist  $60 \mu\text{m}$ ) enters from the port #9. The ports #11 to #14 are dedicated for slower. The Port #15 was used for initial pump down. Two ion gauges are placed on the ports #16 and #17. A Ti-sub pump is installed on the port #18. The detailed schematics of the Fermi-I vacuum system can be found in Appendix A.

## 2.2.1 Atomic ovens

The atomic ovens provide the sources of alkali atoms. They are the starting point of the whole atom trapping and cooling process. The “healthiness” of an oven often reflects on the final atom number in the quantum degenerate states.

Solid alkali atoms are initially placed inside the oven and then heated beyond their melting points to generate high vapor pressure for producing strong atomic beams. The goal of an atomic oven is to provide high atomic flux but still maintain the vacuum quality in the main chamber. Hence a small intermediate chamber is attached to the oven chamber serving as a buffer between the oven chamber and the main chamber as shown in Fig. 2-5. For the Li/Na oven, we basically followed the design by Claudiu Stan [72, 71]. However, at room temperature potassium has higher vapor pressure ( $\sim 10^{-8}$  torr) than lithium and sodium ( $< 10^{-11}$  torr) as shown in Fig. B-1, it is necessary to have a special setup (a “cold cup”) to collect the divergent atomic beam which otherwise can cause permanent deposition of potassium on the vacuum parts, limiting the vacuum quality. The cold cup is cooled down to  $-18^\circ\text{C}$  by a thermoelectric cooler (Swiftech MCW60-T) which is directly attached to the cold cup feedthrough. Fig. 2-7 shows a 3D schematic of the cold cup assembly. The 0.375" diameter copper feedthrough is for better heat conduction. At a temperature of  $-18^\circ\text{C}$ , the vapor pressure of potassium is less than  $10^{-8}$  torr which is comparable to the typical pressure in the oven chamber. A differential pumping tube (DPT-I in Fig. 2-5) with dimensions of 4.5" long and 0.25" OD (0.18" ID) is installed between the oven chamber and the intermediate chamber. In the ultra-high vacuum regime where the mean free path of the gas particles is larger than the size of the chamber, a tube of length  $l$  and diameter  $D$  has conductivity  $C \propto l^2/D^2$  and the ratio between the pressures at the two ends of this tube follows [73]:

$$C(P_1 - P_2) = SP_2 \rightarrow \frac{P_1}{P_2} = \frac{S}{C} \quad (2.1)$$

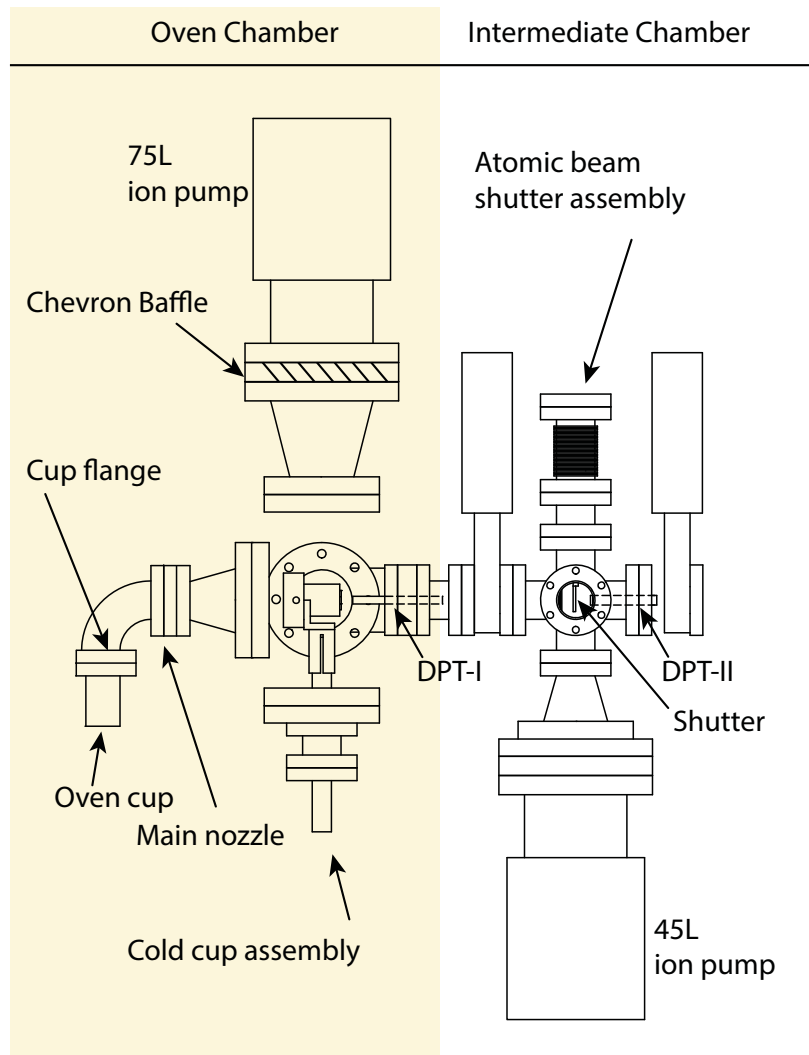


Figure 2-5: An exploded view of the potassium oven which is made of two small vacuum chambers: an oven chamber and an intermediate chamber. The potassium source is placed inside the oven cup and heated up to  $190^{\circ}\text{C}$  to provide a high flux atomic beam. A cold cup assembly is designed to collect the divergent atomic beam from the nozzle to prevent deposition of potassium on the vacuum parts. Two differential pumping tubes (DPT-I and DPT-II) are installed to achieve high differential pressure. A chevron baffle (custom made from Sharon Vacuum) is used to prevent the 75 L/s ion pump from being poisoned by alkali atoms. The typical pressure in the oven chamber is  $\sim 5 \times 10^{-8}$  torr and  $\sim 1 \times 10^{-10}$  torr in the intermediate chamber during operation.

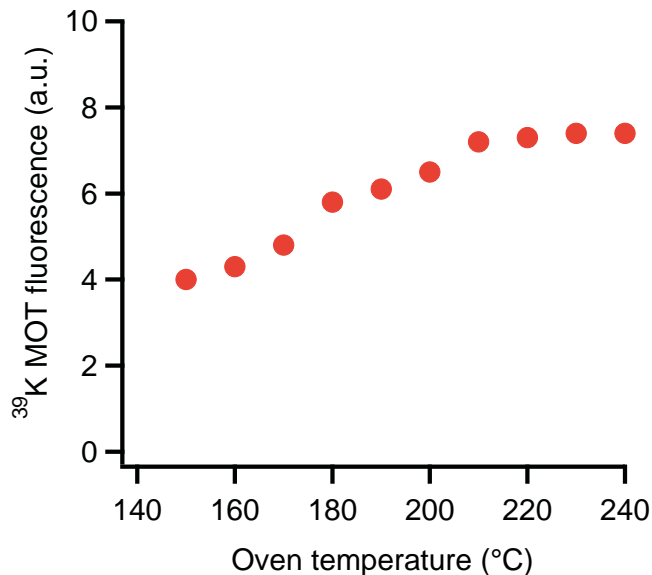


Figure 2-6: <sup>39</sup>K MOT fluorescence signal as a function of the oven cup temperature. Around 200 °C the <sup>39</sup>K MOT starts to saturate.

where  $S$  is the pumping speed in the low pressure region and here we have assumed  $P_2 \ll P_1$ . For a typical pumping speed of 45 L/s, a pressure differential up to 3 orders of magnitude can be reached between the oven chamber and the intermediate chamber. Another differential pumping tube (DPT-II in Fig. 2-5) is installed after the intermediate chamber before the slower to further improve the vacuum quality in the main chamber. The design of the differential pumping tubes can be found in Claudiu Stan's thesis [72]. An atomic beam shutter is placed in the intermediate chamber to switch off the atomic beam. Its on-off motion is realized by connecting the shutter stick to a bellow which can be slightly bent with an external actuator outside vacuum. Two pneumatic gate valves (MDC GV-1500M-P, later on both gate valves failed on the K oven side and one gate valve, closer to the oven chamber, failed on the Li/Na oven side) and one manual valve (VAT 48132-CE01-0002, installed after the MDC valves failed) are used to protect the main chamber during alkali source change in each oven.

To find the optimal temperature for operating the K oven, we measured the <sup>39</sup>K

MOT fluorescence signal as a function of the oven temperature. Fig. 2-6 shows that the  $^{39}\text{K}$  MOT fluorescence signal saturates at an oven cup temperature of  $210^\circ\text{C}$ . As we know, the lifetime of atomic source reduces exponentially with the increase of oven temperature after their melting point. In order to save the potassium source, we decided to operate the oven at  $190^\circ\text{C}$  as a compromise. Table 2.1 lists the temperature settings for different parts of the K oven. It is worthwhile to note that we implemented a micro-channel nozzle in the early stage of our experiment (see Fig. 2-8) for saving atoms and collimating atomic beams better. Unfortunately, it could easily clog after several months of usage. As a result, it had been replaced by the old nozzle design from Claudiu Stan during an atomic source change. For the Li/Na oven temperature, we used the settings from BEC-I as listed in table 2.2.

Main Nozzle	K Cup	K Cup Flange
190	190	220

Table 2.1: Potassium oven temperature settings ( $^\circ\text{C}$ ).

Main Nozzle	Li Cup	Li Cup flange
440	400 (390)	410 (390)
Mixing Nozzle	Na Cup	Na Cup Flang
440	300	300

Table 2.2: Lithium-sodium oven temperature settings ( $^\circ\text{C}$ ). The numbers in the parentheses are used when operating sodium oven only.

## 2.2.2 Vacuum Pumps

The lifetime of ultracold atoms strongly depends on the the environmental vacuum quality since any residual gas particles can collide with trapped atoms and remove them from the trap. To maintain an ultra-high vacuum environment, the Fermi-I machine employs five ion pumps (three  $75\text{ L/s}$  and two  $45\text{ L/s}$ , from Gamma Vacuum). A commercial Ti-sub pump (from Varian Vacuum) is installed next to the main

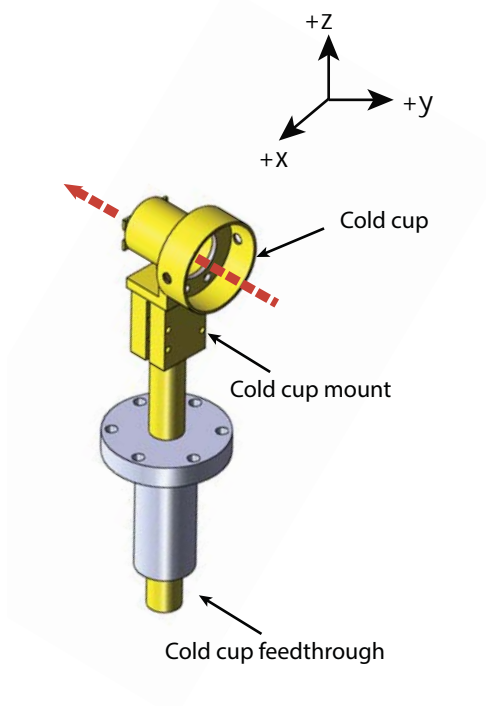


Figure 2-7: 3D schematic of the cold cup assembly. The parts in gold are made of 316 copper with nickel plated on their surface for better thermal contact. The red dashed arrow indicates the direction of the atomic beam.

chamber on a large stainless steel tube (the port #18 in Fig. 2-4) to maximize the pumping surface. On top of these traditional pumping methods, we also implemented a special vacuum coating technique in our vacuum chamber to further improve its vacuum quality:

### **Titanium-Zirconium-Vanadium coating**

Some materials (e.g. barium, titanium etc.) have special chemical absorption properties for trapping gases - the so-called getter. Generally, the bonding between gas particles and the getter occurs only between the first few layers of gas molecules and the surface. Therefore, as long as the getter have absorbed a few layers of gas particles, it becomes saturated and loses its pumping property. By heating the getter, it is possible to “clean up” the getter surface and revive its pumping property - a so-called

Micro-channels

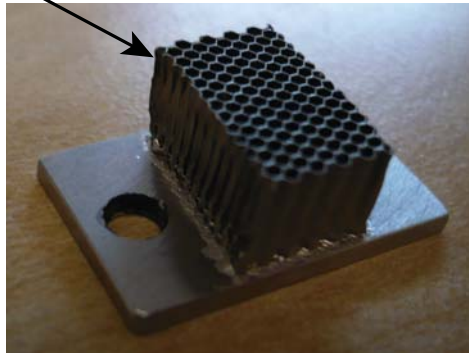


Figure 2-8: The micro-channel nozzle. Each channel is made of a tiny stainless steel tube with a diameter of 0.8 mm and a length of 6 mm

sorption process (gas particles diffuse into the inner layers of the getter). However, the required temperature for the sorption process to happen in these materials are generally higher (e.g. Ti :  $\sim 600^\circ\text{C}$  [74]) than the temperature that most vacuum windows can stand ( $\sim 250^\circ\text{C}$ ). Therefore, it becomes difficult to integrate the getter pumps with the vacuum windows because depositions can happen on the windows during coating.

A special kind of alloy has been developed to reduce the sorption temperature - an alloy made of Titanium (Ti), Zirconium (Zr) and, Vanadium (V). This alloy can have a sorption temperature as low as  $180^\circ\text{C}$ . Hence, one can first coat this alloy on the vacuum chamber with viewports being sealed by blanks and then change the blanks to windows after the coating has been completed. Although the coating surface is saturated during the window change, a 24 hours  $180^\circ\text{C}$  baking can then reactive the coating.

This alloy was first invented in CERN and realized in the Large Hadron Collider [75, 76]. For this alloy to work, it requires a deposition of roughly even thickness of each metallic layer and the total thickness of the coating needs to  $>300\text{ nm}$ . Instead of sputtering coating (the technique being used in LHC which requires a high voltage

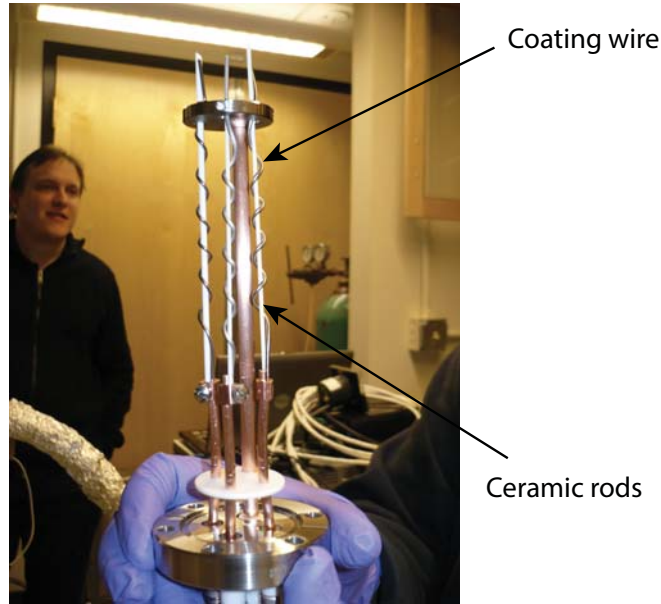


Figure 2-9: A picture of a “ready to go” TiZrV coating assembly. The white rods are the ceramic rods for supporting the Ti, Zr, and V wires.

source), we developed a simple and rapid coating method by replacing a commercial Ti-sub pump with the Ti, Zr, and V wires as shown in Fig. 2-9. With finely adjusted current applied on each wire, we were able to deposit the desired thickness of each metallic layer. It is important to note that these wires, especially the V wire, can sag during the coating process. We overcame the problem by adding ceramic rods to support them (the white rods in Fig. 2-9). Initially, it was not very trivial for us to find the correct current for each wire; however, with some trials eventually we realized that the thickness of a metallic layer, deposited on a microscope slide, could be estimated from its transmissivity to a laser beam. So we first coated each metal individually in a test chamber with a microscope slide placed in a fixed distance away from the coating assembly. After coating for a certain amount of time, we took out the microscope slide and measured the transmissivity of a normal incidence laser beam (767nm). From the transmissivity and index of refraction of each metal [77, 78, 79] we were able to estimate the thickness of the coating. A web service (<http://www.luxpop.com>) provides

the function for calculating the thickness of a metallic layer from its transmissivity of monochromatic light. Table 2.2.2 summarizes the experimentally measured coating parameters for current, voltage, and resulted thickness.

Ti (dia. 1.5mm)		
Current (A)	Voltage (V)	Thickness after 10 mins coating (nm)
31	4.2	55
31.5	4.25	110
32	4.3	175
33	4.46	opaque

Zr (dia. 1.5mm)		
Current (A)	Voltage (V)	Thickness after 10 mins coating (nm)
40	3.6	19
42	3.99	65
45	4.29	135

V (dia. 1.2 mm)		
Current (A)	Voltage (V)	Thickness after 10 mins coating (nm)
33	4.95	163
35	5.46	opaque

Table 2.3: Summary of experimentally found parameters for the TiZrV coating. The coating thickness is measured from a microscope slide placed 10 cm away from the coating assembly and the total coating time is 10 minutes.

Elements	n	k
Ti	2.787	2.872
Zr	2.4	1.1
V	3.231	3.106

Table 2.4: A list of indices of refraction  $N=n+ik$  for Ti, Zr, and V at room temperature [77, 78, 79].

## 2.3 Zeeman slowers

In this section, I will describe the designs of our Zeeman slowers (K and Li/Na Zeeman slowers). The main advantage of using a Zeeman slower for potassium is that we are

able to cool and study all three potassium isotopes together. The essential feature of a slower is that the magnetic fields maintain the resonance between atoms in the atomic beam and the slower laser beam by compensating for the Doppler shifts using the Zeeman effect [80]. For the Li/Na slower, we basically followed the design from Ananth Chikkatur [62] with some small modifications. However, for the K slower, we needed to design it from scratch. Two types of slowers are commonly used: the positive-field and the spin-flip slowers [15]. We have implemented a spin-flip slower since it brings about several advantages. First, a smaller maximum absolute value of the magnetic field is required. Second, the slower laser beam is non-resonant with the atoms exiting the slower and thus does not push them back into the slower, neither it perturbs the atoms trapped in the MOT. Each spin-flip slower contains two parts: 1. a section where the magnetic field is decreasing along the beam path, the “decreasing field” part, and 2. a section where the magnetic is increasing along the beam path, the “increasing field” part. Both Li/Na and K slowers are made of 1/8” square tubing with a 0.0625” square hole wound on a brass tube with 1” OD (0.87” ID). The advantage of square tubing is that it maximizes electrical conductivity per unit volume, leaving no gaps between wires. The hollow wires allow for water cooling because pressurized water can flow through the hollow core and cool the current carrying wires. The wire was purchased from Small Tube Products, and was insulated by Double Dacron Glass.

In order to keep the slower laser beam always on resonance with atoms, the profile of the magnetic field as a function of distance must go as described by equation (2.2).

$$B(z) = B_i - \frac{kv_c}{\mu_B} \left( 1 - \sqrt{1 - \frac{2fa_{max}z}{v_c^2}} \right) \quad (2.2)$$

where  $B_i$  is the initial magnetic field of the decreasing slower,  $v_c$  is the capture velocity ( $kv_c = \mu_B B_i - \delta$ , where  $\delta = 2\pi \times$  detuning),  $\mu$  is Bohr magneton,  $a_{max} = \frac{\hbar k \Gamma}{2M}$  is the maximum deceleration (requiring infinite laser power), and  $f$  is the fraction of the

maximum deceleration that can be achieved given the finite intensity of a slower laser beam and it also acts as a fudge factor that is chosen to compensate for imperfections.

Table 2.5 lists our design parameters for both slowers.

Species	$^{40}\text{K}$ (K slower)	$^{23}\text{Na}$ (Li/Na slower)
transition used	$F = 9/2 \rightarrow F' = 11/2$	$F = 2 \rightarrow F' = 3$
detuning (MHz)	-180	-1000
oven temperature (K)	460	553
max. capture velocity (m/s <sup>2</sup> )	540	950
$f$ factor	0.6 (0.4)	0.6 (0.2)
decreasing slower length (cm)	90	52
increasing slower length (cm)	18	38

Table 2.5: Design parameters for the K and the Li/Na slowers. The K slower is optimized for slowing  $^{40}\text{K}$  and the Li/Na slower is optimized for slowing  $^{23}\text{Na}$ . The  $f$  factors in the parentheses are used for the increasing parts, whereas for decreasing parts.

### 2.3.1 The potassium Zeeman slower

Some design choices needed to be made when choosing the detuning for the K slower beam in order to avoid possible frequency conflicts between the slower and MOT laser beams of the three isotopes. Table 2.3.1 summarizes the conflicts we found in different detunings (Fig. 2-10 provides a graphical representation of the detuning conflicts). At the end, we chose -180 MHz as our K slower laser beam detuning. Fig. 2-11 shows the winding profile for the K slower. The unusually long decreasing part is because of the choice of the detuning. Fig. 2-12 and Fig. 2-13 show the measured, simulated, and ideal profiles for the decreasing and increasing parts of the K slower, respectively.

### 2.3.2 The lithium-sodium Zeeman slower

Basically, the Li/Na slower followed Ananth Chikkatur's design [62] with very small modifications. The slower was made to maximize the cooling efficiency for sodium (it will automatically work for lithium as well, since lithium is lighter than sodium which

Detuning (MHz)	Conflicts	
-110	<sup>41</sup> K Slower repumping	VS <sup>39</sup> K MOT repumping
-170	<sup>39</sup> K Slower repumping	VS <sup>41</sup> K MOT cooling
-260	<sup>41</sup> K Slower repumping	VS <sup>41</sup> K MOT cooling
-280	<sup>40</sup> K Slower cooling	VS <sup>41</sup> K MOT repumping
-330	<sup>41</sup> K Slower cooling	VS <sup>39</sup> K MOT cooling
-370	<sup>40</sup> K Slower cooling	VS <sup>39</sup> K MOT repumping
-450	<sup>39</sup> K Slower cooling	VS <sup>40</sup> K MOT repumper
-480	<sup>39</sup> K Slower repumping	VS <sup>39</sup> K MOT cooling
-520	<sup>40</sup> K Slower cooling	VS <sup>41</sup> K MOT cooling
-570	<sup>41</sup> K Slower repumping	VS <sup>39</sup> K MOT cooling
-760	<sup>41</sup> K Slower cooling	VS <sup>40</sup> K MOT repumping
-830	<sup>40</sup> K Slower cooling	VS <sup>39</sup> K MOT cooling
-910	<sup>39</sup> K Slower repumping	VS <sup>40</sup> K MOT repumping
-1000	<sup>41</sup> K Slower repumping	VS <sup>40</sup> K MOT repumping

Table 2.6: Possible detuning conflicts considered in the potassium slower design. In order to avoid conflicts, we chose -180 MHz for the detuning.

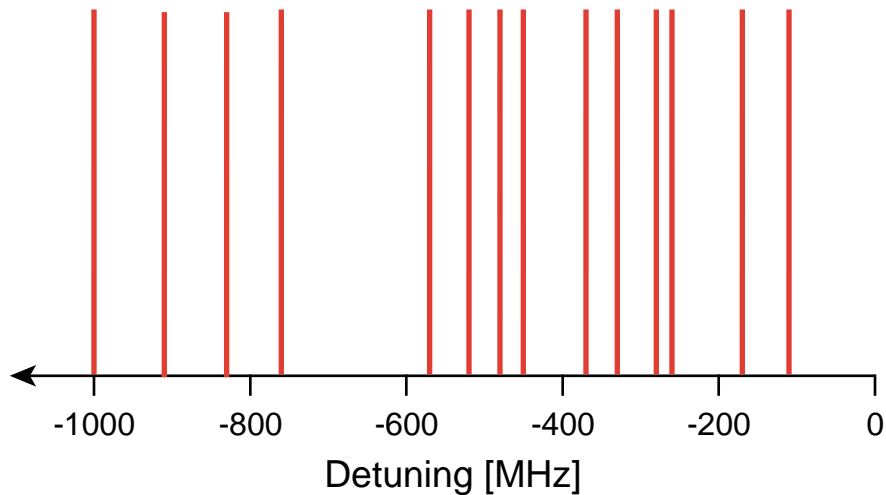


Figure 2-10: Graphical representation of possible detuning conflicts considered in the potassium slower design. The vertical lines represent the conflicts on different detunings.

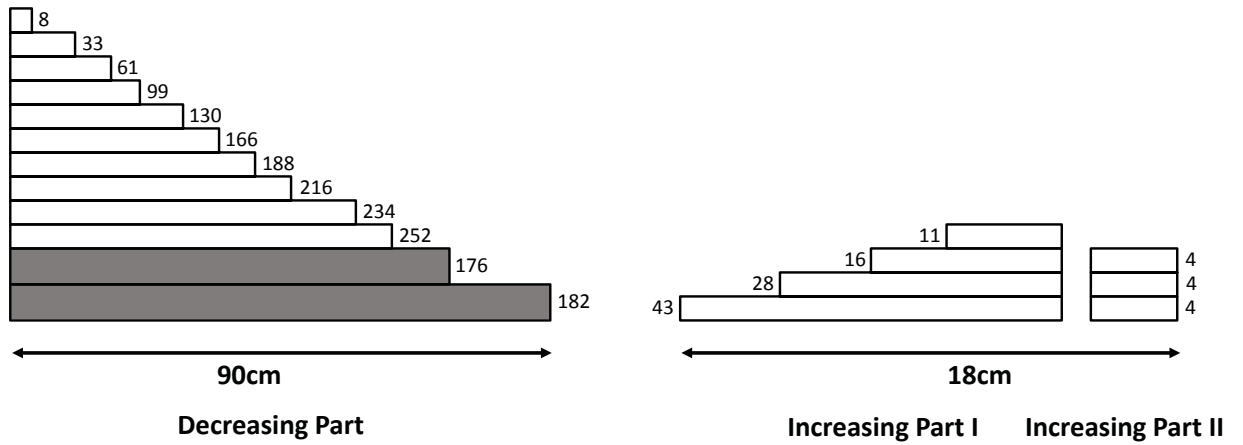


Figure 2-11: The winding profile of the potassium slower. The numbers indicate the turns of winding. The bottom two layers of the decreasing part slower (covered in gray) are made of 3/16" square copper wires, instead of 1/8" wires used elsewhere.

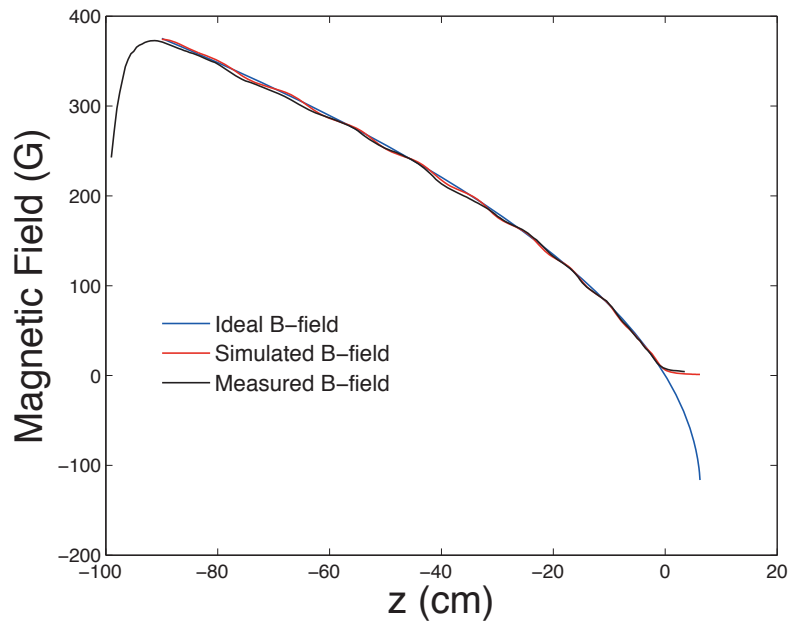


Figure 2-12: The potassium decreasing part slower magnetic field profiles: the ideal (blue), simulated (red), and measured (black) profiles.

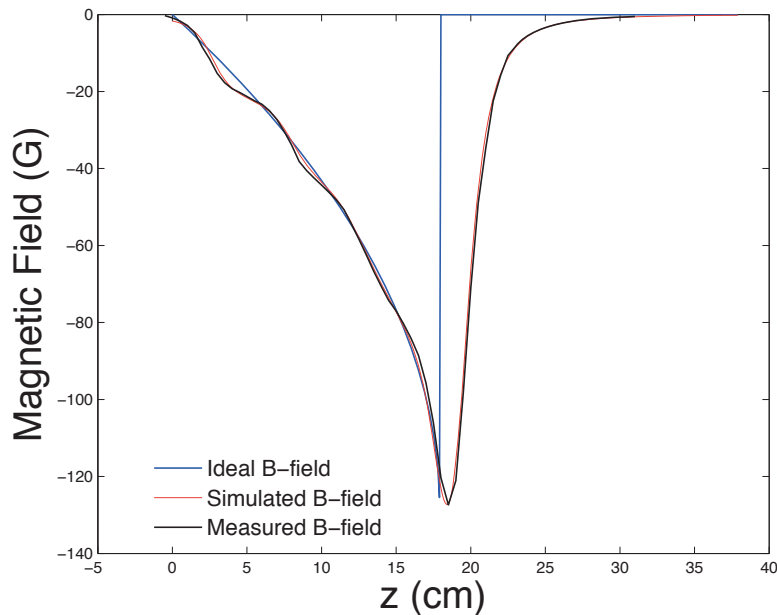


Figure 2-13: The potassium increasing part slower magnetic profiles: the ideal (blue), simulated (red), and measured (black) profiles.

is equivalent to having a reduced  $f$  factor for sodium). The detuning of the slower laser beam was chosen to be -1.0 GHz for sodium in order to use the same laser setup as in BEC-I. Fig. 2-14 shows the winding profile of the Li/Na slower. Fig. 2-15 and 2-16 show the measured, simulated, and ideal field profiles for the decreasing and increasing parts of the Li/Na slower, respectively.

### 2.3.3 Getting the slowers to work

Although the measured fields match with the simulated fields pretty well for both slowers, the real challenge comes after mounting the slowers onto the main experimental apparatus. Will the slowers actually work? The best settings for the detuning and current can be a bit off from the theoretical values which makes observing the first MOT signal difficult. Without a clear MOT signal, tweaking the slower settings to maximize the flux of slow atoms is not trivial. Experimentally, we figured out

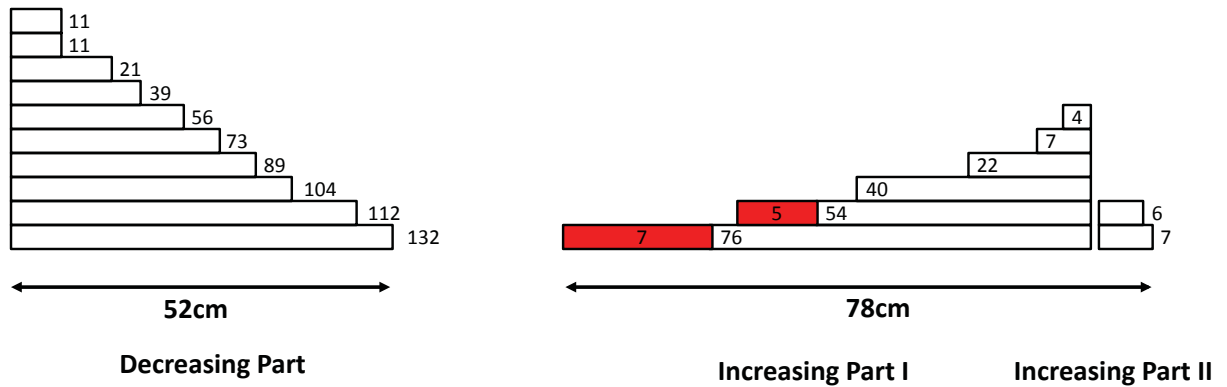


Figure 2-14: The winding profile of the lithium-sodium slower. The numbers indicate the turns of winding. The last part of the bottom two layers of the increasing part slower (covered in red) are wound in double spacing.

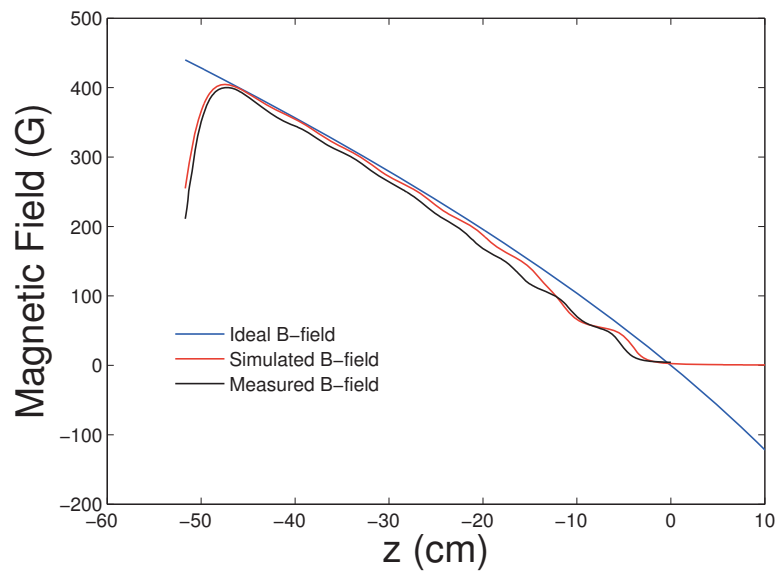


Figure 2-15: The lithium-sodium decreasing part slower magnetic profiles: the ideal (blue), simulated (red), and measured (black) profiles.

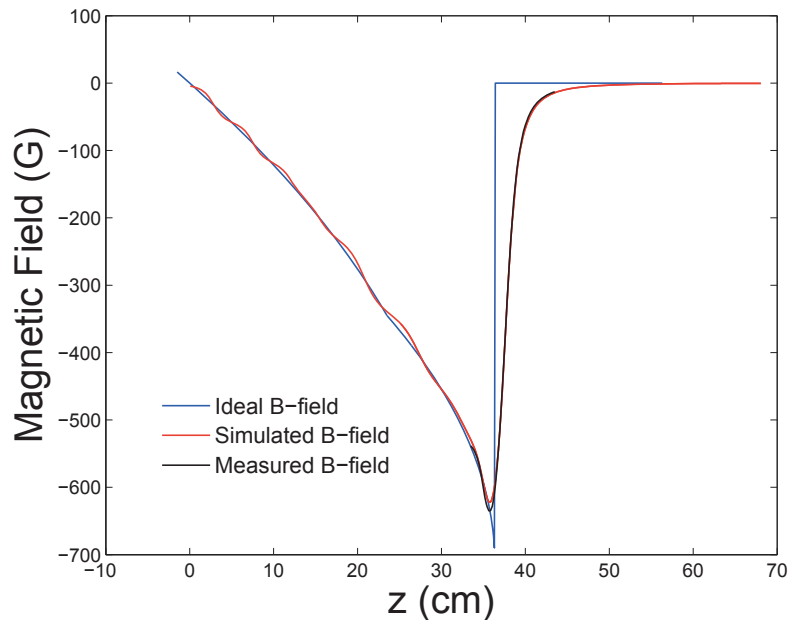


Figure 2-16: The lithium-sodium increasing part slower magnetic profiles: the ideal (blue), simulated (red), and measured (black) profiles.

that the best slower settings could be obtained by sending in one of the MOT cooling beams (this beam needs to be in the Doppler sensitive direction with respect to the atomic beam - the direction that is not perpendicular to the atomic beam) and maximizing the atomic fluorescence signal illuminated from that cooling beam. This method gave us a signal that was proportional to the number of slow atoms. Table 2.7 summarizes the current settings we found after maximizing the MOT signal for all species.

	Increasing Part I	Increasing Part II	Decreasing	Compensation
${}^6\text{Li}$	35.5A	107.7A	19.0A	11.0A
${}^{23}\text{Na}$	35.8A	107.7A	18.3A	11.0A
${}^{39}\text{K}$	5.7A	20.6A	7.6 (5.3)A	1.5A
${}^{40}\text{K}$	6.2A	23.4A	11.4 (5)A	1.4A
${}^{41}\text{K}$	5.2A	21.6A	7.8 (6.7)A	1.3A

Table 2.7: List of experimentally found best slower currents for each species. The values in the parentheses are used in the bottom two layers of the potassium slower.

## 2.4 Magneto-optical traps (MOT)

The MOT is the first stage of all ultracold atom experiments. Its number and temperature often reflects on the final atom number in the quantum degenerate states after forced evaporation. Therefore, it is crucial to have a “healthy” MOT to begin with. However, in our experiment, this becomes challenging since the experimental setup needs to accommodate three different alkali species simultaneously in the presence of light-assisted collisions. A detailed description of the physical principle of MOT can be found in Ref. [63]. Here we will focus on discussing our setup and how to obtain the best MOT for each species.

### 2.4.1 Configuration of the MOT beams

In order to simultaneously trap three different alkali species, it is required to have a delicate arrangement for the laser beams due to space constraints. For lithium and potassium, we use fiber manifolds ( $2 \times 4$  for lithium and  $4 \times 4$  for potassium, the first number indicates the number of input fibers and second number indicates the number of output fibers) to combine the MOT cooling and repumping beams on the laser table and transmit them to the experimental table. A non-polarization-maintaining (non-PM)  $4 \times 4$  fiber manifold was used in the potassium laser setup (4 inputs were used for the MOT cooling and repumping beams of two potassium isotopes) but it suffered from a problem that the output power did not distribute evenly in all the fibers. Balancing the MOT beams was extremely hard with this non-ideal fiber manifold. After we replaced it with a PM  $4 \times 4$  fiber manifold, the issue of imbalance output power was solved and the potassium MOT was significantly improved. In the lithium setup, fortunately, the non-PM  $2 \times 4$  fiber manifold does not cause the same problem. On the experimental table the four output fibers are arranged in such a way that two fibers are dedicated for the MOT beams in the vertical direction (the top and

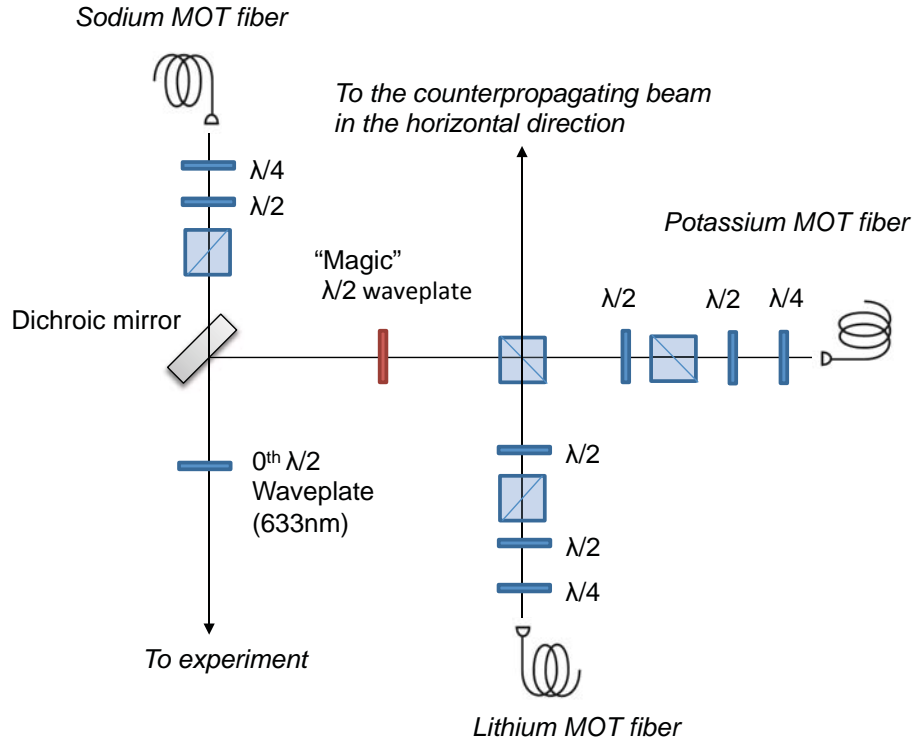


Figure 2-17: Schematic of the MOT beams setup on the experimental table. In front of each fiber output, we place a compact optics module (PBS +  $\lambda/2$  +  $\lambda/4$  waveplates) to clean up the polarization for each beam. The potassium and lithium MOT beams are first combined on a PBS and then sent through a “magic”  $\lambda/2$  waveplate, which only affects the polarization of the potassium beam, to make both beams have the same polarization. Finally the sodium MOT beam is combined with the lithium and potassium MOT beams on a dichroic mirror before sending them into the chamber.

bottom beams) and the beam from each of the other two fibers is split into the beams that become a counter propagating beam pair for one horizontal axis of the MOT. The lithium and potassium MOT beams are first combined on a polarizing beam splitter (PBS) and then sent through a “magic waveplate” (from CVI) which only rotates the polarization of the potassium MOT beams. After this magic waveplate, the polarizations of the potassium and lithium MOT beams can be aligned on the same axis. Unlike the potassium and lithium MOT beams which carry both the cooling and repumping light, the sodium MOT beams only contain the cooling light.

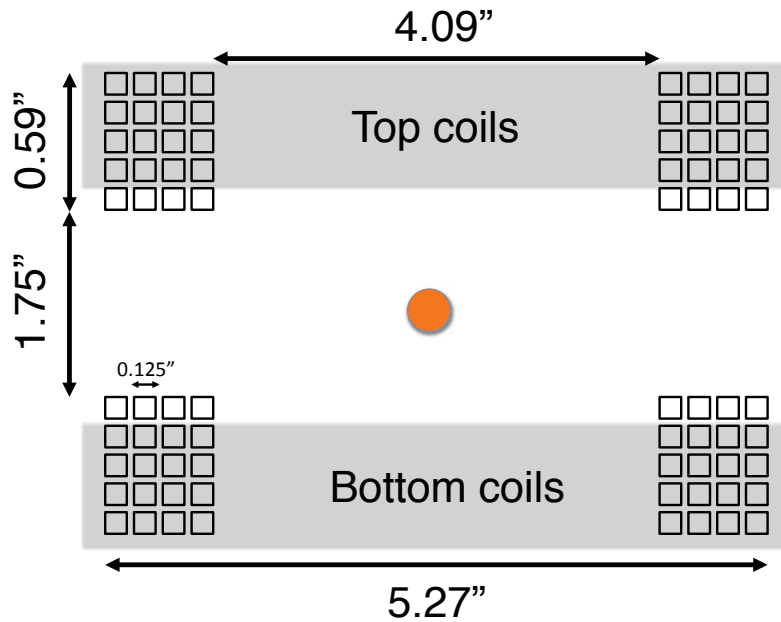


Figure 2-18: Configuration of the MOT, magnetic trap (anti-Helmholtz configuration), and Feshbach coils (Helmholtz configuration). Only the first four layers (covered in gray) are used for the MOT, magnetic trap, and Feshbach magnetic fields. The fifth coil is usually for providing a magnetic field gradient to separate atoms with different magnetic moments in a Stern-Gerlach experiment. The red dot indicates the MOT position.

An  $1 \times 6$  non-PM fiber manifold is used to bring the sodium MOT cooling light from the laser table to the experimental table. Each output fiber of the sodium fiber manifold is dedicated to one MOT beam. The sodium MOT cooling beams are then combined with the lithium and potassium MOT beams on a dichroic mirror as shown in the Fig. 2-17 before sending them into the main chamber. For the sodium MOT repumping light, a single laser beam is used to pump only the outer shell of the sodium MOT by imaging a dark spot (2 mm dia.) at the position of the MOT to achieve a high density dark MOT [81].

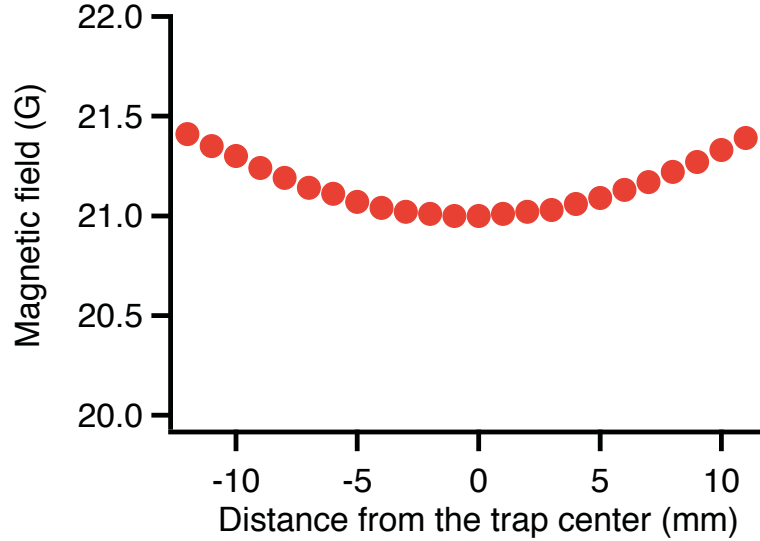


Figure 2-19: Measurement of the magnetic field as a function of the distance to the coil center in the Helmholtz configuration at 7A. The residual curvature is  $0.07 \text{ G/cm}^2/\text{A}$ .

### 2.4.2 MOT coils

The MOT, magnetic trap, and Feshbach magnetic fields are all created by the same coils in our experiment. The last two will be discussed in later sections. The coils are wound from  $1/8''$  square copper wire made of copper alloy 101 and have a  $0.0625''$  square hole - it is the same wire used as in slowers. Fig. 2-18 shows the winding profile of the coils. It is designed to be in the anti-Helmholtz configuration for the MOT and magnetic trap stages, but in Helmholtz configuration for the Feshbach field stage. Fig. 2-19 shows our “off-line” measurement of the magnetic field as a function of the distance from the coil center in the Helmholtz configuration. In this configuration, at the center in between the coils, the strength of the magnetic field as a function of current was measured to be  $\sim 3.0 \text{ G/A}$  (the residual curvature is  $0.07 \text{ G/cm}^2/\text{A}$ ). For the anti-Helmholtz configuration, we measured the magnetic field gradient by finding the trap bottom of  $^{41}\text{K}$  atoms in the stretched state. We found that at 13.0 A atoms started leaking out from the magnetic trap at the point where gravity exactly canceled the force from the magnetic field. Thus, we measured the magnetic field

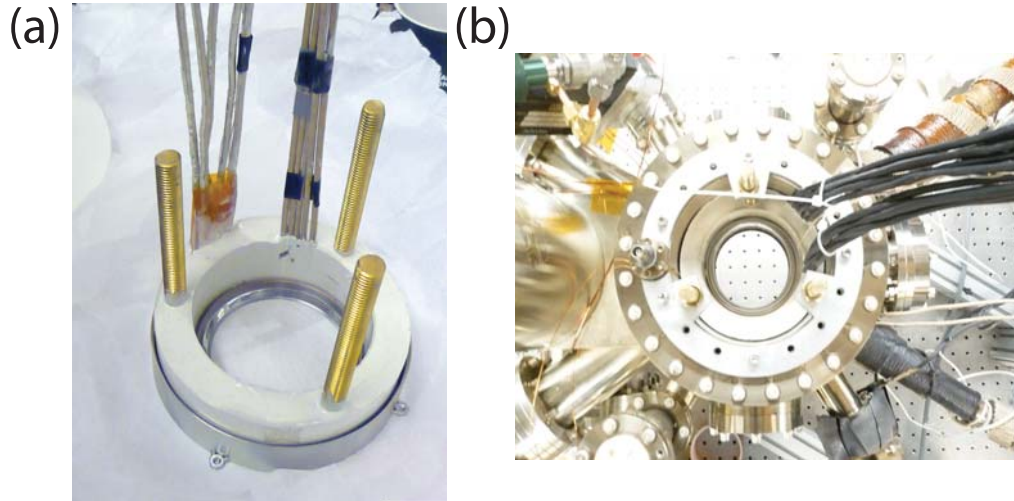


Figure 2-20: Pictures of the real coils which provide the MOT, magnetic trap, and Feshbach magnetic fields. (a) A picture shows that the coils sit in the ring shape groove around the 4" glass window. (b) A top view of the main chamber shows that coils are secured by mounting the brass rods to the recessed viewports

gradient as a function of current to be  $0.55 \text{ G/cm/A}$ . Fig. 2-20 shows a picture of the actual coils. The coils sit in a ring shape groove next to the glass window inside the top and bottom recessed viewports. The separation between the top and bottom coils is  $1.75''$ . Both coils are secured by brass rods (the rods in Fig. 2-19(a)) to the main chamber. A detailed description of how to make trap coils can be found in Christian Schunck's Diploma thesis [82].

### 2.4.3 Parameters for the MOTs

In this subsection, I will describe how we trap and optimize the potassium MOT for each isotope. It was a long but exciting journey for us to figure out the correct MOT parameters for all three potassium isotopes. Unlike  $^6\text{Li}$  and  $^{23}\text{Na}$ , for which the cooling and trapping techniques are well established at MIT [17, 83, 37, 84], the study of potassium isotopes was relatively new by the time when I joined the group.

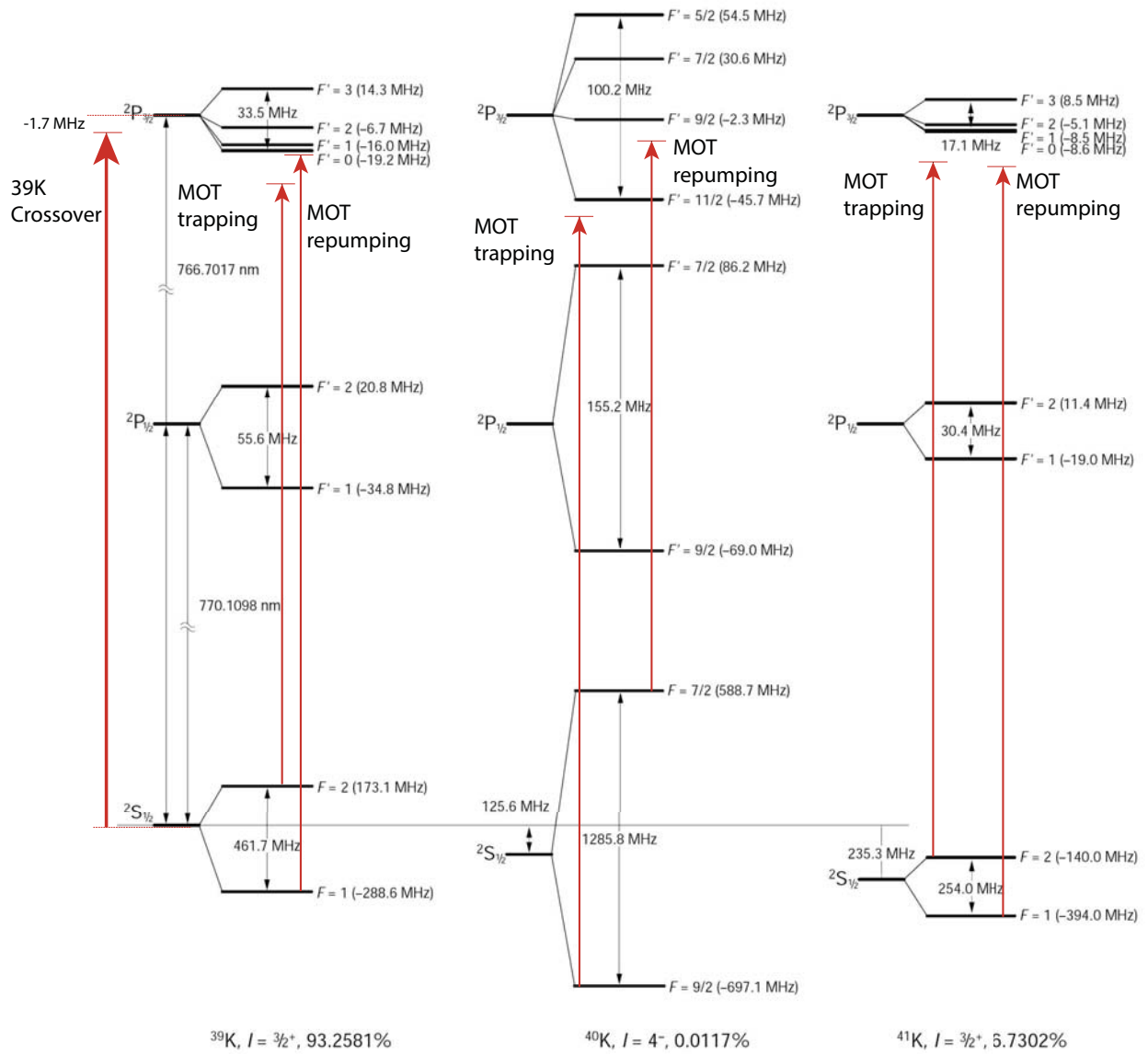


Figure 2-21: The potassium energy level scheme. The arrowed lines indicate the cooling and repumping transitions used in each isotopes. For the  $^{39}\text{K}$  MOT, we use a cooling beam with a detuning  $\Delta_{(F=2 \rightarrow F'=3)} = -47\text{ MHz}$  and a repumping beam with a detuning  $\Delta_{(F=1 \rightarrow F'=2)} = -15\text{ MHz}$ . For the  $^{40}\text{K}$  MOT, we use a cooling beam with a detuning  $\Delta_{(F=9/2 \rightarrow F'=11/2)} = -14\text{ MHz}$  and a repumping beam with a detuning  $\Delta_{(F=7/2 \rightarrow F'=9/2)} = -11\text{ MHz}$ . For the  $^{41}\text{K}$  MOT, we use a cooling beam with a detuning  $\Delta_{(F=2 \rightarrow F'=3)} = -30\text{ MHz}$  and a repumping beam with a detuning  $\Delta_{(F=1 \rightarrow F'=2)} = -11\text{ MHz}$ .

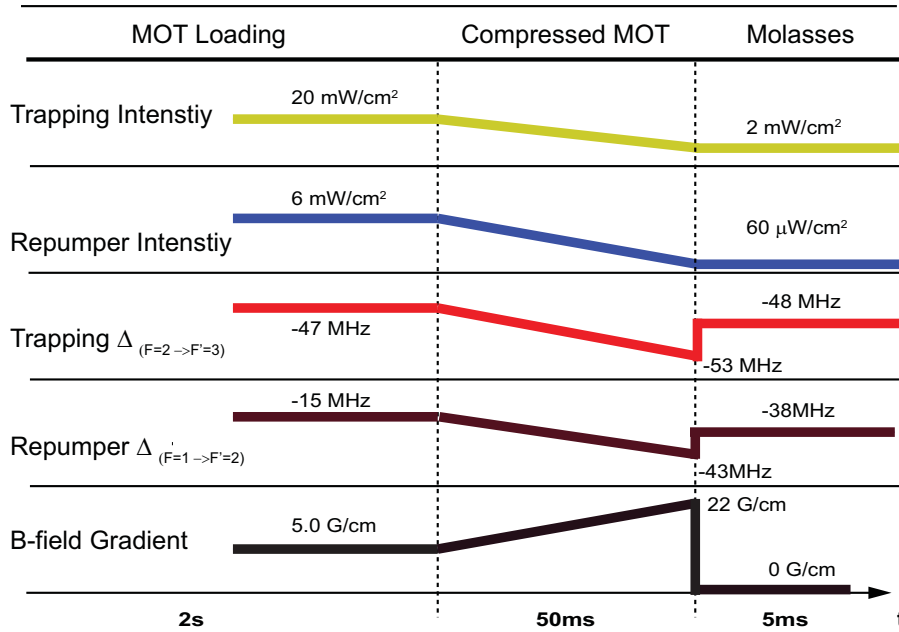


Figure 2-22: Experimentally found best parameters and sequences for the  $^{39}\text{K}$  MOT. The most important step is ramping down the MOT repumping beam power in the compressed MOT stage. The parameters were tweaked to optimize the phase space density in the magnetic trap.

### $^{39}\text{K}$ MOT

The  $^{39}\text{K}$  MOT was the first MOT obtained in Fermi-I because it has the largest natural abundance among all potassium isotopes and thus makes the MOT easiest to be observed. Obtaining the first  $^{39}\text{K}$  MOT signal took us about one day; however, maximizing its phase space density took us approximately one month. The main obstacle originates from the fact that the excited hyperfine states of  $^{39}\text{K}$  are not well resolved within their natural line width as shown in Fig. 2-21 and thus sub-Doppler cooling is hard to realize in this system. For the same reason, the light force from the repumping beam is essentially as strong as the force from the cooling beam which can directly heat the MOT to several mK. Pioneering work on cooling  $^{39}\text{K}$  in the group of Prof. Inguscio at LENS [85, 86, 87, 88, 89] shows that certain tricks can be applied to improve the phase space density of the MOT: a compressed MOT and an optical molasses. Fig. 2-22 shows our optimized experimental sequence for cooling the  $^{39}\text{K}$

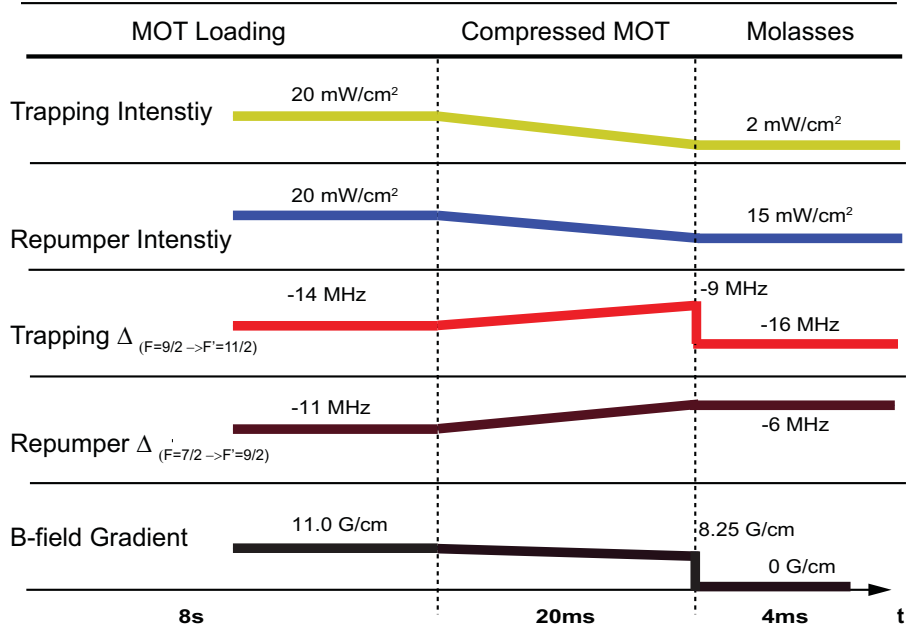


Figure 2-23: Experimentally found best parameters and sequences for the  $^{40}\text{K}$  MOT. The parameters were tweaked to optimize the atom number in the magnetic trap.

MOT. We used the phase space density at the beginning of the magnetic trap as the figure of merit to improve the MOT because the best phase space density in the MOT does not always have the best mode matching to the magnetic trap.

### $^{40}\text{K}$ MOT

Because of the low natural abundance of  $^{40}\text{K}$ , the atom number of  $^{40}\text{K}$  in the MOT is mostly limited by the atomic flux. At equilibrium, the atom number in the MOT is proportional to the ratio of the supply rate to the loss rate. Therefore, one can expect that the atom number of a  $^{40}\text{K}$  MOT is about four orders of magnitude less than the atom number of a  $^{39}\text{K}$  MOT if we simply assume that the supply rate is proportional to the natural abundance of each isotope. At first glance, this seems to be a major roadblock. Fortunately, in our experiment  $^{40}\text{K}$  will be sympathetically cooled by another species; hence most of the  $^{40}\text{K}$  atoms should be preserved during evaporation. Similarly to  $^{39}\text{K}$ , we tweaked the  $^{40}\text{K}$  MOT by monitoring its atom

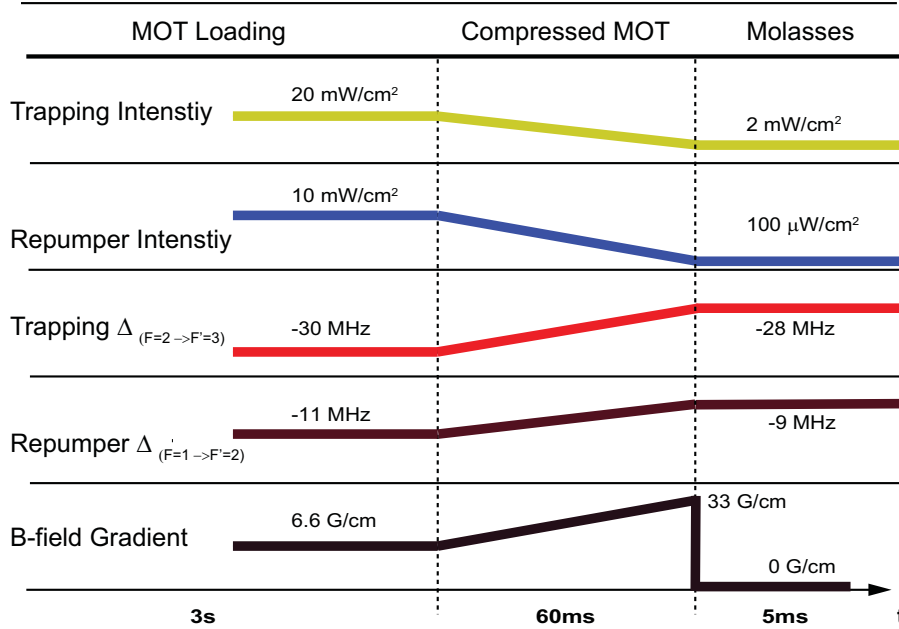


Figure 2-24: Experimentally found best parameters and sequences for the  $^{41}\text{K}$  MOT. The most important step is ramping down the MOT repumping beam power in the compressed MOT stage. The parameters were tweaked to optimize the phase space density in the magnetic trap.

number in the magnetic trap; however,  $^{40}\text{K}$  is not readily visible in absorption images at this stage due to its low density. We implemented a fluorescence imaging technique for quantifying the  $^{40}\text{K}$  atom number by switching back on the MOT cooling and repumping beams while atoms were in the magnetic trap and collecting atomic fluorescence on a CCD camera. Fig. 2-25 shows a typical fluorescence image of  $^{40}\text{K}$  after loading into the magnetic trap and Fig. 2-23 shows the experimentally found parameters for the best  $^{40}\text{K}$  MOT.

### $^{41}\text{K}$ MOT

The cooling scheme for the  $^{41}\text{K}$  MOT is quite similar to the  $^{39}\text{K}$  MOT since its excited hyperfine states are also not resolved. Kishimoto *et al.* reported the first direct evaporative cooling of  $^{41}\text{K}$  into a BEC [90]. Our cooling scheme was initially guided by their work. Fig. 2-24 shows the experimentally found best parameters

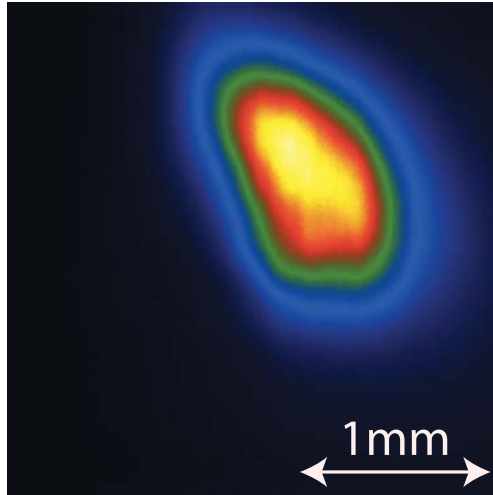


Figure 2-25: A  $^{40}\text{K}$  fluorescence image in the magnetic trap. The image was taken by switching back on the MOT beams and collect the atomic fluorescence on a CCD camera.

for the  $^{41}\text{K}$  MOT. The most important step is to lower the repumping beam power in the molasses stage (same for the  $^{39}\text{K}$  MOT). The compressed MOT stage is to increase the density while the molasses stage is to reduce the temperature. Because the power of the repumping beam is dramatically reduced during the molasses stage, most atoms can stay in the dark state ( $F = 1$  state) without being heated by the cooling beam forming a temporal dark MOT. By doing so, we were able to reduce the MOT temperature by a factor of 5 and increase the MOT density by a factor of 2.

## 2.5 Optically plugged magnetic trap

After the MOT stage, atoms are loaded into a quadrupole magnetic trap (the same quadrupole field used for the MOT). The quadrupole field is switched off during the molasses and optical pumping stages and then switched back on for magnetic trap-

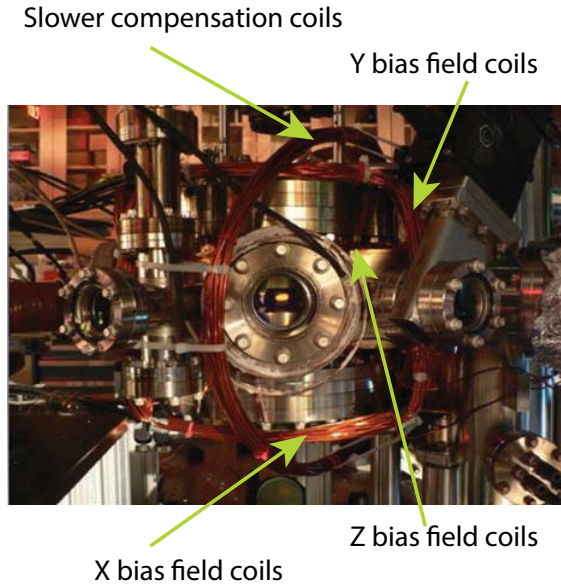


Figure 2-26: A side view of the main chamber. XYZ bias coils are wound around the main chamber as well as the slower compensations coils.

ping. IGBT 1 in Fig. 2-18 serves as a fast switch for the quadrupole field which has a typical rise time (fall time) of  $2\ \mu\text{s}$  (650 ns). For the best loading efficiency, it is necessary to pre-charge the power supply (Lambda ES 30-500) for the magnetic trap so that when the IGBT is switched on, the current can overshoot. We empirically observed that this overshooting mechanism is actually critical to the final atom number in the magnetic trap. Loading atoms from a MOT to a magnetic trap is a delicate process. The loading efficiency strongly depends on the “mode matching” between these two stages [91]. Hence, the center positions of the MOT and the magnetic trap should be as close as possible for an optimal mode matching. This can be achieved by fine tuning the bias fields in the  $x$ ,  $y$ , and  $z$  directions in both stages. The coils which provide the bias fields are wound around the main chamber as shown in Fig. 2-26.

There are two reasons to choose a quadrupole magnetic trap over a Ioffe-Pritchard trap: 1. a better optical access, 2. tighter magnetic field confinement which can lead to faster evaporation. Nevertheless, the Ioffe-Pritchard trap has the advantage that its trapping potential can be modeled by a harmonic potential which makes the study of



Figure 2-27: A picture of the inner RF antenna. The coils are made of 22 AWG wires. The wire is wound on four screws which are secured by four nuts welded evenly on the edge of the recessed viewport.

atoms in the magnetic trap easier [17]. However, in order to study Feshbach physics in a uniform magnetic field, trapping atoms in a pure optical trap is necessary. Therefore, one can afford to evaporate atoms in a magnetic trap with tighter confinement for faster evaporation. However, a quadrupole magnetic trap suffers from loss at the trap bottom where atoms can undergo spin-flips from a trappable state to a non-trappable state - the so-called Majorana loss. A 17.5 W 532 nm green laser with  $1/e^2$  beam waist  $60 \mu\text{m}$  is used to “plug” the Majorana hole [2]. The beam waist of the plug laser was chosen to not only plug the Majorana hole but also to push atoms away from the “dangerous zone” where low frequency electromagnetic wave noises from the environment (e.g.  $\sim 10 - 20$  kHz noise from switching power supplies) can spin flip atoms to a non-trappable state causing atom loss.

## 2.6 RF coils

The technique of radio frequency evaporation paves the way towards ultracold quantum degenerate gases [16]. To address multiple species, two sets of RF coils are installed in the Fermi-I machine. One is inside the main vacuum chamber, the inner antenna, and the other one is inside the top recessed viewport but outside vacuum, the outer antenna. Fig. 2-27 shows a picture of the inner antenna. The coils are wound by kapton insulated copper wires (22 AWG) around four 6-32 screws which are attached to the top recessed viewport by four nuts welded evenly on the edge of the inner side of the viewport. Each coil has dimensions of  $10.8 \times 2$  cm. The inner antenna was originally designed for the frequency range below 100 MHz. We use it mostly for spin flipping atoms between different Zeeman sublevels in the experiment. The coils were spot welded to a miniflange BNC vacuum feedthrough. This feedthrough was attached to one of the miniflange ports on the top recessed viewport (see Fig. A-1). The outer antenna is made of a single loop ( $\sim 3''$  dia.) of  $1/8''$  square hollow core copper wire. It was first used for  $^{39}\text{K}$  and  $^{41}\text{K}$  RF evaporation at  $\sim 500$  MHz and later on it was also used for  $^{23}\text{Na}$  RF evaporation at  $\sim 1.8$  GHz.

## 2.7 Crossed optical dipole trap

At the end RF evaporation, atoms are loaded into a crossed optical dipole trap (ODT) which consists of two 1064 nm laser beams with  $1/e^2$  beam waist of 73 and 135  $\mu\text{m}$  and power of 4.7 and 17 W, respectively. The ODT beams are provided by a Nufern fiber amplifier seeded with an Innolight Mephisto laser. Each ODT beam is sent through an 80 MHz acoustic optical modulator (AOM) to shift its frequency (the two beams are shifted in opposite directions) and also to control its power. To stabilize the ODT power, a tiny amount ( $<1\%$ ) of each beam is picked up by an AR coated mirror and sent to a photodiode. The photodiode output is then fed into a high-speed servo

controller (Newport LB1005) to be compared with the computer generated reference voltage.

It is a delicate process to load atoms, especially a BEC, from a magnetic trap into an ODT- as a quote from my colleague, Jee Woo Park, “it is like catching an egg without breaking its yolk”. At low temperature, the atomic cloud in the magnetic trap splits into two pockets due to the potential barrier from the optical plug. This makes the mode matching between the magnetic trap and the ODT difficult. On the other hand, when the temperature is still high, loading into the ODT requires more power - it is a trade off. Experimentally, we found the best loading condition by varying the final RF frequency and monitoring the atom number in the ODT. Both ODT beams are ramped up during the final decompression of the magnetic trap. In order to let atoms fall into the ODT, it is crucial to align the ODT beams about one beam waist below the magnetic trap center. At the end of the decompression, the magnetic trap is completely switched off, and atoms stay in the ODT. As mentioned earlier, the two ODT beams enter the chamber from the ports #8 and #9. This arrangement has the advantage that one can easily align the ODT beams with atoms on the cameras.

## 2.8 The Feshbach field

After atoms are completely loaded into the ODT, the trap coils are switched from the anti-Helmholtz to the Helmholtz configuration to provide a uniform bias field for accessing Feshbach resonances. The coil configuration is changed using four mechanical relays. As shown in Fig. 2-28, while relays 1(2) and 3(4) are closed and 2(1) and 4(3) are open, the coils are in the anti-Helmholtz (Helmholtz) configuration. It takes about 200 ms for the relays to completely switch. Two IGBTs are used in the Helmholtz configuration: IGBT 2 (as a switch) and IGBT 3 (as a current regulating

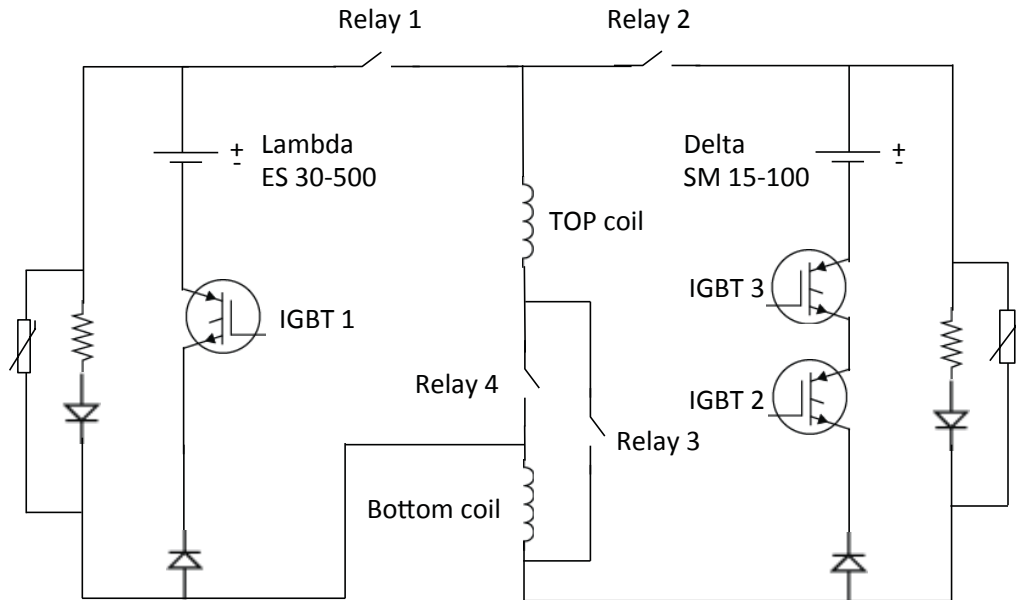


Figure 2-28: The circuit schematic of the magnetic trap and the Feshbach magnetic fields. When the magnetic trap (Feshbach magnetic field) is operating, Relay 1(2) and Relay 3(4) are closed but Relay 2(1) and Relay 4(3) are open. IGBT 1 is used as a switch for the magnetic trap. IGBT 2 and IGBT 3 are used as a switch and a current regulating valve, respectively, for the Feshbach magnetic field.

valve).

### 2.8.1 Stabilizing the Feshbach field

In order to perform high precision RF and Feshbach loss spectroscopy, a stable and homogeneous magnetic field is highly required. The best figure of merit of the field stability can be obtained by directly “asking” atoms by either taking a RF spectrum to extract the field stability from the spectral width or performing a Rabi oscillation measurement to extract the field stability from the decoherence time (see Chapter 5).

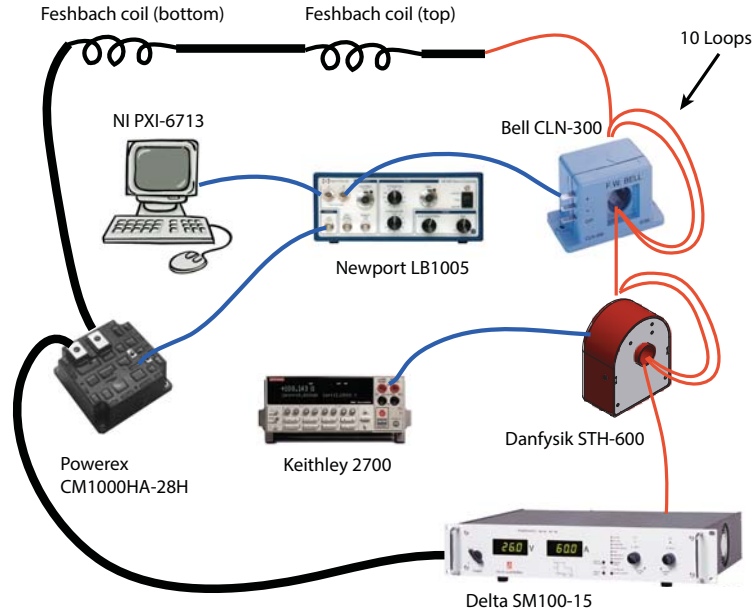


Figure 2-29: Schematic of the detection and stabilization circuits for the Feshbach magnetic field.

However, both methods require running through a complete experimental sequence which could be quite time consuming. Therefore, we implemented a field detection scheme to measure the field stability without loading atoms. Fig. 2-29 shows a schematic of our Feshbach current detection and stabilization circuits. Two hall probes are used to measure the current: Danfysik STH-600 (for monitoring) and F.W. Bell CLN-300 (for feedback). In order to boost the sensitivity of the current reading, the copper wire which carries the Feshbach current was wound 10 times around each hall probe. By doing so, the sensitivity of the current reading can be amplified by a factor of 10. The voltage output from the Danfysik probe is then fed into a high precision voltage meter (Keithley 2700) and the voltage output from the Bell probe is fed into a high-speed servo controller (Newport LB1005) to be compared with a reference voltage generated from an analog card (NI PXI-6713). The voltage output from the servo controller goes into an IGBT (IGBT 3 in Fig. 2-28) to provide feedback on the current. To obtain the best current stability, it is important to operate the IGBT

control voltage around 7.9 V where the slope of current to voltage is the steepest. The figure of merit in this setup is the stability of the reading on the voltage meter. By fine tuning the overhead voltage (which also changes the operating voltage of IGBT 3) of the Feshbach power supply (Delta SM 15-100 set to the voltage control mode) and feedback parameters of the servo controller, we observed a clear improvement on the field stability. We also modified the acquire switch of the servo controller by replacing it with an external relay which can be switched with an external TTL signal. This modification allows us to rapidly ramp up the current to the set point and then activate the feedback so that the feedback circuit does not have to fight with the enormous current jump in the beginning. After modifying the servo controller, we were able to adjust the feedback speed to  $\sim 1$  kHz. The final stability of our Feshbach magnetic field is  $\sim \pm 5$  mG at 100 G which is sufficient for later experiments.

## 2.9 Water cooling systems

The power dissipated in the slower coils and the trap coils can heat them up significantly in the absence of active cooling. Thus, we used square hollow copper tubing to make both coils so that pressurized water can flow. The dissipated power (W) for this tubing is given by [62]

$$P = 2.65 \times 10^{-3} \times I^2 \times l. \quad (2.3)$$

where  $I$  is the current (A) and  $l$  is the length of the wire (m). This formula provides us with an idea of how much water flow is required to cool the coils. For instance, the wire in each layer of the trap coil is about 2 m and it is expected to dissipate 850 W when running with the maximum current of 400 A, which is limited by our power supply. In order to carry away the heat generated by the coils, it is absolutely necessary to cool the wires during experimental sequences with pressurized water.

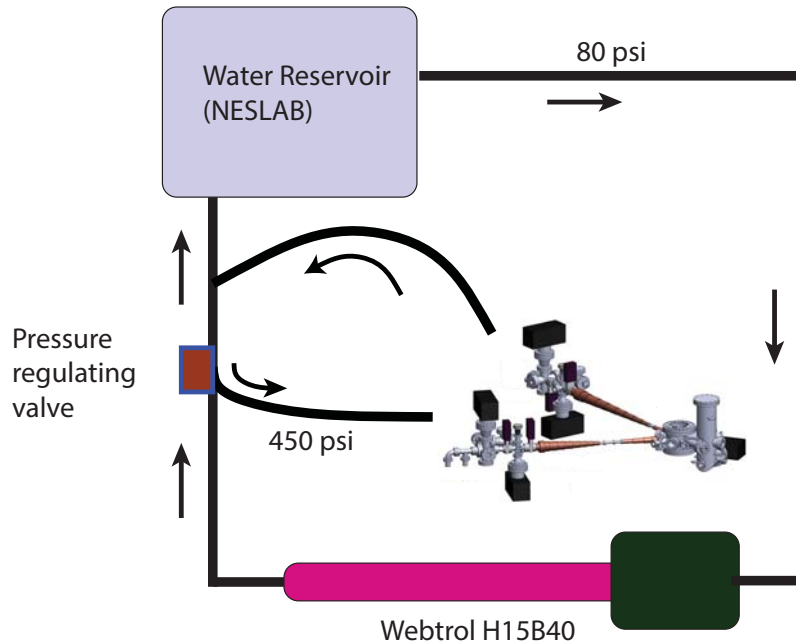


Figure 2-30: Overview of the Fermi-I water cooling system. The slower and the trap coils are cooled by pressurized water generated from a high pressure booster pump which is supplied by a water reservoir (NESLAB). A pressure regulating valve (indicated in red square) is used to bypass water to the water reservoir in order to prevent damage in the booster pump.

The required flow rate for the pressurized water is [62]:

$$F = 14.3 \times P / \Delta T_{H_2O} \quad (2.4)$$

where  $F$  is the flow rate (ml/min),  $P$  is the dissipated power (W), and  $\Delta T_{H_2O}$  is the estimated change in the water temperature ( $^{\circ}\text{C}$ ). For 850 W, setting the maximum temperature change to be  $10^{\circ}\text{C}$ , the required flow rate is 1215 ml/min. The Hazen-Williams equation relates the flow rate of water in a pipe with the pressure drop due to friction [92]:

$$\Delta P = \frac{4.52 \times L F^{1.85}}{C^{1.85} d^{4.87}} \quad (2.5)$$

Where  $\Delta P$  is the pressure drop over a length of the pipe (psi),  $L$  is the length of the pipe (feet),  $F$  is the flow rate (gal/min), and  $d$  is the inner pipe diameter (inch). The factor  $C$  is  $\sim 140$  for copper. In order to maintain a flow rate of 1215 ml/min (0.32 gal/min), the pressure drop over a 2 m wire (with 0.0625" ID) needs to be  $\sim 300$  psi. To achieve such high pressure, a booster pump (Webtrol H15B40) is used to boost the water pressure from 80 psi to 450 psi. It is extremely crucial to have sufficient water flow in the booster pump; otherwise, the plastic rotors inside the pump will be damaged. We increased the water flow by bypassing it to the water reservoir (NESLAB). Fig. 2-30 shows an overview of the Fermi-I water cooling system.

## 2.10 Optics

Three independent laser systems (589 nm, 671 nm, and 767 nm) were constructed for each alkali species. The sodium laser system was set up on an independent optical table, while the lithium and potassium laser systems were set up on the same optical table (see Fig. 2-1). Laser beams are transmitted from the laser tables to the experimental table by optical fibers. In the following, we will discuss each laser system.

### 2.10.1 The potassium laser systems

The potassium laser system is capable of trapping and cooling two potassium isotopes simultaneously (it is arranged for  $^{40}\text{K}$  and  $^{41}\text{K}$  in the current setup). It consists of one master laser - a grating stabilized laser (Toptica DL Pro) locked to the  $^{39}\text{K}$  D2 crossover (see Fig. 2-21) by Frequency Modulation (FM) spectroscopy [93] - four slave lasers, and four tapered amplifiers. Before the master laser seeds the slave laser<sup>1</sup>, its frequency is shifted by AOMs to generate the cooling and repumping beams for each species. In order to boost the laser power, we have four tapered amplifiers<sup>2</sup> seeded

---

<sup>1</sup>Eagleyard laser diode (EYP-RWE-0790-04000-0750-SOT01-0000).

<sup>2</sup>Eagleyard tapered amplifier chip (EYP-TPA-0765-01500-3006-CMT03-0000).

by each slave laser. The slower cooling and repumping beams are generated by splitting the MOT cooling and repumping beams after the tapered amplifiers before coupling into the MOT fibers and their frequencies are prepared by two double pass AOMs. The imaging and optical pumping beams are generated by splitting the slower beams into a Tandem AOM setup for frequency tuning. The imaging and optical pumping beams are transmitted with the same optical fiber from the laser table to the experimental table. For the MOT beams, we use a  $4 \times 4$  PM fiber manifold as described earlier. Detailed schematics of the potassium laser system can be found in Fig. C-1, C-2, C-3, and C-4 in Appendix C.

### 2.10.2 The lithium laser system

A master laser (a grating stabilized laser, Toptica DL Pro) provides the source of 671 nm laser light. It is locked to the  $^6\text{Li}$  D2 crossover by FM spectroscopy [93]. Before the master laser beam is sent into the lithium cell, its frequency is shifted by a double pass AOM ( $2 \times +105$  MHz). As a result, the laser frequency from the master laser is -210 MHz detuned from the  $^6\text{Li}$  D2 crossover. Then approximately 15 mW of the master laser power is used to seed a tapered amplifier (Toptica BoosTA) which can boost the laser power up to 360 mW. The tapered amplifier output is split into three beams for seeding the slower laser<sup>3</sup>, seeding the MOT repumping laser<sup>3</sup>, and directly being coupling into the fiber. Two +80 MHz AOMs are installed in the MOT cooling and repumping beam paths to regulate the beam power. Fig. C-5 in Appendix C shows a schematic of the lithium laser system.

### 2.10.3 The sodium laser system

For a long time, the dye laser was the only source for the 589 nm light. But they are difficult to operate and also expensive. This has made sodium an “unfriendly”

---

<sup>3</sup>Mitsubishi laser diode (ML1016R).

atom to study. Our group implemented the first solid state laser system for sodium. It consists of a 1178 nm grating stabilized diode laser (Toptica DL Pro), a Raman fiber amplifier (MPBC VRFA-SF series), and a second harmonic generation crystal (packaged by MPBC). Fig. C-6 shows a schematic of the sodium master laser system. This setup is able to provide up to 2 W of 589 nm laser light which is sufficient for a sodium cooling and trapping experiment. A detailed description of our sodium laser system can be found in Ibon Santiago's thesis [94].

## Chapter 3

# Strongly Interacting Isotopic Bose-Fermi Mixture Immersed in a Fermi Sea

*In this chapter, I am going to present how we simultaneously cool three different atomic species, the bosonic species  $^{41}\text{K}$  and two fermionic species  $^{40}\text{K}$  and  $^6\text{Li}$ , into quantum degenerate states simultaneously. The bosonic species is shown to be an efficient coolant for the two fermionic species, paving the way towards studying fermionic superfluids with imbalanced masses. We observe multiple heteronuclear Feshbach resonances, in particular a wide s-wave resonance for the isotopic combination  $^{41}\text{K}$ - $^{40}\text{K}$ , opening up the path for the study of a strongly interacting Bose-Fermi mixture with tiny mass difference and almost identical trapping potentials. Furthermore, for large imbalance, we enter the polaronic regime of dressed impurities immersed in a bosonic or fermionic bath.*

## 3.1 Introduction

Ultracold atomic systems provide a great advantage to study interactions between different atomic species. In particular, species with different masses can introduce a new parameter to the system - the mass ratio between atoms. Moreover, the control of interactions, offered in a unique way by Feshbach resonances [3], is a feature that has not been available in traditional condensed matter experiments. With ultracold gases, Bose-Bose [67, 95], Bose-Fermi [35, 34, 83, 96, 97, 98, 3, 47], Fermi-Fermi [99, 100, 101], and even triply degenerate Bose-Fermi-Fermi mixtures [99] can be studied with great controls of density, temperature, and atom number. Particularly, the control of atom number allows us to study polaron physics which is the building block of quantum many-body phenomena. On one hand, strongly interacting Bose-Fermi mixtures offer a unique platform to study the whole spectrum of polaron problems. By changing the number balance between bosons and fermions, one can study the system evolving from Bose polarons [56], bosons being the majority atoms, to Fermi polarons [9, 8], fermions being the majority atoms. On the other hand, strongly interacting Fermi-Fermi mixtures provide a different prospect of the Fermi polaron problems in which many-body pairing can potentially happen between unlike fermions [10].

Here we present a system where strongly interacting Bose-Fermi and Fermi-Fermi mixtures can be studied simultaneously. We use  $^{41}\text{K}$  as a coolant to cool the fermionic species,  $^6\text{Li}$  and  $^{40}\text{K}$ , and show that  $^{41}\text{K}$  is a superior coolant compared to all current experiments on fermionic  $^{40}\text{K}$ . In comparison to experiments employing  $^{87}\text{Rb}$  to cool the same fermionic species to triple degeneracy [99], we reach a significantly higher degree of degeneracy in  $^6\text{Li}$ . A triply degenerate mixture of  $^6\text{Li}$  -  $^{40}\text{K}$  -  $^{41}\text{K}$  has been achieved at the end of evaporation, offering the choices of studying either a Bose-Fermi ( $^{41}\text{K}$  -  $^{40}\text{K}$ ) or a Fermi-Fermi ( $^6\text{Li}$  -  $^{40}\text{K}$ ) mixture. Our system allows us to study not only the established tunable Fermi-Fermi mixture of  $^6\text{Li}$  -  $^{40}\text{K}$  [50] but also a new widely tunable Bose-Fermi mixture of  $^{41}\text{K}$  -  $^{40}\text{K}$ . Importantly,  $^{40}\text{K}$  and  $^{41}\text{K}$  experience

almost identical external potentials and essentially have equal masses so that the only relevant difference is quantum statistics. Therefore, our system surpasses other non-isotopic Bose-Fermi mixtures of  $^{23}\text{Na}$ - $^6\text{Li}$  [38],  $^{87}\text{Rb}$ - $^{40}\text{K}$  [102],  $^{87}\text{Rb}$ - $^6\text{Li}$  [3], and  $^{85}\text{Rb}$ - $^6\text{Li}$  [103] which are plagued by typically unequal trapping potentials and the large mass difference.

## 3.2 A new coolant for fermionic alkali species: $^{41}\text{K}$

Cooling of spin-polarized fermions to degeneracy is hindered by insufficient thermalization due to the absence of “head-on” collisions in the s-wave regime at low temperature, which makes Fermi gas experiments more complex than their bosonic counterparts. Common solutions include direct cooling of two hyperfine spin populations [68], or sympathetic cooling using another atom as the coolant [6]. Particularly with RF evaporation, the latter method has the advantage of mostly conserving the fermionic species in the cooling process [37]. Adverse spin-changing collisions between coolant and fermion can still reduce the fermion number [97, 99]. In this experiment we have employed  $^{41}\text{K}$  for sympathetic cooling and find it to be an efficient coolant for both  $^{40}\text{K}$  and  $^6\text{Li}$ , with negligible loss of fermions.

### 3.2.1 Why $^{41}\text{K}$ ?

Although  $^{39}\text{K}$  has a larger nature abundance (93.3%) than  $^{41}\text{K}$  (6.7%), which can result in a larger atom number in the  $^{39}\text{K}$  MOT, the fact that it has a negative s-wave background scattering length at zero magnetic field makes direct cooling of  $^{39}\text{K}$  to quantum degeneracy challenging [87]. We notice this effect by observing that the temperature of  $^{39}\text{K}$  stops going down even though RF evaporation continues (see Fig. 3-1). This is because a system with a negative background scattering length will have a zero crossing of the scattering length at low temperature, where collisions

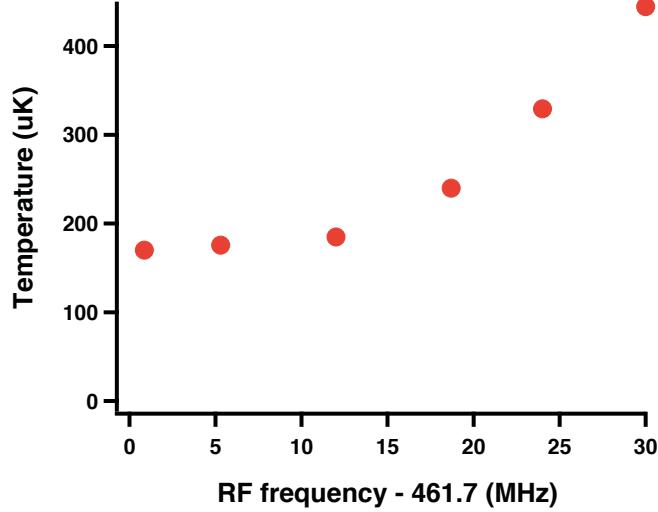


Figure 3-1: The temperature of  $^{39}\text{K}$  as a function of the final RF knife frequency above the  $^{39}\text{K}$  hyperfine transition of 461.7 MHz. Around 15 MHz above the hyperfine transition, evaporative cooling stops strongly indicating a zero crossing of the scattering length at a temperature of  $\sim 180 \mu\text{K}$ .

between atoms are not happening [104]. The same physics happens in  $^7\text{Li}$  [105]. Fig. 3-1 shows the temperature of  $^{39}\text{K}$  atoms as a function of the RF knife frequency. The plateau at  $180 \mu\text{K}$  strongly indicates a zero crossing of the scattering length. This issue does not exist in  $^{41}\text{K}$ , since it has a positive  $s$ -wave background scattering length. The  $s$ -wave background scattering lengths for potassium isotopes can be found in Ref. [106].

### 3.2.2 Making $^{41}\text{K}$ Bose-Einstein condensates

Kishimoto *et al.* first showed that  $^{41}\text{K}$  could be directly evaporated into a Bose-Einstein condensate [90]. Their work inspired us to use  $^{41}\text{K}$  as a coolant for the fermionic species.

Typically, we are able to load  $\sim 1 \times 10^9$   $^{41}\text{K}$  atoms into the MOT with a rather high temperature of 2 mK. Following the MOT loading and cooling schemes (compressed MOT and molasses) mentioned in Chapter 2, we are able to reach a phase space

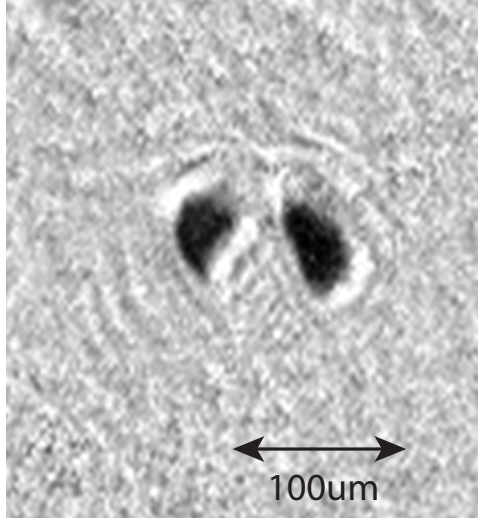


Figure 3-2: Absorption image of the  $^{41}\text{K}$  atoms in the optically plugged quadrupole magnetic trap towards the end of evaporation. The atomic cloud splits into two pockets separated by the optical plug beam.

density of  $\sim 1 \times 10^{-8}$  in the beginning of the magnetic trap which is enough for starting a runaway evaporation [16]. After the molasses stage, atoms are prepared in the stretched hyperfine state  $|F, m_F\rangle = |2, 2\rangle$  by a  $500 \mu\text{s}$ ,  $450$  ( $250$ )  $\mu\text{W}/\text{cm}^2$ ,  $F = 2 \rightarrow F' = 3$  ( $F = 1 \rightarrow F' = 2$ ) optical pumping pulse.

### Evaporation in an optically plugged magnetic trap

Evaporative cooling of  $^{41}\text{K}$  is performed in an optically plugged quadrupole magnetic trap with a  $B'_z = 220 \text{ G/cm}$  ( $B'_\perp = 110 \text{ G/cm}$ ) magnetic field gradient along the vertical (horizontal) direction. To avoid Majorana spin flips, the magnetic field zero, in the center of the trap, is “plugged” by a repulsive (blue-detuned) laser beam (power  $15 \text{ W}$ , wavelength  $532 \text{ nm}$ ) focussed to a beam waist of  $20 \mu\text{m}$  to prevent atoms from undergoing a spin-flip into an untrapped state near the magnetic field zero [2]<sup>1</sup>.

Towards the end of evaporation the atomic can split into two pockets as shown in Fig. 3-2 due to the two potential minima formed around the optical plug. This

<sup>1</sup>Later on we increase the plug beam waist to  $60 \mu\text{m}$  for the study of NaK mixtures.

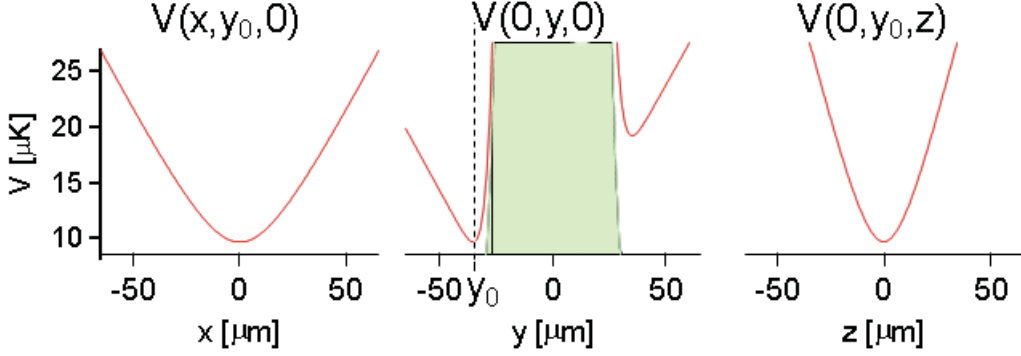


Figure 3-3: The simulated potential of the biased optically plugged magnetic trap for  $^{41}\text{K}$  in three different directions. The optical plug beam is along the  $x$ -axis.  $y_0$  represents the new global minimum of the trap. For this simulation, we use  $B' = 110 \text{ G/cm}$ ,  $P = 15 \text{ W}$ ,  $w = 20 \mu\text{m}$ , and  $B_{y_0} = 100 \text{ mG}$ ; gravity is neglected.

effect can reduce the efficiency of evaporation [107]. The solution is to create a single global potential minimum by biasing the magnetic trap with an external bias field. One can model the biased optically plugged quadrupole trap as:

$$V = \mu_B \sqrt{(B'x/2)^2 + (B_{y_0} + B'y/2)^2 + (B'z)^2} + \frac{\alpha_K P}{\frac{\pi}{2}w^2} \exp\left(-2\frac{y^2 + z^2}{w^2}\right) \quad (3.1)$$

where the first term describes the magnetic potential with  $\mu_B$  being the Bohr magneton,  $B'$  the magnetic field gradient in the  $z$  directions, and  $B_{y_0}$  the external bias field; the second term describes the optical plug potential with  $\alpha_K$  being the polarizability of  $^{41}\text{K}$  in 532 nm,  $P$  the power of the optical plug beam, and  $w$  the beam waist. Fig. 3-3 shows the simulated trapping potential profiles (neglecting gravity). The new potential minimum has been shifted to  $y_0$  under the external bias field. With this technique, we ensure that there is only one atomic cloud towards the end of evaporation, which is important for later quantitative studies of the degenerate gases.

Unlike a constant trapping frequency in a harmonic trap, the trapping frequency in a linear trap is not well-defined. Slow atoms experience faster trapping frequency

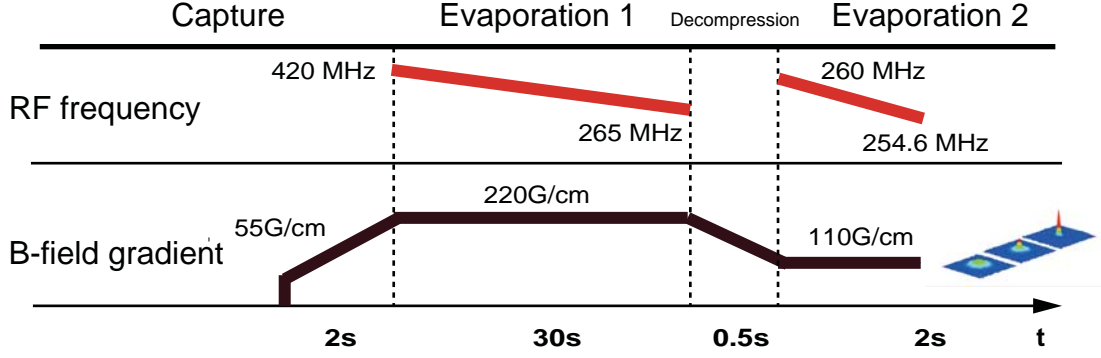


Figure 3-4: The optimized profiles of the magnetic field gradient and the RF knife frequency for cooling  $^{41}\text{K}$  atoms towards Bose-Einstein condensation. The 0.5 s decompression stage helps to reduce three-body losses at the end of evaporation 1. We are able to obtain a pure BEC of  $\sim 3 \times 10^5$  atoms at the end of evaporation 2

than fast atoms ( $\omega \propto \frac{1}{(k_B T)^{1/2}}$ ). Hence, it is necessary to decompress the magnetic trap to avoid three-body losses when close to quantum degeneracy. However, it is a bit tricky to change the magnetic field confinement in an optically plugged trap since any imperfection of the trap coils can cause the zero of the magnetic field to move during decompression. Thus, it is a delicate process to keep the magnetic field zero always at the position of the plug beam. This can be achieved by carefully adjusting the XYZ bias fields during decompression. In our setup, the zero of the magnetic field does not move linearly with the gradient strength which makes tuning the bias fields even more difficult.

Fig. 3-4 shows the profiles of the magnetic trap gradient and the RF knife frequency during evaporation. The “push” bias field is only turned on during the last 2 s of evaporation to shuffle the atoms into a single potential minimum by displacing the center of the magnetic trap by  $10 \mu\text{m}$ . Evaporation is performed by driving  $|2, 2\rangle \rightarrow |1, 1\rangle$  RF transitions above the hyperfine transition of 254.0 MHz. Note that evaporation between Zeeman sub-levels (instead of the hyperfine transition) shortens the lifetime of trapped atoms due to  $|2, 1\rangle + |2, 0\rangle \rightarrow |2, 2\rangle + |2, 0\rangle$  spin relaxation processes. For the last 2 s of evaporation, the trap is decompressed to  $B'_z = 110 \text{ G/cm}$

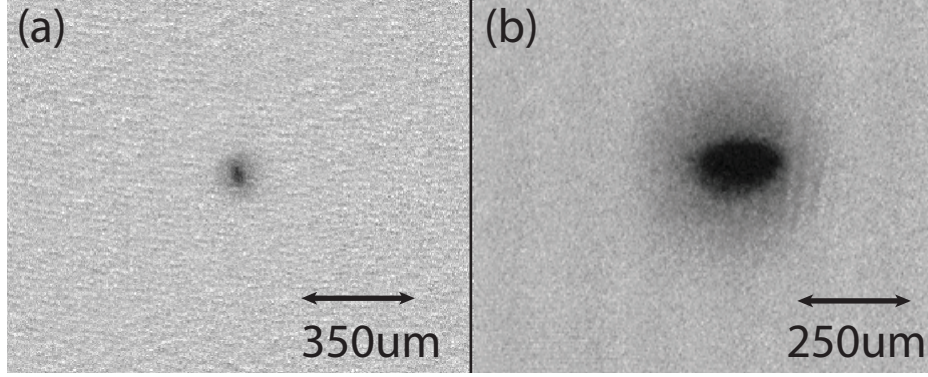


Figure 3-5: (a) A absorption image of the first  $^{41}\text{K}$  BEC born in the Fermi-I machine which shows a BEC with  $\sim 1 \times 10^4$  atoms. (b) After improving the MOT loading stage and the RF evaporation sequence we achieve a BEC with  $\sim 3 \times 10^5$  atoms.

to suppress three-body losses. Fig. 3-5(a) shows an image of the first  $^{41}\text{K}$  BEC in the Fermi-I machine which was born at 2:30 am, October 13<sup>th</sup> 2009. The condensate contained  $\sim 10^4$  atoms. During improving the compressed MOT and molasses stages, we realized that the MOT beam balance was extremely critical for the molasses to work. Eventually we obtained a pure  $^{41}\text{K}$  BEC with  $\sim 3 \times 10^5$  atoms as shown in Fig. 3-5(b) which was comparable to the number obtained by Kishimoto *et al.* Fig. 3-6 shows that the  $^{41}\text{K}$  BEC emerges from a thermal cloud.

### 3.3 A new quantum degenerate Bose-Fermi-Fermi mixture: $^{41}\text{K}$ - $^6\text{Li}$ - $^{40}\text{K}$

As the bosonic coolant ( $^{41}\text{K}$ ) has been brought into quantum degeneracy, we can test its cooling power by introducing the two fermionic species,  $^6\text{Li}$  and  $^{40}\text{K}$ , into the system. Experimentally, the collisional properties between  $^6\text{Li}$  and  $^{41}\text{K}$ , as well as  $^{40}\text{K}$  and  $^{41}\text{K}$ , are unknown. We are the first research group studying these mixtures. Fortunately, theoretical predictions provide us with a very good guidance. Table 3.1 summarizes the predicted values for the interspecies background scattering length

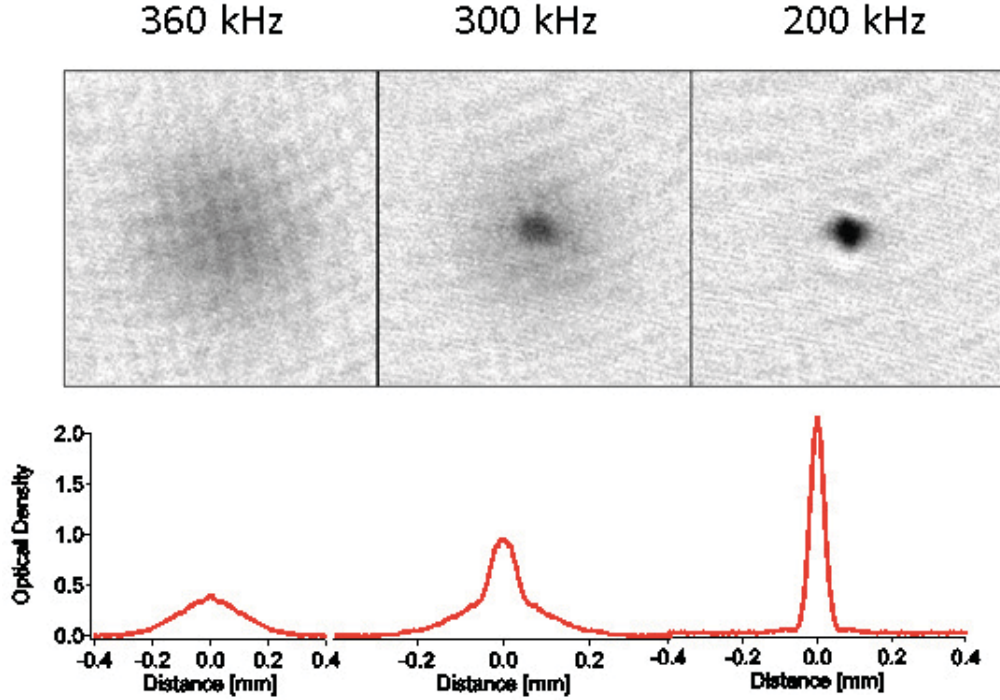


Figure 3-6:  $^{41}\text{K}$  BEC emerges from a thermal cloud. The listed frequencies indicate the RF knife frequency above the  $^{41}\text{K}$  hyperfine transition 254.0 MHz. The bottom plots show the azimuthally averaged density profiles where a clear bimodal feature can be observed.

among these species [108]. It suggests that  $^{41}\text{K}$  is likely to be an efficient coolant for both  $^6\text{Li}$  and  $^{40}\text{K}$  since their interspecies background scattering lengths are in the favorable range. Indeed, it turns out experimentally that sympathetic cooling of the fermionic species with  $^{41}\text{K}$  as a coolant works surprisingly well! We do not observe significant losses on the fermionic species during evaporation. We do not even have to adjust much on the RF evaporation sequence; the sequence is similar to cooling  $^{41}\text{K}$  alone. The only additional step necessary to accommodate three species is a spin purification scheme (see below) after the MOT loading stage. For the MOT loading, we first load  $^{40}\text{K}$  because of its slow loading rate. After one second of only loading  $^{40}\text{K}$ , the  $^{41}\text{K}$  MOT beams are then switched on together with the  $^{40}\text{K}$  MOT beams (during this time we observe  $\sim 30\%$  reduction of the  $^{40}\text{K}$  MOT fluorescence). The  $^6\text{Li}$  MOT beams are only switched on in the last second of the MOT loading stage.

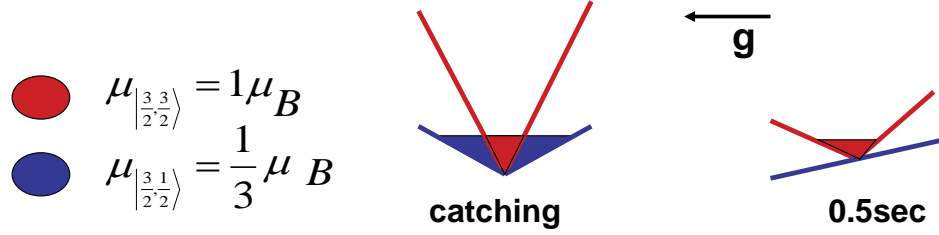


Figure 3-7: Illustration of the gravity assisted spin purification scheme. Blue and red indicate the two different hyperfine states of  ${}^6\text{Li}$ . Experimentally, we capture all spin states initially with a tight confinement, followed by a 0.5 s purification stage where the magnetic trap is ramped down to a critical gradient which can only hold the atoms in the stretched state,  $|F, m_F\rangle = |3/2, 3/2\rangle$ , against gravity.

The total MOT loading time takes about 5-6 seconds.

Mixture	$a_s(a_0)$	$a_t(a_0)$
${}^6\text{Li} / {}^{41}\text{K}$	52	64
${}^6\text{Li} / {}^{40}\text{K}$	42	60
${}^{40}\text{K} / {}^{41}\text{K}$	-54	97

Table 3.1: List of the interspecies background scattering lengths.  $a_s$  and  $a_t$  are the singlet and triplet scattering lengths, respectively [108].

### Purification of spin states

Although optical pumping can pump  $\sim 75\%$  of  ${}^6\text{Li}$  atoms to their stretched state  $|F, m_F\rangle = |3/2, 3/2\rangle$ , it is still essential to clean up the spin imperfections in the beginning of the magnetic trap, otherwise the energy released from spin relaxation can heat up the system significantly. In a quadrupole magnetic trap, cleaning the spin states with RF frequency is not possible since atoms do not experience a constant bias field as in a Ioffe-Pritchard trap [37]. We come up with a novel solution to this problem - a so-call gravity assisted purification scheme. As illustrated in Fig. 3-7, atoms in all spin states are first captured by tight confinement. Then the trap is decompressed to a critical gradient, where only atoms in the stretched state can be

held against gravity. Finally, the trap is recompressed back before evaporation starts. By this we obtain  $\sim 100\%$  pure stretched state atoms in the magnetic trap. Fig. 3-8(a) shows the  ${}^6\text{Li}$  atom number as function of the purification gradient. The peak around  $2.8\text{ G/cm}$  indicates the critical gradient which can only hold the  $|3/2, 3/2\rangle$  atoms in the magnetic trap. Fig. 3-8(b) shows the lifetime curve of  ${}^6\text{Li}$  with (black dots) and without (red dots) applying the purification scheme.

However, because of the fact that potassium is heavier than lithium,  $2.8\text{ G/cm}$  can not hold any potassium atoms in the magnetic trap. In order to simultaneously load all three species,  ${}^6\text{Li}$ ,  ${}^{40}\text{K}$ , and  ${}^{41}\text{K}$ , we need to compromise. Experimentally we use a gradient of  $15\text{ G/cm}$  which is the critical gradient for potassium. Purifying the spin states of potassium is not essential for cooling  ${}^{41}\text{K}$  alone; however, it becomes important while using  ${}^{41}\text{K}$  as a coolant since any imperfection of  ${}^{41}\text{K}$  spin states can undergo spin relaxation with  ${}^6\text{Li}$  atoms (e.g.,  ${}^{41}\text{K } |2, 1\rangle + {}^6\text{Li } |3/2, 3/2\rangle \rightarrow {}^{41}\text{K } |2, 2\rangle + {}^6\text{Li } |3/2, 1/2\rangle$ ). Note that spin relaxation between  ${}^{40}\text{K}$  and  ${}^{41}\text{K}$  is prohibited by energy conservation.

### Calculating the phase space density (PSD)

In order to quantify the cooling power of  ${}^{41}\text{K}$ , we need to extract the phase space density (PSD) of each species during evaporation. Here temperature may not be a good parameter to characterize the degeneracy of atoms since the trapping potential and atom number can all be traded with temperature. However, as mentioned earlier, because of the trap geometry of our magnetic trap, it is less convenient to calculate the PSD of atoms than a pure harmonic trap. In order to do so, we distinguish two regimes in the calculation of phase space density: the quadrupole trap regime and the harmonic trap regime. Our magnetic trap is not a perfect quadrupole trap since it is plugged with a  $15\text{ W } 532\text{ nm}$  laser beam at its center. Hence, a harmonic approximation is appropriate to describe the bottom of the potential when atoms are

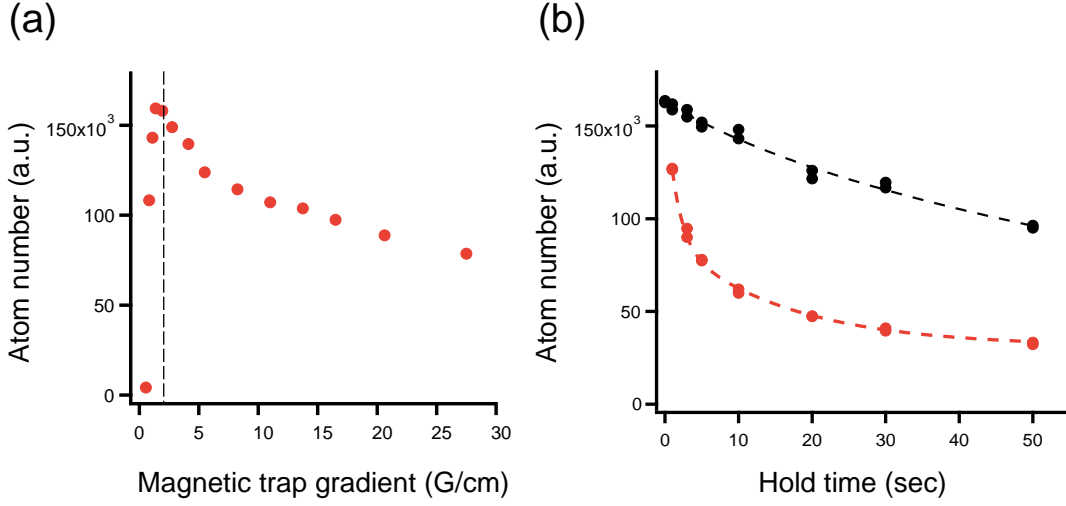


Figure 3-8: Effect of the  ${}^6\text{Li}$  spin purification scheme. (a) The atom number of  ${}^6\text{Li}$  after 20 s wait time in a tight magnetic trap (220 G/cm) as a function of the magnetic field gradient during the 0.5 s purification stage at the beginning of the magnetic trapping. (b) The lifetime curves taken in a tight magnetic trap (220 G/cm) of  ${}^6\text{Li}$  with (black dots,  $\tau = 102$  s) and without (red dots,  $\tau = 19$  s) the spin purification scheme.

close to degeneracy (with the “push” bias field on). While atoms are still hot, they mostly fell the linear potential of the quadrupole trap and we treat them as thermal gases in a quadrupole potential. Below I summarize our calculations for the PSD for thermal gases, bosons, and fermions.

**PSD for thermal gases in a quadrupole trap** The quadrupole potential is given by  $V(x, y, z) = -\mu_B \sqrt{(B'x/2)^2 + (B'y/2)^2 + (B'z)^2}$ . Hence, in thermal equilibrium the total number of atoms can be written as:

$$N = \int_0^\infty n_0 e^{-\beta V(\mathbf{r})} d^3\mathbf{r} \quad (3.2)$$

where  $N$  is the total atom number,  $n_0$  is the maximum atom density, and  $\beta = 1/(k_B T)$ . With a change of variables from  $x \rightarrow x/2$ ,  $y \rightarrow y/2$ , we get:

$$N = 4 \int_0^\infty n_0 e^{-\beta \mu V(\mathbf{r})} d^3 \mathbf{r} = n_0 \frac{32\pi}{(\beta \mu B')^3} \quad (3.3)$$

The phase-space density, being defined as  $\rho = n_0 \lambda_{dB}^3$ , where  $\lambda_{dB}$  is the thermal de Broglie wavelength, can be calculated for a thermal gas as:

$$\rho = n_0 \lambda_{dB}^3 = N \frac{(\beta \mu B')^3}{32\pi} \left( \frac{h}{\sqrt{2\pi m k_B T}} \right)^3 \quad (3.4)$$

**PSD for bosons in a harmonic trap** In a harmonic potential, the  $n_0$  for bosons is given by [17]:

$$n_0 = \frac{1}{\lambda_{dB}^3} g_{3/2}(e^{\mu/k_B T}) \quad (3.5)$$

Therefore  $\rho = n_0 \lambda_{dB}^3 = g_{3/2}(e^{\mu/k_B T})$  ( $g_j(z)$  is defined to be  $\sum_i z^i / i^j$ ). To extract this value experimentally, one can make use of the time of flight density profile. At large times ( $t \gg \omega_x^{-1}, \omega_y^{-1}, \omega_z^{-1}$ ), the density profile can be written as:

$$n_{tof}(\mathbf{r}, t) = \frac{1}{\lambda_{dB}^3} \frac{1}{(\bar{\omega}t)^3} g_{3/2}(e^{(\mu - \frac{mr^2}{2t^2})/k_B T}) \quad (3.6)$$

Hence,  $n_0 = n_{tof}(0, t) \cdot (\bar{\omega}t)^3$ .

**PSD for fermions in a harmonic trap** For fermions, it is required to have a special treatment for calculating PSD because the Pauli blocking limits the maximum PSD to be unity for fermions. Hence, instead of a thermal de Broglie wavelength  $\lambda_{dB}$ , we introduce a different de Broglie wavelength  $\lambda_v = \frac{h}{m\sqrt{\langle v^2 \rangle}}$  calculated from the characteristic velocity  $v$  which is the thermal velocity for thermal gases or the Fermi velocity as degeneracy is approached. Let  $\sqrt{\langle v^2 \rangle} = R/t$ , where  $R = \sqrt{\frac{N}{n_{2D}(0)}}$  with  $n_{2D}(0)$  being the peak column density. Finally, the PSD yields:

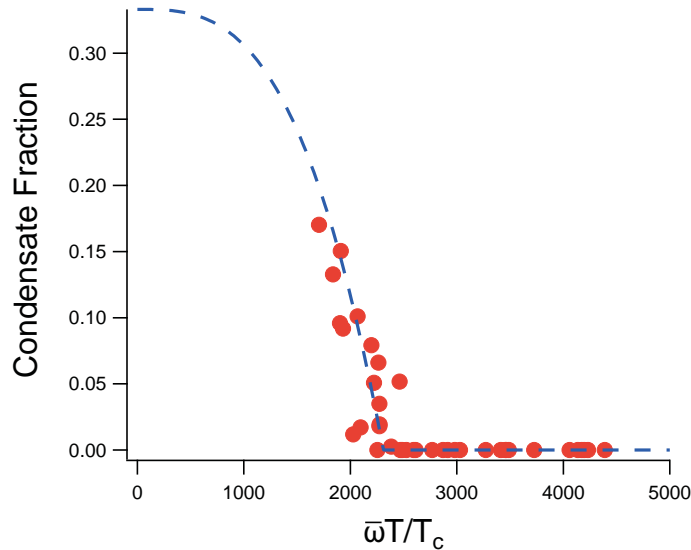


Figure 3-9: Extracting the trapping frequency of the biased optically plugged magnetic trap from condensate fraction. We vary the condensate fraction by changing the MOT loading time. The red dots are the experimental data points and the blue dashed line is a fit to the data with a function  $f(x) = \beta(1 - \frac{1}{\omega^3}x^\alpha)$ , with  $\beta$  and  $\alpha$  being floating to accommodate distortion of the condensate due to saturation and interaction effects.

$$n_0\lambda_v^3 = n_0 \left( \frac{\hbar t}{mR} \right)^3 = n_{tof}(0, t) \left( \frac{(\bar{\omega}t)\hbar t}{mR} \right)^3 \quad (3.7)$$

### Obtaining triple degeneracy

In order to extract the final PSD, one needs to know the temperature, the magnetic field gradient for a quadrupole trap, the trapping frequency for a harmonic trap, and the atom number for each species. We use  $^{41}\text{K}$  for the thermometry assuming thermal equilibrium within the three species. We calibrate the field gradient by balancing the gravitational force and the magnetic force on atoms. We measure the trapping

frequency with the  $^{41}\text{K}$  condensate fraction [17]:

$$\left(\frac{N_c}{N}\right) = 1 - \left(\frac{T}{T_c}\right)^3 \quad (3.8)$$

where  $N_c$  is the atom number in the BEC and  $T_c$  is the BEC critical temperature which can be expressed as:

$$T_c = \frac{1}{k_B} \hbar \bar{\omega} \left(\frac{N}{g_3(1)}\right)^{1/3}, \quad \text{where } \left(\frac{1}{g_3(1)}\right)^{1/3} \approx 0.94 \quad (3.9)$$

Therefore,

$$\left(\frac{N_c}{N}\right) = 1 - \frac{1}{\bar{\omega}^3} \left(\frac{\bar{\omega}T}{T_c}\right)^3 = 1 - \frac{1}{\bar{\omega}^3} \frac{g_3(1)}{N} \left(\frac{k_B T}{\hbar}\right)^3 \quad (3.10)$$

The condensate fraction can be obtained from a fit to the cloud profile with a bimodal distribution and the temperature can be extracted from the wings of the cloud in time of flight images [17]. Fig. 3-9 shows the condensate fraction of  $^{41}\text{K}$  as a function of  $\bar{\omega}T/T_c = \left(\frac{g_3(1)}{N} \left(\frac{k_B T}{\hbar}\right)^3\right)^{1/3}$ . From a fit to the data with equation (3.10) we obtained  $\bar{\omega} = 2\pi \cdot 380(20)$  for  $^{41}\text{K}$ .

Experimentally we use the decompression between two evaporation sequences to distinguish the two potential regimes. Before the decompression the data are analyzed in a quadrupole trap; after the decompression a harmonic trap is used. The procedure is validated by extending the harmonic analysis to the end of evaporation 1 and we find that it matches with the PSD obtained from a quadrupole trap. Fig. 3-10 shows the final result of the evolution of PSD as a function of atom number  $N$ . The efficiency of evaporation is measured by  $\Gamma \equiv -\partial \ln(\text{PSD})/\partial \ln(N)$ . Thanks to the small fermion number, the evaporation efficiency for  $^{41}\text{K}$  is similar with and without load,  $\Gamma \approx 3$  [90]. The near-vertical slope of PSD vs.  $N$  for the fermionic species demonstrates efficient sympathetic cooling of  $^6\text{Li}$  ( $^{40}\text{K}$ ) with  $\Gamma = 12$  (15). At the end of evaporation we obtain quantum degeneracy of each species which can directly be seen in the time

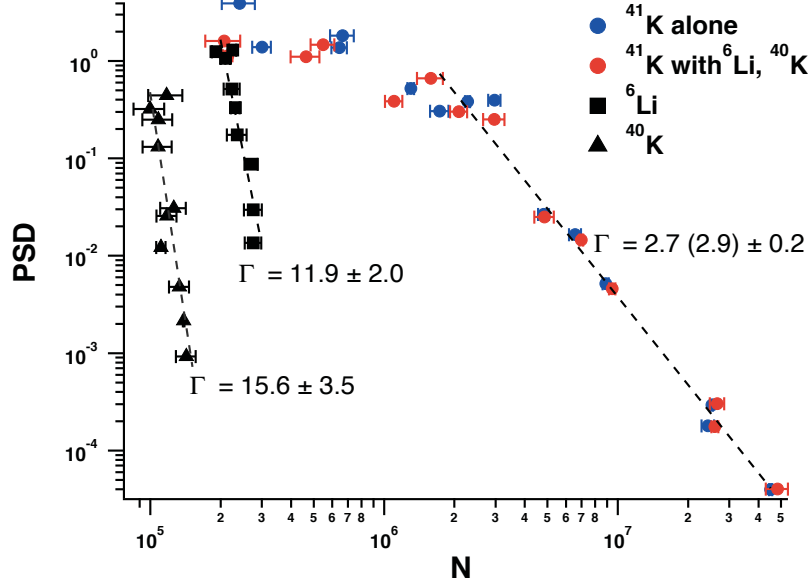


Figure 3-10: The evolution of the phase space density (PSD) with atom number ( $N$ ) during evaporation of  $^{41}\text{K}$ . The  $\Gamma$  value in the parenthesis refers to cooling  $^{41}\text{K}$  alone.

of flight images as shown in Fig. 3-11. Observing a  $^{41}\text{K}$  Bose condensate in thermal contact with a cloud of  $^{40}\text{K}$  and  $^6\text{Li}$  fermions each of roughly the same atom number already implies degeneracy of the fermionic species. If  $T = T_{c,^{41}\text{K}}$ , then  $T/T_{F,^{40}\text{K}} = \frac{\bar{\omega}_{^{41}\text{K}}}{\bar{\omega}_{^{40}\text{K}}} \frac{1}{(6\zeta(3))^{1/3}} \approx 0.51$  and analogously  $T/T_{F,^6\text{Li}} = 0.2$ . Consistent with this expectation, Thomas-Fermi fits to the time-of-flight distributions in Fig. 3-11 reveal  $T/T_{F,^6\text{Li}} = 0.16$  ( $N_{^6\text{Li}} = 2.0 \cdot 10^5$ ) and  $T/T_{F,^{40}\text{K}} = 0.51$  ( $N_{^{40}\text{K}} = 1.1 \cdot 10^4$ ), while  $T/T_{C,^{41}\text{K}} = 0.9$ . Evaporating further to obtain essentially pure condensates, we achieve  $T/T_{F,^6\text{Li}} = 0.08$  for  $^6\text{Li}$  and  $T/T_{F,^{40}\text{K}} = 0.35$  for  $^{40}\text{K}$ . For  $^6\text{Li}$ , the degree of degeneracy is about four times higher than what has been achieved in [99] with  $^{87}\text{Rb}$  as the coolant. For  $^{40}\text{K}$ , the performance is similar. We directly observe Pauli pressure and Bose condensation in the triply degenerate quantum mixture. For this, we determine the  $1/e$  width  $R$  of a gaussian fitted to the fermionic and bosonic distributions, and compare the release energy  $E \equiv \frac{1}{2}mR^2/t^2$  measured after time-of-flight  $t$  to the Fermi energy, defined for each species as  $E_F = k_B T_F = \hbar\bar{\omega}(6N)^{1/3}$ . In Fig. 3-12 we show  $E/E_F$  as a function of the reduced temperature  $T/T_F$ . Thermometry is provided by fitting Bose functions

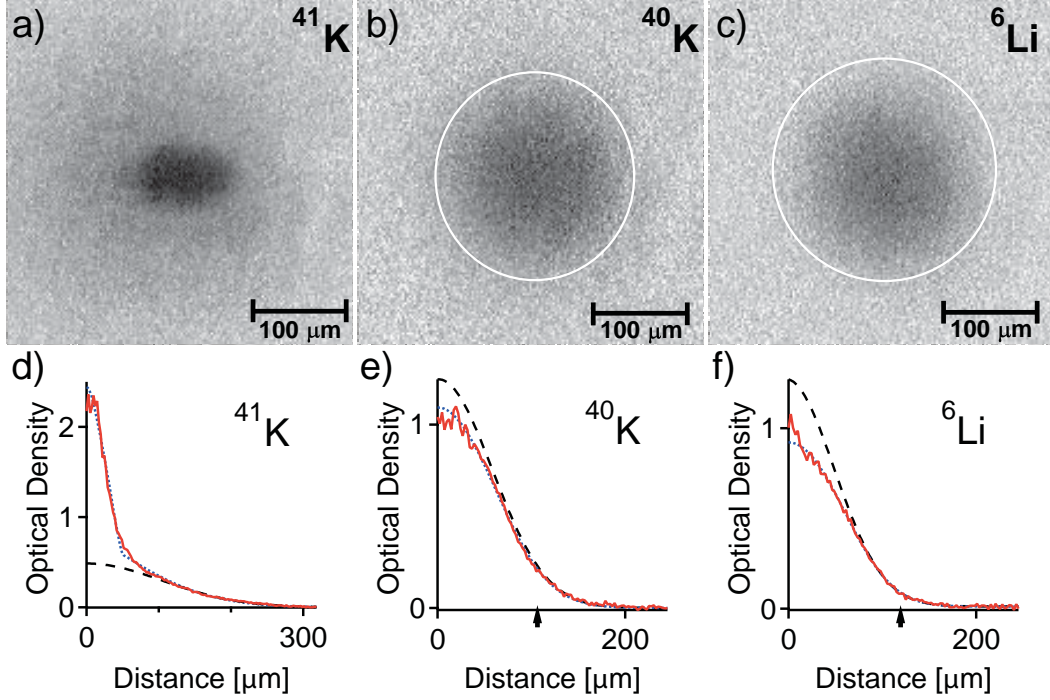


Figure 3-11: a)-c): Absorption images of triply degenerate quantum gases of  $^{41}\text{K}$ ,  $^{40}\text{K}$  and  $^6\text{Li}$ , imaged after 8.12 ms, 4.06 ms and 1 ms time-of-flight from the magnetic trap, respectively. The final rf-knife frequency is 500 kHz above the 254.0 MHz hyperfine transition of  $^{41}\text{K}$ . The white circles indicate the Fermi radius in time-of-flight  $t$ ,  $R_F = \sqrt{2E_F/m} t$ . d)-f): Azimuthally averaged column density. Solid dots: gaussian fit to the wings of the column density. Solid black and blue lines are Gaussian and Fermi-Dirac fits to the entire profile. The deviation of the gaussian fit from the data is more pronounced for the more deeply degenerate  $^6\text{Li}$  at  $T/T_F = 0.16$  than for  $^{40}\text{K}$  at  $T/T_F = 0.51$ . The arrows indicate the Fermi radii. The atom numbers for  $^6\text{Li}$ ,  $^{41}\text{K}$  and  $^{40}\text{K}$  are  $2.0 \times 10^5$ ,  $1.6 \times 10^5$ , and  $1.1 \times 10^5$ , respectively.

to the wings of the  $^{41}\text{K}$  distribution. At high temperatures,  $E/k_B$  simply equals the temperature of each gas. At low temperatures, the release energy of a trapped Fermi gas saturates due to Pauli pressure [34, 35], while for a Bose cloud  $E$  is suddenly reduced as a condensate forms [2].

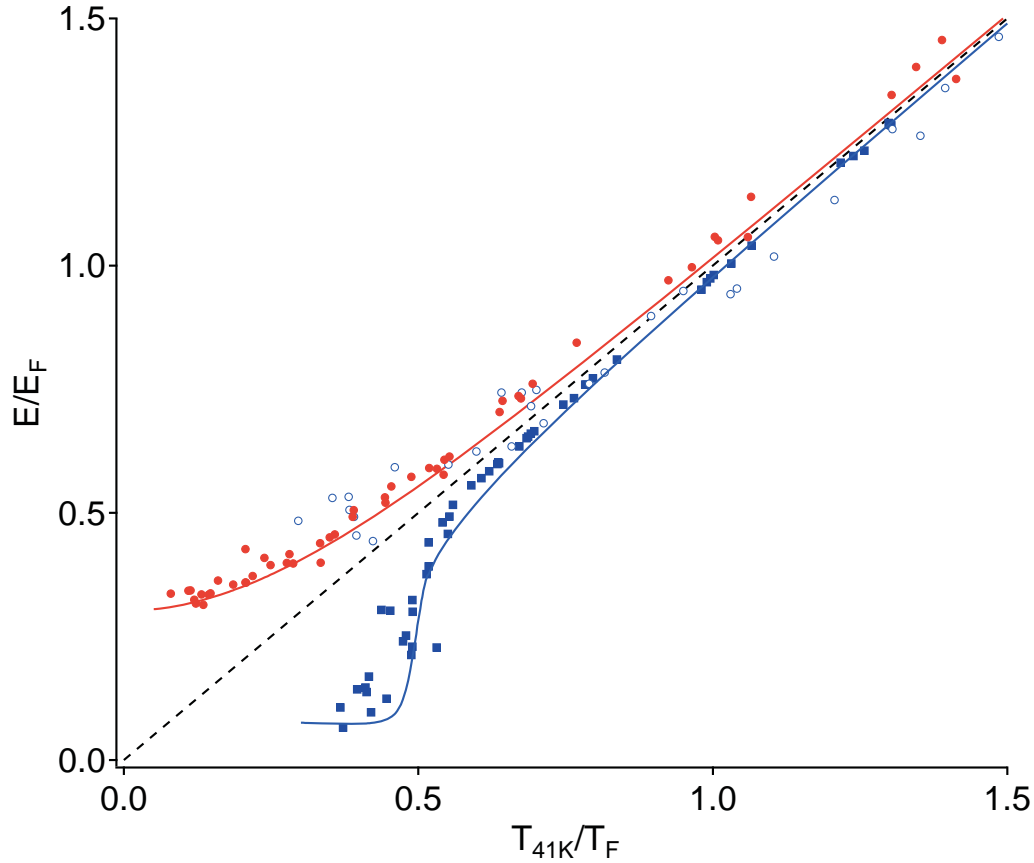


Figure 3-12: Observation of Pauli pressure and Bose condensation in a triply degenerate quantum mixture. Shown is the normalized release energy  $E/E_F$  of each cloud versus the normalized temperature  $T/T_F$ . Solid circles:  $^6\text{Li}$ , open circles:  $^{40}\text{K}$ , solid squares:  $^{41}\text{K}$ . Solid lines: theory for an interacting Bose gas and a non-interacting Fermi gas. Bose condensation of  $^{41}\text{K}$  occurs at  $T_c/T_F = 0.52$ . Dashed line: Boltzmann gas.

### 3.4 Observation of interspecies Feshbach resonances: towards strongly interacting Bose-Fermi mixtures:

By the time when we cooled  ${}^6\text{Li}$ ,  ${}^{40}\text{K}$ , and  ${}^{41}\text{K}$  into quantum degeneracy, there was no published theoretical prediction on their interspecies Feshbach resonances. We were first guided by Tom Hanna and Eite Tiesinga from NIST to explore the resonances between  ${}^6\text{Li}$  and  ${}^{41}\text{K}$ . For discovering  ${}^{40}\text{K}$  and  ${}^{41}\text{K}$  Feshbach resonances, we did a brute force search. I remember vividly that there was one night we discovered the 2.5 G wide resonance accidentally without any guidance from the theory. Later on we consulted Andrea Simoni from Université de Rennes who then provided us with his predictions on the interspecies resonance structures for  ${}^{40}\text{K}$  -  ${}^{41}\text{K}$ . Indeed, the 2.5 G wide resonance we found is a predicted  $p$ -wave resonance. From his predictions, there should be one wide  $s$ -wave just near by. We immediately adjusted the magnetic field and started searching for it. Without too much effort, we observed a 12 G wide Bose-Fermi interspecies Feshbach resonance.

To search for Feshbach resonances, atoms are loaded after evaporation into an optical dipole trap formed by two crossed laser beams of wavelength 1064 nm, each focussed to a waist of  $100\ \mu\text{m}$  at 7 W of power. For the study of  ${}^6\text{Li}$ - ${}^{41}\text{K}$  Feshbach resonances, atoms are transferred into the hyperfine ground state via a Landau-Zener sweep of the bias magnetic field in the presence of 261.3 and 234.2 MHz RF-radiation. For  ${}^{40}\text{K}$ - ${}^{41}\text{K}$ , only  ${}^{41}\text{K}$  is transferred into the ground state. This mixture is stable against spin-changing collisions due to the inverted hyperfine structure and the large nuclear spin of  ${}^{40}\text{K}$ . Feshbach resonances are detected via atom loss from three body collisions, after a fixed wait time, as a function of magnetic field. A list of observed resonances is given in table 3.2.

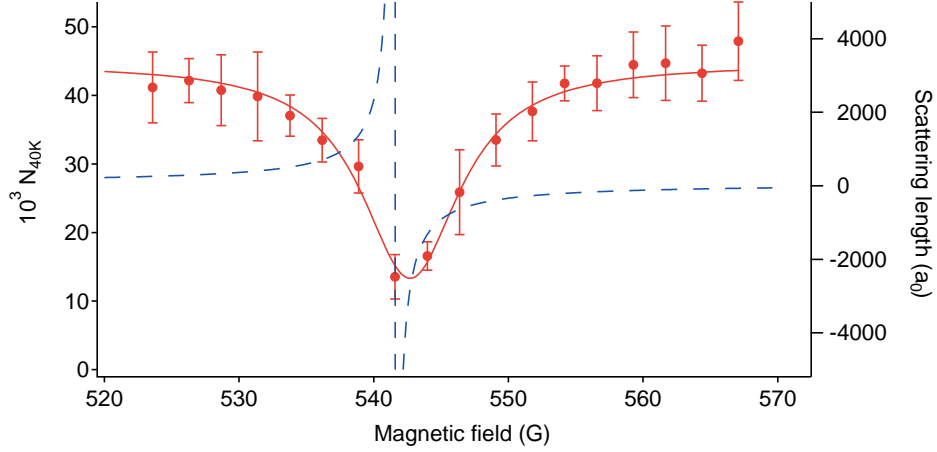


Figure 3-13: Observation of a wide Feshbach resonance in the isotopic Bose-Fermi mixture of  $^{41}\text{K}$ - $^{40}\text{K}$ . The plot shows the atom number of  $^{40}\text{K}$  versus the magnetic field. The loss feature is centered at  $B_0 = 542.7 \pm 0.5$ . From a fit to the data point with a gaussian function we obtained its gaussian width to be 12 G. The blue dashed lines are the theoretical predictions on the scattering length in the vicinity of this resonance [109].

### A gift of nature: broad interspecies Feshbach resonance between $^{40}\text{K}$ and $^{41}\text{K}$ .

As mentioned above, we observe a wide Feshbach resonance in collisions of  $^{40}\text{K}$  in state  $|9/2, 9/2\rangle$  with  $^{41}\text{K}$  in state  $|1, 1\rangle$  at 543 G (Fig. 3-13). This resonance is theoretically predicted [109] to occur at  $B_0 = 541.5$  G with a width of  $\Delta B = 52$  G, defined via the scattering length  $a = a_{\text{bg}}(1 - \Delta B/(B - B_0))$ , where  $a_{\text{bg}} = 65 a_0$  is the background scattering length in the vicinity of the resonance. This isotopic Bose-Fermi mixture with essentially no gravitational sag and wide tunability of its interaction strength is very promising for controlled many-body experiments, where the only relevant difference between the two atoms is quantum statistics.

### Entering the polaronic regime

We also checked the feasibility of studying polaron physics in this isotopic mixtures by immersing a Bose-Einstein condensate of  $^{41}\text{K}$  into a Fermi sea of  $^{40}\text{K}$  or vice versa with

Mixture	$B_0$ [G]	$\Delta B_{\text{exp}}$ [G]	Resonance type
${}^6\text{Li}   1/2, 1/2\rangle {}^{41}\text{K}   1, 1\rangle$	31.9	0.2	<i>s</i> -wave [110]
${}^6\text{Li}   1/2, 1/2\rangle {}^{41}\text{K}   1, 1\rangle$	335.8	1.1	<i>s</i> -wave [110]
${}^{40}\text{K}   9/2, 9/2\rangle {}^{41}\text{K}   1, 1\rangle$	472.6	0.2	<i>s</i> -wave [109]
${}^{40}\text{K}   9/2, 9/2\rangle {}^{41}\text{K}   1, 1\rangle$	432.9	2.5	<i>p</i> -wave [109]
${}^{40}\text{K}   9/2, 9/2\rangle {}^{41}\text{K}   1, 1\rangle$	542.7	12	<i>s</i> -wave [109]

Table 3.2: Observed interspecies Feshbach resonances between  ${}^6\text{Li}$ - ${}^{41}\text{K}$  and  ${}^{40}\text{K}$ - ${}^{41}\text{K}$  atoms. The width of the resonance,  $\Delta B_{\text{exp}}$ , is determined by a phenomenological gaussian fit to the observed loss feature (see e.g. Fig. 3-13). For the *p*-wave resonance, the width is measured at  $T = 8 \mu\text{K}$ .

resonant interactions. Fig. 3-14 shows the coexistence of a Bose-Einstein condensate of  ${}^{41}\text{K}$  and a Fermi sea of  ${}^{40}\text{K}$  on resonance. The condensate survives for about 5 ms, and the remaining thermal atoms decay with a  $1/e$  lifetime of 25 ms at initial densities  $1 (3) \times 10^{12} \text{ cm}^{-3}$  for  ${}^{40}\text{K}$  ( ${}^{41}\text{K}$ ). Our initial temperatures are low enough, and the condensate lifetime long enough so that polarons should form [111, 112]. At the rim of the condensate, where bosons are the minority, bosons are dressed into Fermi polarons, possibly yielding a Fermi polaron condensate [112]. The formation time of such a dressed quasi-particle state should be on the order of  $\hbar/E_B \sim 1 \text{ ms}$ , where  $E_B = 0.6E_{F,{}^{40}\text{K}}$  is the polaron energy [9].

In the center of the gas, where fermions are the minority, they can be expected to be dressed by the Bose condensate. It will be intriguing to perform locally resolved RF spectroscopy on this unconventional potential state of polaronic matter and to directly demonstrate dressing of fermionic and bosonic impurities [9]. Fig. 3-15 shows (a) a lifetime measurement of such a resonant system and (b) the evolution of the cloud temperature as a function of the hold time. The slow heating rate provides a clear pathway to study strongly interacting Bose-Fermi mixtures.

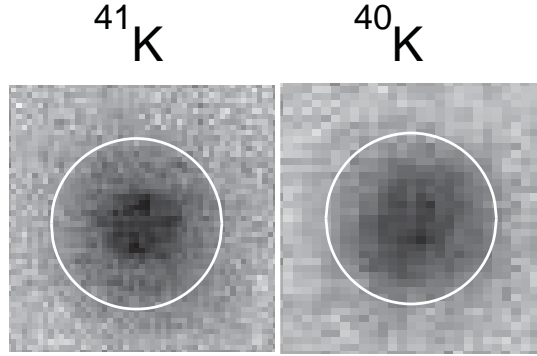


Figure 3-14: Absorption images of the Bose and Fermi clouds after short time of flight. The  $^{40}\text{K}$  image is scaled by the ratio of expansion factors of the Bose and Fermi cloud, the images thus approximately illustrate the in-trap density distribution. The white rim indicates the Fermi radius

### 3.5 Conclusion

We have successfully created a triply degenerate quantum gas of  $^{41}\text{K}$ ,  $^{40}\text{K}$  and  $^6\text{Li}$ , through sympathetic cooling of the fermions by the bosonic species  $^{41}\text{K}$ . In the Bose-Fermi mixtures of  $^6\text{Li}$ - $^{41}\text{K}$  and  $^{41}\text{K}$ - $^{40}\text{K}$ , five interspecies Feshbach resonances are identified, with  $s$ - and  $p$ -wave character. The isotopic potassium mixture could become a pristine model system for strongly interacting Bose-Fermi mixtures, for example for the study of polarons [9, 8, 113, 53, 56, 114], observation of polaron condensation [112], and universal transport of mixtures with unlike statistics [115]. The doubly degenerate  $^{40}\text{K}$ - $^6\text{Li}$  Fermi-Fermi mixture holds promise for the observation of fermionic superfluidity and Cooper pairing between unlike fermions. Imposing species-dependent optical potentials on mixtures will allow the study of systems with mixed dimensionality [116] and impurity physics such as Anderson localization [117] and the interaction of localized impurities with fermionic superfluids [118].

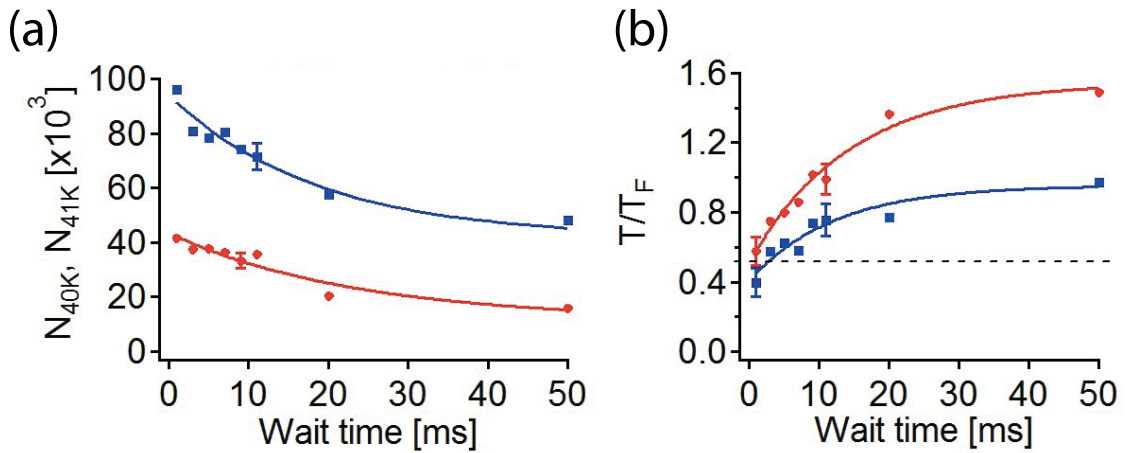


Figure 3-15: The Bose-Fermi lifetime and the evolution of temperature in the strongly interacting regime. (a) The atom number of  $^{40}\text{K}$  (blue squares) and  $^{41}\text{K}$  (red dots) atoms as a function of wait time in the crossed optical dipole trap. The condensate survives for the first 5 ms and the remaining thermal atoms decay with a  $1/e$  lifetime of 25 ms at initial densities  $1$  ( $3$ )  $\times 10^{12} \text{ cm}^{-3}$  for  $^{40}\text{K}$  ( $^{41}\text{K}$ ). (b) The reduced temperature  $T/T_F$  versus wait time on the Feshbach resonance. The dashed line indicates the BEC threshold  $T_c/T_F = 0.52$ .

# Chapter 4

## A New Ultracold Quantum

## Mixture of $^{23}\text{Na}^{40}\text{K}$

*In this chapter, we will describe a new system where we have created and studied the first quantum degenerate Bose-Fermi mixture of  $^{23}\text{Na}$  and  $^{40}\text{K}$  with widely tunable interactions via broad interspecies Feshbach resonances. Over 30 Feshbach resonances between  $^{23}\text{Na}$  and  $^{40}\text{K}$  are identified, including  $p$ -wave multiplet resonances. Our work opens up the prospect to create chemically stable, fermionic ground state molecules of  $^{23}\text{Na}^{40}\text{K}$  where strong, long-range dipolar interactions would set the dominant energy scale.*

### 4.1 Introduction

Since the first degenerate Bose-Fermi mixture of  $^6\text{Li}$  -  $^7\text{Li}$  [34], a variety of such systems has been realized [83, 96, 119, 49, 120, 121, 122, 97, 99, 123, 46, 124]. However, before our study only one mixture,  $^{87}\text{Rb}$ - $^{40}\text{K}$ , has allowed tunability of interspecies interactions by means of a moderately wide ( $\Delta B \approx 3\text{ G}$ ) Feshbach resonance [102]. Bose-Fermi mixtures with widely tunable interactions can be used to study boson mediated interactions between fermions and possibly boson induced  $p$ -wave super-

fluidity [125, 126]. The properties of impurities in a Fermi sea [9] or a Bose condensate [46, 111, 112] can also be studied, and new quantum phases of matter are predicted in optical lattices [127].

In this chapter, we will show the realization of a new Bose-Fermi mixture of  $^{23}\text{Na}$  -  $^{40}\text{K}$  and the observation of over 30  $s$ - and  $p$ -wave Feshbach resonances at low magnetic fields. We demonstrate that  $^{23}\text{Na}$  is an efficient coolant for sympathetic cooling of  $^{40}\text{K}$ . A pattern of wide  $s$ -wave resonances exists for most of the energetically stable hyperfine combinations, the widest being located at 138 G with a width of about 30 G in the  $^{23}\text{Na}|1, 1\rangle + ^{40}\text{K}|9/2, -5/2\rangle$  hyperfine configuration. We also observe  $p$ -wave multiplet resonances that are resolved due to their location at low magnetic fields.

## 4.2 A new coolant for $^{40}\text{K}$ : $^{23}\text{Na}$

We introduced sodium to the Fermi-I machine as a new coolant for the fermionic species. Meanwhile, we learned from Ref. [128] that the interspecies background scattering length between  $^{23}\text{Na}$  and  $^{40}\text{K}$  was relatively large compared to the scattering length between  $^{40}\text{K}$  and  $^{87}\text{Rb}$ , meaning that the three-body loss rate in our system could be quite significant. Therefore, we originally intended to load atoms into the ODT as early as possible and performed most of the evaporation in the ODT with a favorable scattering length using Feshbach resonances. At the end of the journey of exploring the Feshbach resonance structure between  $^{23}\text{Na}$  and  $^{40}\text{K}$ , we realized that this mixture was extremely versatile and furthermore it could potentially produce a chemically stable ground state molecule of  $^{23}\text{Na}^{40}\text{K}$ .

### 4.2.1 Making the $^{23}\text{Na}$ Bose-Einstein condensate

We started installing the  $^{23}\text{Na}$  MOT optics at the end of January 2010 and we obtained the first  $^{23}\text{Na}$  BEC at beginning of March 2010. For getting a healthy sodium BEC, we basically followed the procedure in [37, 84]. Below we summarize some important points to note for producing a large  $^{23}\text{Na}$  BEC in the Fermi I experiment.

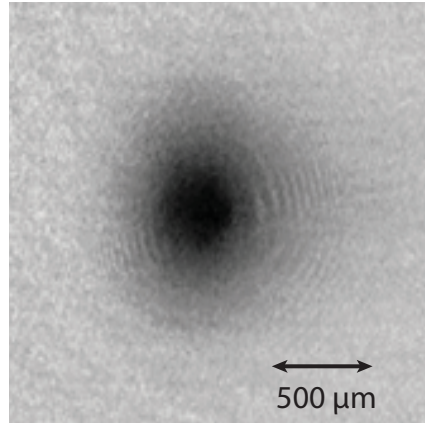


Figure 4-1: An absorption image of the  $^{23}\text{Na}$  Bose-Einstein condensate immersed in a sodium thermal bath in the  $F = 2$  state in the magnetic trap. A pure BEC with  $\sim 10^7$  atoms can be obtained with further evaporation.

#### Optically saturated dark MOT

An absorption monitor is absolutely required to tweak the  $^{23}\text{Na}$  MOT since atoms are mostly stored in the dark state, which makes the fluorescence signal from the MOT unreliable. We use a 0.5 mm dia. beam split from the  $F = 1$  imaging light sending through the center of the MOT. Its frequency is scanned by a tandem AOM setup [94] about  $\pm 80$  MHz. A photodiode is used to measure the absorption of this beam as a function of the scanned frequency. Typically, a good  $^{23}\text{Na}$  MOT requires a flat plateau (optical density  $> 100$ ) with a width MHz greater than 80 MHz in the frequency scan [81]. To achieve this large range of high optical density, imaging the dark spot onto the MOT, carefully choosing the dark spot size ( $\sim 1/2$  of the MOT

size), and eliminating all possible reflection of the repumping beam from the chamber windows are necessary.

### **High PSD at the beginning of evaporation in the magnetic trap**

The best MOT does not always guarantee the best mode matching for loading into the magnetic trap. Therefore the final figure of merit for the MOT optimization is the PSD after loading  $^{23}\text{Na}$  into the magnetic trap. In order to maximize the loading efficiency a sudden change of the XYZ bias fields to move the magnetic during loading is necessary since the center position of the MOT could be a bit different from the center of the magnetic trap. A initial PSD of  $\sim 5 \times 10^{-8}$  in the magnetic trap can guarantee a runaway evaporation.

### **Spin purification**

This step is only required when cooling atoms in the  $F = 2$  state. Spin imperfections can cause spin relaxation and therefore heat up the atoms (e.g.,  $|2, 1\rangle + |2, 0\rangle \rightarrow |2, 2\rangle + |2, -1\rangle$ ). We use the gravity assisted purification scheme as explained in Chapter 3 to clean up the spin states of  $^{23}\text{Na}$  immediately after loading the magnetic trap.

### **Decompression of the magnetic trap**

The three-body loss rate is proportional to  $n^3$  and the thermalization rate is proportional to  $n^2$ . Therefore, towards the end of evaporation atomic density becomes extremely high and the three-body loss rate surpasses the thermalization rate. At this point, it is essential to decompress the magnetic trap to decrease the atomic density. Decompression in an optically plugged magnetic trap requires more care since the magnetic trap center can move during decompression due to the imperfection of the coils. In order to keep the plug beam always aligned with the center of the magnetic

trap, ramping XYZ bias fields to a new set of values during decompression is required.

Following the procedures listed above, we are able to obtain a pure  $^{23}\text{Na}$  BEC with  $\sim 10^7$  atoms in the  $F = 2$  state at the end of evaporation. Fig. 4-1 shows an absorption image of a  $^{23}\text{Na}$  BEC immersed in a thermal bath in the magnetic trap. In order to obtain a round BEC, we need to turn off the plug beam simultaneously with the magnetic trap when releasing the atoms.

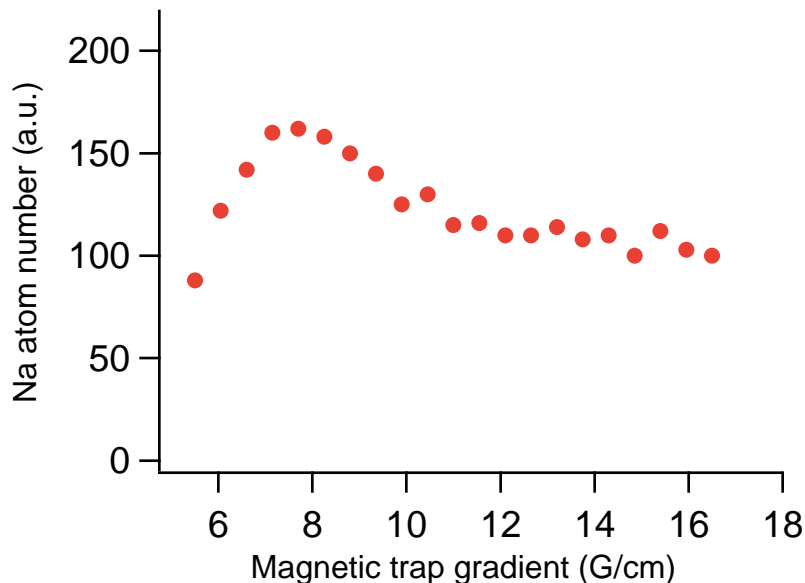


Figure 4-2: The  $^{23}\text{Na}$  atom number as a function of the purification field gradient after 10 s wait time in the magnetic trap. The peak around  $\sim 8$  G corresponds to the threshold gradient which can hold only the  $^{23}\text{Na}$   $|2, 2\rangle$  state against gravity.

### 4.2.2 Two stage MOT loading technique

Due to the large background scattering length between  $^{23}\text{Na}$  and  $^{40}\text{K}$ , one must cool  $^{40}\text{K}$  using  $^{23}\text{Na}$  in the  $|2, 2\rangle$  state while in the magnetic trap. Otherwise, cooling with  $^{23}\text{Na}$  in the  $|1, -1\rangle$  state can cause strong spin relaxation. Indeed, experimentally, we observe no  $^{40}\text{K}$   $|9/2, 9/2\rangle$  atoms survive after  $\sim 1$  s in the presence of  $^{23}\text{Na}$   $|1, -1\rangle$  atoms in the magnetic trap. However, cooling  $^{23}\text{Na}$  in the  $|2, 2\rangle$  state requires spin

purification [37]. Since potassium is heavier than sodium, it is impossible to perform gravity assisted purification on the mixture without sacrificing all  $^{40}\text{K}$  atoms. Without purifying the sodium spin states, we observe strong atom losses in both sodium and potassium. Fig. 4-2 shows the atom number of  $^{23}\text{Na}$  as a function of the purification field gradient. The peak at the  $\sim 8 \text{ G/cm}$  corresponds to the threshold gradient which can only hold  $^{23}\text{Na} |2, 2\rangle$  atoms against gravity. Fig. 4-3 shows the lifetime of  $^{40}\text{K}$  with and without pre-purifying  $^{23}\text{Na}$ . Therefore, spin purifying  $^{23}\text{Na}$  is absolutely necessary to reduce losses of  $^{40}\text{K}$  in the magnetic trap. In order to resolve this problem, one of my colleagues, Jee Woo Park, came out with an idea: the two stage MOT loading technique. The two state MOT loading technique can not only purify the spin states of  $^{23}\text{Na}$  without affecting  $^{40}\text{K}$  but also avoid the atom losses from the light-assisted collisions in the MOT loading stage. It works as the following:

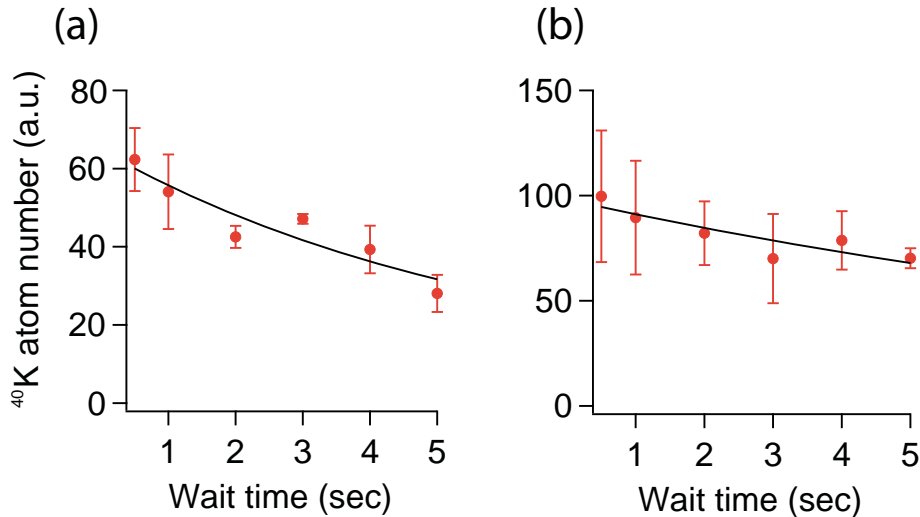


Figure 4-3: Lifetime curves of  $^{40}\text{K}$  in the magnetic trap with (a) and without (b)  $^{23}\text{Na}$ . With  $^{23}\text{Na}$  in the magnetic trap we observe a lifetime of 5.2 s; however without  $^{23}\text{Na}$  the lifetime increases to 12.5 s. One can also see that the initial atom number of  $^{40}\text{K}$  is different with and without  $^{23}\text{Na}$  due to light-assisted collisions in the MOT loading stage.

$^{23}\text{Na}$  atoms are first loaded into the MOT and optically pumped to the  $|2, 2\rangle$  stretched state (optical pumping efficiency is  $\sim 75\%$ ), and then captured in the

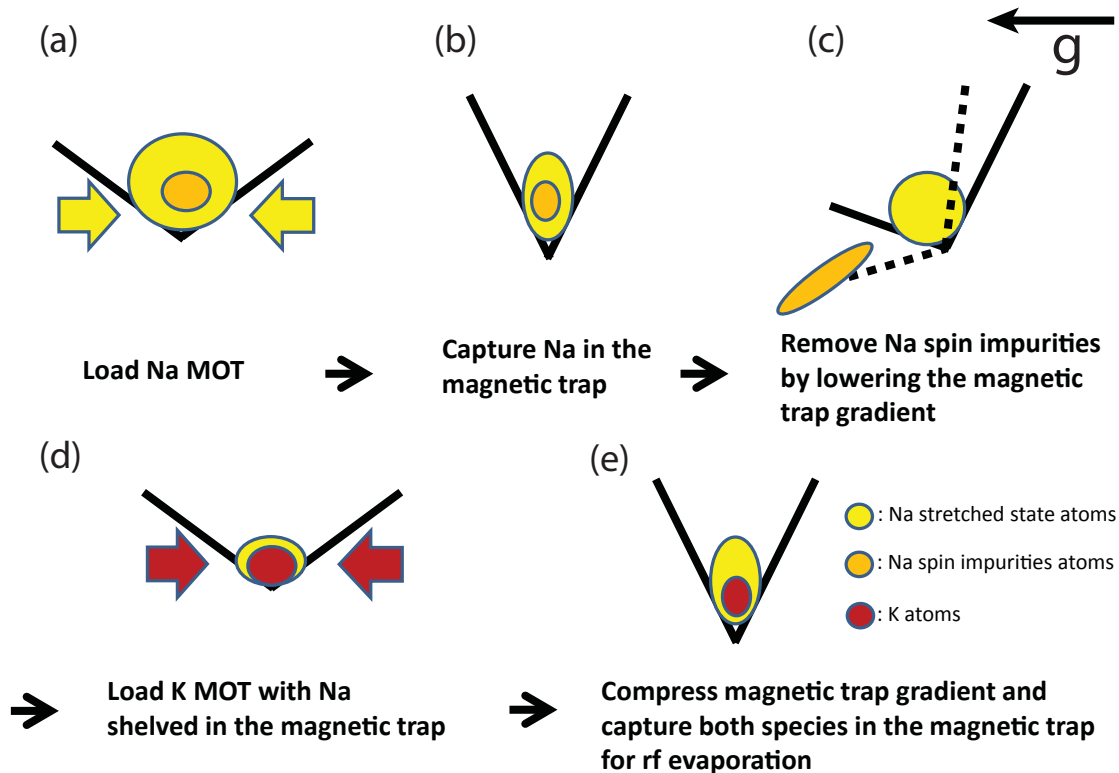


Figure 4-4: Illustration of the two stage MOT loading technique. (a) Only the MOT and slower beams for  $^{23}\text{Na}$  are switched on to load  $^{23}\text{Na}$  into the MOT with a magnetic field gradient of 11 G/cm. (b) The stretched state and the other spin states of  $^{23}\text{Na}$  are all captured in the magnetic trap. (c) The magnetic field gradient is reduced to a critical value (8 G/cm) where only the stretched state of  $^{23}\text{Na}$  can be held against gravity. (d) The magnetic field gradient is increased back to 11 G/cm and the MOT and slower beams for  $^{40}\text{K}$  are switched on to load the  $^{40}\text{K}$  MOT with  $^{23}\text{Na}$  shelved in the magnetic trap. (e) After loading the  $^{40}\text{K}$  MOT, the magnetic field gradient is increased to 220 G/cm and then RF evaporation starts.

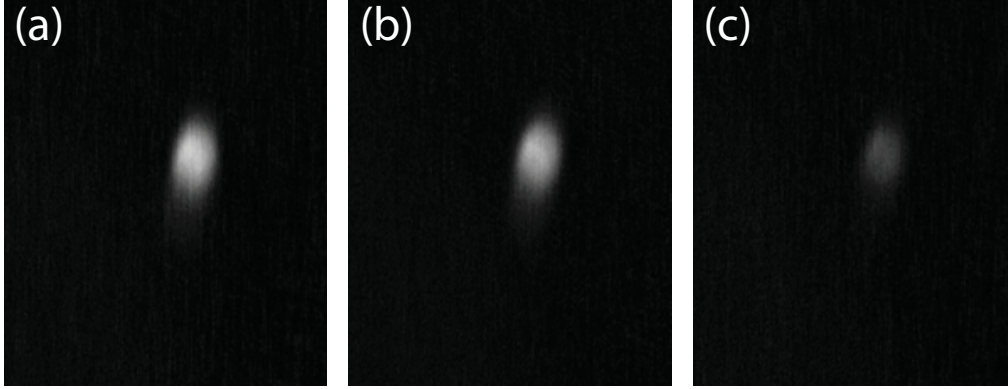


Figure 4-5: Fluorescence images of  $^{40}\text{K}$  in the magnetic trap. (a) shows an image of  $^{40}\text{K}$  before evaporation, right after loading into the magnetic trap. Here the atom number of  $^{40}\text{K}$  is  $\sim 7 \times 10^5$ . (b) shows an image after the first evaporation with applying the two stage MOT loading technique. Here the atom number of  $^{40}\text{K}$  is  $\sim 5 \times 10^5$ . (c) shows an image after the first evaporation without applying the two stage MOT loading technique. Here the atom number of  $^{40}\text{K}$  is  $\sim 1 \times 10^5$ .

magnetic trap. Next, the trap gradient is reduced to 8 G/cm to only support the stretched state of  $^{23}\text{Na}$  against gravity. With this gradient left on, and the  $^{23}\text{Na}$  thus “shelved in the dark” in a purely magnetic trap, the gradient is increased to 11 G/cm, and the MOT and slower beams for  $^{40}\text{K}$  are switched on to load the  $^{40}\text{K}$  MOT. This scheme guarantees that only  $^{23}\text{Na}$  atoms in the  $|2, 2\rangle$  state are present in the magnetic trap before loading  $^{40}\text{K}$ , and it also potentially reduces light-assisted collisions that would be encountered in a double-species MOT. A detailed illustration of this technique can be found in Fig. 4-4. After applying this technique we observe no significant loss of  $^{40}\text{K}$  atoms in the magnetic trap after the first evaporation. Fig. 4-5(a) shows a fluorescence image of  $^{40}\text{K}$  before evaporation, (b) shows a fluorescence image of  $^{40}\text{K}$  after the first evaporation with applying the two stage MOT loading technique, and (c) shows a fluorescence image of  $^{40}\text{K}$  without applying the two stage MOT loading technique. We observe almost a factor of five improvement in the  $^{40}\text{K}$  atom number with the two stage MOT loading technique.

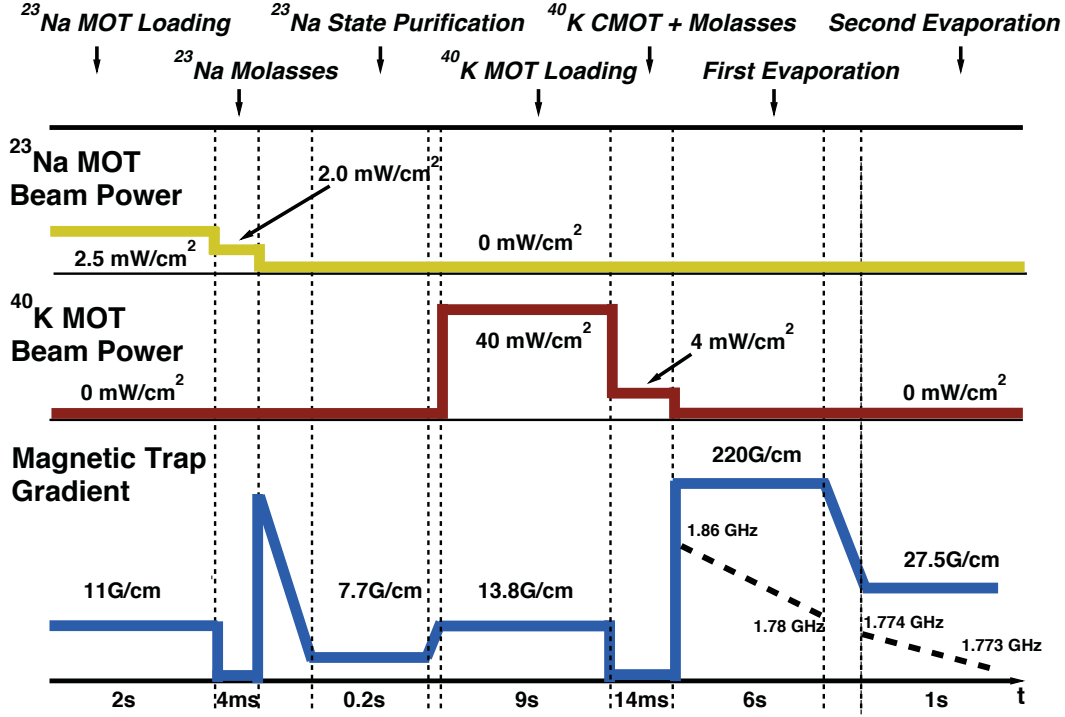


Figure 4-6: The experimental sequence of the two stage MOT loading technique and the RF evaporation. The orange solid line and red solid line indicate the  $^{23}\text{Na}$  and  $^{40}\text{K}$  MOT beam power as a function of the sequence time, respectively. The blue solid line indicates the magnetic field gradient and the black dashed line is the RF frequency. The ODT is ramped up in last 0.5s during the final decompression (from 27.5 G/cm to 0 G/cm) which is not shown in this figure.

### 4.2.3 Obtaining double degeneracy

Once both species are loaded into the optically plugged magnetic trap, the mixture is cooled for 6 s by RF evaporation of  $^{23}\text{Na}$ , where thermally excited  $^{23}\text{Na}$  atoms in the  $|2, 2\rangle$  state are removed from the trap by coupling to the high field seeking state of  $|1, 1\rangle$ . The experimental sequence is shown in Fig. 4-6 and Fig. 4-7 shows the in-trap images of  $^{23}\text{Na}$  and  $^{40}\text{K}$  after the first evaporation where we typically have an atom number of  $2 \times 10^6$  for  $^{23}\text{Na}$  and  $2 \times 10^5$  for  $^{40}\text{K}$ . We decompress the initial field gradient of 220 G/cm to 27.5 G/cm at the end of first evaporation to reduce three-body losses. After the second evaporation, the 5  $\mu\text{K}$  cold mixture is then loaded into a crossed ODT (laser wavelength 1064 nm, maximum power 4.7 and 17 W, beam waist 73 and

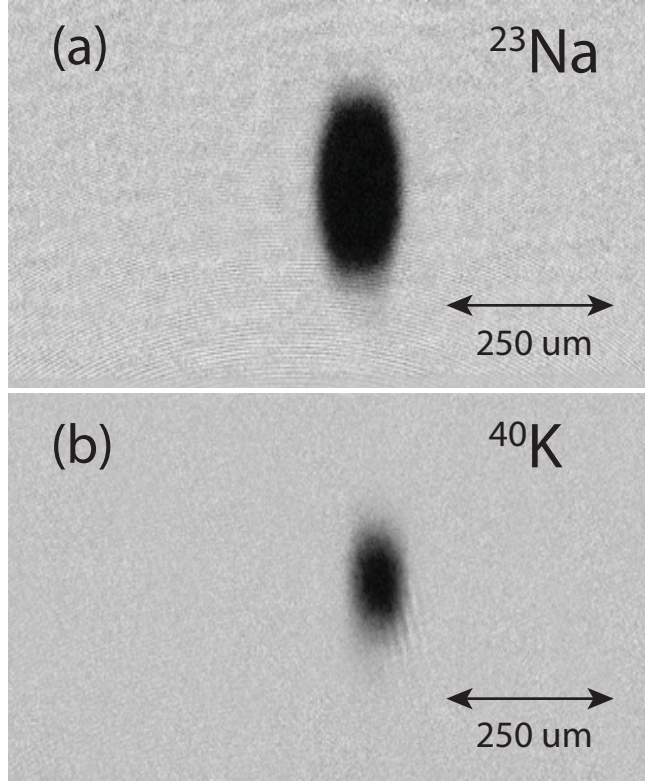


Figure 4-7: In-trap images of (a)  $^{23}\text{Na}$  and (b)  $^{40}\text{K}$  after the first evaporation in the magnetic trap with a gradient of 220 G/cm. The measured atom number at this point is  $\sim 2 \times 10^6$  for  $^{23}\text{Na}$  and  $\sim 2 \times 10^5$  for  $^{40}\text{K}$ .

135  $\mu\text{m}$ ).

At this stage, the  $1/e$  lifetime of the mixture, with  $^{23}\text{Na}$  and  $^{40}\text{K}$  still in their stretched states, is about  $\tau = 250$  ms, still signaling a strong attractive interaction increasing three-body losses and spin-changing dipolar losses. We thus immediately transfer  $^{23}\text{Na}$  atoms into their hyperfine ground state  $|1, 1\rangle$  via a Landau-Zener sweep, and remove any remaining  $|2, 2\rangle$  atoms via a resonant light pulse. In the  $^{23}\text{Na}|1, 1\rangle + ^{40}\text{K}|9/2, 9/2\rangle$  state, the mixture now lives for  $\tau = 20$  s. The gas is further evaporatively cooled in this spin mixture for 2 s by reducing the intensity of the ODT beams.

At the end of evaporation, a degenerate Fermi gas of  $^{40}\text{K}$  with  $2 \times 10^5$  atoms and  $T/T_F = 0.6$  coexists with a Bose-Einstein condensate of  $^{23}\text{Na}$ . Two sets of absorption

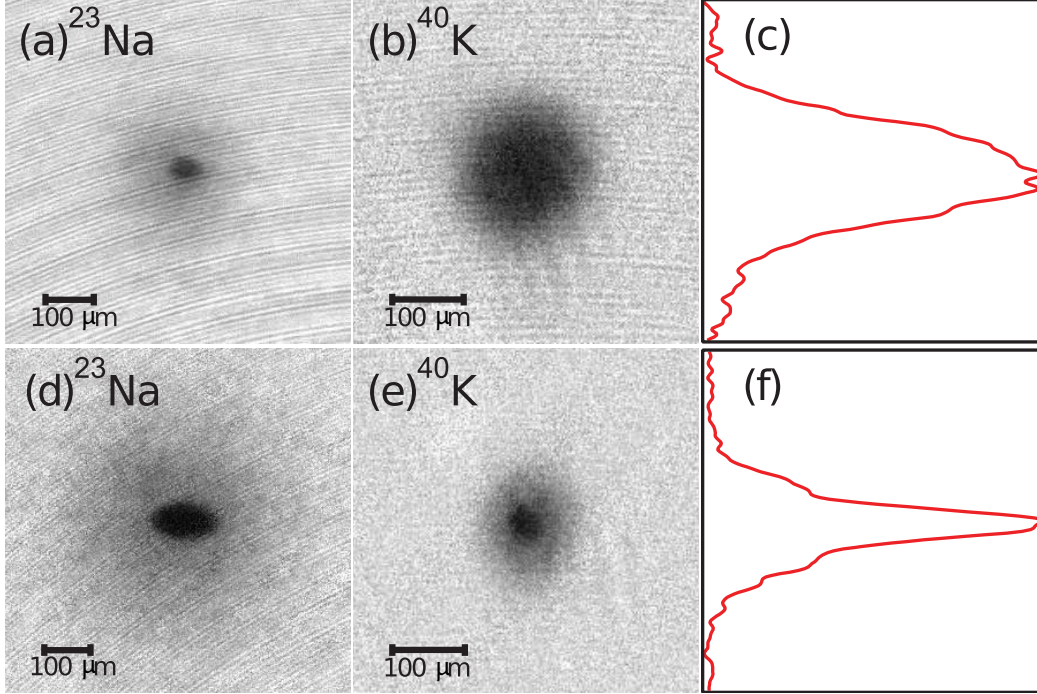


Figure 4-8: Simultaneous quantum degeneracy of  $^{23}\text{Na}$  and  $^{40}\text{K}$  atoms. (a)-(b) and (d)-(e) are pairs of time of flight (TOF) absorption images of a  $^{23}\text{Na}$  BEC and  $^{40}\text{K}$  Fermi clouds with different atom number balance. Strong attractive interactions between the two species is observed in (e) as a sharp increase of the central density in the fermionic cloud in the presence of a Bose condensate. (c) and (f) are the center-sliced column density of the fermionic clouds of (b) and (e), respectively. TOF is (a) 11 ms, (b) 7 ms, (d) 17 ms, (e) 5 ms. Atom numbers are (a)  $2.4 \cdot 10^5$ , (b)  $2 \cdot 10^5$ , (d)  $8.2 \cdot 10^5$ , (e)  $6.7 \cdot 10^4$ .

images of the mixture for different values of  $^{23}\text{Na}$  and  $^{40}\text{K}$  atom numbers are shown in Fig. 4-8, where atom numbers are varied by changing the MOT loading times of the two species. The strong attractive interaction between  $^{23}\text{Na}$  and  $^{40}\text{K}$  in the  $^{23}\text{Na}|1, 1\rangle + ^{40}\text{K}|9/2, 9/2\rangle$  state is apparent. As the condensate grows, the fermionic cloud acquires a bimodal density distribution as it experiences the strong mean-field potential of the bosons [129] (see Fig. 4-8(e)).

The evolution of the phase space densities (PSDs) and the atom numbers  $N$  of both species during evaporation is shown in Fig. 4-9. Temperature is determined by fitting a thermal profile to the wings of the  $^{23}\text{Na}$  cloud. The cooling efficiency

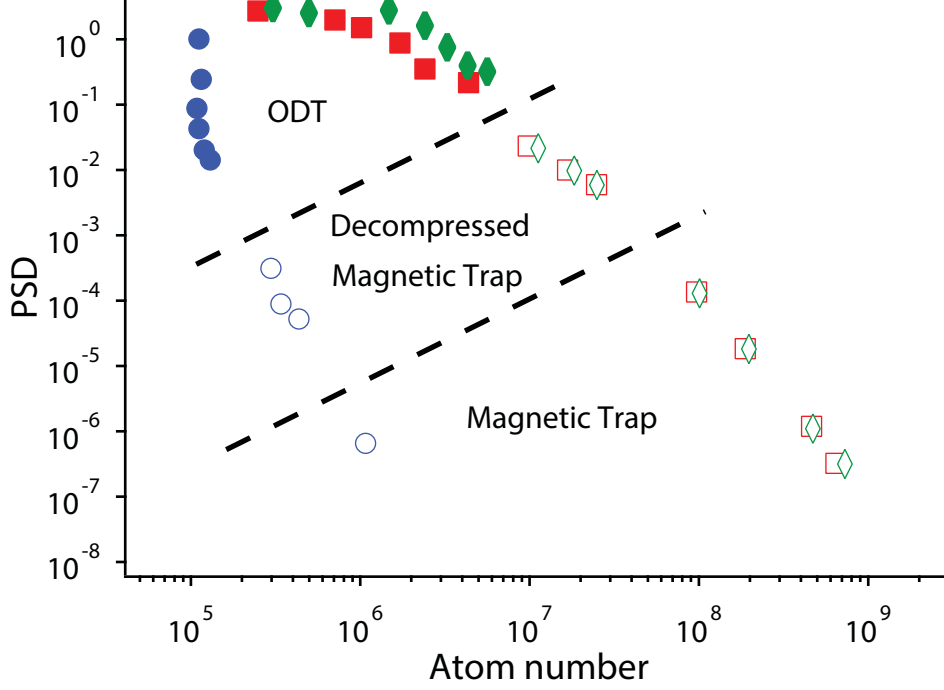


Figure 4-9: Evolution of the phase space density (PSD) as a function of the atom number ( $N$ ). Blue circles:  $^{40}\text{K}$ , Red squares:  $^{23}\text{Na}$  with  $^{40}\text{K}$ , Green diamonds:  $^{23}\text{Na}$  alone. Empty and solid symbols represent the PSD in the magnetic trap and optical trap, respectively.

$\Gamma = -d\ln(\text{PSD})/d\ln(N)$  for sodium in the magnetic trap is  $\Gamma_{\text{Na}} = 2.7$ , a rather high value thanks to the step confinement in the plugged trap. This efficiency is not affected by the presence of the relatively small admixture of  $^{40}\text{K}$ . Sympathetic cooling is less efficient than in other mixtures [37, 46] as  $^{40}\text{K}$  is seen to be lost due to three-body collisions in the magnetic trap. We find  $\Gamma_{\text{K}} = 4.6$  for  $^{40}\text{K}$ . In the crossed ODT, with  $^{23}\text{Na}$  in the  $|1, 1\rangle$  state, the sodium cooling becomes less efficient due to the weaker confinement,  $\Gamma_{\text{Na}} = 0.9$ , but the  $^{40}\text{K}$  number is essentially conserved in this mixture so that sympathetic cooling is highly efficient, with  $\Gamma_{\text{K}} = 15.3$ . The lowest  $T/T_F$  achieved for  $^{40}\text{K}$  after evaporating all of  $^{23}\text{Na}$  is  $T/T_F = 0.35$  with  $3 \times 10^5$  atoms.

## 4.3 Feshbach resonances between $^{23}\text{Na}$ and $^{40}\text{K}$

The natural next step after successfully cooling both species to quantum degeneracy is to search for interspecies Feshbach resonances. There have been theoretical indications for resonances below 100 G [128]. In addition, a large and negative triplet scattering length was predicted [130], a value that has recently been refined to  $a_t = -575_{-532}^{+191}$  [128], indicating that the triplet potential has an almost bound, virtual state right above threshold. A large background scattering length is often a catalyst for wide Feshbach resonances [131], caused by strong coupling of molecular states to the almost resonant open channel. A famous example is the 300 G wide Feshbach resonance in  $^6\text{Li}$  [132].

### 4.3.1 Spin state preparation

In order to perform Feshbach loss spectroscopy in different combinations of hyperfine states, being able to change the spin states at will is important. We summarize some key points for performing a successful spin transfer:

#### Sufficient magnetic field

A magnetic field  $> 10\text{ G}$  to create sufficiently large Zeeman splitting is necessary; otherwise, ambient electromagnetic noise (e.g., switching power supplies) can spin transfer atoms undesirably.

#### Stable and homogeneous magnetic field

The magnetic field needs to be stable during the Landau-Zener sweep so that atoms can adiabatically follow the spin state. Random fluctuations in the magnetic field can cause random fluctuations in the resonance frequency. We note that high RF power affects electronic devices (e.g., power supplies) and causes enormous field fluctuations.

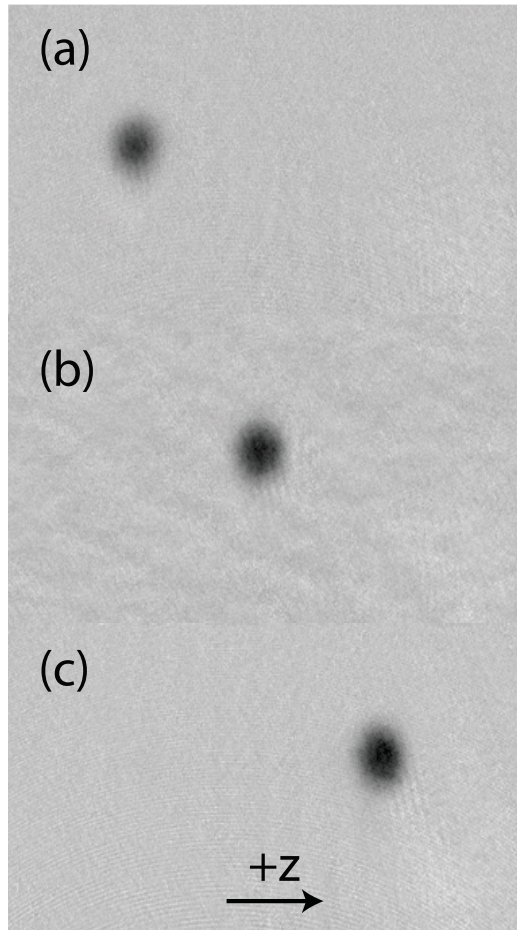


Figure 4-10: The Stern-Gerlach experiment for identifying the spin states of  $^{40}\text{K}$ . (a) shows  $^{40}\text{K}$  in the  $|9/2, 9/2\rangle$  state where the magnetic field gradient pushes atoms in the  $-z$  direction during time of flight. (b) Normal time of flight image without the Stern-Gerlach field. (c) shows  $^{40}\text{K}$  in the  $|9/2, -9/2\rangle$  state where the magnetic field gradient pushes atoms in the  $+z$  direction during time of flight.

To check the stability of spin transfer, we perform a Stern-Gerlach measurement by suddenly switching on the fifth layer of the quadrupole coils (in anti-Helmholtz configuration) during time of flight. Due to the magnetic field gradient, atoms experience a magnetic field force which is proportional to the magnetic moments. Fig. 4-10 shows a demonstration of the Stern-Gerlach experiment. Atoms with opposite magnetic moments fly in opposite directions in the Stern-Gerlach field. From the positions of the atoms, we can identify their spin states.

### 4.3.2 Feshbach loss spectroscopy

We search for interspecies Feshbach resonances by mapping out the atom numbers of both species as a function of the magnetic field. Because there is no theoretical prediction on the resonance positions, we first perform a brute force search by scanning the magnetic field in a wide range (typically around 10 G) and look for tiny atom loss signals. Over 30 Feshbach resonances are observed in four different spin state combinations of  $^{23}\text{Na}|1, 1\rangle + ^{40}\text{K}|9/2, m_F\rangle$ , from the ground spin state  $m_F = -9/2$  up to  $m_F = -3/2$ . Spin states of  $^{40}\text{K}$  are prepared starting from  $m_F = +9/2$  by a single Landau-Zener sweep through the intermediate  $m_F$  states at 15 G. The experimentally observed resonance positions and widths are reported in Table 4.1. Many wide *s*-wave Feshbach resonances at low magnetic fields are identified, the widest one at 138 G for collisions between  $^{23}\text{Na}|1, 1\rangle + ^{40}\text{K}|9/2, -5/2\rangle$ , with a width of 30 G (see Fig. 4-11).

### 4.3.3 *p*-wave multiplets

*p*-wave Feshbach resonances are known to split into a doublet structure due to different projections of the orbital angular momentum onto the magnetic field axis [133]. In the NaK system, however, we observe triplet features for many *p*-wave resonances (see Fig 4-12). The multiplets originate from the magnetic dipole-dipole interaction of the constituent atoms which can be written as:

$^{23}\text{Na} 1, 1\rangle+$ $^{40}\text{K} 9/2, m_F\rangle$	$B_0^{\text{expt}}$ (G)	$\Delta B_{\text{expt}}$ (G)	$B_0^{\text{th}}$ (G)	$\Delta B_{\text{th}}$ (G)	Res. type
-9/2	6.35, 6.41, 6.47, 6.68	0.02	7.2		<i>p</i>
	19.12, 19.18, 19.27	0.02	18.3		<i>p</i>
	78.3	1.1	75.5	1.1	<i>s</i>
	88.2	4.3	84.5	5.4	<i>s</i>
-7/2	7.32, 7.54	0.2, 0.03	8.7		<i>p</i>
	23.19, 23.29	0.05, 0.05	22.1		<i>p</i>
	81.6	0.2	82.1	0.04	<i>s</i>
	89.8	1.1	87.3	0.6	<i>s</i>
-5/2	108.6	6.6	105.7	13.1	<i>s</i>
	9.23, 9.60	0.14, 0.11	11.0		<i>p</i>
	29.19, 29.45, 29.52	0.04	27.8		<i>p</i>
	96.5	0.5	97.2	0.04	<i>s</i>
-3/2	106.9	1.8	103.8	0.45	<i>s</i>
	148 (138*)	37 (30*)	137.1	26	<i>s</i>
	12.51, 12.68	0.16, 0.06	14.8		<i>p</i>
	39.39, 39.86	0.15, 0.14	37.2		<i>p</i>
	116.9	0.5	118.3	0.07	<i>s</i>
	129.5	4.6	127.2	0.39	<i>s</i>
	175	20	187.8	50.5	<i>s</i>

\* The resonance position and width have been refined by measuring the molecular binding energies via rf spectroscopy [47].

Table 4.1: Data summary on the Feshbach resonances between  $^{23}\text{Na}$  in  $|1, 1\rangle$  and  $^{40}\text{K}$  in  $|9/2, m_F\rangle$ . The positions and widths of the resonances,  $B_0^{\text{expt}}$  and  $\Delta B_{\text{expt}}$ , are determined by phenomenological Gaussian fits ( $\propto e^{-(B-B_0^{\text{expt}})^2/\Delta B_{\text{expt}}^2}$ ) to the observed loss features. For *p*-wave resonances, we report the positions and widths of the resolved features, i.e., doublets and multiplets.  $B_0^{\text{th}}$  and  $\Delta B_{\text{th}}$  give the theoretical positions and widths from the ABM model.

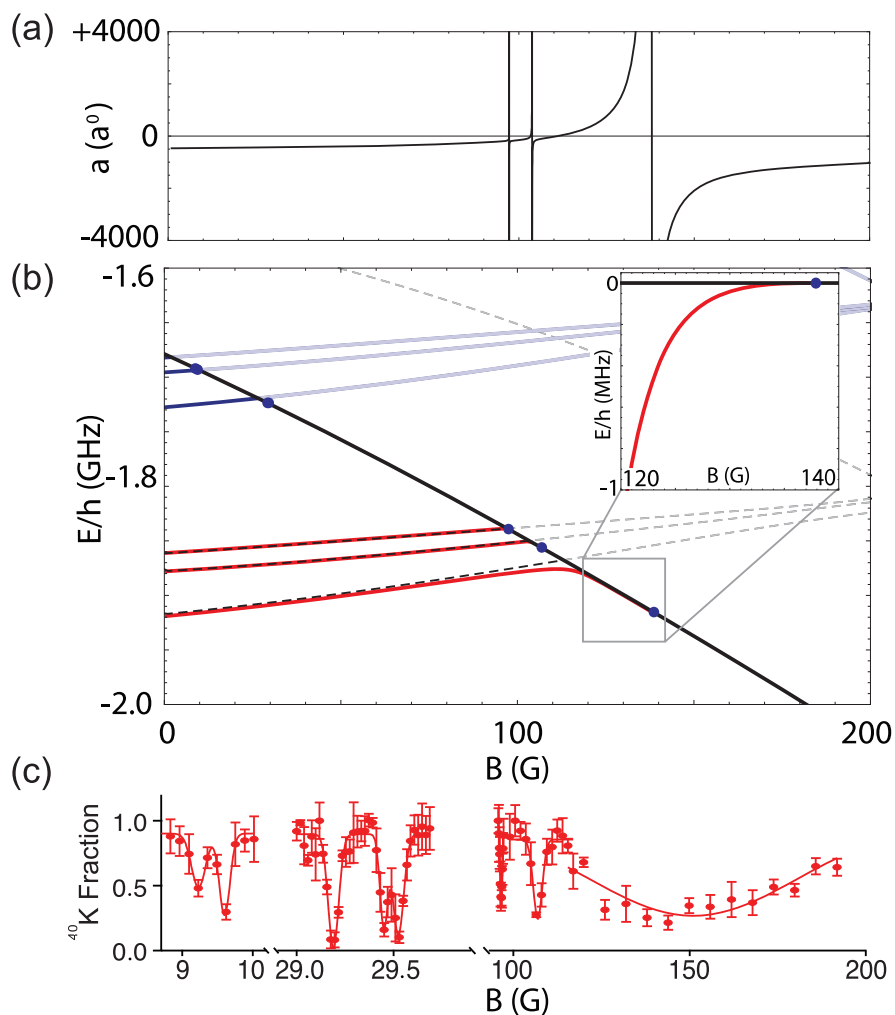


Figure 4-11: Feshbach resonances in  $^{23}\text{Na}$ - $^{40}\text{K}$ , here for  $^{23}\text{Na}|1, 1\rangle + ^{40}\text{K}|9/2, -5/2\rangle$  collisions. (a) Scattering length from the ABM model. (b) Open channel threshold energy (black solid line), uncoupled ( $s$ -wave: dashed lines,  $p$ -wave: light blue lines) and coupled molecular states ( $s$ -wave: red solid lines,  $p$ -wave: blue solid lines). The blue dots denote experimentally measured resonances. The inset shows the energy, relative to threshold, of the molecular state at the wide  $s$ -wave resonance at 138 G [47]. (c) Experimental loss spectra of  $^{40}\text{K}$  in the presence of  $^{23}\text{Na}$ . Three  $s$ -wave resonances and two  $p$ -wave manifolds are found, the latter resolved in one doublet and one triplet.

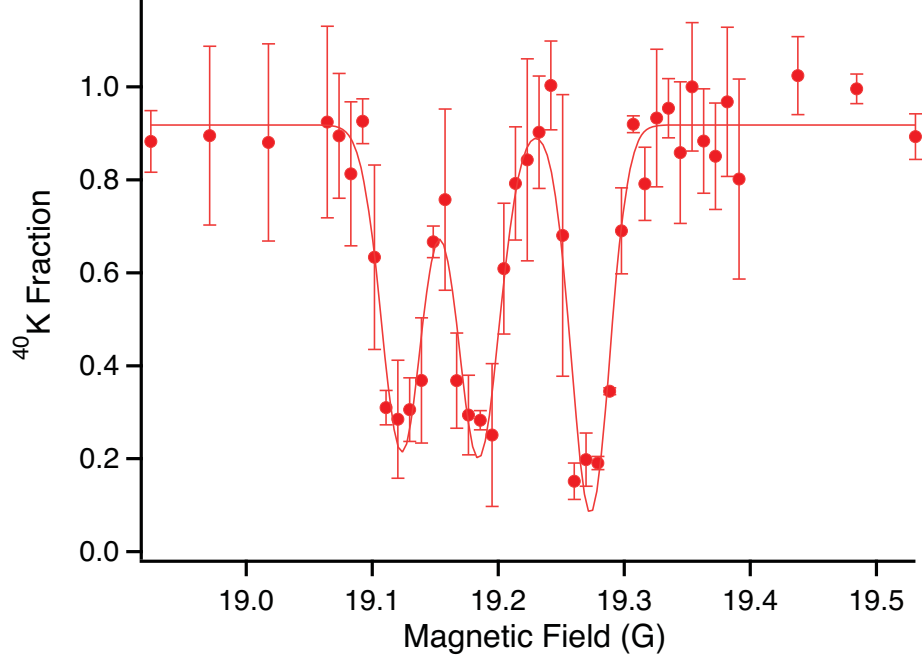


Figure 4-12: Triplet structure of the  $p$ -wave resonance at 19.1 G for the  $^{23}\text{Na}|1, 1\rangle + ^{40}\text{K}|9/2, -9/2\rangle$  spin configuration. A phenomenological triple Gaussian fit is applied as a guide to the eyes.

$$H_{ss} = -\alpha^2 \frac{(\hat{R} \cdot \hat{s}_1)(\hat{R} \cdot \hat{s}_2) - \hat{s}_1 \cdot \hat{s}_2}{R^3}, \quad (4.1)$$

where  $\alpha$  is the fine structure constant,  $\hat{s}_i$  is the spin of the valence electron on atom  $i$ ,  $R$  is the interatomic distance, and  $\hat{R}$  is the normal vector defined by the interatomic axis. This Hamiltonian couples molecular states with different total internal spin and its matrix element can be expressed as [134]:

$$H_{ss} = -\frac{\alpha^2 \sqrt{6}}{2R^3} \langle l' m'_l | C^2(\theta, \phi) | l, m_l \rangle \times \langle F'_1, m'_{F_1} | \langle F'_2, m'_{F_2} | (s_1 \otimes s_2)^2 | F_1, m_{F_1} \rangle | F_2, m_{F_2} \rangle, \quad (4.2)$$

where  $C^2(\theta, \phi)$  is a reduced spherical harmonic that depends only on the orientation of the atoms and  $(s_1 \otimes s_2)^2$  is the second rank tensor formed from the rank-1 spin operators. Here we have already assumed elastic collisions and for the  $p$ -wave collision,

namely  $l = l' = 1$ . Note that the spin and the spatial contributions do not decouple because the term  $(s_1 \otimes s_2)^2$  still takes into account the relative orientation of the two spins to the interatomic axis. Equation (4.2) can be worked out with the Wigner D-functions:

$$\begin{aligned}
H_{ss} = & -\frac{\alpha^2\sqrt{6}}{2R^3} \langle l' m'_l | C^2(\theta, \phi) | l, m_l \rangle \\
& \times \langle \Omega'_1, F'_1, m'_{F_1} | D_{\Delta M_{F_1}, 0}^1 | \Omega_1, F_1, m_{F_1} \rangle \langle \Omega'_2, F'_2, m'_{F_2} | D_{\Delta M_{F_2}, 0}^1 | \Omega_2, F_2, m_{F_2} \rangle \\
& \times \begin{pmatrix} 1 & 1 & 2 \\ m_{F_1} - m'_{F_1} & m_{F_2} - m'_{F_2} & m_l - m'_l \end{pmatrix}
\end{aligned} \tag{4.3}$$

Here  $(\dots)$  is a 3-J symbol that describes the addition of two angular momenta,  $\Omega_i$  is  $F_i$ 's projection onto the molecular axis, and  $D_{M_0}^J$  is the Wigner D-function. The first term of this Hamiltonian induces an energy shift that differs for the  $m_l = 0$  and  $|m_l| = 1$  quantum numbers, giving rise to the well known doublet structures. The second and third terms couple different values of  $m_l$  while conserving the total angular momentum  $m_l + m_{F_1} + m_{F_2}$  (the bottom row of the 3-J symbol must sum to zero to yield a nonzero result). The second term in most mixtures do not contribute to the energy shift since the molecular states with different values of  $m_{F_1} + m_{F_2}$  have to be nearly degenerate to result in a significant energy shift. However, due to the low-field nature of the NaK  $p$ -wave resonances, multiple molecular states are nearly degenerate with the open channel spin state, allowing for the triplet structures to be resolved.

### 4.3.4 Understanding the NaK Feshbach resonances

To understand the observed Feshbach resonances, we collaborate with Tobias Tiecke at Harvard University. His assignment of  $s$ - and  $p$ -wave characters of the resonances follows from a simple, but powerful model of the molecular states involved. The singlet and triplet potentials of the interatomic potential allow for a variety of bound states. From the known scattering length [128] and the Van der Waals coefficient  $C_6$  [135], the weakest  $s$ -wave bound states are expected at about  $E_s^s = -150(10)$  MHz and  $E_t^s = -1625(50)$  MHz for the singlet and triplet  $s$ -wave potentials, where the errors reflect uncertainties of the scattering lengths from [128]. The  $p$ -wave bound states follow from the  $s$ -wave bound states as [133] and are slightly adjusted to fit the observed resonance positions. As described in [136, 38], as a first guess for locations of Feshbach resonances one can neglect the part of the hyperfine interaction that couples singlet and triplet bound states. This already provides the pattern of the positions of Feshbach resonances, where these (uncoupled) molecular states cross the atomic (open-channel) threshold. The analysis shows that the observed resonances are caused by the triplet bound states. Next, we use the asymptotic bound state model (ABM) to include the singlet-triplet coupling of molecular states [41]. To couple the molecular states to the open channel, we follow Marcelis *et al.* [131] and only include the effect of the virtual state causing the large and negative triplet scattering length. The spin part of the coupling matrix element is obtained from the ABM Hamiltonian and the spatial part, i.e., the wavefunction overlap between the respective bound state and the virtual state, is taken as one free fit parameter. For the background scattering length of the low-field resonances the effect of broad resonances is included. The virtual state causes strong coupling of several  $s$ -wave molecular states to the open channel, leading to wide, open-channel dominated resonances as known from the case of  ${}^6\text{Li}$ . The theoretical values obtained with this model are shown in Table 4.1. An exceptionally broad resonance for  $m_F = -3/2$  is predicted to be even wider and to

be shifted further, possibly hinting at a shift between the loss maximum and the actual Feshbach resonance position. Our approach leads to a refined triplet bound state energy of  $E_t^s = -1654(3)$  MHz and  $E_t^p = -1478(7)$  MHz, and using the long range potential from [128], we find a refined value of the triplet scattering length of  $a_t = -830(70) a_0$ . The errors correspond to one standard deviation of a least-squares fit to the eight narrowest  $s$ -wave resonances that are least sensitive to the coupling to the scattering states and hence the error induced by the ABM is expected to be small [41].

## 4.4 Conclusion

we have produced a degenerate Bose-Fermi mixture of  $^{23}\text{Na}$  and  $^{40}\text{K}$ , and identified over 30  $s$ - and  $p$ -wave interspecies Feshbach resonances, including several exceptionally broad resonances. Remarkably, many  $p$ -wave Feshbach resonances are observed to be triplets or even multiplets. Our strongly interacting  $^{23}\text{Na}$ - $^{40}\text{K}$  mixture near these Feshbach resonances should allow the study of Bose or Fermi polarons [9], of boson mediated interactions between fermions, and possibly of novel states of matter in optical lattices. The formation of fermionic Feshbach molecules will be discussed in next chapter. In the rovibrational ground state, NaK molecules possess a large induced electric dipole moment (2.7 Debye [137]) and are stable against exchange reactions. Especially, the dipole-dipole interaction is proportional the dipole moment squared. As a result, one can thus hope to create a Fermi gas of polar molecules with strong dipole-dipole interactions that dominate the many-body physics of the gas.

# Chapter 5

## Ultracold Fermionic Feshbach

## Molecules of $^{23}\text{Na}^{40}\text{K}$

*In this chapter, I will discuss the formation of ultracold weakly bound Feshbach molecules of  $^{23}\text{Na}^{40}\text{K}$ , the first fermionic molecule that is chemically stable in its absolute ground state. We observe more than 100 ms lifetime of the nearly degenerate molecular gas in the vicinity of the Feshbach resonance. The measured dependence of the molecular binding energy on the magnetic field demonstrates the open-channel character of the molecules over a wide field range and implies significant singlet admixture. This will enable efficient transfer into the singlet rovibrational ground state, resulting in a stable molecular Fermi gas with strong dipolar interactions.*

### 5.1 Introduction

Physical rules are often governed by interactions. Introducing a new interaction usually gives rise to new physical phenomena. So far, the contact interaction has been able to explain most ultracold atomic systems (e.g., the Gross - Pitaevskii equation [138, 139] for describing a interacting BEC and the BEC-BCS crossover theory for explaining a two-component Fermi gas in the vicinity of a Feshbach res-

onance [4, 140, 141, 142, 143, 32, 5, 144]). The contact interaction is isotropic and only short ranged. But it has already provided us with so many rich and interesting physical phenomena, such as the formation vortices inside a BEC [145, 146] and the superfluid to Mott insulator transition in an optical lattice [33, 147, 148, 149]. The physics is expected to be extremely rich once we introduce a long-range and anisotropic interaction - the dipolar interaction. Basically, we would like to create and study *a soup of quantum dipoles*. The tool to study the dipolar interaction is the ground state fermionic molecules. The molecules need to be fermionic because the Pauli exclusion principle can ensure that there is no contact interaction between identical fermions at low temperature and they also need to be in the absolute rovibrational ground state because any excited state molecules can easily decay and release energy, hence heating up the system. Most importantly, the induced electric dipole moments of these molecules can be tuned via an external electric field.

However, nature is not always generous. Most alkali fermionic molecules suffer from chemical instability in their absolute ground state. Table 5.1 shows the chemical stability and the permanent electric dipole moment of different alkali fermionic molecules in their singlet rovibrational ground state. Unfortunately, all combinations with Li are unstable and NaK and KCs are the only two stable fermionic molecules. In order to access novel phases of matter in dipolar Fermi gases [12, 150], *stable* fermionic ground state molecules with large electric dipole moment are essential. So far,  $^{40}\text{K}^{87}\text{Rb}$  is the only fermionic ground state molecule that has been produced at nearly degenerate temperatures [11]. However, the gas is unstable against the exchange reaction  $\text{KRb} + \text{KRb} \rightarrow \text{K}_2 + \text{Rb}_2$  in its absolute rovibrational ground state [151]. Here we report on the production of ultracold weakly bound fermionic molecules of  $^{23}\text{Na}^{40}\text{K}$  near a broad Feshbach resonance [152]. The NaK molecule is chemically stable in its absolute ground state [153]. In addition, it possesses a large induced electric dipole moment of 2.72 Debye in its singlet ground state [137, 154],

compared to 0.57 Debye for KRb [11]. Therefore, fermionic ground state molecules of NaK can form a Fermi sea with strong, long-range anisotropic dipolar interactions. The Feshbach molecules we create provide an ideal starting point for the formation of ground state molecules. They are nearly degenerate and long-lived, with a lifetime exceeding 100 ms. We demonstrate their largely open channel character in a wide magnetic field range. The open channel has significant admixture of the electronic spin singlet state, thus opening up a direct pathway towards the singlet rovibrational ground state using stimulated rapid adiabatic passage (STIRAP) via a singlet excited molecular state [11, 155].

fermionic bialkali molecules	chemical stability [153]	electric dipole moment (D)
LiNa	×	0.53(2) [156, 157]
LiK	×	3.51(4) [156, 157]
LiRb	×	4.05(8) [156, 157]
LiCs	×	5.36(12) [156, 157]
<b>NaK</b>	✓	<b>2.72(6)</b> [154, 137]
KRb	×	0.57(2) [11]
KCs	✓	1.90(2) [156]

Table 5.1: A list of the chemical stability and permanent electric dipole moments of fermionic molecules in the singlet rovibrational ground state.

## 5.2 Formation of fermionic NaK Feshbach molecules

To form Feshbach molecules, we prepare a Bose-Fermi mixture of  $^{23}\text{Na}$  and  $^{40}\text{K}$  with  $150 \times 10^3$  atoms each in a crossed ODT as described in Chapter 4<sup>1</sup>.  $^{23}\text{Na}$  is in its absolute hyperfine ground state  $|F, m_F\rangle = |1, 1\rangle$ , which forms a stable mixture with any hyperfine state of  $^{40}\text{K}$  in the  $F = 9/2$  lower hyperfine manifold. From the Feshbach spectroscopy study, one particular resonance stands out due to its exceptional width of 30 G at 138 G between  $^{23}\text{Na}$   $|1, 1\rangle$  and  $^{40}\text{K}$   $|9/2, -5/2\rangle$  atoms. Expecting

<sup>1</sup>The trap frequencies for  $^{40}\text{K}$  [ $^{23}\text{Na}$ ] are  $\nu_x = 108(5)$  Hz [85(5) Hz],  $\nu_y = 127(5)$  Hz [101(6) Hz] and  $\nu_z = 187(4)$  Hz [148(3) Hz]. The differential gravitational sag is only  $4 \mu\text{m}$ .

open-channel dominated molecules with potentially long lifetimes, we decide to use this resonance to form fermionic Feshbach molecules of  $^{23}\text{Na}^{40}\text{K}$ . In order to reach the desired states and minimize losses, we first cool the mixture close to the critical temperature of condensation of  $^{23}\text{Na}$  and then perform a spin transfer of  $^{40}\text{K}$  from  $|9/2, 9/2\rangle$  to  $|9/2, -1/2\rangle$  at 15 G in 50 ms. Then we ramp up the Feshbach field followed by another spin transfer from  $|9/2, -1/2\rangle$  to  $|9/2, -3/2\rangle$  in 1 ms. This special detour avoids going through other Feshbach resonances and therefore gives the best atom number of both species at the end of the experimental sequence. Fig. 5-1 shows the experimental sequence of the spin preparation process. In our experiment, since the Feshbach field and the magnetic trap are produced with the same coils, it takes about 200 ms for the mechanical relays to switch the coil configurations (from anti-Helmholtz to Helmholtz). Fortunately, this does not create a problem since the lifetime of the  $^{23}\text{Na}$   $|1, 1\rangle$  and  $^{40}\text{K}$   $|9/2, -1/2\rangle$  mixture is larger than 10 s in the ODT.

### 5.2.1 Magnetic field control

A stable and homogeneous magnetic field is required for the molecular association spectroscopy which will be discussed in the later sections. Our field stabilization scheme is described in Chapter 2. Here I elaborate more on how we check the magnetic field stability. We use two different methods for measuring the field stability with atoms as the sensors - Rabi oscillation and RF spectroscopy.

#### Rabi oscillation

Experimentally, we perform Rabi oscillation measurements between two Zeeman sub levels of  $^{40}\text{K}$ . Field fluctuations directly affect the detuning  $\Delta$  of the Rabi flopping which leads to a fluctuating Rabi frequency according to:

$$P_e(t) = \frac{\omega_R^2}{\Omega_R^2} \sin^2 \left( \frac{\Omega_R t}{2} \right) \quad (5.1)$$

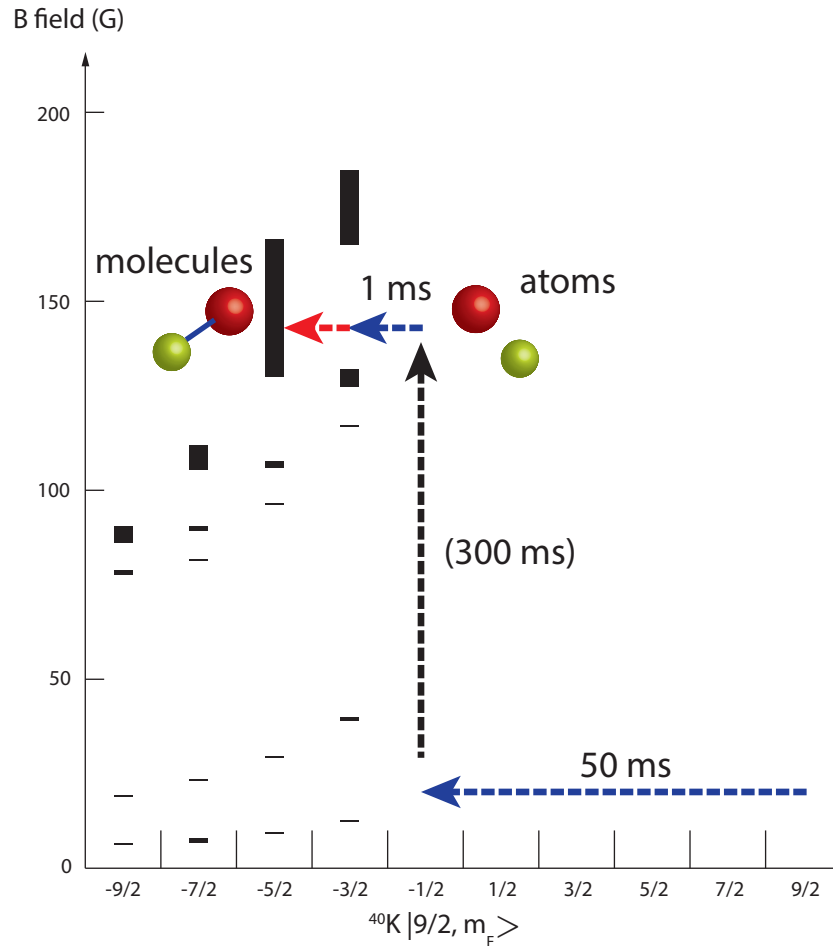


Figure 5-1: Experimental sequence for preparing  $^{40}\text{K}$  atoms in the  $|9/2, -3/2\rangle$  state at high field. First at a low field of about 15 G, a 50 ms Landau-Zener sweep transfers the atoms from  $|9/2, +9/2\rangle$  to  $|9/2, -1/2\rangle$ . Then it takes about 200 ms for the mechanical relays to switch the coil configurations. After the relays have been switched, the field can be ramped up in a few ms but it takes another 100 ms for the PID feedback circuit to completely activate which is mostly limited by a mechanical PID switch (the bandwidth of our feedback system is about 1 kHz). Finally, another 1 ms Landau - Zener sweep brings atoms down to  $|9/2, -3/2\rangle$ , which is the starting state for making molecules. The molecular association RF pulse is indicated by the red arrow. The black bars indicate the experimentally found Feshbach resonances (the width of the black bars refers to the measured width of each resonance).

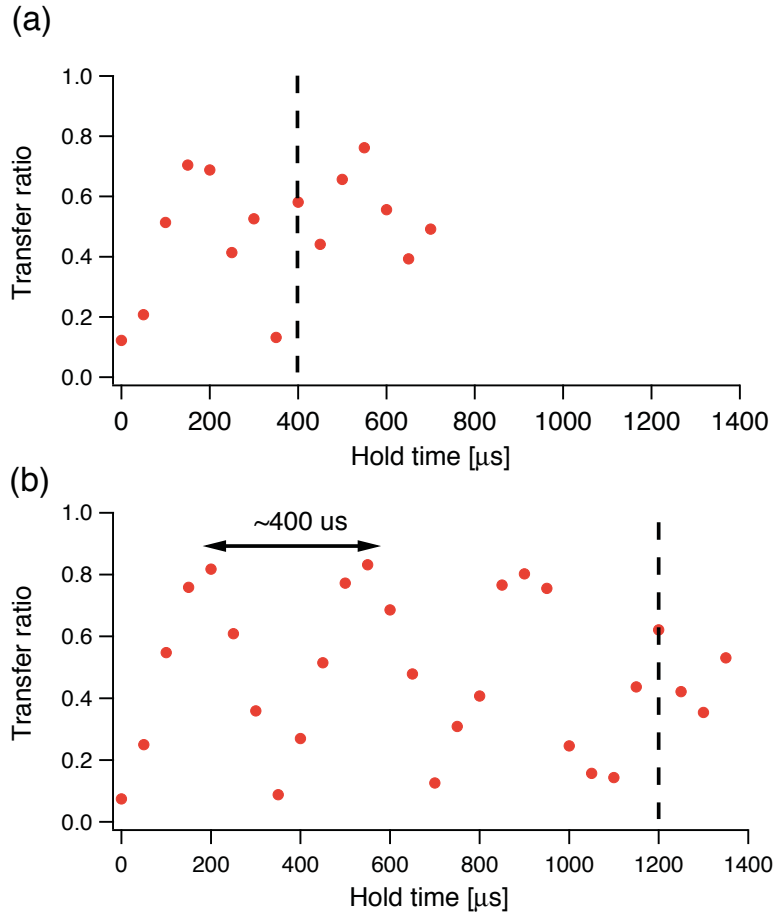


Figure 5-2: Rabi oscillation measurements in two different field stability regimes (a) shows a decoherence time of  $\sim 400 \mu\text{s}$  which corresponds to a field stability of 17 mG. (b) shows a decoherence time of  $\sim 1.2 \text{ms}$  which corresponds to a field stability of  $\pm 5 \text{mG}$ . The improvement on the field stability is achieved by carefully tweaking the PID parameters of the feedback circuit. The dashed lines indicate the decoherence times. Note that the RF power is identical for both regimes. Therefore, the observed Rabi frequency is identical.

Where  $P_e(t)$  is the time-dependent excited state population,  $\omega_R$  is the Rabi frequency and  $\Omega_R = \sqrt{\omega_R^2 + \Delta^2}$  is the generalized Rabi frequency.  $\Delta$  is the detuning which depends on the bias magnetic field and RF photon frequency ( $\Delta \equiv \omega_{res}(B) - \omega_{RF}$ , with  $\omega_{res}(B)$  being the resonant frequency and  $\omega_{RF}$  being the RF photon frequency). We can decompose  $\Delta$  into a fixed detuning  $\Delta_0$  and a random variable  $\Delta_N$  associated with the field fluctuation. Thus, we can rewrite the Rabi oscillation formula as:

$$P_e(t) = \frac{\omega_R^2}{\Omega_R^2} \sin^2 \left( \frac{\sqrt{\omega_R^2 + \Delta_0^2 + 2\Delta_0\Delta_N + \Delta_N^2}t}{2} \right) \xrightarrow{\Delta_0=0} \frac{\omega_R^2}{\Omega_R^2} \sin^2 \left( \frac{\omega_R t}{2} + \frac{\Delta_N^2 t}{4\omega_R} \right) \quad (5.2)$$

Here we have already assumed  $\Delta_0 = 0$  without loss of generality and  $\omega_R \gg \Delta_N$ . When  $\frac{\Delta_N^2 t}{4\omega_R} \sim \pi$  atoms start decohering. Hence, from the decoherence rate, we are able to extract the field fluctuation when the Rabi frequency is known. Fig. 5-2 shows a comparison of Rabi oscillation measurement in two different field stability regimes. In Fig. 5-2(a), we estimate the decoherence time to be  $\sim 400 \mu\text{s}$  and the Rabi frequency  $\omega_R$  to be  $\sim 2.5 \text{ kHz}$ . As a result, we have  $\Delta_N/2\pi \sim 3.5 \text{ kHz}$ . The measurement is performed at 130 G between  $^{40}\text{K}$   $|9/2, -3/2\rangle$  and  $|9/2, -5/2\rangle$  states, a 3.5 kHz detuning fluctuation can be directly translated into a magnetic field fluctuation of  $\sim 17 \text{ mG}$ . From the data in Fig. 5-2(b), we estimate a decoherence time of  $\sim 1.2 \text{ ms}$ , corresponding to  $\Delta_N/2\pi \sim 2.0 \text{ kHz}$  and a field fluctuation of  $\sim \pm 5 \text{ mG}$ . Rabi oscillation is a sensitive tool to measure field fluctuations since the decoherence time increases quadratically with the field fluctuation.

## RF spectroscopy

From the width of a RF spectrum, we can also read out the field stability because field fluctuations can affect the spectral width as long as the Fourier width is not the dominant factor. Fig. 5-3(a) shows a typical RF spectrum taken between  $^{40}\text{K}$

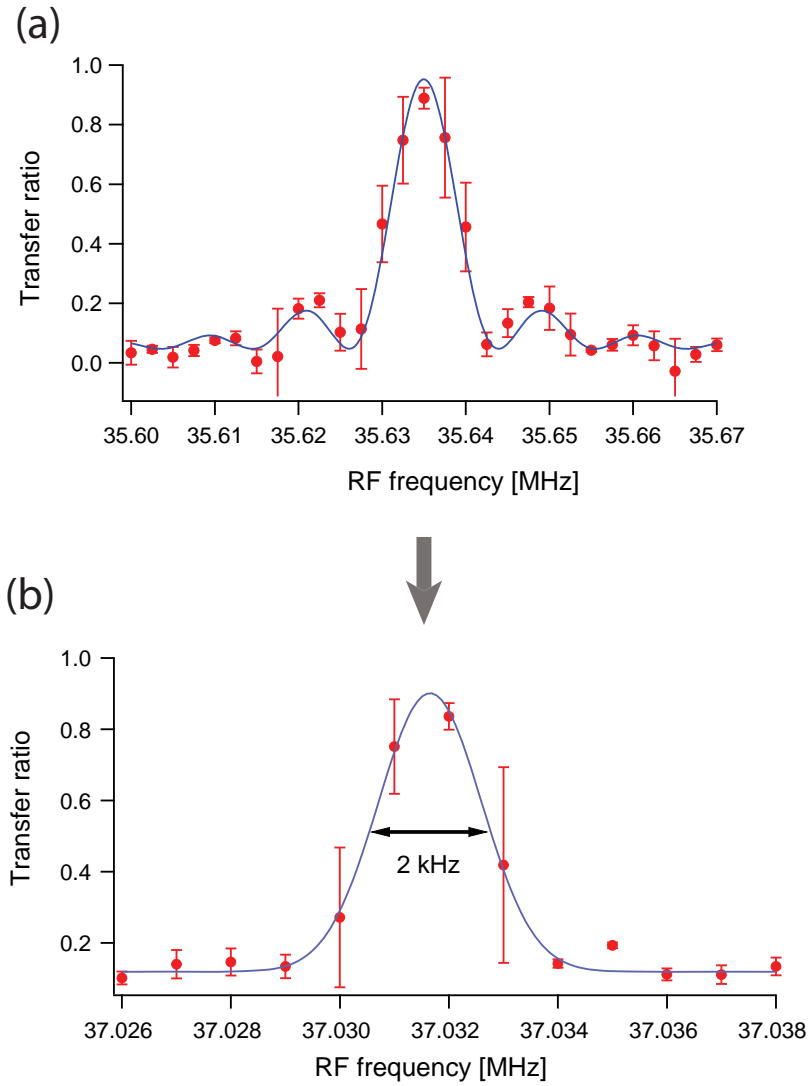


Figure 5-3: RF spectra taken between the  $^{40}\text{K}$   $|9/2, -3/2\rangle$  and  $|9/2, -5/2\rangle$  states at 130 G. For the spectrum (a) a  $100\ \mu\text{s}$  square pulse is used, showing the characteristic sinc-shaped envelope and the spectral width is dominated by the Fourier width. The spectrum (b) is obtained by using a 1.2 ms Blackman pulse [158] Here, the sinc lobes are absent and the spectral width reflects the field stability which is measured to be  $\pm 5\ \text{mG}$ .

$|9/2, -3/2\rangle$  and  $|9/2, -5/2\rangle$  states. The spectrum is taken with a  $100\ \mu\text{s}$  square pulse and its width is dominated by the Fourier width. In order to get rid of the sinc lobes, we implement the Blackman pulse [158]. Fig. 5-3(b) shows a RF spectrum taken with a 1.2 ms Blackman pulse. The width of this spectrum ( $\sim 2\ \text{kHz}$ ) is now completely dominated by the field stability at this field (130 G) which is about 10 mG.

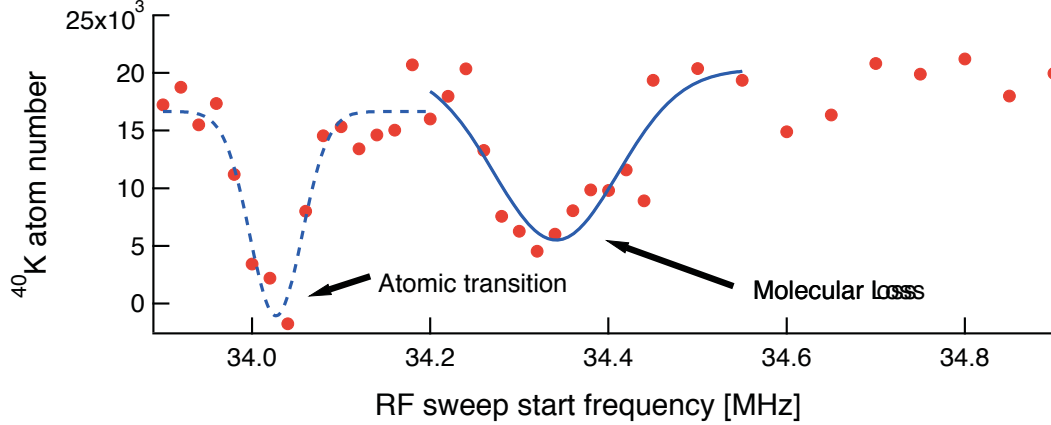


Figure 5-4: The first signal of NaK molecules. The system is initially prepared in the  $^{23}\text{Na}$   $|1, 1\rangle$  and  $^{40}\text{K}$   $|9/2, -3/2\rangle$  states. A high power RF sweep (200 ms, 20 kHz) is used to search molecules. Imaging is taken on the  $^{40}\text{K}$   $|9/2, -3/2\rangle$  state. The left dip corresponds to bare atomic transition (to  $^{40}\text{K}$   $|9/2, -5/2\rangle$  state) and right dip is molecular signal.

## 5.2.2 The first molecular signal

Our ultracold  $^{23}\text{Na}$  -  $^{40}\text{K}$  mixture is new system and therefore contains a lot of "unknowns". One of the greatest unknowns, which can affect the production of molecules, is the lifetime of NaK molecules. At least the KRb system gives us a hint on the molecular lifetime about 1 ms, without removing excess atoms. So we might guess the lifetime of NaK molecules to be on the order of  $100\ \mu\text{s}$  to 10 ms. If nature was not on our side, we would have had a hard time to directly observe the NaK molecule. To be on the safe side, we first perform a loss spectroscopy using high power RF sweeps measuring the remaining  $^{40}\text{K}$  atom number in the  $|9/2, -3/2\rangle$  state. This

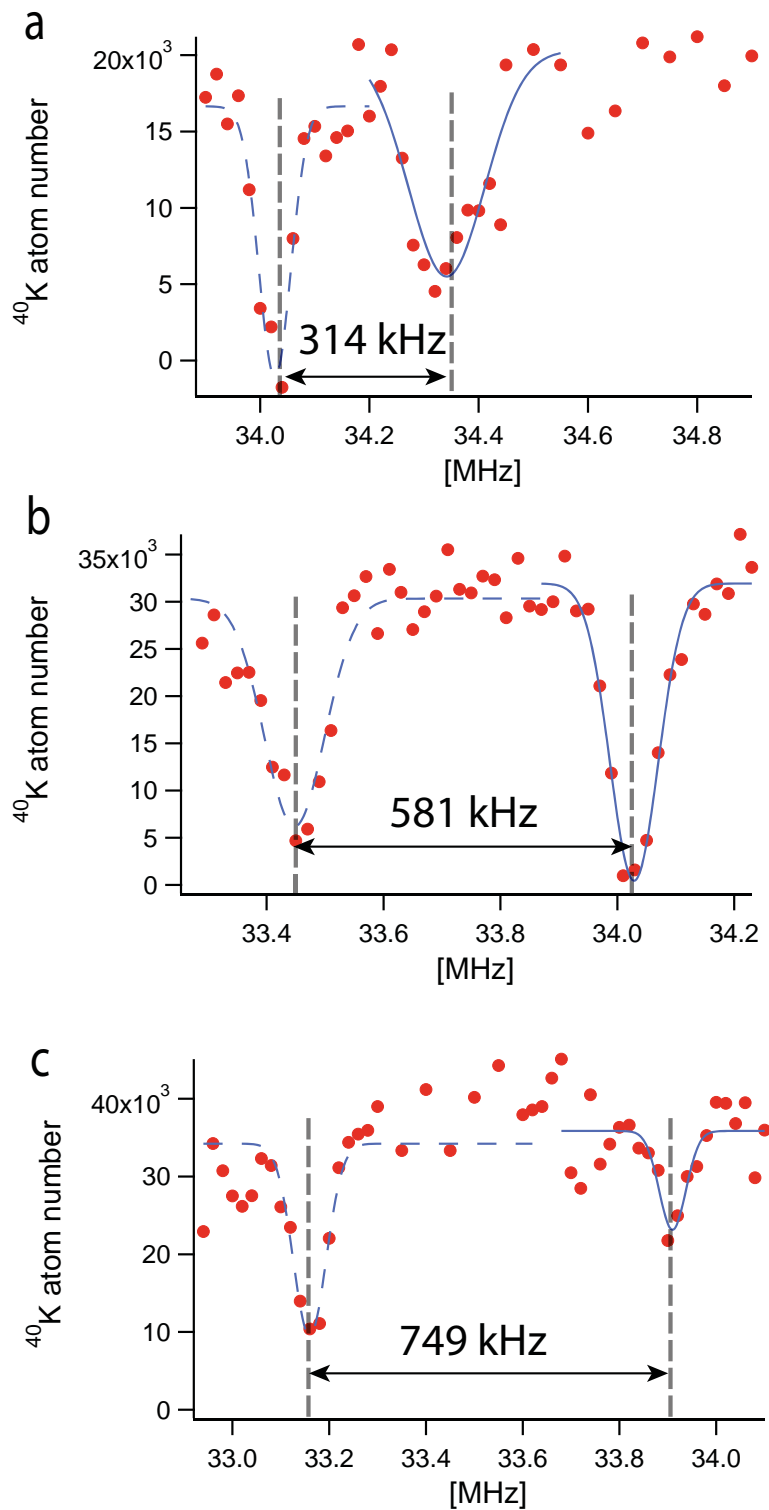


Figure 5-5: Molecular loss spectroscopy as a function of the magnetic fields. (a) 125.5 G. (b) 123.0 G. (c) 121.7 G. The distance between the atomic transition and molecular loss feature changing with respect to the magnetic fields is the smoking gun of the molecular signal.

method does not depend on the molecular lifetime since we do not intend to observe the molecules but rather the missing atoms. As the RF frequency coincides with the molecular binding energy, molecules should form and appear as losses on the atom number in the initial state. Fig. 5-4 shows the first molecular signal observed in our system. The experiment is performed at 125 G. We monitor the atom number of  $^{40}\text{K}$  in the  $|9/2, -3/2\rangle$  state and sweep the RF frequency across 20 kHz in 200 ms. The left dip at 34.02 MHz corresponds to the bare atomic transition where atoms in the  $|9/2, -3/2\rangle$  state has been transferred to the  $|9/2, -5/2\rangle$  state and then become invisible in our imaging system. The right dip at 34.35 MHz is the molecular signal where the strong loss is due to continuous formation of molecules.

To prove what we observe is really the molecular signal, we jump to different bias magnetic fields and perform the same measurement. The frequency difference between the atomic transition and the molecular loss feature should vary as a function of the magnetic field due to the change of the molecular binding energy. Indeed, Fig. 5-5 shows the molecular loss spectra in different bias magnetic fields providing a clear evidence of the molecular signal!

### 5.2.3 Radio frequency association of NaK molecules

After confirming that the loss feature is indeed the molecular signal, the natural next step is to form and image NaK molecules. There are several established methods to associate Feshbach molecules [5]. For wide Feshbach resonances, where the molecular wavefunction can have a large extent and offer good overlap with two unbound atoms, a particularly clean way to form molecules is via RF association [129, 159, 160, 161].

Here again, we prepare  $^{23}\text{Na}$  and  $^{40}\text{K}$  atoms in the non-resonantly interacting hyperfine states  $|1, 1\rangle$  and  $|9/2, -3/2\rangle$ , respectively. For optimized phase space overlap between the two species [160], we choose a temperature  $T$  of the mixture that is close to the critical temperature  $T_C$  for Bose-Einstein condensation of  $^{23}\text{Na}$ , corresponding

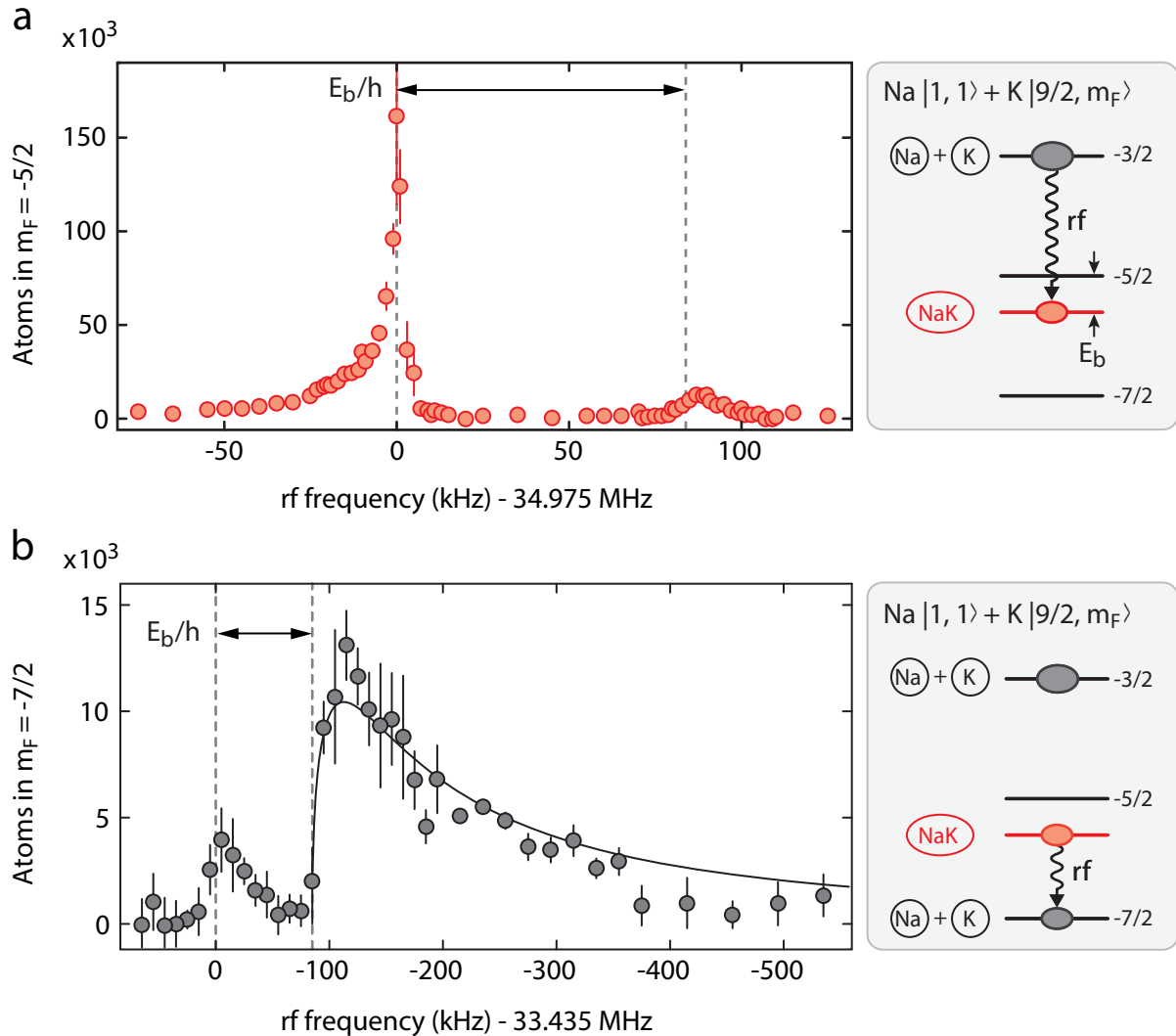


Figure 5-6: (a) Association of fermionic Feshbach molecules. Starting with a mixture of  $|1, 1\rangle_{\text{Na}}$  and  $|9/2, -3/2\rangle_{\text{K}}$  atoms, RF spectroscopy near the  $|9/2, -3/2\rangle_{\text{K}}$  to  $|9/2, -5/2\rangle_{\text{K}}$  hyperfine transition reveals free  $^{40}\text{K}$  atoms repulsively interacting with the  $^{23}\text{Na}$  bath (near zero rf offset), as well as associated molecules (near 85 kHz rf offset). The magnetic field corresponding to the atomic transition at 34.975 MHz is 129.4 G. (b) Dissociation of Feshbach molecules. Driving the  $|9/2, -5/2\rangle_{\text{K}}$  to  $|9/2, -7/2\rangle_{\text{K}}$  transition yields the molecular dissociation spectrum, showing a sharp onset at an RF frequency shifted by  $E_b/h$  from the atomic transition. The solid line shows the fit of a model  $\propto \theta(\nu - \nu_b)\sqrt{\nu - \nu_b}/\nu^2$  [5], yielding  $\nu_b = E_b/h = 85(8)$  kHz.

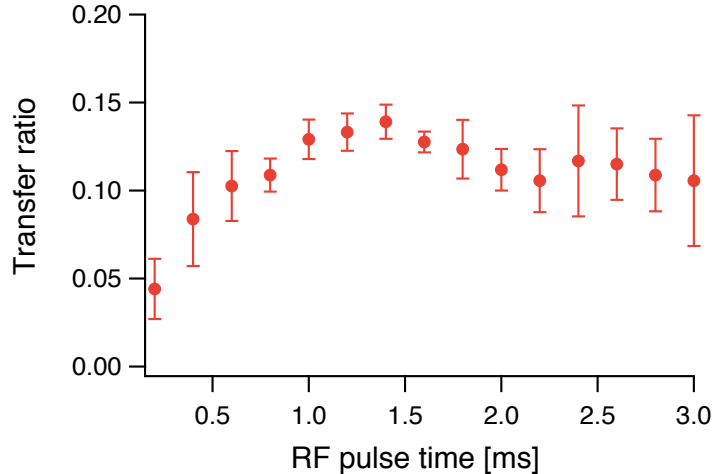


Figure 5-7: Molecular conversion efficiency as a function of the RF pulse time without removing excess atoms. The almost constant conversion efficiency after 1.5 ms may be due to the competition between continuous molecule production and decay.

to  $T/T_F \approx 0.4$  for  $^{40}\text{K}$ . Via a RF pulse<sup>2</sup> near the  $^{40}\text{K}$   $|9/2, -3/2\rangle$  to  $|9/2, -5/2\rangle$  hyperfine transition, we then transfer the unbound  $^{40}\text{K}$  atoms into the molecular bound state with  $^{23}\text{Na}$ . In order to image the created molecules (the bound  $^{40}\text{K}$  in the molecules), special attention needs to be paid when imaging molecules inside the atomic bath. At 129.5 G, atoms in the  $|9/2, -3/2\rangle$  state still off-resonantly scatter which makes it difficult to unambiguously image bound  $^{40}\text{K}$  in the  $|9/2, -5/2\rangle$  state. Therefore we perform another RF sweep during the first 1 ms time of flight to transfer atoms from  $|9/2, -3/2\rangle$  to  $|9/2, -1/2\rangle$  state. By doing so, we are able to detect only the molecular signal without seeing residual atoms. Experimentally, we image both atoms and molecules on the same CCD camera - using the kinetic mode. After the first  $40\ \mu\text{s}$  of exposure for imaging bound  $^{40}\text{K}$  atoms in the  $|9/2, -5/2\rangle$  state, the exposed image is shifted to the masked part of the CCD chip in 1 ms, which is blocked by a razor blade to prevent being exposed to the imaging light. Then another  $40\ \mu\text{s}$  of exposure is used to image  $^{40}\text{K}$  atoms in the  $|9/2, -1/2\rangle$  state. As

<sup>2</sup>A 1.2 ms long Blackman pulse [158] is used, allowing for Fourier-limited spectroscopy given the magnetic field stability of  $\pm 3\ \text{mG}$  that translates into about  $3\ \text{kHz}$   $\sigma$ -width of transitions.

a result, we can image molecules and atoms in only 1 ms time difference. A typical RF association spectrum at a magnetic field on the molecular side of the Feshbach resonance is shown in Fig. 5-6(a). Two features are observed: an atomic peak near the unperturbed hyperfine transition, and a molecular peak arising from  $^{40}\text{K}$  atoms that have been RF associated into NaK molecules. The distance between the atomic peak and the onset of the molecular feature yields the binding energy  $E_b$ . Note that direct absorption imaging of weakly bound Feshbach molecules is possible using light resonant with the atomic transition [27, 129, 159, 160, 161]. We typically detect up to  $20 \times 10^3$  molecules, corresponding to a conversion efficiency of  $^{40}\text{K}$  atoms into molecules of about 15%. The molecular conversion efficiency as a function of RF pulse time can be found in Fig. 5-7. It peaks around 1.5 ms and then stays constant possibly due to the competition between continuous molecule production and decay. The atomic feature at the hyperfine transition from  $|9/2, -3/2\rangle$  to  $|9/2, -5/2\rangle$  shows a strong mean-field shift towards lower frequencies, which is a direct signature of the repulsive interactions between  $^{23}\text{Na}$   $|1, 1\rangle$  and  $^{40}\text{K}$   $|9/2, -5/2\rangle$  atoms on the repulsive branch of the Feshbach resonance. The free-free spectrum is directly proportional to the number of fermions that experience a given density of bosons. The exceptionally long tail towards lower frequencies is caused by a small fraction of condensed bosons (about 10%) present in the mixture.

For accurate extraction of the molecular binding energy  $E_b$ , the functional form of the molecular association spectrum is required. The lineshape can be modeled via Fermi's Golden rule as

$$\Gamma_{\text{mol}}(\omega) \propto \mathcal{F}(E_b - \hbar\omega) \times p(E_b - \hbar\omega) \quad (5.3)$$

Where the molecular binding energy  $E_b$  is provided by both the RF photon energy  $\hbar\omega$  and the original relative kinetic energy of the unbound Na-K atom pair  $E_k$ , i.e.

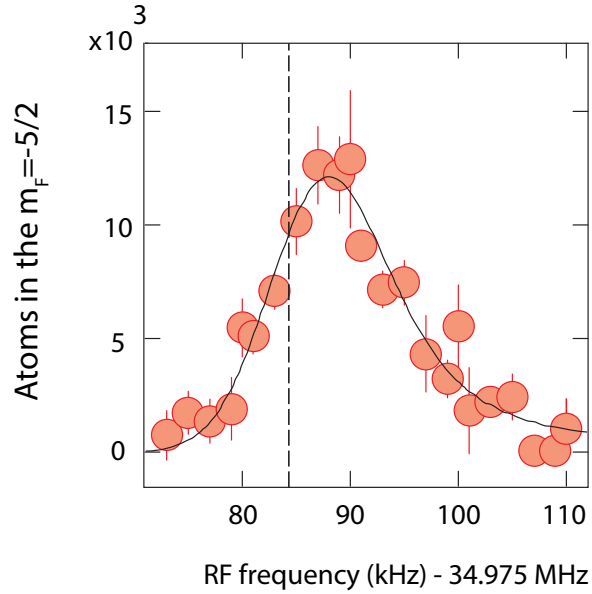


Figure 5-8: A fit to the molecular association spectrum. The fitting function is from the equation (5.9) convoluted with the experimental resolution. From the fit we are able to extract the binding energy of molecules to be  $E_b = h \times 84(6)$  kHz (indicated by dashed line) which is in good agreement with the association threshold.

$\hbar\omega + E_k = E_b$ .  $\mathcal{F}(E_b - \hbar\omega)$  is the Franck-Condon factor between the wavefunctions of an unbound Na-K atom pair and a bound Feshbach molecule, and  $p(E_b - \hbar\omega)$  is the probability density to find a pair of potassium and sodium atoms with relative kinetic energy  $E_k = E_b - \hbar\omega$ . The Franck-Condon factor can be calculated based on the asymptotic behavior of the bound ( $\phi_b$ ) and scattering ( $\Psi_s$ ) wave functions (here we have used the low energy limit,  $E_k \rightarrow 0$ ),

$$\phi_b = \sqrt{\frac{2}{a}} e^{-r/a} \quad (5.4)$$

$$\Psi_s = \sqrt{\frac{2\mu}{\pi\hbar^2 k}} \sin(kr + \arctan(-ka_{bg})) \quad (5.5)$$

thus,

$$\mathcal{F}(k, a, a_{bg}) = \left| \int_0^\infty \Psi_s^*(r) \phi_b(r) dr \right|^2 = \frac{4a(a - a_{bg})^2 k \mu}{\pi \hbar^2 (1 + a^2 k^2) (1 + a_{bg}^2 k^2)} \quad (5.6)$$

where  $k$  is the wave number associated with the relative kinetic energy  $E_k$  ( $E_k = \hbar^2 k^2 / 2\mu$ , here  $\mu = \frac{m_{\text{Na}} m_{\text{K}}}{m_{\text{Na}} + m_{\text{K}}}$ ).  $a$  and  $a_{bg}$  are the scattering length and the background scattering length, respectively. We evaluate the probability density assuming thermal gas distributions for both species:

$$p(E_k) = \int d^3 p_{Na} \int d^3 p_K f_{Na}(\mathbf{p}_{Na}, T) f_K(\mathbf{p}_K, T) \delta(E_k - (E_b - \hbar\omega)) \quad (5.7)$$

where  $p_{Na}$  and  $p_K$  are the momenta of sodium and potassium atoms, respectively and the function  $f_X(\mathbf{p}_X, T) = e^{-\frac{p_X^2}{2M_X k_B T}}$  is the probability density function for a thermal gas. The integral can be calculated by restricting  $p_{Na} - \hbar k < p_K < p_{Na} + \hbar k$ . After some algebra, we have

$$p(E_k = \frac{\hbar^2 k^2}{2\mu}) = \frac{\mu k}{\pi \hbar^2} \left( \frac{2\pi \hbar^2}{(m_{Na} + m_K) k_B T} \right)^{3/2} e^{-\frac{\hbar^2 k^2}{2(m_{Na} + m_K) k_B T}} \quad (5.8)$$

which can be summarized as  $p(k) = \rho(k) \lambda_M^3 e^{-\frac{\hbar^2 k^2}{2M k_B T}}$ , where  $\rho(k)$  is the density of states with relative kinetic energy  $E_k$ ,  $\lambda_M = \sqrt{\frac{2\pi \hbar^2}{M k_B T}}$  is the thermal de Broglie wavelength for an atom pair, and  $M = m_{\text{Na}} + m_{\text{K}}$ . So the resulting transition rate can be written as

$$\Gamma_{\text{mol}}(\omega) \propto \frac{4a(a - a_{bg})^2 k \mu}{\pi \hbar^2 (1 + a^2 k^2) (1 + a_{bg}^2 k^2)} \times \rho(k) \lambda_M^3 e^{-\frac{\hbar^2 k^2}{2M k_B T}} \quad (5.9)$$

with  $k = \sqrt{\frac{2\mu}{\hbar^2}(\hbar\omega + E_b)}$ . Fig. 5-8 shows a fit of this lineshape, convoluted with the experimental resolution, to the molecular feature, giving a binding energy of  $E_b = h \times 84(6)$  kHz at a magnetic field of  $B = 129.4$  G. The uncertainty 6 kHz reflects the initial distribution of the relative momenta between bosons and fermions and, indeed, is found to be compatible with the temperature of the sodium and potassium

clouds. A complementary demonstration of molecule formation is the observation of a dissociation spectrum [162], as shown in Fig. 5-6(b). To dissociate molecules, we drive the  $^{40}\text{K}$   $|9/2, -5/2\rangle$  to  $|9/2, -7/2\rangle$  transition after RF association of molecules. The onset of transfer is observed at  $E_b/h = 85(8)$  kHz, in good agreement with the association threshold in Fig. 5-6(a). We make use of molecule dissociation in the lifetime measurements discussed below to ensure the exclusive detection of molecules. In particular, without the dissociation scheme, the measurement will not be sensitive to the decay of molecules because one can not distinguish between the “broken” molecules and the bound molecules.

### 5.3 The singlet admixture of molecules

In view of the ultimate goal to create molecules in the singlet rovibrational ground state, it is interesting to know how much singlet admixture the Feshbach molecules have. This information is contained in the binding energy dependence of magnetic field. Therefore, we have studied the molecular binding energies as a function of magnetic field as shown Fig. 5-9(a). The approximately quadratic dependence of the binding energy on magnetic field reflects the open-channel character of the molecular state over a wide field range, where the binding energy follows the law  $E_b \approx \frac{\hbar^2}{2\mu(a-\bar{a})^2}$ , with  $\bar{a} = 51a_0$  the mean scattering length for NaK and  $a(B) \approx a_{\text{bg}} \left(1 + \frac{\Delta B}{B-B_0}\right)$  the dependence of the scattering length on magnetic field near the resonance [3]. The large and negative background scattering length  $a_{\text{bg}} = -690_{-130}^{+90} a_0$  [152]<sup>3</sup> indicating that the closed channel molecular state is predominantly coupled to a virtual state [131, 163] of energy  $E_{\text{vs}} = \frac{\hbar^2}{2\mu(a_{\text{bg}}-\bar{a})} = k_B \times 11(3) \mu\text{K}$ . In this case, the binding energy  $E_b$  is

---

<sup>3</sup>From the potential in [128], modified to yield the triplet binding energy found in [152], we obtain a triplet scattering length  $a_t = -805_{-150}^{+100} a_0$ , where the error bar reflects not only the uncertainty in the triplet binding energy, as in [152], but also the uncertainty in the  $C_6$  coefficient [128].

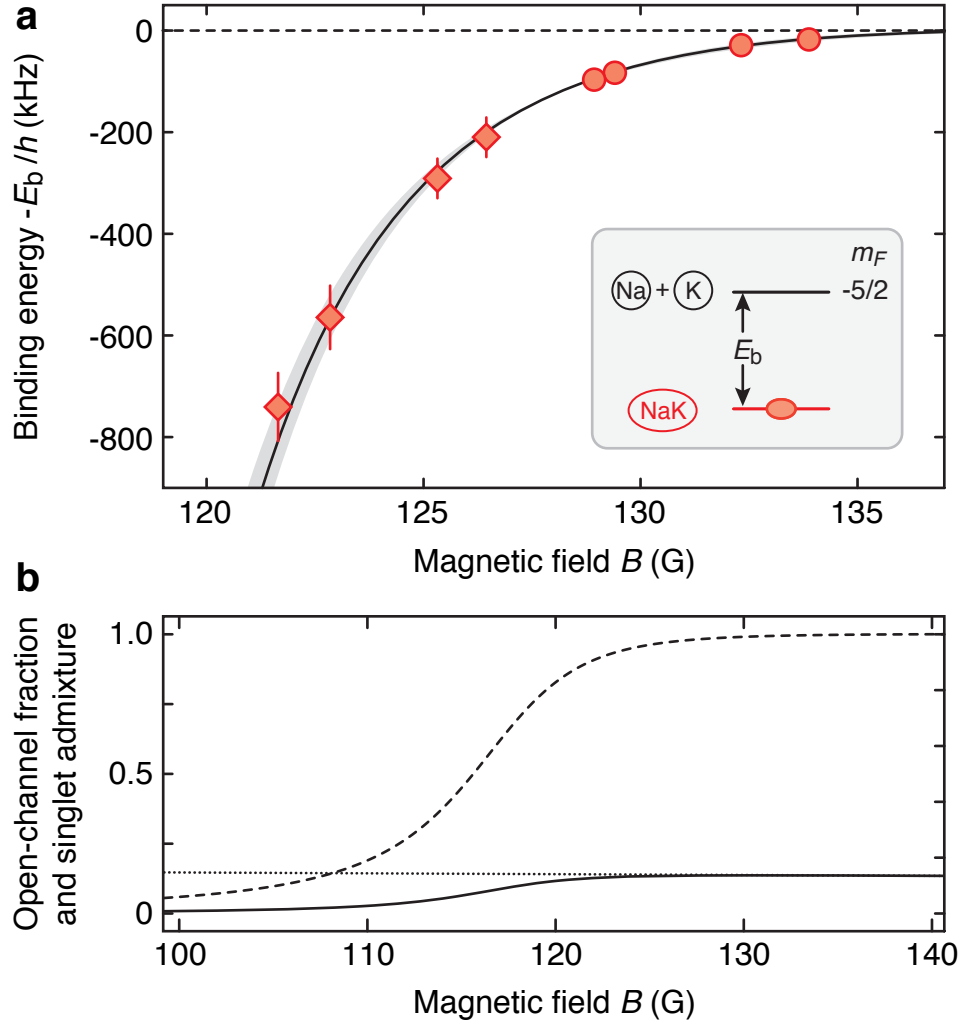


Figure 5-9: (a) Binding energy of NaK Feshbach molecules at the wide Feshbach resonance between  $|1, 1\rangle_{\text{Na}}$  and  $|9/2, -5/2\rangle_{\text{K}}$ . Binding energies smaller than 200 kHz (circles) are obtained by direct detection of molecules (see Fig. 5-6), while larger binding energies (diamonds) with weaker free-bound coupling are measured by detecting simultaneous atom loss in  $|1, 1\rangle_{\text{Na}}$  and  $|9/2, -3/2\rangle_{\text{K}}$  (see Fig. 5-5). The solid line is a one-parameter fit to the model described in the text, and the shaded region displays the uncertainty. (b) Open-channel fraction (dashed line) and singlet admixture of the molecular state (solid line), derived from the binding energy curve in (a), and singlet admixture of unbound pairs (dotted line).

given by solving

$$E_b + E_c(B) - \frac{\frac{1}{2}A_{vs}}{E_{vs} \left(1 + \sqrt{\frac{E_b}{E_{vs}}}\right)} = 0. \quad (5.10)$$

where  $E_c(B)$  is the magnetic field dependent energy of the closed channel molecule relative to the scattering threshold, known from the asymptotic bound state model [152], and  $A_{vs}$  is the squared magnitude of the coupling matrix element between the closed channel molecular state and the virtual state [131, 163]. With  $A_{vs}$  as the only fit parameter, we obtain excellent agreement with the data, finding  $A_{vs} = (h \times 5.2(6) \text{ MHz})^2$ . The uncertainty in the background scattering length translates into the shaded uncertainty region in Fig. 5-9(a). The Feshbach resonance position is found to be  $B_0 = 139.7_{-1.4}^{+2.1} \text{ G}$ , its width (distance from resonance to the zero-crossing of the scattering length) is  $\Delta B = 29(2) \text{ G}$ .

From the change of the binding energy with magnetic field we can directly deduce the closed-channel fraction  $Z = \frac{\partial E_b}{\partial E_c} \approx \frac{1}{\Delta\mu} \frac{\partial E_b}{\partial B}$  [3], where  $\Delta\mu = 2.4\mu_B$  is the difference between the magnetic moments of the closed channel molecular state and the two free atoms near resonance. In Fig. 5-9(b), we show the open-channel fraction  $1 - Z$  along with the singlet admixture of the molecular state. Although the closed channel molecular state is a bound state in the  $a(1)^3\Sigma^+$  triplet potential, the strong coupling to the entrance channel, which is 14% singlet, gives the Feshbach molecules a mixed singlet-triplet character. This will allow for direct two-photon coupling to the  $v = 0$ ,  $X(1)^1\Sigma^+$  singlet rovibrational ground state via the singlet excited  $B(1)^1\Pi$  state.

## 5.4 The kinetic energy of molecules

The temperature of the molecules is an interesting parameter since the temperature of the Feshbach molecules will directly reflect on the temperature of the ground state molecules [11]. To obtain an estimate for the temperature of the molecules we study their time-of-flight expansion right after association at  $E_b = h \times 84 \text{ kHz}$ . The

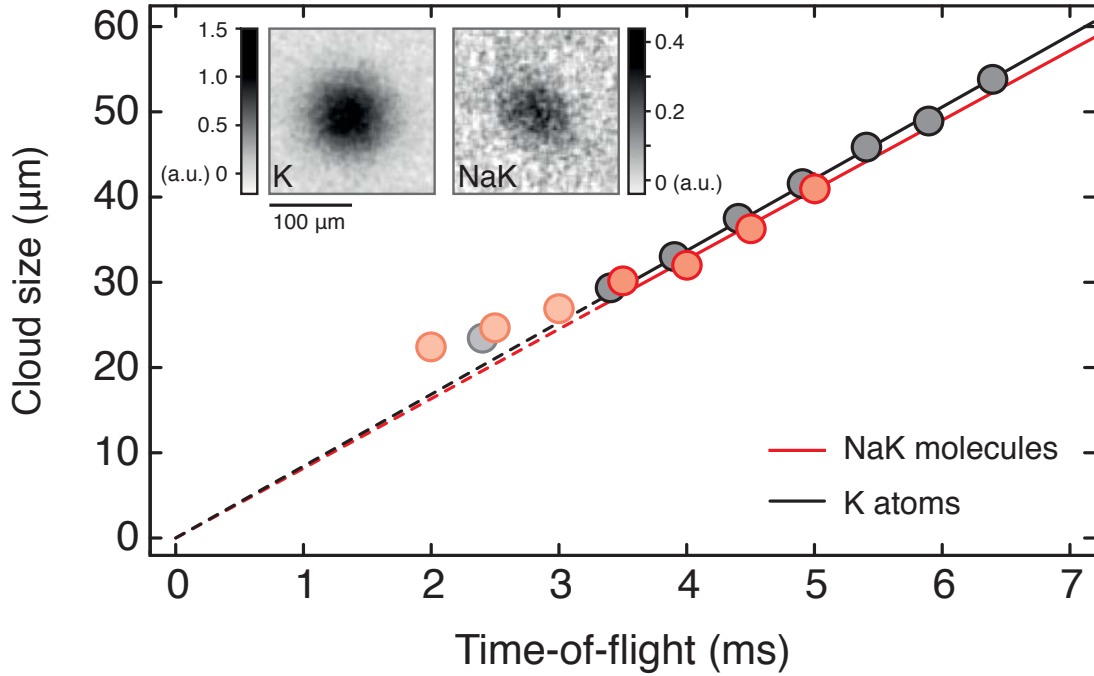


Figure 5-10: Time-of-flight expansion of leftover  $^{40}\text{K}$  atoms and associated molecules at 129.4 G (binding energy  $h \times 84$  kHz) right after RF association. Assuming a classical gas model, the width of the cloud corresponds to an average kinetic energy of 340 nK for the  $^{40}\text{K}$  cloud and 500 nK for the molecular cloud. Free atoms are transferred and detected in the  $m_F = -1/2$  state, while potassium atoms bound in NaK molecules are imaged in the  $m_F = -5/2$  state. The insets show an average of 20 absorption images for K atoms (NaK molecules) after 4.5 ms (4.0 ms) time-of-flight.

association is performed by a 1.2 ms RF pulse. We measure an effective temperature (average kinetic energy) of 500 nK (see Fig. 5-10) for the molecules by fitting the cloud size with a classical model [17]. We note that the molecular cloud might not be in thermal equilibrium since there is no sufficient time for the molecules to rethermalize after association. From their number and trapping frequencies, this corresponds to a degeneracy factor of  $T/T_{F,\text{mol}} \approx 1.7$ . The molecular gas is more energetic than the sodium and potassium bath, which has a temperature of 220 nK. This partially reflects the broader momentum distribution of the  $^{40}\text{K}$  Fermi gas at  $T/T_F \approx 0.4$  due to Pauli pressure. Indeed, the momentum distribution of molecules after RF association is a convolution of the momentum distributions of the bosonic and fermionic clouds. At zero temperature, with bosons condensed and fermions fully occupying the Fermi sea, molecules would inherit the broad momentum distribution of the atomic Fermi gas. We also observe heating of the molecular cloud in the presence of sodium, likely due to three-body losses, that can occur already during the association pulse.

## 5.5 The lifetime of molecules

To study the lifetime of molecules, we first associate molecules with a 1.2 ms RF pulse and then hold the molecules for a certain wait time. At the end of the wait time, another RF pulse is applied to dissociate molecules to the  $|9/2, -7/2\rangle$  state. This ensures that the molecular signal we detect at the end of the sequence is indeed coming from remaining molecules in the trap and *not* from atoms that originate from the decay of molecules during the wait time. Fig. 5-11 shows the lifetime of molecules close to the Feshbach resonance at a binding energy of  $h \times 32$  kHz. With the bosonic species still present, the lifetime is about 8 ms. Considering that the bosons can resonantly scatter with the fermions bound in the NaK molecules, this is already an impressive lifetime. However, the bosons can be selectively removed from the ODT as

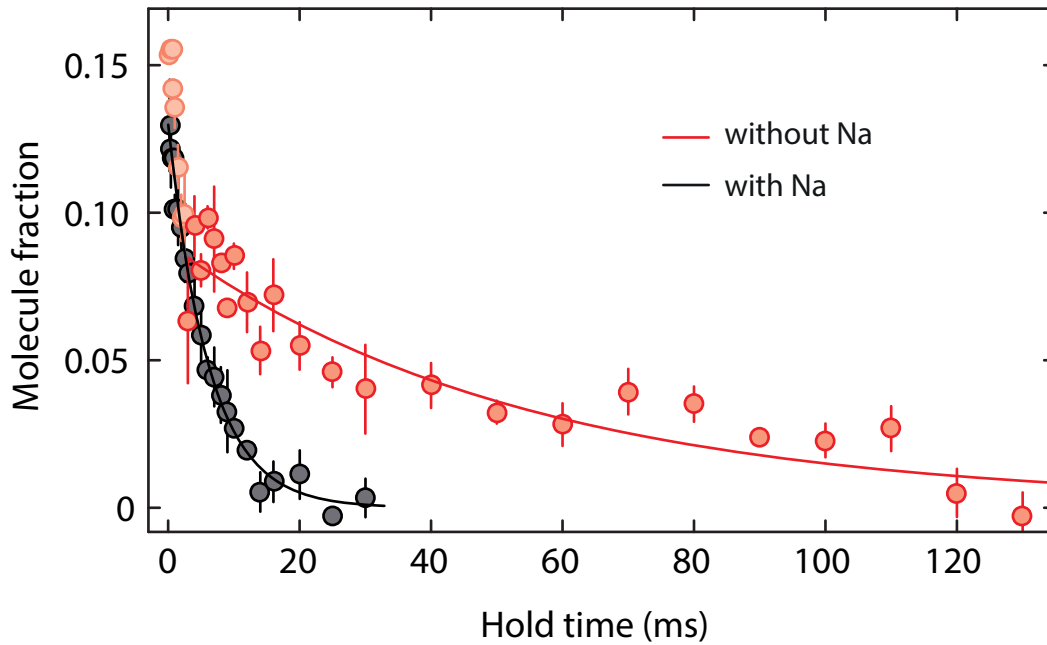


Figure 5-11: (color online). Lifetime of fermionic Feshbach molecules. The measurement is performed at a magnetic field of 132.2 G, corresponding to a binding energy of 32 kHz. The red (black) data points show the number of molecules as a function of hold time with (without) removing sodium from the dipole trap directly after association. Solid lines correspond to exponential fits yielding a  $1/e$ -time of 54(13) ms and 8(1) ms, respectively.

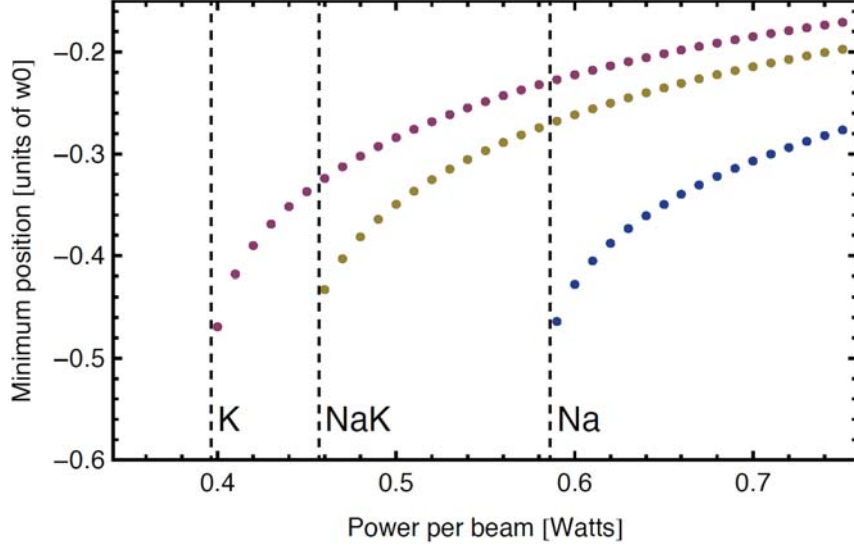


Figure 5-12: Gravitational sag of different species in ODT. Although NaK molecules are heavier than Na atoms, the NaK molecules suffer from a smaller gravitational sag than Na atoms, thanks to a larger polarizability. Therefore, we can remove sodium atoms by lowering the ODT power without affecting NaK molecules.

its depth is species selective, being more confining for NaK molecules and  $^{40}\text{K}$  atoms than for  $^{23}\text{Na}$ . Fig. 5-12 shows the position of the trap centers for each species, in the presence of gravity, with respect to the ODT beam center as a function of the ODT power. As one can see,  $^{23}\text{Na}$  is first species leaving the trap when lowering the ODT power. By carefully choosing the ODT power, we are able to remove  $^{23}\text{Na}$  atoms but still keep molecules inside the trap. We note that it takes about 2.5 ms until  $^{23}\text{Na}$  atoms have completely left the trap. Therefore the first few points in Fig. 5-11 are shaded. Fig. 5-13 shows an illustration of the experimental sequence for removing  $^{23}\text{Na}$  atoms. With bosons removed, the lifetime increases significantly to 54(13) ms, and further up to 140(40) ms at a binding energy of  $h \times 25$  kHz. Fig. 5-14 shows the lifetime of molecules as a function of scattering length. The lifetime  $\tau$  is likely limited by the presence of leftover  $^{40}\text{K}$  atoms in the  $|9/2, -3/2\rangle$  state. For collisions with

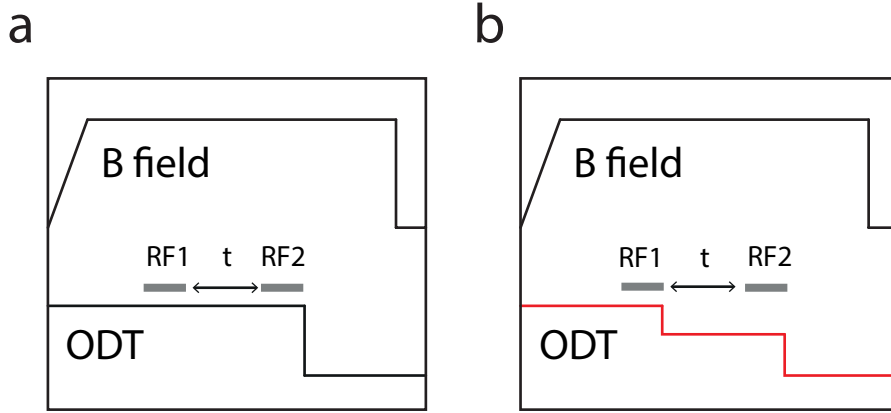


Figure 5-13: Schematic of the experimental sequence for removing sodium atoms from the ODT. (a) shows the sequence without removing sodium where RF1 stands for the molecular association pulse, RF2 stands for the dissociation pulse, and  $t$  is the wait time. (b) shows the sequence with removing sodium by lowering the ODT power.

non-resonant and distinguishable atoms, the molecular loss rate goes like [164]:

$$\beta \propto \left(\frac{r_0}{a}\right)^{2(J+1)} a^{2l+1} \quad (5.11)$$

where  $r_0$  is the characteristic size of the two-body potential,  $J$  is the total angular momentum of the system, and  $l$  is the atom-molecule relative angular momentum. For our case, both  $J$  and  $l$  are zero. As a result, the molecular loss rate in the presence of distinguishable and non-resonant atoms is simply inversely proportional to scattering length.

$$\beta \propto \frac{1}{a} \quad (5.12)$$

Indeed, we observe a dramatic increase in the lifetime with scattering length for  $a \lesssim 2300 a_0$  (binding energies  $E_b \gtrsim h \times 25$  kHz). The lifetime decreases again for even larger scattering lengths, most likely due to thermal dissociation when the binding energy becomes comparable to the temperature.

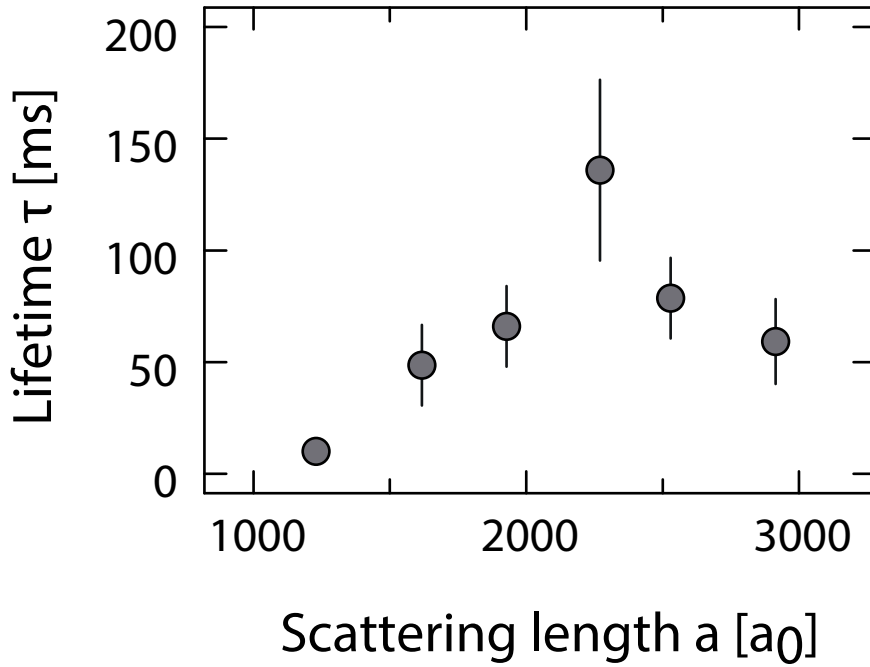


Figure 5-14: Lifetime of NaK molecules as a function of scattering length. The initial rise is due to the reduced wavefunction overlap with lower-lying vibrational states. The descent beyond 2300  $a_0$  is possibly due to thermal dissociation when the binding energy becomes comparable to the temperature.

The average density of remaining  $^{40}\text{K}$  atoms in the  $|9/2, -3/2\rangle$  state is  $n_A = \frac{1}{N} \int n^2 d^3r = 1 \times 10^{12} \text{ cm}^{-3}$ , yielding a loss rate of  $\beta = \frac{1}{n_A \tau} = 8(2) \times 10^{-12} \text{ cm}^3/\text{s}$ . As is studied in Ref. [159], the loss rate strongly depends on whether the collision partner is distinguishable or indistinguishable from the constituents of the molecule. For our case of distinguishable fermions as the collision partners, the above loss rate is one order of magnitude lower than the corresponding rate in KRb. In fact, it is still three times lower than the lowest rate measured in KRb for any collision partner [159]. Our loss rate even rivals that found for bosonic Feshbach molecules formed in a heteronuclear Fermi-Fermi mixture of LiK [165].

## 5.6 Conclusion

We have created ultracold fermionic Feshbach molecules of  $^{23}\text{Na}^{40}\text{K}$ , a molecule that is chemically stable in its absolute vibrational ground state. The molecular gas is formed close to degeneracy and is found to be long-lived near the Feshbach resonance. As revealed by the binding energy measurements, the Feshbach molecules are open-channel dominated over a wide magnetic field range, where they possess significant singlet character. These are ideal starting conditions for a two-photon transfer into the singlet rovibrational ground state [11]. Combined with the large induced dipole moment of 2.72 Debye, NaK presents us with a unique opportunity to create a stable, strongly dipolar Fermi gas with dominating long-range anisotropic interactions.

# Chapter 6

## Conclusion and Outlook

During my PhD at MIT, I constructed, calibrated, and performed measurements on one of the most complex ultracold atom systems - the Fermi I machine. This machine has shown its capability of cooling and trapping three different species simultaneously. Its initial goal was to study a Fermi-Fermi mixture of  $^6\text{Li}$  and  $^{40}\text{K}$ . On the way to pursue this goal, we discovered that  $^{41}\text{K}$  is an efficient sympathetic coolant for the fermionic species. Subsequently, simultaneously triple degeneracy of  $^6\text{Li}$ ,  $^{40}\text{K}$ , and  $^{41}\text{K}$  was demonstrated. As opposed to using rubidium as the coolant for  $^6\text{Li}$  and  $^{41}\text{K}$  in Kai Dieckmann's group [99], our approach exhibits a better simplicity. As a bonus of using  $^{41}\text{K}$ , we also discovered a broad *s*-wave Feshbach resonance between  $^{40}\text{K}$  and  $^{41}\text{K}$  [46], opening up a new pathway to the study of strongly interacting isotopic Bose-Fermi mixtures in which bosons and fermions almost perfectly overlap spatially due to the tiny mass difference between  $^{40}\text{K}$  and  $^{41}\text{K}$ . In particular, the fact that  $^{41}\text{K}$  is an efficient sympathetic coolant for  $^{40}\text{K}$  provides the possibility for studying strongly interacting Bose-Fermi mixtures in an only potassium experiment.

Sodium was originally introduced to improve the atom number of the fermionic species. Unexpectedly, a new and exciting mixture of  $^{23}\text{Na}$  and  $^{40}\text{K}$  has arisen. We demonstrated the first sympathetic cooling of  $^{40}\text{K}$  using  $^{23}\text{Na}$  as a coolant and most

importantly, more than thirty interspecies Feshbach resonances were identified. Realizing the fact that the NaK molecule in the absolute ground state is stable against chemical reaction, the study of NaK molecules has become a rising star in the field, because of the great potential of being the best candidate for studying quantum dipolar gases. We are the first group cooling this mixture to quantum degeneracy. Moreover, we have successfully created the first NaK Feshbach molecule [47] which is an important stepping stone to form the absolute ground state molecule of  $^{23}\text{Na}^{40}\text{K}$ .

Feshbach resonances are the prerequisite not only for making the Feshbach molecules but also for studying tunable ultracold quantum gases. In both  $^{40}\text{K}$ - $^{41}\text{K}$  and  $^{23}\text{Na}$ - $^{40}\text{K}$  mixtures, we have discovered outstandingly broad *s*-wave Feshbach resonances at 541 G and 138 G, respectively. These discoveries provide us with the opportunities to study polaron physics in different interaction regimes, in particular the Bose polaron problem.

## 6.1 Bose polarons

The interaction of electrons with ion vibrations strongly influences the transport properties of metals and semiconductors. In order to describe the behavior of electrons inside ion lattices it is essential to consider the quantum excitations of ion lattices - so called phonons. The corresponding electron-phonon interaction can cause phase transitions, including superconductivity. In particular, if the characteristic phonon energy is sufficiently low, the local displacement of ions caused by the electron, creates a potential well, which traps the electron even in a perfect crystal lattice. This self-trapping phenomenon was first predicted by Landau [166] in 1933. It was later studied in greater detail in Refs. [167, 168, 113, 169, 170] where the electron, dressed with the phonon fields, is considered as a quasi-particle - a so called large or continuum polaron. The large-polaron wave functions and corresponding lattice distortion can

spread over many lattice sites. Therefore, in a perfect lattice (without defects), the self-trapping is never complete. If the polaron motion is sufficiently slow, the ion lattice can hence adjust itself to follow the polarons. These slow moving polarons in the lattice can be treated as free electrons with an enhanced effective mass.

Ultracold quantum gases have the potential to shed light on the polaron problem. Importantly, the interactions between impurities and the environment can be tuned via Feshbach resonances. Therefore one can hope to study the effective mass of polarons as a function of the interaction strength. The Fermi polaron (an impurity moving in a fermionic environment) problem has been studied in Refs. [8, 9, 10] experimentally and in Refs. [171, 172, 173, 56] theoretically. It has been shown that in the strongly interacting regime, an impurity in a Fermi sea can renormalize itself to a new weakly interacting quasi-particle - the Fermi polaron- with a well-defined energy and effective mass. However, the Bose polaron (an impurity moving in a Bose condensate) problem, which is more related to the electron-phonon interaction problem, has not yet been realized in any ultracold atom experiment. A widely tunable Bose-Fermi mixture will be an ideal system to study the Bose polaron. In Chapters 3 and 4, I have shown that we have created two promising mixtures ( $^{40}\text{K}$  -  $^{41}\text{K}$  and  $^{23}\text{Na}$  -  $^{40}\text{K}$ ) where the Bose polaron problem can be studied with the discovered broad Feshbach resonances.

### 6.1.1 The Bose polaron Hamiltonian

The Hamiltonian of a single impurity atom immersed in a Bose gas can be written as:

$$\hat{H} = \frac{\hat{p}^2}{2m_I} + \sum_{\mathbf{k}} \epsilon_{\mathbf{k}} \hat{a}_{\mathbf{k}}^\dagger \hat{a}_{\mathbf{k}} + \frac{1}{2} \sum_{\mathbf{k}, \mathbf{k}', \mathbf{q}} V_{BB}(\mathbf{q}) \hat{a}_{\mathbf{k}'-\mathbf{q}}^\dagger \hat{a}_{\mathbf{k}+\mathbf{q}}^\dagger \hat{a}_{\mathbf{k}} \hat{a}_{\mathbf{k}'} + \sum_{\mathbf{k}, \mathbf{q}} V_{IB}(\mathbf{q}) \rho_I(\mathbf{q}) \hat{a}_{\mathbf{k}'-\mathbf{q}}^\dagger \hat{a}_{\mathbf{k}'}$$
(6.1)

Here the first term represents the kinetic energy of the impurity atom with mass  $m_I$ . The second is the kinetic energy of the bosons above the chemical potential. The operator  $\hat{a}_{\mathbf{k}}^\dagger, \hat{a}_{\mathbf{k}}$  create and annihilate bosons with mass  $m_B$ , wave number  $\mathbf{k}$ , and energy  $\epsilon_{\mathbf{k}} = (\hbar k)^2/2m_B - \mu$  where  $\mu$  is the chemical potential. The third term describes the interaction energy within the bosons. The interaction  $V_{BB}(\mathbf{q})$  is the Fourier transform of the boson-boson interaction potential. The interaction between the bosonic atoms and the impurity atom is described by the fourth term where the potential  $V_{IB}(\mathbf{q})$  coupling the boson density to the impurity density  $\rho_I(\mathbf{q})$ , which can be expressed as:

$$\rho_I(\mathbf{q}) = \int d^3\mathbf{r} e^{-i\mathbf{q}\cdot\mathbf{r}} \delta(\mathbf{r} - \mathbf{r}_I) \quad (6.2)$$

If now the bosonic bath forms a condensate, in a homogeneous system, under a Bogoliubov transform [174] the above Hamiltonian can be written as:

$$\hat{H} = E_{GP} + N_0 V_{IB}(\mathbf{0}) + \frac{\hat{p}^2}{2m_I} + \sum_{\mathbf{k} \neq \mathbf{0}} E_{\mathbf{k}} \hat{b}_{\mathbf{k}}^\dagger \hat{b}_{\mathbf{k}} + \sum_{\mathbf{k} \neq \mathbf{0}} \sqrt{\frac{\xi_{\mathbf{k}} N_0}{E_{\mathbf{k}}}} V_{IB}(\mathbf{k}) \rho_I(\mathbf{k}) (\hat{b}_{\mathbf{k}} + \hat{b}_{-\mathbf{k}}^\dagger) \quad (6.3)$$

The operator  $\hat{b}_{\mathbf{k}}, \hat{b}_{\mathbf{k}}^\dagger$  create and annihilate Bogoliubov excitations with wave number  $\mathbf{k}$ , respectively. The energy of the Bogoliubov excitations satisfies

$$E_{\mathbf{k}} = \sqrt{\xi_{\mathbf{k}}(\xi_{\mathbf{k}} + 2N_0 V_{BB}(\mathbf{k}))} \quad (6.4)$$

where  $\xi_{\mathbf{k}} = (\hbar k)^2/2m_B$ . The first term in equation (6.3) is the Gross-Pitaevskii energy

$$E_{GP} = N_0 \epsilon_0 + \frac{N_0^2}{2} V_{BB}(\mathbf{0}) + \frac{1}{2} \sum_{\mathbf{k} \neq \mathbf{0}} N_0 V_{BB}(\mathbf{k}) \quad (6.5)$$

and the second term is the interaction shift due to the impurity. Therefore the Hamiltonian 6.3, despite a constant shift, can be mapped onto the famous Fröhlich

polaron Hamiltonian [168]

$$\hat{H}_{pol} = \frac{\hat{p}^2}{2m_I} + \sum_{\mathbf{k} \neq \mathbf{0}} \hbar\omega_{\mathbf{k}} \hat{b}_{\mathbf{k}}^\dagger \hat{b}_{\mathbf{k}} + \sum_{\mathbf{k} \neq \mathbf{0}} V_{\mathbf{k}} e^{i\mathbf{k} \cdot \mathbf{r}} (\hat{b}_{\mathbf{k}} + \hat{b}_{-\mathbf{k}}^\dagger) \quad (6.6)$$

with

$$\hbar\omega_{\mathbf{k}} = ck\sqrt{1 + (\xi k)^2/2} \quad (6.7)$$

$$V_{\mathbf{k}} = \sqrt{N_0} \left( \frac{(\xi k)^2}{(\xi k)^2 + 2} \right)^{1/4} g_{IB} \quad (6.8)$$

Here we have already used contact pseudopotentials  $V_{BB}(\mathbf{r} - \mathbf{r}') = g_{BB}\delta(\mathbf{r} - \mathbf{r}')$  and  $V_{IB}(\mathbf{r} - \mathbf{r}') = g_{IB}\delta(\mathbf{r} - \mathbf{r}')$  for both the bosos-boson interaction and the boson-impurity interaction. So in the above expression  $\xi = 1/\sqrt{8\pi a_{BB}n_0}$ , where  $\frac{4\pi\hbar^2 a_{BB}}{m} \equiv g_{BB}$ , is the healing length of the BEC with a density of  $n_0 = N_0/V$  and  $c = \hbar/(\sqrt{2}m_B\xi)$  is the speed of sound in the BEC. The Fröhlich Hamiltonian was originally introduced to describe a conduction electron in an ionic crystal. Interestingly, the largest Fröhlich polaron coupling realized in any solid state system so far is not large enough to enter the strongly interacting regime where the polaron wave function obeys the “Product-Ansatz” [175] ( $|\Phi\rangle = |\Psi(\mathbf{r})\rangle|\text{Bose field}\rangle$ ), with  $|\Psi(\mathbf{r})\rangle$  being the impurity wave function. The “Product-Ansatz” leads to the result of the “self-trapping” polaron originally predicted by Landau in 1933 [166].

### 6.1.2 Simulated radio-frequency spectra

A very powerful tool to probe the quantum state of polarons is radio-frequency spectroscopy which has been demonstrated on Fermi polarons [9, 10]. It allowed to measure the energy and the quasiparticle residue of Fermi polarons. One can perform similar experiments on Bose polarons. Since the three-body loss is not prohibited in a Bose gas, an easy way to conduct the experiment is to prepare impurity atoms in a non-interacting state and transfer them into an interacting state. This is in contrast

to initially preparing impurity atoms in the interacting state, as in the study of Fermi polarons [9, 8]. As a result of this scheme, RF spectroscopy actually probes the polaronic state which is dressed with all possible excitations of the condensate. To understand Bose polaron spectra, let us first consider a localized ( $\mathbf{r} = 0$  in equation (6.6)) single impurity which has two internal states,  $|\uparrow\rangle$  and  $|\downarrow\rangle$  (e.g., two hyperfine states), such that the  $|\uparrow\rangle$  state interacts with bosons, while  $|\downarrow\rangle$  does not. When the interaction is switched off, the spectrum to transfer this impurity from  $|\downarrow\rangle$  to  $|\uparrow\rangle$  is simply a delta-function,  $A(\omega) \propto \delta(\omega - \omega_0)$ , here  $\hbar\omega_0$  is the energy difference between the two internal states. When the interaction is switched on, it can be shown [176] that the absorption probability starts to reveal an incoherent part, which corresponds to exciting different combinations of Bogoliubov quasiparticles upon absorption. The weight of the delta function therefore gets smaller as the impurity-BEC coupling is increased. The absorption probability can be decomposed into a coherent part and an incoherent part [176]: (similar analysis for Fermi polarons can be found in Ref. [177]).

$$A(\omega) = A_{coh}(\omega) + A_{inc}(\omega) \quad (6.9)$$

The coherent part of the absorption spectrum is simply a reduced delta function:

$$A_{coh}(\omega) \propto e^{-\alpha} \pi \delta(\omega) \quad (6.10)$$

where  $\alpha$  is proportional to  $n_0 g_{IB}^2$ . The behavior of the incoherent part of the absorption probability  $A(\omega)_{inc}$  is non-trivial and it has been worked out by Dmitry Abanin [176] :

$$A(\omega)_{inc} \propto \int e^{i\omega t - C(\beta, t)} - e^{i\omega t - C(\beta, \infty)} dt \quad (6.11)$$

where  $C(\beta, t)$  is a function that depends on the coupling parameter  $\beta$  which is defined as:

$$\beta \equiv \frac{\pi}{\sqrt{2}} \left( \frac{a_{IB}^2}{a_{BB}\xi} \right) \left( \frac{m_B}{m_r} \right)^2 \quad (6.12)$$

Fig. 6-1 plots the real and imaginary parts of  $C(t)/\beta$  obtained in Ref. [176].

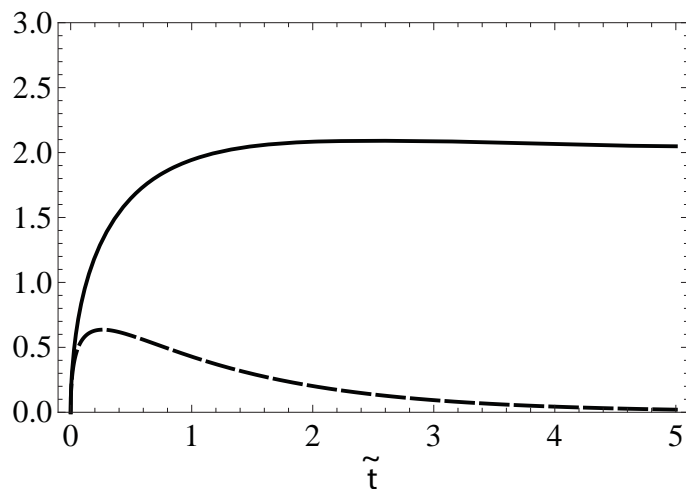


Figure 6-1: Real (solid line) and imaginary (dashed line) parts of the function  $C(\tilde{t})/\beta$ .

With the obtained  $C$ -function, now we can numerically calculate  $A(\omega)$  for different interactions [176]. We observe that, for weak interaction,  $A(\omega)$  is dominated by a  $\delta$ -peak (see Fig. 6-2 (a)). As the interaction strength increases, an incoherent hump develops and the  $\delta$ -peak shrinks. Eventually, the  $\delta$ -peak disappears and the spectrum is dominated by  $A_{inc}(\omega)$  (see Fig. 6-2 (d)).

The discussion above focuses on the immobile impurities. For the mobile impurities, we expect some changes on the absorption spectrum<sup>1</sup>. First, the kinetic energy of the impurities will change in the interacting state due to a change of the effective

---

<sup>1</sup>Note that in order to stay in the Fröhlich polaron regime, the speed of the impurities cannot exceed the speed of sound in the condensate, namely  $p/m_I \ll c$ , where  $p$  is the momentum of the impurity atom.

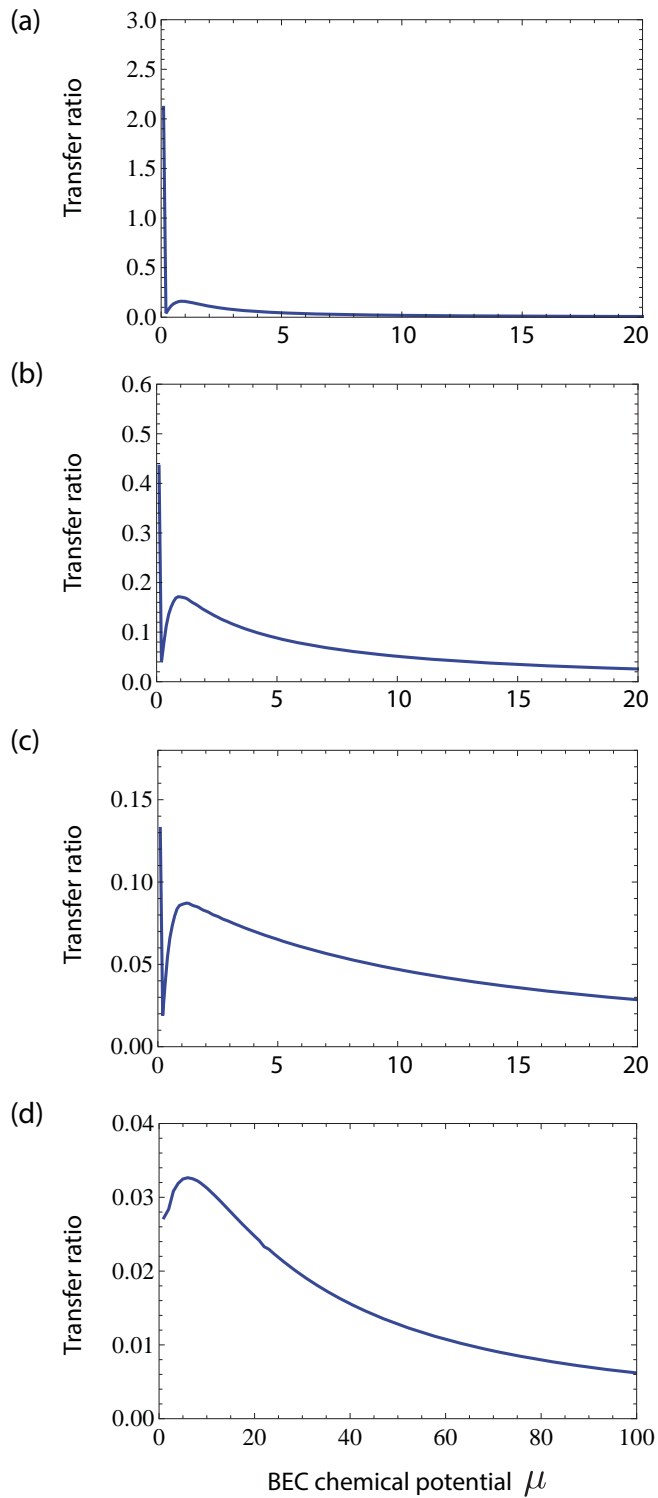


Figure 6-2: The simulated RF spectra for transferring impurities from non-interacting state to interacting state in different interaction strengths between impurities and bosons. (a)  $\beta = 0.2$ . (b)  $\beta = 1.0$ . (c)  $\beta = 1.6$ . (d)  $\beta = 2.4$ .

mass and the energy shift is:

$$\Delta E = \frac{p^2}{2m_I} - \frac{p^2}{2m_I^*}, \quad (6.13)$$

where  $m_I^*$  is the effective mass of the polarons. Therefore the  $\delta$ -peak will acquire the same shift. Second, the weight of the  $\delta$ -peak is now given by the overlap of the polaronic state and the boson vacuum. It is associated with the quasiparticle residue. Third, we expect a small quantitative differences in the incoherent part  $A_{inc}(\omega)$  due to the momentum exchange between bosons and impurities.

The broad Feshbach resonances we found in the  $^{40}\text{K}$  -  $^{41}\text{K}$  and  $^{23}\text{Na}$  -  $^{40}\text{K}$  systems will allow us to study the Bose polaron in different interaction regimes. In particular the small mass difference between  $^{40}\text{K}$  and  $^{41}\text{K}$  ensure that the  $^{40}\text{K}$  atoms are completely immersed in the condensate so that the condensate can be considered as a uniform field. Moreover, with ultracold atoms, the population imbalance between the condensate and the impurities can be controlled through the loading process. This provides the opportunity to study the polaron spectrum as a function of the population imbalance.

## 6.2 Quantum dipolar gases

In 2008, Ni *et al.* successfully used the Stimulated Raman Adiabatic Passage (STIRAP) to transfer the KRb Feshbach molecules to the singlet rovibrational ground state [11]. Their results have stimulated great interest in the properties of low temperature systems with dominant dipolar interactions [11, 150, 151, 12], which have long-range and anisotropic character and can be controlled by tuning external electric fields.

Heteronuclear diatomic molecules in the absolute ground state usually possess a large permanent electric dipole moment along the internuclear axis with strength

ranging for one tenth to a few Debye. Without external electric fields, in the lab frame, these molecules are not oriented and therefore do not have an electric dipole moment. In the presence of external electric fields, the dipole moment can be induced and approaches the asymptotic value, corresponding to the permanent dipole moment. This effect allows us to tune the strength of dipole-dipole interactions. The unique tunability of interactions in ultracold polar molecules paves the way to realize novel quantum phenomena which will be discussed later.

### 6.2.1 Dipole-dipole interaction

In contrast to contact interactions, dipole-dipole (dipolar) interactions are long-range and anisotropic:

$$\mathbf{V}_{\text{dd}}(\mathbf{r}) = \frac{\mathbf{d}_1 \cdot \mathbf{d}_2 - 3(\mathbf{d}_1 \cdot \hat{\mathbf{r}})(\mathbf{d}_2 \cdot \hat{\mathbf{r}})}{r^3} \quad (6.14)$$

where  $\mathbf{d}_1$  and  $\mathbf{d}_2$  are the two dipole moments and  $\mathbf{r}$  is the separation between the two dipoles. One can immediately see that dipolar interactions depend on the relative angle between the two dipoles. Furthermore, dipoles can interact with each other even when they are far apart. These two distinct features of dipolar interactions give rise to novel properties in dipolar quantum gases. Here I will focus on the discussion of dipolar interactions in fermionic dipolar quantum gases since the  $^{23}\text{Na}$ - $^{40}\text{K}$  Feshbach molecules we created have a great potential to realize such systems.

### 6.2.2 Fermionic dipolar quantum gases

Here we would like to ask a question: If a Fermi gas is dominated by dipolar interactions, what kind of new phenomena we can expect in a such system. First let us consider the effect due to the long range nature of dipolar interactions

## The effect of long range

The effective interaction in a single-component Fermi gas, including the centrifugal potential, can be written as:

$$V_{\text{eff}}(r) = \frac{\hbar^2 l(l+1)}{2\mu r^2} + V_{dd}(r, \theta) + V_0(r) \quad (6.15)$$

Where  $l$  is the total orbital angular momentum,  $\mu$  is the reduced mass of the two dipoles,  $V_{dd}(r, \theta)$  represents the dipolar interaction ( $\theta$  is the angle between the two dipoles), and  $V_0(r)$  summarizes the residual interactions which can be modeled as a Van der Waals potential and a short-range repulsion

$$V_0(r) = -C_6/r^6 + A/r^{12} \quad (6.16)$$

The dipolar potential  $V_{dd}(r, \theta)$ , averaged over the angle  $\theta$  between the two dipoles, is equal to  $\bar{V}_d = -4d^2/5r^3$ . In the case of identical fermions only odd orbital angular momenta are present due to the Pauli exclusion principle. Let us consider only the  $l = 1$  and  $m_l = 0$  scattering process so that the effective potential is reduced to:

$$V_{\text{eff}}(r) = \frac{\hbar^2}{\mu r^2} - \frac{4d^2}{5r^3} - \frac{C_6}{r^6} + \frac{A}{r^{12}} \quad (6.17)$$

Without  $\bar{V}_d(r)$ , at low temperatures, molecules can not overcome the centrifugal barrier so that no collision can happen. However, thanks to the dipolar interaction, the term  $\bar{V}_d(r)$  counteracts the centrifugal potential. Fig. 6-3 shows that the centrifugal barrier is “eaten” away by the dipolar force. This effect allows identical fermions to collide through the  $p$ -wave scattering channel.

A significant result of dipolar interaction is that many-body pairing can actually happen even in a single-component Fermi gas through the  $p$ -wave pairing. It can result a  $p$ -wave superfluid with a gap that has nodes on the Fermi surface. It can

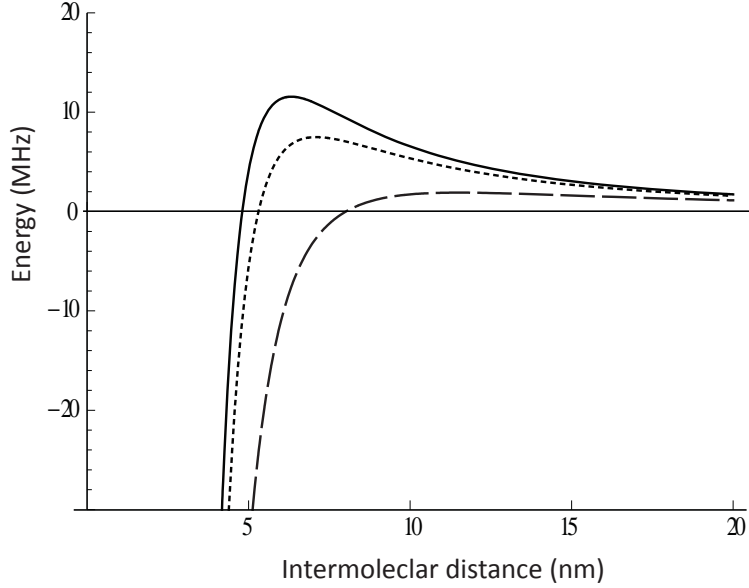


Figure 6-3: Effect of the dipolar interaction on the centrifugal barrier. In this simulation, we neglect the short-range potential and only consider the long-range potential (the first three terms in equation (6.17)). We used  $C_6 = 2550$  au (au is the atomic unit,  $E_h a_0^6$ ),  $\mu = 15$  Da, and  $d = 0.0$  (solid line),  $0.1$  (dotted line),  $0.2$  (dashed line) Debye in this simulation. The centrifugal barrier is “eaten” away by the dipolar interaction allowing  $p$ -wave collisions in a single-component dipolar Fermi gas at low temperatures.

be shown that the superfluid transition temperature in a single-component dipolar Fermi gas has a similar form as in a conventional two-component Fermi gas [178]:

$$k_b T_c = 1.44 \epsilon_F \exp\left(-\frac{\pi}{2k_F |a_d|}\right) \quad (6.18)$$

where  $a_d$  is

$$a_d = -\frac{2md^2}{\pi^2 \hbar^2} \quad (6.19)$$

We notice that  $a_d$  here plays a similar role as the  $s$ -wave scattering length  $a_s$  in a

conventional two-component Fermi gas

$$a_d \sim a_s \tag{6.20}$$

Instead of using the Feshbach resonance to tune the interaction, here we can simply tune the induced dipole moment  $d$ . For example, the permanent electric dipole moment (2.72 Debye) of NaK molecules corresponds to  $a_d = -27000a_0$ , where  $a_0$  is the Bohr radius. In a typical degenerate Fermi gas,  $k_F = (6\pi^2n)^{1/3} = (6\pi^2 \times 10^{13}/\text{cm}^3)^{1/3} = 1/(2300a_0)$ . We learned from a conventional two-component Fermi gas that equation (6.18) is no longer valid once the system starts entering the strongly interacting regime  $k_F a \approx 1$ . It suggests that universal physics in a dipolar Fermi gas of NaK molecules can be well reached.

### The effect of angular dependance

The effect of angular dependance on the dipolar interactions gives rise to many interesting phenomena. Here we will show you two examples:

**Effective mass:** Let us consider a normal Fermi liquid state of a dipolar Fermi gas, which is a generic state for a fermionic dipolar gas at finite temperatures ( $T_c < T < T_F$ ). Due to the anisotropy of dipolar interactions, the Fermi surface in a dipolar Fermi gas is no longer a sphere but rather an ellipsoid, meaning that the modulus of the Fermi momentum depends on the direction [179]:

$$p_F(\mathbf{n}) = \hbar k_F \left[ 1 + \frac{1}{9\pi} a_d k_F (3 \cos^2 \theta_n - 1) \right] \tag{6.21}$$

where  $\mathbf{n}$  is a unit vector in momentum space,  $\theta_n$  is the angle between  $\mathbf{n}$  and the  $z$ -axis which is in the direction of induced dipoles. And the Fermi velocity at the Fermi

surface can be defined as:

$$\mathbf{v}_F = \mathbf{n} \frac{p_F(\mathbf{n})}{m_L^*(\mathbf{n})} + \mathbf{e}_\theta \frac{p_F(\mathbf{n})}{m_T^*(\mathbf{n})} \quad (6.22)$$

where  $\mathbf{e}_\theta$  is the polar angle unit vector. Unlike the conventional Fermi liquid, the effective mass can be decoupled into longitudinal  $m_L^*$  and transverse  $m_T^*$  components which follow [180]

$$\frac{m}{m_L^*(\mathbf{n})} = \left[ 1 - \frac{1}{6\pi} a_d k_F (3 \cos^2 \theta_n - 1) \right] \quad (6.23)$$

$$\frac{m}{m_T^*(\mathbf{n})} = \frac{1}{3\pi} a_d k_F \sin 2\theta_n$$

**Pairing gap:** The profound effect of anisotropic Fermi momentum directly results in an anisotropic pairing gap. For temperature  $T$  close to  $T_c$ , the pairing gap on the Fermi surface ( $p = p_F$ ) has the form [178]

$$\Delta(p_F, \mathbf{n}) \approx 2.5 T_c \sqrt{1 - \frac{T}{T_c}} \alpha(\mathbf{n}) \quad (6.24)$$

where

$$\alpha(\mathbf{n}) = \sqrt{2} \sin \left( \frac{\pi}{2} \cos \theta_{\mathbf{n}} \right) \quad (6.25)$$

Fig. 6-4 shows the pairing gap as a function of the angle between the Fermi momentum and the  $z$ -axis. The gap reaches its maximum in the direction parallel to the dipoles ( $\theta_{\mathbf{n}} = 0, \pi$ ), while it vanishes in the direction perpendicular to the dipoles ( $\theta_{\mathbf{n}} = \pi/2$ ). The vanishing of the pairing gap at  $\theta_{\mathbf{n}} = \pi/2$  allows single particle excitations at low temperatures  $T \ll T_c$ . As a consequence, the density of states in the vicinity of the Fermi energy is linearly proportional to the energy,  $\rho(\epsilon \sim E_F) \propto \epsilon$ . Therefore, the temperature dependent part of the energy of the system is proportional

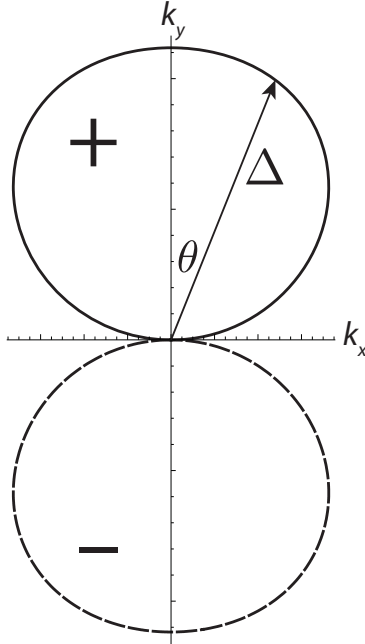


Figure 6-4: Pairing gap  $\Delta$  as a function of the angle  $\theta$  between the Fermi momentum and the dipoles. The solid and dashed lines indicate the positive and negative gap regions, respectively. The length of the arrow represents the magnitude of the pairing gap. The pairing gap vanishes in the direction perpendicular to the dipoles, resulting in the  $T^2$  dependence on the specific heat at low temperatures. The simulation was performed at  $T = 0.9T_c$ . The arrow corresponds a pairing gap of energy  $k_B T_c$ .

to  $T^3$ . This results in the  $T^2$  dependence of the specific heat as opposed to  $T^3$  dependence in the conventional  $s$ -wave pairing where the low-temperature specific heat is determined by the contribution of collective modes. Above we briefly described the effect of dipolar interactions in a single-component Fermi gas. There are further interesting phenomena waiting to be explored in other ultracold dipolar gas systems. For example, in a two-component dipolar Fermi gas where contact interactions have been switched on, there are now two competing pairing channels: molecules need to decide to pair with distinguishable or indistinguishable partners - a competition between  $s$ -wave pairing and  $p$ -wave pairing. In such systems, attractive contact interactions can favor the pairing between distinguishable partners by increasing the critical temperature of the singlet pairing and make it larger than that for the triplet

one such that the ground state corresponds to an interspecies singlet pairing [181].

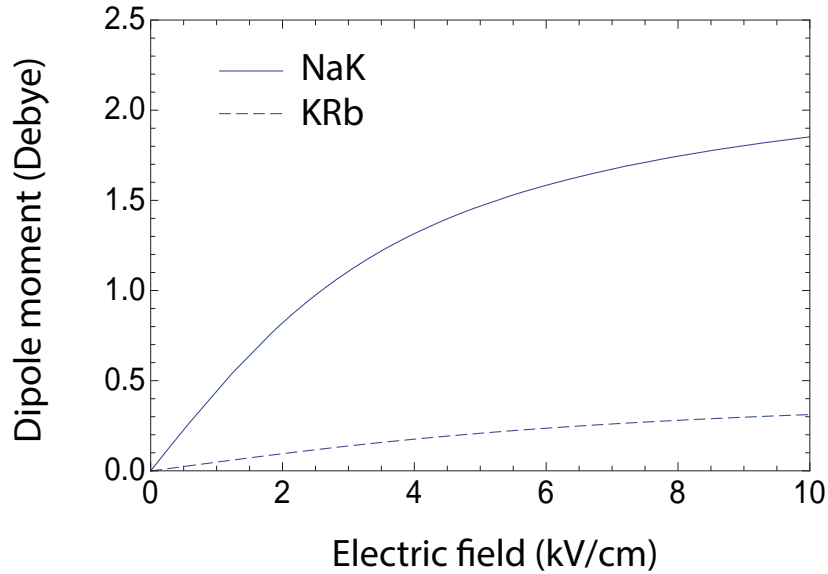


Figure 6-5: Induced electric dipole moments of NaK and KRb molecules as a function of external electric fields.

More exotic phases can form in lower dimensions. In a 2D Monolayer, a single-component Fermi gas can form a so-called  $p_x + ip_y$  superfluid [182, 183] which is a topological superfluid. Especially when the chemical potential of this system is larger than zero  $\mu > 0$ , it forms a topologically nontrivial phase. In particular, vortices inside this superfluid support Majorana fermions at their cores which can possibly be used for topologically protected quantum information processing [184, 185, 186]. In a 2D multilayer, pairing can actually happen between molecules in different layers. By increasing interlayer coupling, a BCS state can smoothly transform into a BEC state of tightly bound interlayer molecules when the interparticle separation in each layer is larger than the size of the bound state [187, 188]. In a 1D tube, a gas of dipolar molecules (no matter whether we have bosonic or fermionic molecules) can form a so-called Tomonaga-Luttinger liquid (TLL) [189, 190, 191] which is based on a Luttinger liquid [192, 193], but with long-range interactions. The TLL was originally introduced

to describe electrons in one-dimensional systems such as carbon nanotubes.

As we learned from the previous discussion, the induced dipole moment in dipolar quantum gases opens up the possibility of studying  $p$ -wave superfluidity in a single-component Fermi gas. In order to explore the physics in different interaction regimes, a widely tunable induced dipole moment is highly desirable. The  $^{23}\text{Na}$ - $^{40}\text{K}$  Feshbach molecules we created (see chapter 5) is so far the best candidate to study quantum dipolar Fermi gases. These molecules possess a permanent electric dipole moment of 2.7 Debye and are expected to be stable against chemical reactions [153]. Fig. 6-5 compares the induced electric dipole moments of ground state NaK and KRb molecules as a function of external electric fields. Thanks to the quadratic dependence of the dipolar interaction energy on dipole moment, the dipolar interaction energy can be as high as 30% of the Fermi energy in a NaK molecular gas which is one order of magnitude higher than the energy in a KRb molecular gas.

Since 2008, the first paper on the production of KRb ground state molecules has been cited more than 720 times [11]. Unfortunately, the KRb molecule is not stable against chemical reaction in its absolute ground state. A stable dipolar gas will allow us to explore not only exotic quantum phases but also universal dipolar scattering processes where all dipolar scattering behaves similarly and the cross section can be parametrized by mass, induced dipole moment, and collision energy [194, 195, 196]. The Fermi I machine is on the verge of entering a completely new realm of physics where the dipolar interaction dominates. Now is an exciting moment and the best is yet to come...

# Appendix A

## Schematics of the Fermi I vacuum chamber

This appendix includes the schematics of the bucket windows from UKAEA and the main chamber schematics sent to Sharon Vacuum for production.

# Large and small bucket windows from UKAEA

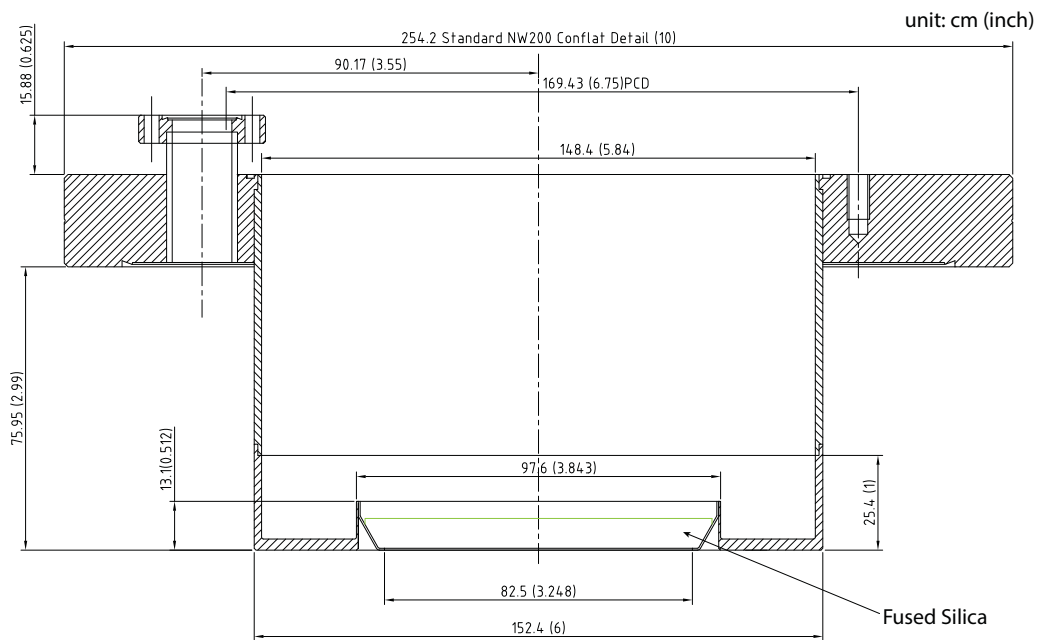


Figure A-1: Schematic of the 4" recessed viewport from UKAEA.

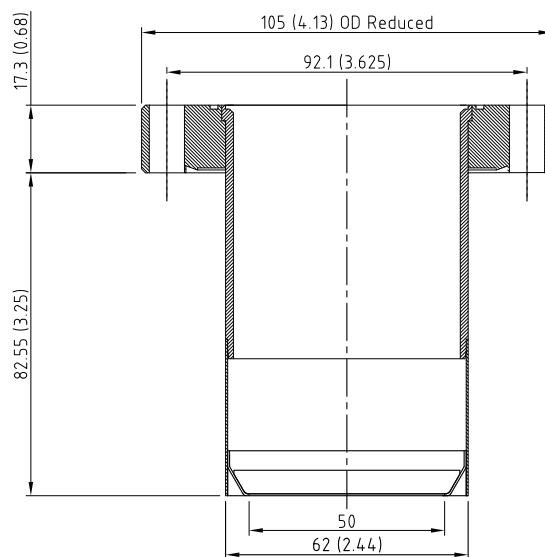


Figure A-2: Schematic of the 2.5" recessed viewport from UKAEA.

# Fermi I Chamber Drawing for Sharon Vacuum (2008)

Page1 : List of Content

Page2 : Port information and special notes

Page3 : Projected View

Page4 : Top View

Page5 : Side View 1

Page6 : Side View 2

Page7 : Detail of spot-welded nuts

Page8: Offset Adapter (quantity 2)

Cheng-Hsun Wu  
 MIT  
 Phone: 617/253-6677; Email: wuch@mit.edu  
 Trapping Chamber: 19Aug2008

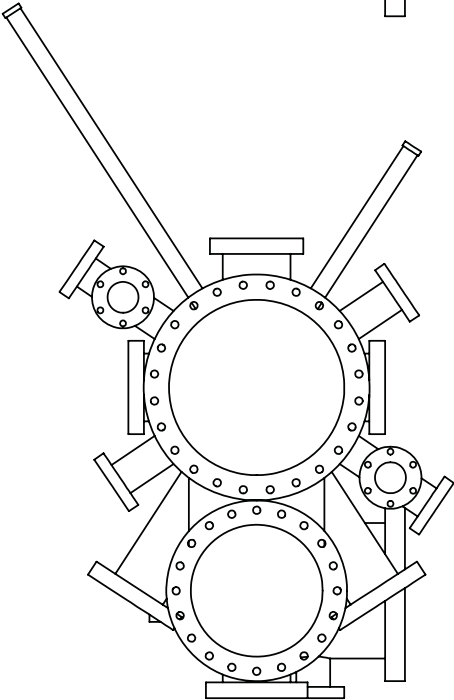
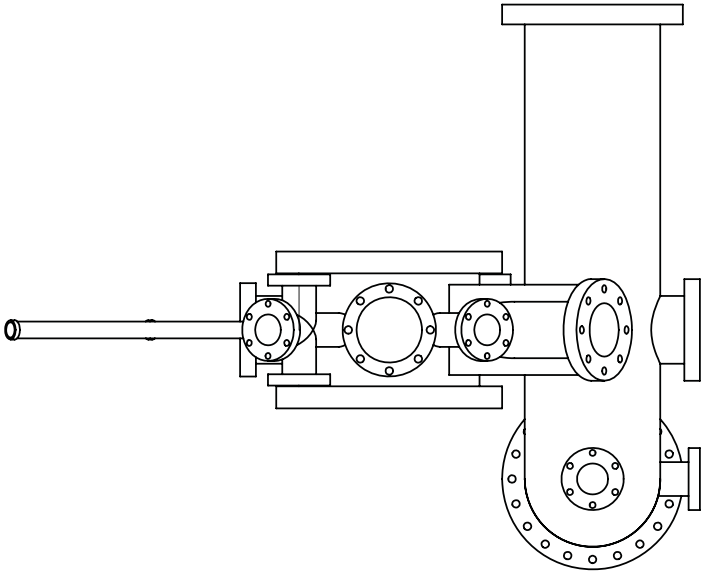
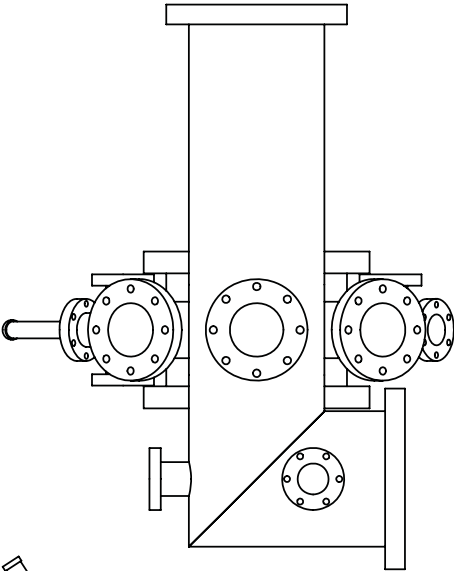
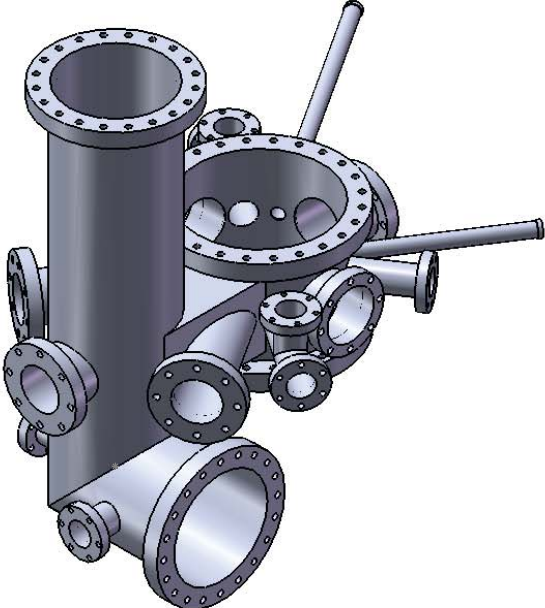
Material: 304 Stainless steel. Please quote price for electropolishing.  
 Units: inches. All flanges with clearance holes. Port length measured to outside of flange.  
 Bold italic port# indicates special consideration required - see notes.

**Focus points: (X,Y,Z)**

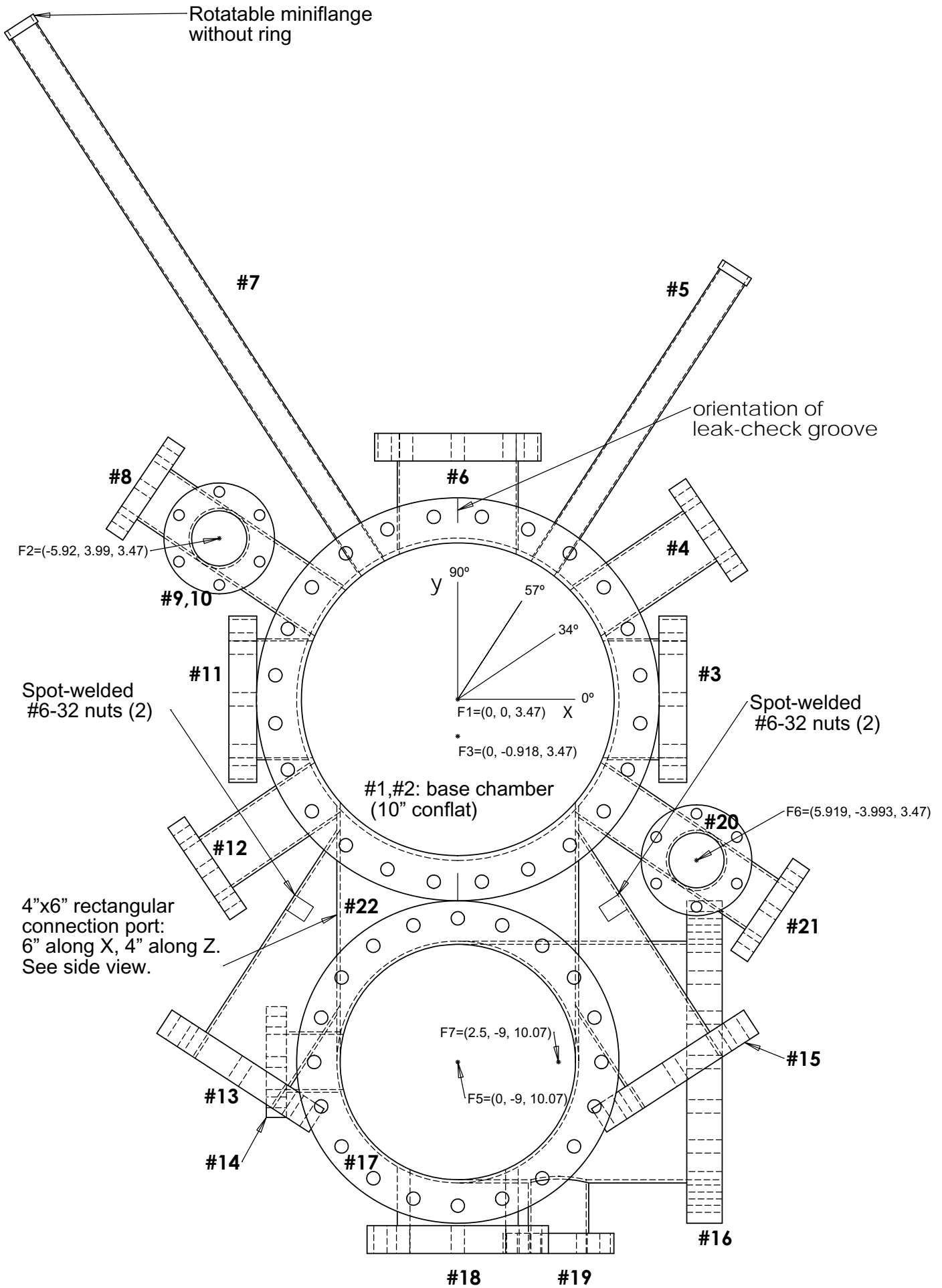
F1 (0, 0, 3.47)  
 F2 (-5.92, 3.99, 3.47)  
 F3 (0, -0.918, 3.47)  
 F4 (-5.365, -9.179, 3.47)  
 F5 (0, -9.00, 10.07)  
 F6 (5.919, -3.993, 3.47)  
 F7 (2.5, -9.00, 10.07)

Port #	Flange Size	Flange Type	Tube size (OD)	Focal Point	Focal Length	Polar Angle	Azimuthal Angle	Notes
<b>1</b>	10		8	F1	3.47	180		#1,2: custom length nipple. Align leak check grooves with Y axis.
<b>2</b>	10		8	F1	3.47	0		
<b>3</b>	<b>4.13</b> (4 1/2)		OD=3, ID=2.9	F1	5.68	90	0	4.5 flange OD machined to 4.13, ID=2.9 for oversized tube
<b>4</b>	2 3/4		1.5	F1	7.75	90	34.0	
<b>5</b>	1 1/3	R	0.75	F1	12.72	90	57.0	Omit flange retaining ring - really!
#5&7: This nonstandard flange scheme will allow a magnet windings to slide over the flange. Please supply 4 miniflange retaining rings cut (between screw holes) into 2 semi-circles.								
<b>6</b>	<b>4.13</b> (4 1/2)		OD=3, ID=2.9	F1	6.60	90	90.0	4.5 flange OD machined to 4.13, ID=2.9 for oversized tube
<b>7</b>	1 1/3	R	0.75	F1	20.00	90	123.0	Omit flange retaining ring - really!
<b>8</b>	2 3/4		1.5	F1	9.60	90	146	
<b>9</b>	2 3/4		1.5	F2	2.46	180		
<b>10</b>	2 3/4		1.5	F2	2.46	0		
<b>11</b>	<b>4.13</b> (4 1/2)		OD=3, ID=2.9	F1	5.68	90	180	4.5 flange OD machined to 4.13, ID=2.9 for oversized tube
<b>12</b>	2 3/4		1.5	F1	7.75	90	214	
<b>13</b>	4 1/2	R	2.5	F3	10.25	90	237	spot-weld #6-32 nuts
#13&15: nuts located 1.75" from intersection with rectangular tube, measured along axis of port #13&15								
<b>14</b>	2 3/4		1.5	F5	4.75	90	180	
<b>15</b>	4 1/2	R	2.5	F3	10.25	90	303	spot-weld #6-32 nuts
<b>16</b>	8	R	6	F5	6.56	90	0	Miter joint with #17
<b>17</b>	8		6	F5	21.00	180		
<b>18</b>	4 1/2		OD=3, ID=2.9	F1	13.75	90		Tube should extend 1.5" inside chamber from weld
#19: Tube extension shields #19 window from Ti-Sub pump on port 17 (miter as shown in side view). If this is too inconvenient, just cut tube flush with surface - I can improvise a shield later.								
<b>19</b>	2 3/4		1.5	F7	4.75	90		
<b>20</b>	2 3/4		1.5	F6	2.46	180		
<b>21</b>	2 3/4		1.5	F1	9.60	90	326	
<b>22</b>	(none)		4x6 rectangle	F1	[9.00]	90	270	6" along X, 4" along Z, length along Y

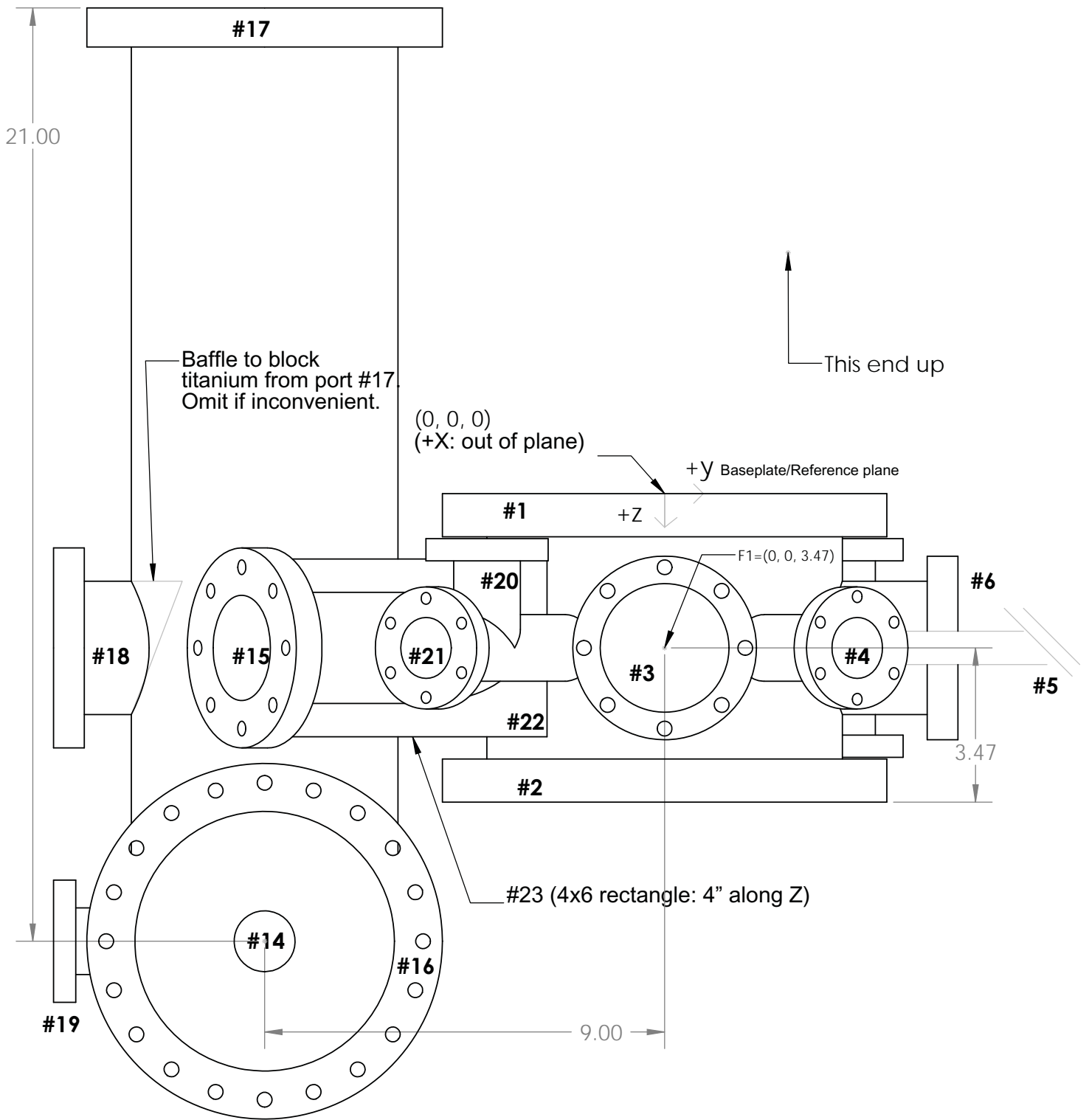
Projected View



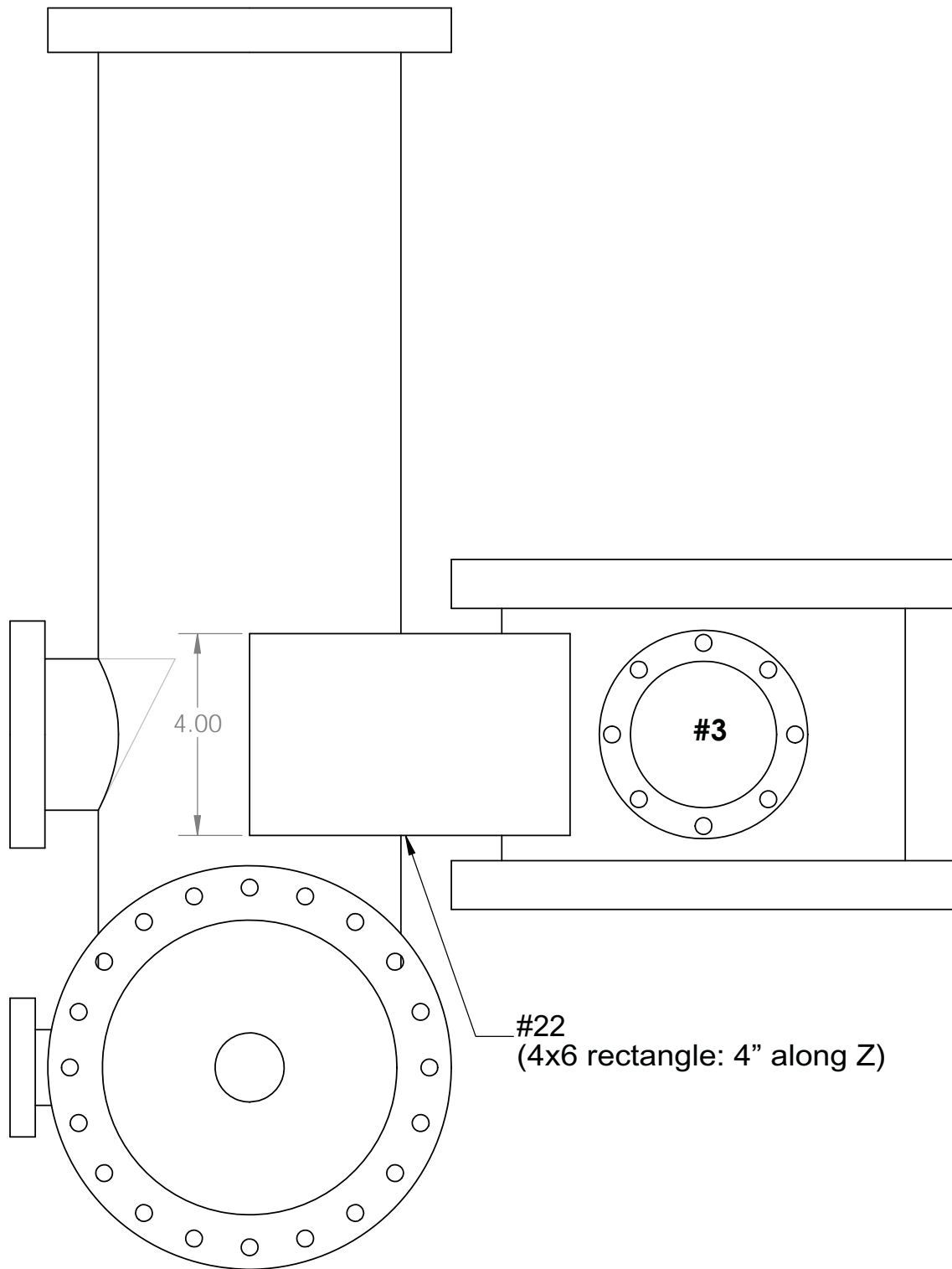
# Top View



# Side View1



**Side View 2**  
(Other radial ports omitted for simplicity)

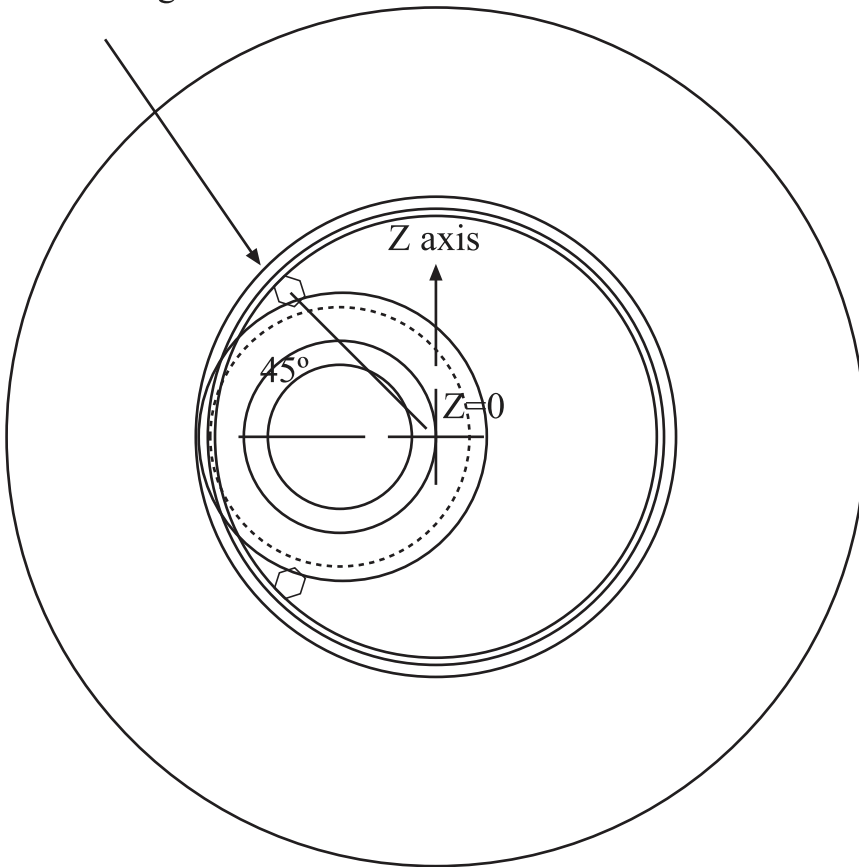


View through Port#13 flange

Todd Gustavson  
MIT  
617/253-7423  
8Feb2000

**Fig.#1c** Port 13 Nut spot-weld

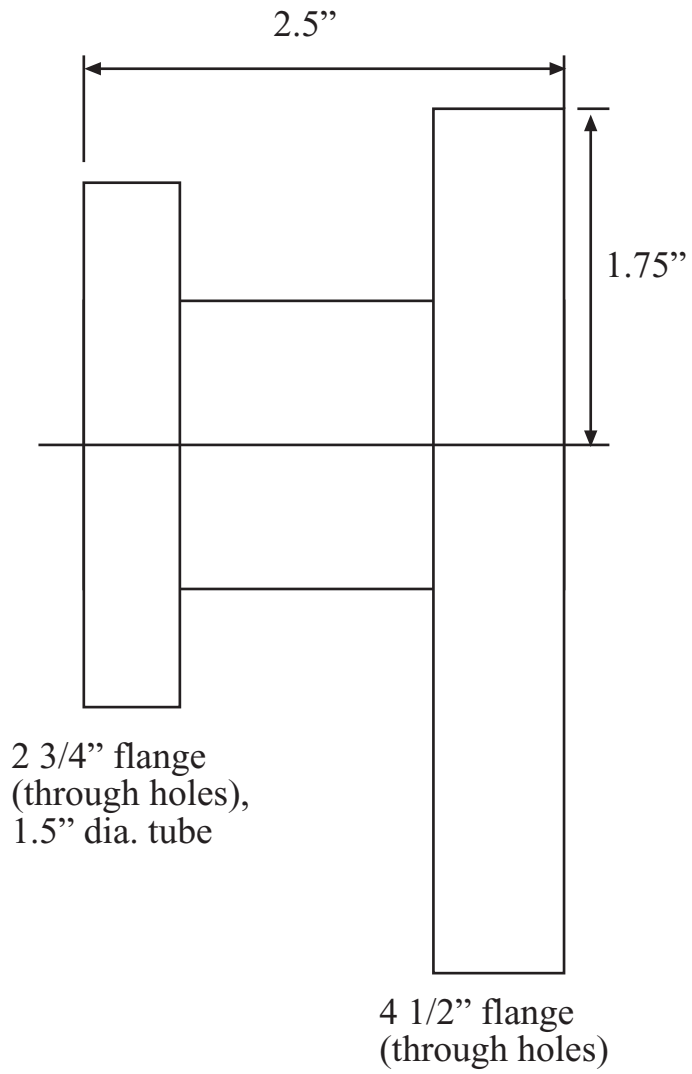
Spot-weld #6-32 nuts (2)  
screw axis parallel to port.  
Weld plane is 1.75"  
from intersection between  
Port#13 and rectangular tube.



←—————→  
Z=0 Baseline, defined by Port#1

Todd Gustavson  
MIT  
617/253-7423  
8Feb2000

**Fig.#3** Offset Adapter

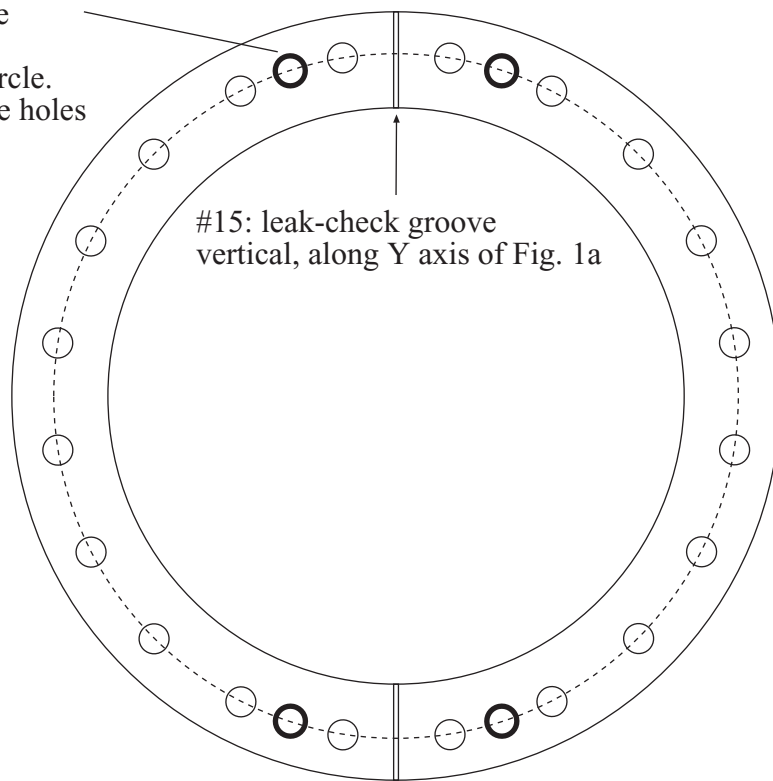


Todd Gustavson  
MIT  
617/253-7423  
8Feb2000

Ports #15, 17:  
8" conflat  
flange with clear holes

**Fig.#1d** Flange Mounting  
Back side (non-vacuum side)

Drill & tap 4 holes  
for 5/16"-18, 0.75" deep  
on back side of flange  
(away from knife)  
on 7.128" dia. bolt circle.  
Bisect standard flange holes  
(with 18° spacing)



## Appendix B

# Vapor pressure curves of different elements

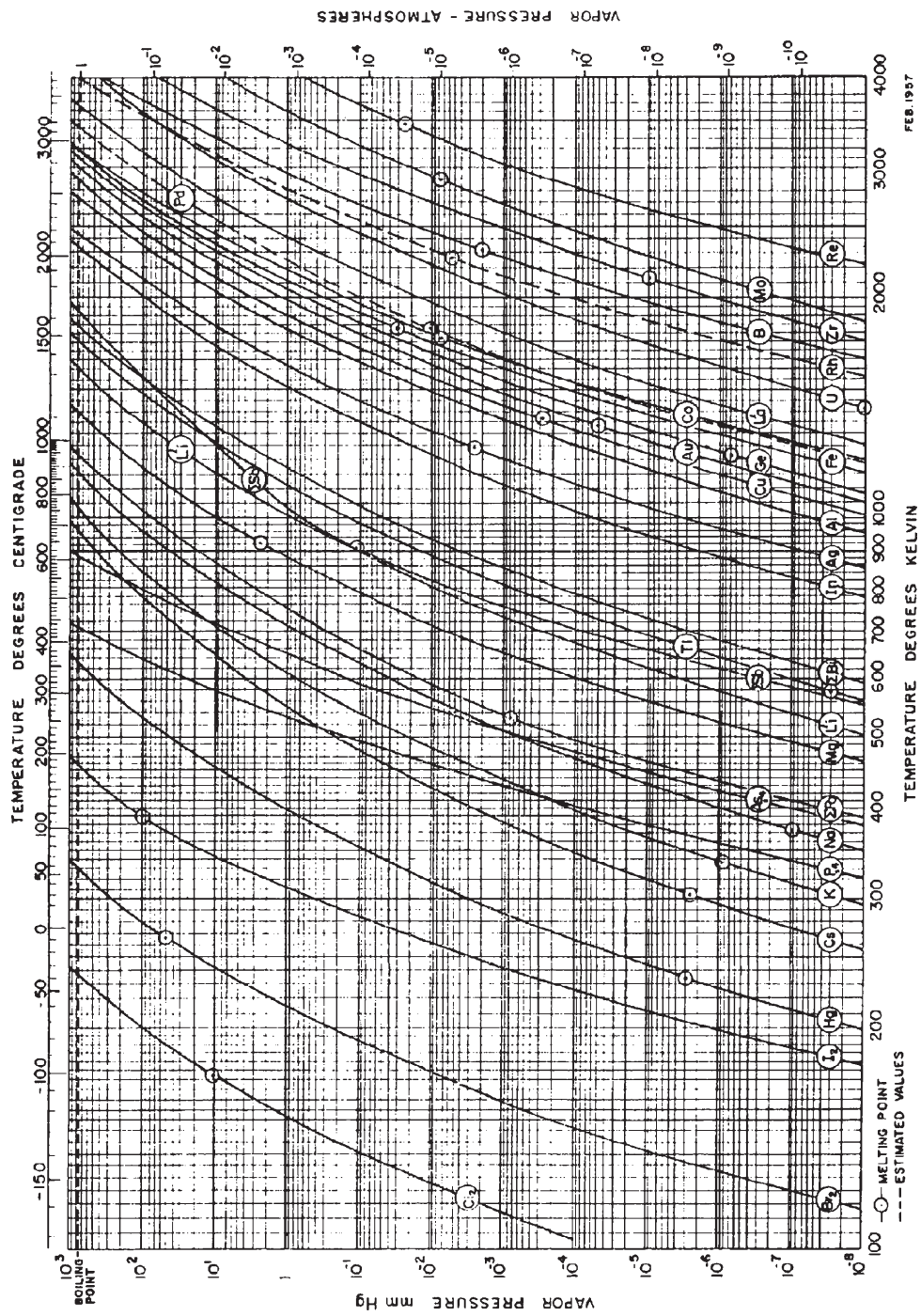


Figure B-1: Vapor pressure curves of different elements [197]

# Appendix C

## Schematics of the Fermi I laser systems

This appendix includes the detailed schematics of the lithium and potassium laser systems. The schematic of the sodium laser system can be found in Ibon Santiago's thesis [94]

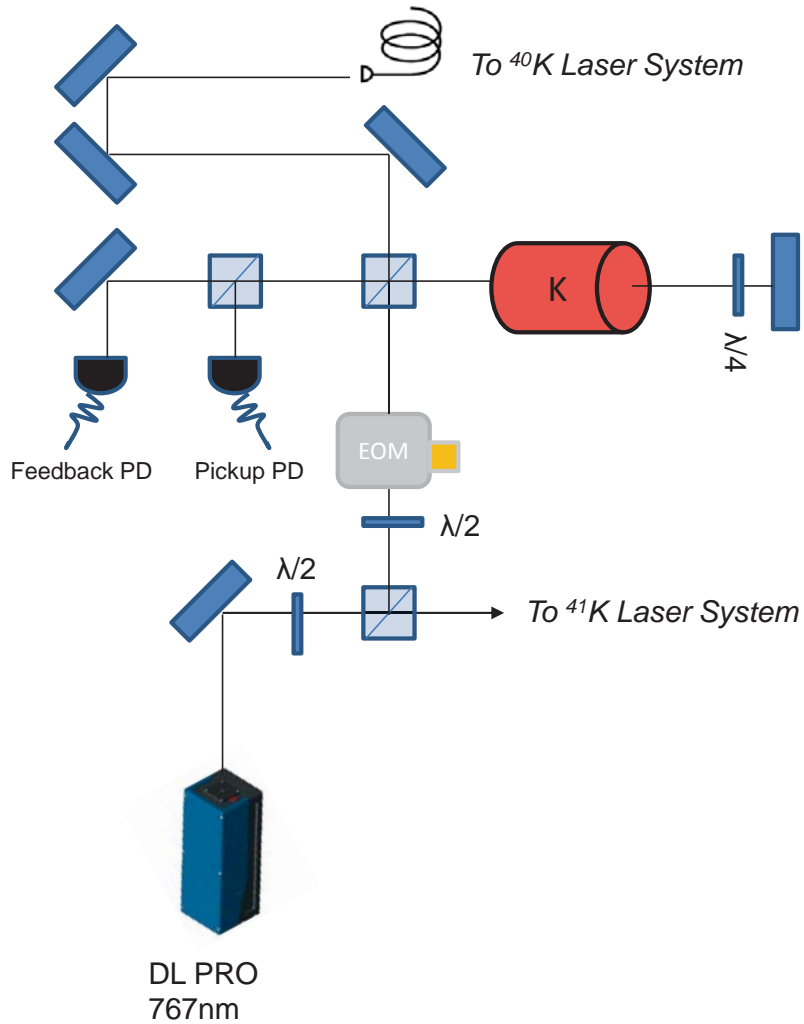


Figure C-1: The potassium FM spectroscopy setup. The laser beam coming out from the DL Pro grating stabilized laser is send though an electrical optical modulator (fed by 2 W, 55 MHz RF) to create frequency sidebands and then split into the pump and probe beams for the Doppler free saturated absorption spectroscopy [?]

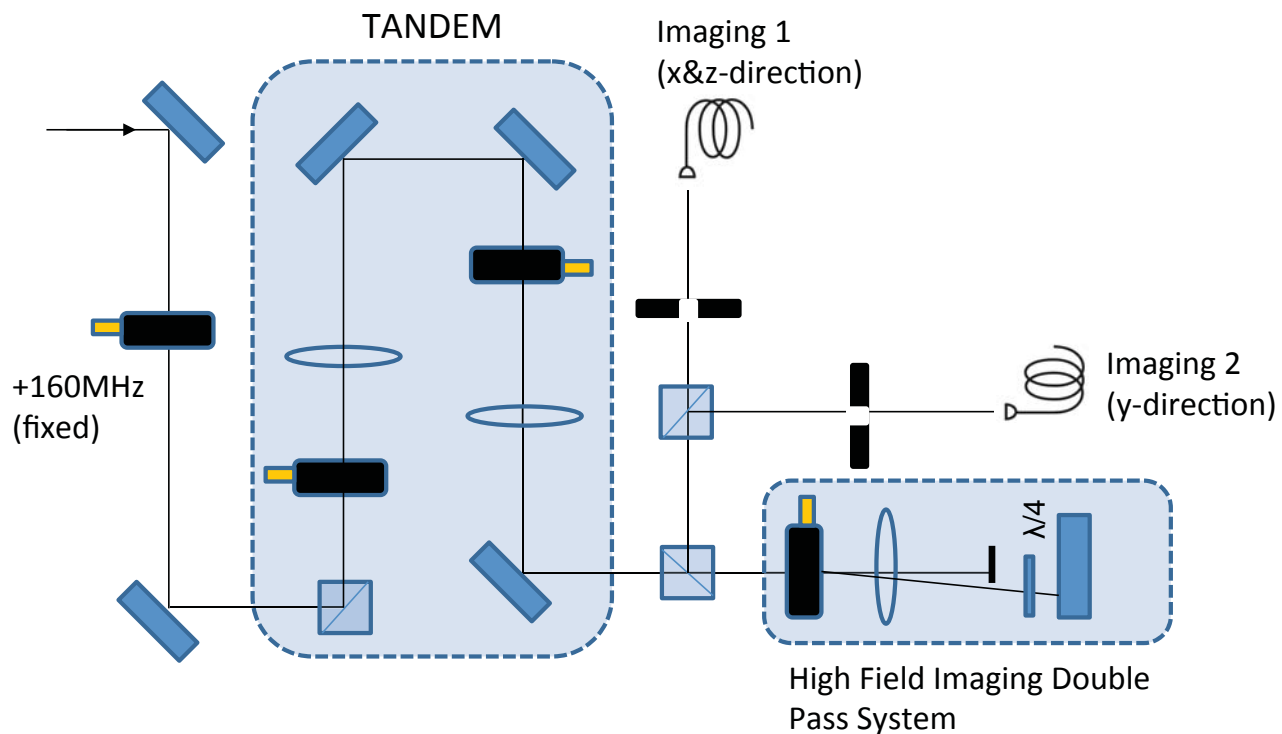


Figure C-2: The potassium imaging and optical pumping system. A tandem AOM setup which has a tuning range of  $\pm 60$  MHz is used to change the laser frequency without affecting its power. A double pass AOM setup is placed after the tandem setup to increase the dynamic range of the imaging system in order to bridge the frequency jump when imaging at higher magnetic fields.

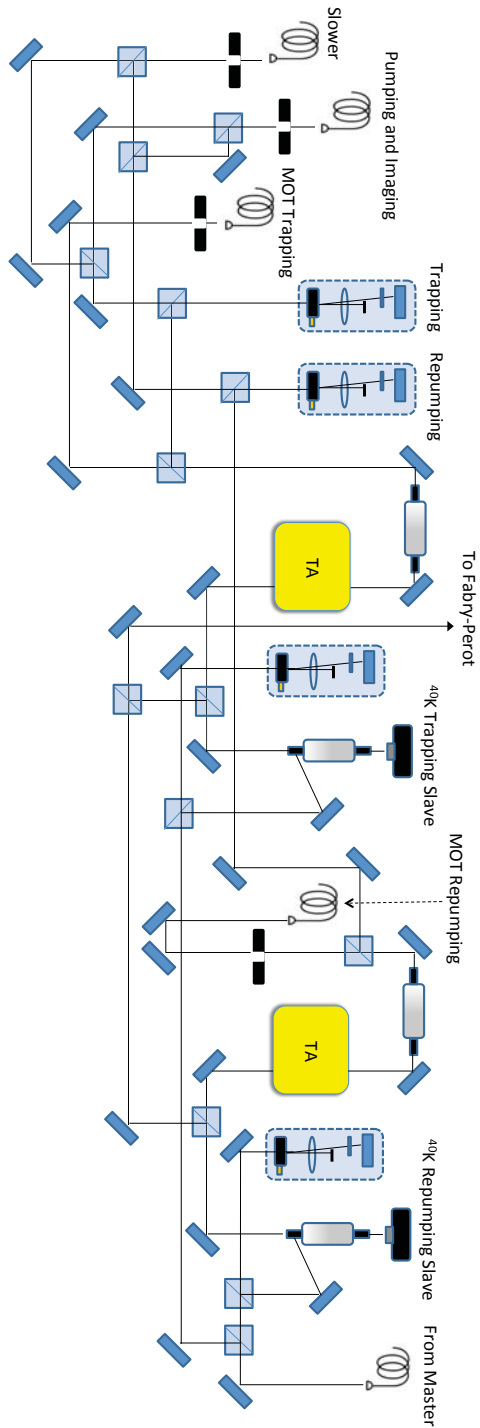


Figure C-3: Schematic of the  $^{40}\text{K}$  laser system.

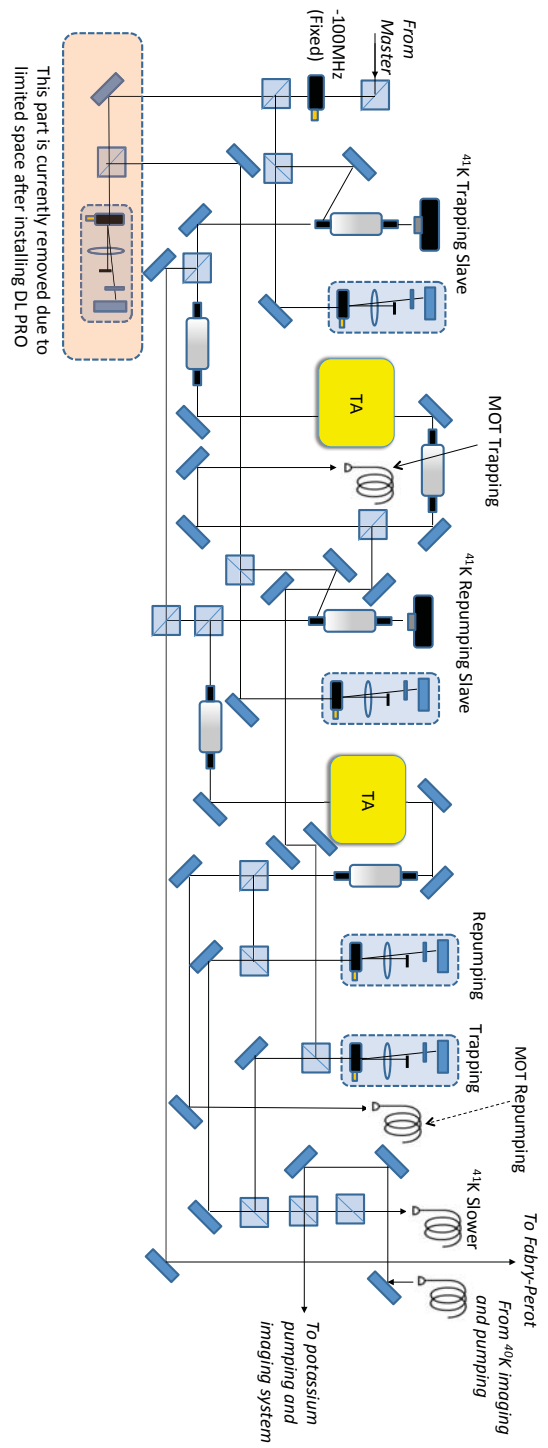


Figure C-4: Schematic of the  $^{41}\text{K}$  laser system.

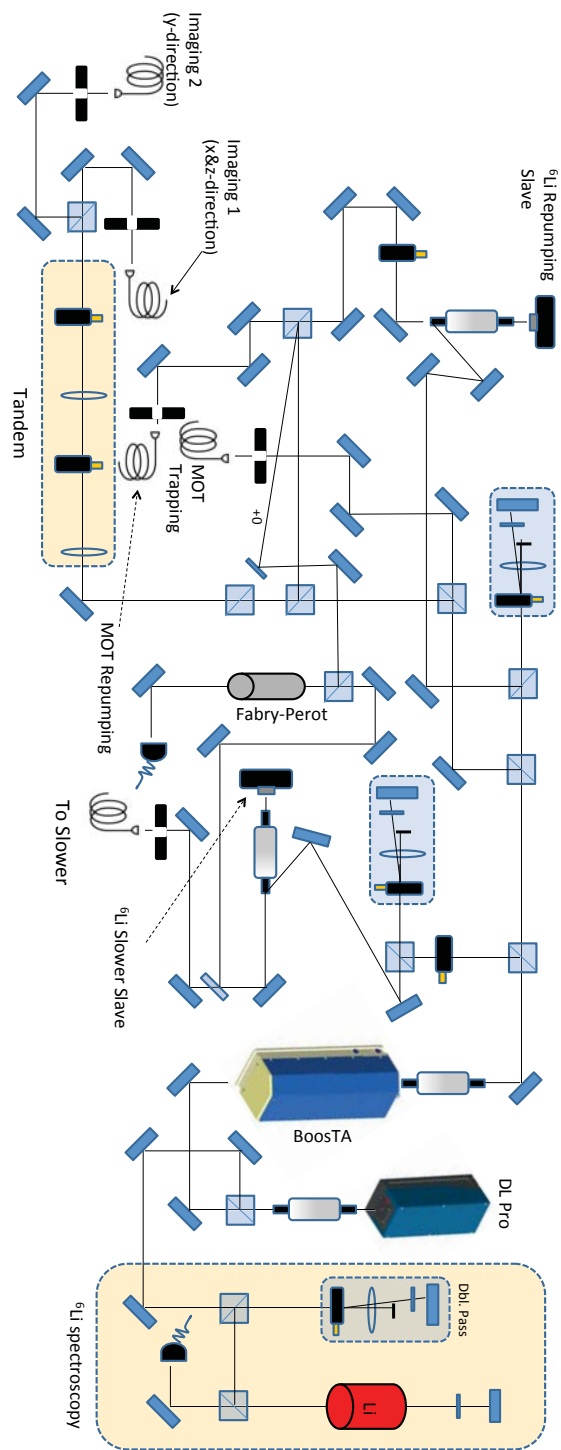


Figure C-5: Schematic of the  $^6\text{Li}$  laser system.

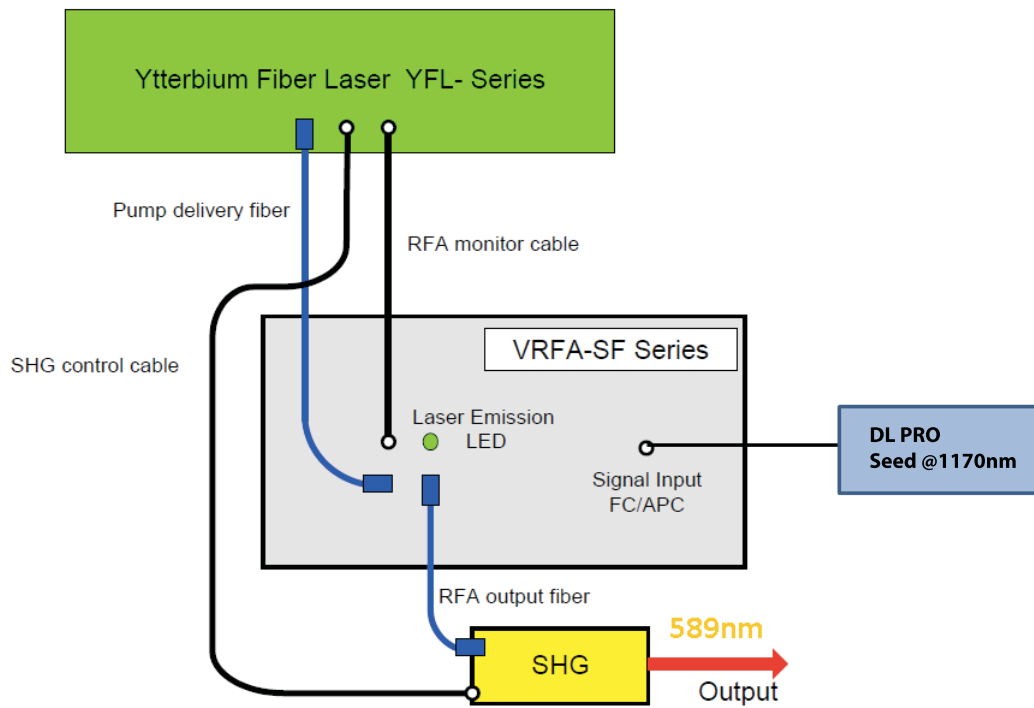


Figure C-6: Diagram of Raman Fiber Amplifier (MPBC VRFA-SF series) pumped by Ytterbium Fiber Laser (MPBC YFL series). The seed laser is a 1178 nm TOPTICA DL Pro grating stabilized diode laser.

# Appendix D

## Published journal articles

1. Observation of Fermi Polarons in a Tunable Fermi Liquid of Ultracold Atoms, PRL **102**, 230402 (2009)
2. Strongly Interacting Isotopic Bose-Fermi Mixture Immersed in a Fermi Sea, PRA **84**, 011601(R) (2011)
3. Quantum Degenerate Bose-Fermi Mixture of Chemically Different Atomic Species with Widely Tunable Interactions, PRA **85**, 051602(R) (2011)
4. Ultracold Fermionic Feshbach Molecules of  $^{23}\text{Na}^{40}\text{K}$  , PRL **109**, 085301 (2012)



## Observation of Fermi Polarons in a Tunable Fermi Liquid of Ultracold Atoms

André Schirotzek, Cheng-Hsun Wu, Ariel Sommer, and Martin W. Zwierlein

*Department of Physics, MIT-Harvard Center for Ultracold Atoms, and Research Laboratory of Electronics, Massachusetts Institute of Technology, Cambridge, Massachusetts 02139, USA*

(Received 17 February 2009; revised manuscript received 9 April 2009; published 8 June 2009)

We have observed Fermi polarons, dressed spin-down impurities in a spin-up Fermi sea of ultracold atoms. The polaron manifests itself as a narrow peak in the impurities' rf spectrum that emerges from a broad incoherent background. We determine the polaron energy and the quasiparticle residue for various interaction strengths around a Feshbach resonance. At a critical interaction, we observe the transition from polaronic to molecular binding. Here, the imbalanced Fermi liquid undergoes a phase transition into a Bose liquid, coexisting with a Fermi sea.

DOI: [10.1103/PhysRevLett.102.230402](https://doi.org/10.1103/PhysRevLett.102.230402)

PACS numbers: 05.30.Fk, 03.75.Ss, 32.30.Bv, 67.60.Fp

The fate of a single impurity interacting with its environment determines the low-temperature behavior of many condensed matter systems. A well-known example is given by an electron moving in a crystal lattice, displacing nearby ions and thus creating a localized polarization. The electron, together with its surrounding cloud of lattice distortions, phonons, forms the lattice polaron [1]. It is a quasiparticle with an energy and mass that differ from that of the bare electron. Polarons are central to the understanding of colossal magnetoresistance materials [2], and they affect the spectral function of cuprates, the parent material of high- $T_C$  superconductors [3]. Another famous impurity problem is the Kondo effect, where immobile spin impurities give rise to an enhanced resistance in metals below the Kondo temperature [4]. In contrast to the electron moving in a phonon bath, a bosonic environment, in the latter case the impurity interacts with a fermionic environment, the Fermi sea of electrons.

Here we study a small concentration of spin-down impurities immersed in a spin-up Fermi sea of ultracold atoms. This system represents the limiting case of spin-imbalanced Fermi gases and has been recognized to hold the key to the quantitative understanding of the phase diagram of imbalanced Fermi mixtures [5–16]. Unlike in liquid  $^3\text{He}$ , the  $s$ -wave interaction potential between the impurities and the spin-up atoms in this novel spin-imbalanced Fermi liquid is attractive. The vicinity of a Feshbach resonance allows tuning of the interaction strength at will, characterized by the ratio of the interparticle distance  $\sim 1/k_F$  to the scattering length  $a$ , where  $k_F$  is the spin-up Fermi wave vector [17]. Figure 1 depicts the scenario for a single impurity: For weak attraction ( $1/k_F a \ll -1$ ) the impurity propagates freely in the spin-up medium of density  $n_1 = k_F^3/6\pi^2$  [Fig. 1(a)]. It merely experiences the familiar attractive mean field energy shift  $E_1 = 4\pi\hbar^2 a n_1/m < 0$ . However, as the attractive interaction grows, the impurity can undergo momentum changing collisions with environment atoms, and thus starts to attract its surroundings. The impurity “dressed” with the localized cloud of scattered fermions constitutes

the Fermi polaron [Fig. 1(b)]. Dressing becomes important once the mean free path  $\sim 1/n_1 a^2$  of the bare impurity in the medium becomes comparable to the distance  $\sim 1/k_F$  between environment particles or when  $(k_F a)^2 \sim 1$ . Collisions then reduce the bare impurity's probability of free propagation, the quasiparticle residue  $Z$ , from unity. The dressed impurity can instead move freely through the environment, with an energy  $E_1$  shifted away from the simple mean field result. This polaronic state is stable until, for strong attraction ( $1/k_F a \sim 1$ ), equivalent to a deep effective potential well, the spin-down impurity will bind exactly one spin-up atom, thus forming a tightly bound molecule [Fig. 1(c)]. This molecule is itself a dressed impurity, albeit a bosonic one [13].

To prepare and observe Fermi polarons, we start with a spin-polarized cloud of  $^6\text{Li}$  atoms in the lowest hyperfine state  $|1\rangle$  (spin-up), confined in a cylindrically symmetric optical trap (125  $\mu\text{m}$  waist, 145 Hz/22.3 Hz radial/axial trapping frequency) at a magnetic field of 690 G [17]. A two-photon Landau-Zener sweep transfers a small fraction into state  $|3\rangle$  (spin-down), and further cooling results in a cloud containing 2%  $|3\rangle$  impurities immersed in a degenerate Fermi gas of  $5 \times 10^6$   $|1\rangle$  atoms at a temperature  $T = 0.14(3)T_F$ , where  $T_F$  is the Fermi temperature. A 100 G wide Feshbach resonance for scattering between these states is centered at 690 G. For various fields around the

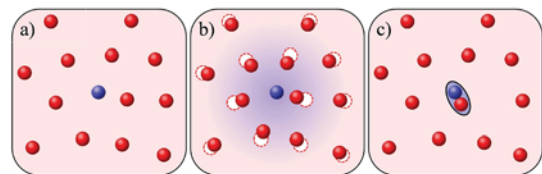


FIG. 1 (color online). From polarons to molecules. (a) For weak attraction, an impurity (blue) experiences the mean field of the medium (red). (b) For stronger attraction, the impurity surrounds itself with a localized cloud of environment atoms, forming a polaron. (c) For strong attraction, molecules of size  $a$  form despite Pauli blocking of momenta  $\hbar k < \hbar k_F \ll \hbar/a$  by the environment.

resonance, we perform rf spectroscopy on the impurity species  $|3\rangle$  and on the environment particles in  $|1\rangle$  by transferring atoms into the empty state  $|2\rangle$ , accessible to either hyperfine state. This state is sufficiently weakly interacting with the initial states to allow a direct interpretation of the resulting spectra [18]. As in previous work, spectra are spatially resolved and tomographically 3D reconstructed [19] via an inverse Abel transform, and are thus local and free from broadening due to density inhomogeneities. In addition, phase contrast images yield the *in situ* density distribution  $n_{\uparrow}$ ,  $n_{\downarrow}$  and thus the local Fermi energy  $\epsilon_F$  of the environment atoms and the local impurity concentration  $x = \frac{n_{\downarrow}}{n_{\uparrow}}$ . The Rabi frequencies  $\Omega_R$  for the impurity and environment rf transitions are measured (on fully polarized samples) to be identical to within 5%.

Figure 2 shows the observed spectra of the spin-down impurities and that of the spin-up environment at low local impurity concentration. The bulk of the environment spectrum is found at zero offset, corresponding to the free (Zeeman plus hyperfine) energy splitting between states  $|1\rangle$  and  $|2\rangle$ . However, interactions between impurity and spin-up particles lead to a spectral contribution that is shifted: The rf photon must supply additional energy to transfer a particle out of its attractive environment into the final, noninteracting state [17]. In Fig. 2(a), impurity and environment spectra above zero offset exactly overlap, signaling two-body molecular pairing. The steep threshold gives the binding energy, the high-frequency wings arise from molecule dissociation into remnants with nonzero momentum [17,20,21]. As the attractive interaction is reduced, however, a narrow peak appears in the impurity spectrum that is not matched by the response of the environment [Figs. 2(b)–2(d)]. This narrow peak, emerging from a broad incoherent background, signals the formation of the Fermi polaron, a long-lived quasiparticle. The narrow width and long lifetime are expected: At zero temperature the zero momentum polaron has no phase space for decay and is stable. At finite kinetic energy or finite temperature  $T$  it may decay into particle-hole excitations [13], but phase space restrictions due to the spin-up Fermi sea and conservation laws imply a decay rate  $\propto (T/T_F)^2 \sim$

1% in units of the Fermi energy. Indeed, the width of the polaron peak is consistent with a delta function within the experimental resolution, as calibrated by the spectra of fully polarized clouds. The background is perfectly matched by the rf spectrum of the environment. This is expected at high rf energies  $\hbar\omega \gg \epsilon_F$  that are probing high momenta  $k \gg k_F$  and thus distances short compared to the interparticle spacing. Here, an impurity particle will interact with only one environment particle, leading to overlapping spectra.

Chevy has provided an instructive variational wave function [5,9] that captures the essential properties of the polaron, even on a quantitative level [16] when compared with Monte Carlo (MC) calculations [6,12,13]:

$$|\Psi\rangle = \varphi_0 |\mathbf{0}\rangle_{\downarrow} |FS\rangle_{\uparrow} + \sum_{|\mathbf{q}| < k_F < |\mathbf{k}|} \varphi_{\mathbf{q}\mathbf{k}} c_{\mathbf{k}\uparrow}^{\dagger} c_{\mathbf{q}\uparrow} |\mathbf{q} - \mathbf{k}\rangle_{\downarrow} |FS\rangle_{\uparrow} \quad (1)$$

The first part describes a single impurity with a well-defined wave vector ( $\mathbf{k}_{\downarrow} = \mathbf{0}$ ) that is not localized and free to propagate in the Fermi sea of up spins  $|FS\rangle_{\uparrow}$ . In the second part the impurity particle recoils off environment particles that are scattered out of the Fermi sea and leave holes behind. This describes the dressing of the impurity with particle-hole excitations. The probability of free propagation is given by the first, unperturbed part,  $Z = |\varphi_0|^2$ . According to Fermi's golden rule [11,15,17,22], the two portions of  $|\Psi\rangle$  give rise to two distinct features of the impurity rf spectrum  $\Gamma(\omega)$  ( $\omega$  is the rf offset from the bare atomic transition):

$$\Gamma(\omega) = 2\pi\hbar\Omega_R^2 Z \delta(\hbar\omega + E_{\downarrow}) + \Gamma^{\text{inc}}(\omega). \quad (2)$$

The first part in  $|\Psi\rangle$  contributes a coherent narrow quasiparticle peak to the minority spectrum. Its position is a direct measure of the polaron energy  $E_{\downarrow}$ , its integral gives the quasiparticle residue  $Z$ . The particle-hole excitations in the second part give rise to a broad, incoherent background  $\Gamma^{\text{inc}}(\omega) \propto \sum_{\mathbf{q},\mathbf{k}} |\varphi_{\mathbf{q}\mathbf{k}}|^2 \delta(\hbar\omega - \epsilon_{\mathbf{q}-\mathbf{k}} - \epsilon_{\mathbf{k}} + \epsilon_{\mathbf{q}} + E_{\downarrow})$ : The polaron energy  $E_{\downarrow}$  is released as the impurity at momentum  $\mathbf{q} - \mathbf{k}$  is transferred into the final state, leaving behind an

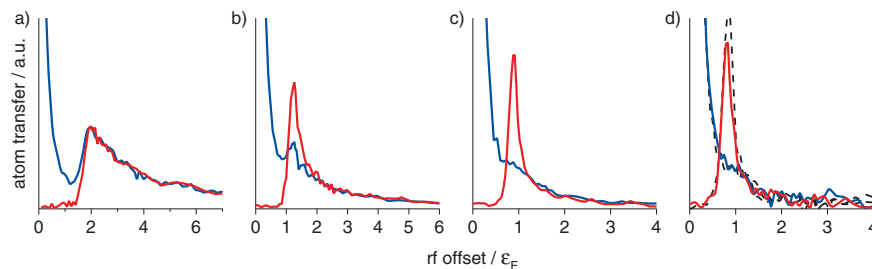


FIG. 2 (color online). rf spectroscopy on polarons. Shown are spatially resolved, 3D reconstructed rf spectra of the environment (blue, state  $|1\rangle$ ) and impurity (red, state  $|3\rangle$ ) component in a highly imbalanced spin-mixture. (a) Molecular limit; (b),(c) Emergence of the polaron, a distinct peak exclusively in the minority component. (d) At unitarity, the polaron peak is the dominant feature in the impurity spectrum, which becomes even more pronounced for  $1/k_F a < 0$  (not shown). For the spectra shown as dashed lines in (d) the roles of states  $|1\rangle$  and  $|3\rangle$  are exchanged. The local impurity concentration was  $x = 5(2)\%$  for all spectra, the interaction strengths  $1/k_F a$  were (a) 0.76(2), (b) 0.43(1), (c) 0.20(1), and (d) 0 (unitarity).

environment particle in  $\mathbf{k}$  above and a hole within the Fermi sea at  $\mathbf{q}$  [22]. These two spectral features are recovered in theoretical rf spectra for a finite number of impurities, i.e., a Fermi liquid [15,23]. For our analysis we do not rely on a theoretical fit to the spectra.

To measure the polaron energy  $E_l$ , we determine the peak position of the impurity spectrum as a function of the local interaction parameter  $1/k_F a$ . The data for 5% impurity concentration are shown in Fig. 3(a), along with the variational upper bound given by the wave function Eq. (1) [22] and the diagrammatic MC calculation of [13]. As final state interactions are weak, they can be included as a simple repulsive mean field shift  $4\pi\hbar^2 a_{fe} n_l / m$ , with  $a_{fe}$  the scattering length between the final state and the environment atoms [24]. Polaron energies have been predicted via the variational ansatz [5], the  $T$ -matrix approach [9,10,15,16], the  $1/N$  expansion [11], fixed-node MC [6,12] and diagrammatic MC calculations [13]. With the exception of the  $1/N$  expansion, these all agree with each other and with the present experiment to within a few percent. In particular, in the unitarity limit where  $1/k_F a = 0$  we find a polaron energy of  $E_l = -0.64(7)\epsilon_F$  ( $-0.72(9)\epsilon_F$ ) when state  $|3\rangle$  ( $|1\rangle$ ) serves as the impurity [25]. This agrees well with the diagrammatic MC calculation,  $-0.615\epsilon_F$  [14], and the analytical result  $-0.6156(2)\epsilon_F$  [16]. Analy-

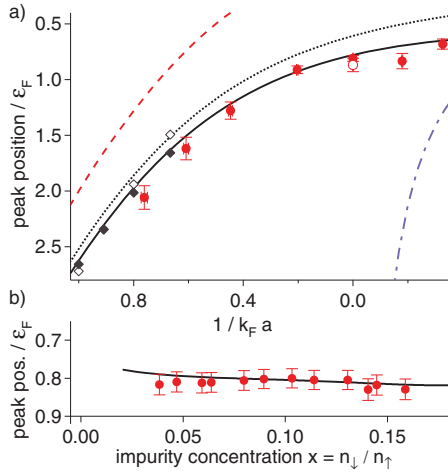


FIG. 3 (color online). Peak position of the impurity spectrum as a measure of the polaron energy  $E_l$ . (a) peak position for various interaction strengths in the limit of low concentration  $x = 5(2)\%$  (solid circles). Open circle: Reversed roles of impurity and environment. Dotted line: polaron energy from variational ansatz Eq. (1) [5], the solid line including weak final state interactions. Dashed line: Energy of a bare, isolated molecule in vacuum. Blue dash-dotted line: Mean field limit for the energy of an impurity atom. Solid (open) diamonds: Diagrammatic MC energy of the polaron (molecule) [13]. (b) Peak position at unitarity ( $1/k_F a = 0$ ) as a function of impurity concentration (solid circles). The line shows the expected peak position,  $\hbar\omega_p / \epsilon_F = A + (1 - \frac{m}{m^*})x^{2/3} - \frac{6}{5}Fx + \frac{4}{3\pi}k_F a_{fe}$ , using the MC value  $A = 0.615$  [13], the analytic result  $m^* = 1.2$  [16], the weak repulsion between polarons with  $F = 0.14$  [12] and weak final state interactions with scattering length  $a_{fe}$ .

sis of experimental density profiles yields a value of  $-0.58(5)\epsilon_F$  [26].

The relatively large value for  $E_l$  directly implies that the normal state, modeled as a Fermi sea of weakly interacting polarons, is favored over the superfluid state up to a critical concentration (44%), much higher than that predicted by mean field theories (4%) [27]. These neglect interactions in the normal state and therefore imply a polaron binding energy of zero.

We have so far considered the limit of few impurities. By increasing their density, we can study the effect of interactions between polarons. In Fig. 3(b) we show that the quasiparticle peak position depends only weakly on the impurity concentration in the unitarity limit. Polarons are thus weakly interacting quasiparticles, despite the strong interactions between the bare impurity and its environment.

The peak position could be modified due to the effective mass  $m^*$  of polarons, larger than the mass of the bare impurity. Transfer of a moving polaron into the free final state then requires additional kinetic energy. This leads to an upshift and a broadening on the order of the Fermi energy difference between initial and final state,  $x^{2/3}\epsilon_F(1 - \frac{m}{m^*})$ . On resonance, this is  $0.04\epsilon_F$  for  $x = 0.1$ . The effect could be partially masked by the predicted weak repulsion between polarons [12] that would downshift the resonance frequency by  $-0.02\epsilon_F$  for  $x = 0.1$ .

The spectral weight of the polaron peak directly gives the quasiparticle residue  $Z$ , a defining parameter of a Fermi liquid. Experimentally, we determine the area under the impurity peak that is not matched by the environment's

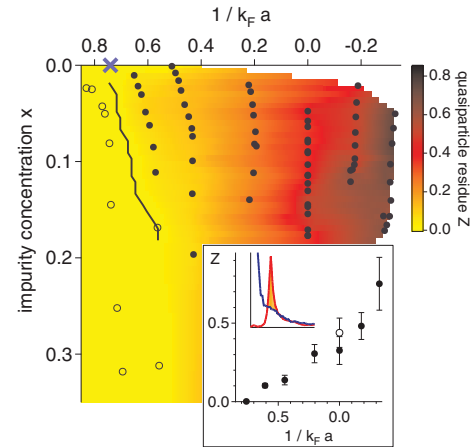


FIG. 4 (color online). Quasiparticle residue  $Z$  as a function of interaction strength and impurity concentration. The color coding indicates the magnitude of  $Z$  and is an interpolation of the data points shown in the graph. Open circles: Data points consistent with zero ( $Z < 0.03$ ), solid circles:  $Z > 0.03$ , the solid line marking the onset of  $Z$ . Blue cross: Critical interaction strength for the Fermi liquid—molecular BEC transition for  $x \rightarrow 0$  [12]. Inset:  $Z$  as a function of interaction strength in the limit of low impurity concentration  $x = 5(2)\%$ . Open circle: Reversed roles,  $|1\rangle$  impurity in  $|3\rangle$  environment. The spectrum in the inset illustrates the determination of  $Z$  [22].

response and divide by the total area under the impurity spectrum (see spectrum in Fig. 4 and [22]). Figure 4 presents  $Z$  as a function of interaction strength and impurity concentration  $x$ , the inset shows  $Z$  for  $x = 5\%$ . As expected,  $Z$  approaches 100% for weak attractive interaction  $k_F a \rightarrow 0^-$ , where the bare impurity only rarely recoils off environment atoms. As the mean free path shortens and the bare impurity starts to surround itself with environment atoms  $Z$  decreases. On resonance, we find  $Z = 0.39(9)$  for  $x = 5\%$ , with only a weak dependence on  $x$  (Fig. 4). Theoretical values for  $Z$  vary: ansatz Eq. (1) predicts  $Z = 0.78$  for a single impurity, while Ref. [11] predicts  $Z = 0.47$  (0.30) for vanishing (5%) impurity concentration. Our procedure might yield a lower bound on the actual value of  $Z$ , as the incoherent part of the impurity spectrum might be depleted around threshold. Eventually, for strong attraction between the impurity and particles of the medium,  $Z$  vanishes and we observe complete overlap of the impurity and environment spectra. This signals the formation of a two-body bound state between the impurity and exactly one environment atom. For a spin-down concentration of 5% we determine the critical interaction strength where the polaron peak vanishes to be  $1/(k_F a)_c = 0.76(2)$ . This is in good agreement with the independently determined critical interaction  $1/k_F a = 0.74(4)$  beyond which one finds a superfluid even for the smallest impurity concentration [28]. This is a multicritical point [12,13,29] where a Fermi liquid of weakly interacting polarons undergoes a phase transition into a Bose liquid of molecular impurities. Fixed-node MC calculations place this transition at a value of  $1/k_F a = 0.73$  for  $x \rightarrow 0$  [12]. Our  $1/(k_F a)_c$  is lower than the value 0.90(2) from diagrammatic MC [13] for a single impurity. Ansatz Eq. (1) does not predict a transition, as it does not test for the formation of molecules. In Fig. 4, the color coding reveals where molecular behavior is observed (yellow), and where the spectra show polaronic behavior (red to black). It can be seen that the critical interaction strength for the formation of molecules depends only weakly on the impurity concentration  $x$ .

In conclusion, we have observed Fermi polarons in a novel, attractive Fermi liquid of spin-down impurity atoms immersed in a spin-up Fermi sea. The energy and residue of this quasiparticle was determined and interactions between quasiparticles were found to be weak. Polarons thus emerge as the quasiparticles of a Landau Fermi liquid description of this strongly interacting Fermi mixture. To study first the impurity limit of  $N + 1$  interacting particles before dealing with the full  $N + M$  many-body system will be a fruitful approach for other strongly correlated systems realized with cold atoms. An intriguing question is how the limit of a weakly interacting polaron liquid containing few impurities connects to the physics of a hydrodynamic, balanced Fermi gas containing Cooper pair fluctuations above the critical temperature for superfluidity. In light of our findings, fermion pair condensation could be viewed as condensation of pairs of polarons with opposite spin. This is also suggested by the large normal state interaction

measured by quasiparticle spectroscopy on the superfluid state [30].

We would like to thank W. Ketterle, M. Randeria, S. Stringari, B. Svistunov, S. Todadri, and W. Zwerger for helpful discussions, and Aviv Keshet for the computer control system. This work was supported by the NSF, an AFOSR-MURI, and the Alfred P. Sloan Foundation.

- 
- [1] L. Landau, Phys. Z. Sowjetunion **3**, 644 (1933).
  - [2] N. Mannella *et al.*, Nature (London) **438**, 474 (2005).
  - [3] P. A. Lee, N. Nagaosa, and X.-G. Wen, Rev. Mod. Phys. **78**, 17 (2006).
  - [4] J. Kondo, Prog. Theor. Phys. **32**, 37 (1964).
  - [5] F. Chevy, Phys. Rev. A **74**, 063628 (2006).
  - [6] C. Lobo *et al.*, Phys. Rev. Lett. **97**, 200403 (2006).
  - [7] C. Schunck *et al.*, Science **316**, 867 (2007).
  - [8] A. Bulgac and M. M. Forbes, Phys. Rev. A **75**, 031605(R) (2007).
  - [9] R. Combescot *et al.*, Phys. Rev. Lett. **98**, 180402 (2007).
  - [10] M. Punk and W. Zwerger, Phys. Rev. Lett. **99**, 170404 (2007).
  - [11] M. Veillette *et al.*, Phys. Rev. A **78**, 033614 (2008).
  - [12] S. Pilati and S. Giorgini, Phys. Rev. Lett. **100**, 030401 (2008).
  - [13] N. V. Prokof'ev and B. V. Svistunov, Phys. Rev. B **77**, 020408(R) (2008).
  - [14] N. V. Prokof'ev and B. V. Svistunov, Phys. Rev. B **77**, 125101 (2008).
  - [15] P. Massignan, G. M. Bruun, and H. T. C. Stoof, Phys. Rev. A **78**, 031602(R) (2008).
  - [16] R. Combescot and S. Giraud, Phys. Rev. Lett. **101**, 050404 (2008).
  - [17] W. Ketterle and M. Zwierlein, in *Proceedings of the International School of Physics "Enrico Fermi", Course CLXIV*, edited by M. Inguscio, W. Ketterle, and C. Salomon (IOS Press, Amsterdam, 2008), p. 95.
  - [18] C. H. Schunck *et al.*, Nature (London) **454**, 739 (2008).
  - [19] Y. Shin *et al.*, Phys. Rev. Lett. **99**, 090403 (2007).
  - [20] C. A. Regal *et al.*, Nature (London) **424**, 47 (2003).
  - [21] We do not observe Pauli blocking effects proposed in [15].
  - [22] See EPAPS Document No. E-PRLTAO-102-040923. For more information on EPAPS, see <http://www.aip.org/pubservs/epaps.html>.
  - [23] W. Schneider, V. B. Shenoy, and M. Randeria, arXiv:0903.3006.
  - [24] The next order correction due to incoherent scattering, where  $a_{\text{fe}}$  is replaced by the full real part of the scattering amplitude, is of order  $(k_F a_{\text{fe}})^2 \approx 5\%$  and thus negligible.
  - [25] Switching roles of states |1> and |3> tests for the influence of final state interactions. They contribute  $E_f = 0.17(1)\epsilon_F$  [0.13(1) $\epsilon_F$ ] to the peak position when state |3> (|1>) serves as the impurity.
  - [26] Y. Shin, Phys. Rev. A **77**, 041603(R) (2008).
  - [27] D. E. Sheehy and L. Radzihovsky, Ann. Phys. (N.Y.) **322**, 1790 (2007).
  - [28] Y. Shin *et al.*, Phys. Rev. Lett. **101**, 070404 (2008).
  - [29] S. Sachdev and K. Yang, Phys. Rev. B **73**, 174504 (2006).
  - [30] A. Schirotzek *et al.*, Phys. Rev. Lett. **101**, 140403 (2008).

# Supplemental Material: “Observation of Fermi Polarons in a Tunable Fermi Liquid of Ultracold Atoms”

André Schirotzek, Cheng-Hsun Wu, Ariel Sommer, and Martin W. Zwierlein

*Department of Physics, MIT-Harvard Center for Ultracold Atoms, and Research Laboratory of Electronics, Massachusetts Institute of Technology, Cambridge, Massachusetts 02139, USA*

(Dated: May 1, 2009)

In this supplemental material we state, starting with the variational Ansatz by Chevy, key properties of the polaron, such as the energy  $E_\downarrow$  and the quasiparticle residue  $Z$ , and we calculate its RF spectrum using Fermi’s Golden Rule. We connect this approach and its implication for finite impurity concentration to the results of Fermi liquid theory and the T-matrix formalism used in [1–4]. Furthermore, details are provided about the extraction of the quasiparticle residue  $Z$ .

## Polaron wavefunction, energy and quasiparticle residue

We start with the hamiltonian for a dilute two component mixture of fermionic atoms interacting via the van-der-Waals potential  $V(\mathbf{r})$  [5]. Thanks to the diluteness of the system, the potential is of short range  $R$  compared to the interparticle distance  $1/k_F$ , so  $k_F R \ll 1$ . Its Fourier transform  $V(\mathbf{k})$  is thus essentially constant,  $g_0$ , below  $k_F$  and rolls off to zero at a momentum on the order of  $1/R \gg k_F$ . The many-body Hamiltonian for the system is then

$$\hat{H} = \sum_{\mathbf{k}, \sigma} \epsilon_{\mathbf{k}} c_{\mathbf{k}\sigma}^\dagger c_{\mathbf{k}\sigma} + \frac{g_0}{\mathcal{V}} \sum_{\mathbf{k}, \mathbf{k}', \mathbf{q}} c_{\mathbf{k}+\frac{\mathbf{q}}{2}\uparrow}^\dagger c_{-\mathbf{k}+\frac{\mathbf{q}}{2}\downarrow}^\dagger c_{\mathbf{k}'+\frac{\mathbf{q}}{2}\downarrow} c_{-\mathbf{k}'+\frac{\mathbf{q}}{2}\uparrow} \quad (1)$$

Here, the label  $\sigma$  denotes the spin state  $\uparrow, \downarrow$ ,  $\epsilon_{\mathbf{k}} = \hbar^2 k^2 / 2m$ ,  $\mathcal{V}$  is the volume of the system and the  $c_{\mathbf{k}\sigma}^\dagger, c_{\mathbf{k}\sigma}$  are the usual creation and annihilation operators for fermions with momentum  $\mathbf{k}$  and spin  $\sigma$ . The trial wavefunction for the Fermi polaron with zero momentum proposed by F. Chevy in [6] is

$$|\Psi\rangle = \varphi_0 |0\rangle_\downarrow |FS\rangle_\uparrow + \sum_{\substack{k > k_F \\ q < k_F}} \varphi_{\mathbf{k}\mathbf{q}} c_{\mathbf{k}\uparrow}^\dagger c_{\mathbf{q}\uparrow} | \mathbf{q} - \mathbf{k} \rangle_\downarrow |FS\rangle_\uparrow \quad (2)$$

The energy is then minimized under variation of the parameters  $\varphi_0$  and  $\varphi_{\mathbf{k}\mathbf{q}}$ , with the constraint of constant norm  $\langle \Psi | \Psi \rangle = |\varphi_0|^2 + \sum_{q < k_F}^{k > k_F} |\varphi_{\mathbf{k}\mathbf{q}}|^2 = 1$ . That is, the quantity to minimize is  $\langle \Psi | \hat{H} | \Psi \rangle - E_\downarrow \langle \Psi | \Psi \rangle$ . The derivation can be found in [6], here we quote the result for the particle-hole excitation amplitudes  $\varphi_{\mathbf{k}\mathbf{q}}$ , the quasiparticle weight  $|\varphi_0|^2 = Z$ , and the energy  $E_\downarrow$  due to addition of the down spin impurity:

$$\varphi_{\mathbf{k}\mathbf{q}} = \varphi_0 \frac{1}{\mathcal{V}} \frac{f(E_\downarrow, \mathbf{q})}{E_\downarrow - \epsilon_{\mathbf{k}} + \epsilon_{\mathbf{q}} - \epsilon_{\mathbf{q}-\mathbf{k}}} \quad (3)$$

$$\frac{1}{|\varphi_0|^2} \equiv \frac{1}{Z} = \left( 1 - \frac{\partial}{\partial E} \frac{1}{\mathcal{V}} \sum_{q < k_F} f(E, \mathbf{q}) \right)_{E=E_\downarrow} \quad (4)$$

$$E_\downarrow = \frac{1}{\mathcal{V}} \sum_{q < k_F} f(E_\downarrow, \mathbf{q}) \quad (5)$$

These all depend on the function  $f(E, \mathbf{q})$  with

$$f^{-1}(E, \mathbf{q}) = \frac{1}{g_0} + \frac{1}{\mathcal{V}} \sum_{k > k_F} \frac{1}{\epsilon_{\mathbf{k}} - \epsilon_{\mathbf{q}} + \epsilon_{\mathbf{q}-\mathbf{k}} - E} \quad (6)$$

It is a measure of the interaction strength between spin up and spin down, modified by the presence of the spin up Fermi sea. As usual,  $g_0$  can be replaced by the physically observable scattering length  $a$  for collisions between spin up and down via [5]  $\frac{1}{g_0} = \frac{m}{4\pi\hbar^2 a} - \frac{1}{\mathcal{V}} \sum_{\mathbf{k}} \frac{1}{2\epsilon_{\mathbf{k}}}$ .

$$f^{-1}(E, \mathbf{q}) = \frac{mk_F}{2\pi^2\hbar^2} \left( \frac{\pi}{2k_F a} - 1 \right) + \frac{1}{\mathcal{V}} \sum_{k > k_F} \left( \frac{1}{\epsilon_{\mathbf{k}} - \epsilon_{\mathbf{q}} + \epsilon_{\mathbf{q}-\mathbf{k}} - E} - \frac{1}{2\epsilon_{\mathbf{k}}} \right) \quad (7)$$

The integral in above expression is convergent and gives

$$f^{-1}(E, \mathbf{q}) = \frac{mk_F}{2\pi^2\hbar^2} \left\{ \frac{\pi}{2k_F a} - 1 + I \left( \frac{E}{E_F}, \frac{q}{k_F} \right) \right\} \quad (8)$$

$$I(\epsilon, y) = \int_1^\infty dx \left( \frac{x}{2y} \ln \left( \frac{2x^2 + 2xy - \epsilon}{2x^2 - 2xy - \epsilon} \right) - 1 \right)$$

An analytic expression for the integral exists but does not provide additional insight. The equation for  $E_\downarrow$  becomes

$$\frac{E_\downarrow}{E_F} = -2 \int_0^1 dy \frac{y^2}{1 - \frac{\pi}{2k_F a} - I \left( \frac{E_\downarrow}{E_F}, y \right)} \quad (9)$$

This implicit equation for  $E_\downarrow$  can be easily solved numerically. The result is shown as the dashed line in Fig. 3 of the main paper. Clearly,  $E_\downarrow$  is negative due to the attractive interactions with the medium. In the weakly interacting limit  $1/k_F a \rightarrow -\infty$ , we can neglect the integral in the denominator and immediately obtain  $E_\downarrow = \frac{2}{3} \frac{2k_F a}{\pi} E_F = 4\pi\hbar^2 a n_\uparrow / m$ , which is the mean field result [7].

The approach turns out to be equivalent to a T-Matrix description, as shown in [7]. In that language,  $f(E, \mathbf{q})$

is (up to a constant) the scattering amplitude in the medium (i.e. the vertex) for the scattering process with total energy and momentum  $E$  and  $q$  of the colliding particles.  $\Sigma(\mathbf{0}, E) \equiv \frac{1}{V} \sum_{q < k_F} f(E_\downarrow + E, \mathbf{q})$  is the self-energy at zero momentum and frequency  $E/\hbar$ . It is real in this approximation. The expression for the quasiparticle residue  $Z$  of a *single* spin down impurity in Eq. 4 is immediately seen to be equivalent to the well-known relation [3]

$$Z_\downarrow^{-1} = \left( 1 - \frac{\partial}{\partial E} \text{Re} \Sigma(k_{F\downarrow}, E) \right)_{E=0} \quad (10)$$

for a spin down quasiparticle on top of a spin down Fermi sea, in the limit of vanishing Fermi momentum  $k_{F\downarrow}$ .

### RF spectrum from the variational Ansatz

Fermi's Golden Rule allows us to directly predict the shape of the impurity RF spectrum. This topic has been studied in detail since the early days of RF spectroscopy, and for the problem of highly imbalanced Fermi gases in [1–4], among others. Chevy's wavefunction offers a simple way of calculating the RF spectrum of a single impurity.

The RF operator  $\hat{V} = \hbar\Omega_R \sum_k c_{k,f}^\dagger c_{k,\downarrow} + h.c.$  promotes the impurity into the free final state  $|f\rangle$  (energy  $E_f$ ) without momentum transfer [5]. In the experiment, the final internal state is the second lowest hyperfine state of  ${}^6\text{Li}$ . Fermi's Golden Rule for the impurity starting in state  $|\Psi\rangle$  is

$$\Gamma(\omega) = \frac{2\pi}{\hbar} \sum_f \left| \langle f | \hat{V} | \Psi \rangle \right|^2 \delta(\hbar\omega - (E_f - E_\downarrow)) \quad (11)$$

Where  $\omega$  is the RF offset from the bare atomic transition frequency between the internal states labeled by  $\downarrow$  and  $f$ . One possible final state is  $|0\rangle \equiv |0\rangle_f |FS\rangle_\uparrow$ , i.e. a zero momentum particle in the final state plus a perfect Fermi sea of up spins, with energy  $E_{|0\rangle} = 0$  relative to the Fermi energy  $E_F$  of the environment. Other possible final states are  $|\mathbf{q}, \mathbf{k}\rangle \equiv |\mathbf{q} - \mathbf{k}\rangle_f c_{\mathbf{k}\uparrow}^\dagger c_{\mathbf{q}\uparrow} |FS\rangle_\uparrow$  with  $q < k_F$  and  $k > k_F$ , i.e. a particle with momentum  $\mathbf{q} - \mathbf{k}$  in the final state and a Fermi sea with a hole at  $\mathbf{q}$  and an excited environment particle above the Fermi sea at  $\mathbf{k}$ . The energy of these states is  $E_{|\mathbf{q}, \mathbf{k}\rangle} = \epsilon_{\mathbf{k}} - \epsilon_{\mathbf{q}} + \epsilon_{\mathbf{q} - \mathbf{k}}$  relative to the environment Fermi energy  $E_F$ . The matrix elements are

$$\begin{aligned} \langle 0 | \hat{V} | \Psi \rangle &= \hbar\Omega_R \varphi_0 \\ \langle \mathbf{q}, \mathbf{k} | \hat{V} | \Psi \rangle &= \hbar\Omega_R \varphi_{\mathbf{k}\mathbf{q}} \end{aligned}$$

This leaves us with two components in the RF spectrum:

$$\Gamma(\omega) = 2\pi\hbar\Omega_R^2 \left( Z\delta(\hbar\omega + E_\downarrow) + \sum_{q < k_F}^{k > k_F} |\varphi_{\mathbf{k}\mathbf{q}}|^2 \delta(\hbar\omega + E_\downarrow - \epsilon_{\mathbf{k}} + \epsilon_{\mathbf{q}} - \epsilon_{\mathbf{q} - \mathbf{k}}) \right) \quad (12)$$

The first part is a delta-peak shifted by the quasiparticle energy. As  $E_\downarrow < 0$ , it is shifted to higher frequencies: The RF photon has to supply additional energy to transfer the impurity out of its attractive environment. The weight of this peak is  $Z$ , the quasiparticle residue, allowing the experimental determination of  $Z$  by simply integrating the area under the prominent peak. Such a delta-peak is typically called "coherent", as a broadband excitation around this energy would not dephase over time. The second part of the spectrum is incoherent, it consists of a broad continuum of frequencies. Broadband excitations of this continuum would rapidly dephase, over a timescale given by the inverse width of the continuum.

### RF spectrum in Fermi Liquid theory

This structure of the RF spectrum is a generic feature of quasiparticle spectra. In Fermi liquid theory, the propagator of a quasiparticle is approximated as a pole at energy  $E(k) > 0$  (relative to the ground state energy), lifetime  $1/\gamma(k)$  and residue  $Z$  plus an incoherent spectrum [3, 8]

$$G_-^R(\mathbf{k}, \omega) = \frac{Z}{\hbar\omega + E(k) + i\hbar\gamma(k)} + G_-^{R,\text{inc}}(\mathbf{k}, \omega) \quad (13)$$

The spectral function is given by  $A_-(\mathbf{k}, \omega) = -\frac{1}{\pi} \text{Im} G_-^R(\mathbf{k}, \omega) = Z \frac{1}{\pi} \frac{\hbar\gamma(k)}{(\hbar\omega + E(k))^2 + \hbar^2\gamma(k)^2} + A_-^{\text{inc}}(\mathbf{k}, \omega)$  which tends to

$$A_-(\mathbf{k}, \omega) = Z\delta(\hbar\omega + E(k)) + A_-^{\text{inc}}(\mathbf{k}, \omega) \quad (14)$$

in the limit of small damping of the quasiparticle.  $A_-(\mathbf{k}, \omega)$  measures the probability that removing a particle with momentum  $\mathbf{k}$  will cost an energy  $-\hbar\omega$ . The RF spectrum in linear response is given by [2]

$$\Gamma(\omega) = 2\pi\hbar\Omega_R^2 \sum_k A_-(\mathbf{k}, \epsilon_{\mathbf{k}} - \mu - \hbar\omega) n_F(\epsilon_{\mathbf{k}} - \mu - \hbar\omega) \quad (15)$$

where  $\mu$  is the chemical potential of the quasiparticle and  $n_F(x) = 1/(e^{\beta x} + 1)$  is the Fermi function that tends to  $\theta(-x)$  at zero temperature. This is intuitively understood: For a given momentum  $\mathbf{k}$ , the RF photon with energy  $\hbar\omega$  has to provide the energy  $\epsilon_{\mathbf{k}} - \mu$  (relative to the initial chemical potential  $\mu$ ) to create a free particle in the final state. The rest,  $\hbar\omega - \epsilon_{\mathbf{k}} + \mu$ , is used to remove a particle from the initial state (probability  $A_-(\mathbf{k}, \epsilon_{\mathbf{k}} - \mu - \hbar\omega)$ ) if there exists such a particle (factor

$n_F(\epsilon_{\mathbf{k}} - \mu - \hbar\omega)$ ). Eq. 15 is equivalent to Fermi's Golden Rule Eq. 11 [9]. In the case where the spectral function is dominated by a quasiparticle peak, the spectrum becomes

$$\Gamma(\omega) = 2\pi\hbar\Omega_R^2 Z \sum_k \delta(\epsilon_{\mathbf{k}} + E(k) - \mu - \hbar\omega) \times n_F(\epsilon_{\mathbf{k}} - \mu - \hbar\omega) + \Gamma^{\text{inc}}(\omega) \quad (16)$$

Connecting to our case of a single quasiparticle with  $\mu = E_{\downarrow}$  and  $k = 0$ , this directly gives

$$\Gamma(\omega) = 2\pi\hbar\Omega_R^2 Z \delta(\hbar\omega + E_{\downarrow}) + \Gamma^{\text{inc}}(\omega) \quad (17)$$

identical to the prediction via the trial wavefunction.

### Polaron spectral function

To connect the single particle and the Fermi liquid description, we calculate the propagator  $G_-^R(\mathbf{k}, \omega)$  for the removal of a single spin down impurity from the wavefunction  $|\Psi\rangle$ . By definition,

$$iG_-^R(\mathbf{k}, t) = \langle \Psi | c_{\mathbf{k}\downarrow}^{\dagger} e^{i\hat{H}t/\hbar} c_{\mathbf{k}\downarrow} | \Psi \rangle \theta(t) \quad (18)$$

Inserting a complete set of eigenstates, this gives

$$iG_-^R(\mathbf{k}, t) = \sum_f |\langle f | c_{\mathbf{k}\downarrow} | \Psi \rangle|^2 e^{iE_f t/\hbar} \theta(t) \quad (19)$$

The state  $c_{\mathbf{k}\downarrow} | \Psi \rangle$  is void of any spin down impurity and has non-vanishing matrix elements only with either the unperturbed spin up Fermi sea,  $|FS\rangle_{\uparrow}$  (if  $\mathbf{k} = \mathbf{0}$ ), or with particle-hole excitations  $|\mathbf{q}, \mathbf{k}'\rangle = c_{\mathbf{k}'\uparrow}^{\dagger} c_{\mathbf{q}\uparrow} |FS\rangle_{\uparrow}$  (in the case  $\mathbf{k} = \mathbf{q} - \mathbf{k}'$ ). These matrix elements are  $\varphi_0 = \sqrt{Z}$  and  $\varphi_{\mathbf{k}'\mathbf{q}}$  resp., the corresponding energies  $E_f = 0$  and  $E_f = \epsilon_{\mathbf{k}'} - \epsilon_{\mathbf{q}}$  relative to  $E_F$ . So one has:

$$iG_-^R(\mathbf{k}, t) = (Z\delta_{\mathbf{k},\mathbf{0}} + \sum_{\substack{k' > k_F \\ q < k_F}} \delta_{\mathbf{k},\mathbf{q}-\mathbf{k}'} |\varphi_{\mathbf{k}'\mathbf{q}}|^2 e^{i(\epsilon_{\mathbf{k}'} - \epsilon_{\mathbf{q}})t/\hbar}) \theta(t)$$

Finally,  $G_-^R(\mathbf{k}, \omega) = \frac{Z}{\hbar\omega + i\eta} \delta_{\mathbf{k},\mathbf{0}} + G_-^{R,\text{inc}}(\mathbf{k}, \omega)$  with infinitesimal  $\eta > 0$ . This is just the Fermi liquid form of  $G_-^R$  but for a single quasiparticle with zero momentum ( $E(0) = 0$  in (13)), as described by  $|\Psi\rangle$ . The spectral function is

$$A_-(\mathbf{k}, \omega) = Z\delta(\hbar\omega)\delta_{\mathbf{k},\mathbf{0}} + \sum_{\substack{k' > k_F \\ q < k_F}} \delta_{\mathbf{k},\mathbf{q}-\mathbf{k}'} |\varphi_{\mathbf{k}'\mathbf{q}}|^2 \delta(\hbar\omega + \epsilon_{\mathbf{k}'} - \epsilon_{\mathbf{q}})$$

With Eq. 15 this exactly gives the RF spectrum of Eq. 12.

### Calculation of the incoherent background

Using Eq. 3, we can write the incoherent part of the spectrum as:

$$\begin{aligned} \Gamma^{\text{inc}}(\omega) &\equiv 2\pi\hbar\Omega_R^2 \sum_{\substack{k > k_F \\ q < k_F}} |\varphi_{\mathbf{k}\mathbf{q}}|^2 \delta(\hbar\omega + E_{\downarrow} - \epsilon_{\mathbf{k}} + \epsilon_{\mathbf{q}} - \epsilon_{\mathbf{q}-\mathbf{k}}) \\ &= \frac{2\pi\Omega_R^2}{\hbar} \frac{Z}{\omega^2} \frac{1}{\mathcal{V}^2} \sum_{\substack{k > k_F \\ q < k_F}} f(E_{\downarrow}, \mathbf{q})^2 \delta(\hbar\omega + E_{\downarrow} - \epsilon_{\mathbf{k}} + \epsilon_{\mathbf{q}} - \epsilon_{\mathbf{q}-\mathbf{k}}) \end{aligned}$$

The integral over  $\mathbf{k}$  exists in analytic form:

$$\begin{aligned} \frac{1}{\mathcal{V}} \sum_{k > k_F} \delta(\hbar\omega + E_{\downarrow} - \epsilon_{\mathbf{k}} + \epsilon_{\mathbf{q}} - \epsilon_{\mathbf{q}-\mathbf{k}}) &= \\ &= \frac{mk_F}{8\pi^2\hbar^2} K\left(\frac{\hbar\omega + E_{\downarrow}}{2E_F}, \frac{q}{k_F}\right) \\ \text{with } K(\epsilon, y) &= \begin{cases} \frac{y_+^2 - y_-^2}{y} & \text{for } y_- > 1, \\ \frac{y_+^2 - 1}{y} & \text{for } y_- < 1 < y_+, \\ 0 & \text{for } 1 > y_+. \end{cases} \\ \text{and } y_{\pm} &= \pm \frac{y}{2} + \sqrt{\frac{y^2}{4} + \epsilon} \end{aligned} \quad (20)$$

The incoherent spectrum is then

$$\Gamma^{\text{inc}}(\omega) = \pi\Omega_R^2 \frac{ZE_F}{\hbar\omega^2} \int_0^1 dy \frac{y^2 K\left(\frac{\hbar\omega + E_{\downarrow}}{2E_F}, y\right)}{\left(1 - \frac{\pi}{2k_F a} - I\left(\frac{E_{\downarrow}}{E_F}, y\right)\right)^2} \quad (21)$$

One can check that the total spectrum obeys the sum rule

$$\int_{-\infty}^{\infty} d\omega \Gamma(\omega) = 2\pi\hbar\Omega_R^2 \quad (22)$$

and in particular that the total weight of the incoherent background is proportional to  $1 - Z$ , which is not obvious from the form in Eq. 21. For RF frequencies close to threshold  $\hbar\omega + E_{\downarrow} \ll 2E_F$ , the hole momentum  $\mathbf{q}$  and the particle momentum  $\mathbf{k}$  must be close to each other to fulfill energy conservation, i.e. they have to be close to the Fermi momentum. The double sum over  $\mathbf{q}$  and  $\mathbf{k}$  thus gives a phase space suppression on the order of  $(\hbar\omega + E_{\downarrow})^2$ , i.e. the spectrum starts like  $(\hbar\omega + E_{\downarrow})^2/\omega^2$ . This is in contrast to the dissociation spectrum of a molecule of binding energy  $E_B$ , where the density of states above threshold gives a spectrum proportional to  $\sqrt{\hbar\omega + E_B}/\omega^2$ . For large RF energies, large particle momenta  $\mathbf{k}$  are involved, the suppression due to the Fermi sea becomes negligible and the spectrum behaves like  $\sqrt{\hbar\omega + E_{\downarrow}}/\omega^2$ , as for a molecule of binding energy  $E_{\downarrow}$ . This is natural as for large momenta, we are probing short-range physics which involves at most two particles, a spin up environment atom and the impurity. In particular, at RF energies  $\hbar\omega \gg E_{\downarrow}$ , we recover the  $\omega^{-3/2}$  behavior of the RF spectrum that is universal for short-range interactions.

## RF Spectrum of a finite concentration of impurities

Since polarons are found to be weakly interacting, they will form a Fermi sea filled up to the impurity Fermi momentum  $k_{F\downarrow}$ . The fact that the dispersion of polarons  $E(k) = \frac{m}{m^*}\epsilon_{\mathbf{k}}$  differs from that of a free particle due to the effective mass  $m^* \neq m$  leads to broadening of the RF spectra. The RF photon has to supply the difference in kinetic energies  $(1 - \frac{m}{m^*})\epsilon_{\mathbf{k}}$  between the initial and the final state, with a maximal shift  $(1 - \frac{m}{m^*})\hbar^2 k_{F\downarrow}^2 / 2m$ . The spectral shape is easily obtained: The spectral function at momentum  $\mathbf{k}$  will be dominated by polarons that occupy that momentum state. The coherent part of the spectral function is thus  $A_-^{\text{coh}}(\mathbf{k}, \omega) = Z\delta(\hbar\omega + E(k))$  with  $E(k) = -\hbar^2 k^2 / 2m^* = -\frac{m}{m^*}\epsilon_{\mathbf{k}}$  relative to the impurity Fermi energy. The coherent part of the spectrum then becomes

$$\Gamma^{\text{coh}}(\omega) = 2\pi\hbar\Omega_R^2 \sum_{\mathbf{k}} A_-^{\text{coh}}(\mathbf{k}, \epsilon_{\mathbf{k}} - E_{\downarrow} - \hbar\omega)$$

where the sum extends up to the impurity Fermi momentum  $k_{F\downarrow}$ . With the free, 3D density of states  $\rho(\epsilon)$ , this is

$$\begin{aligned} \Gamma^{\text{coh}}(\omega) &= 2\pi\hbar\Omega_R^2 \int_0^{E_{F\downarrow}} d\epsilon \rho(\epsilon) Z \delta(\epsilon - E_{\downarrow} - \hbar\omega - \frac{m}{m^*}\epsilon) \\ &= 2\pi\hbar\Omega_R^2 \frac{Z}{1 - \frac{m}{m^*}} \rho\left(\frac{\hbar\omega + E_{\downarrow}}{1 - \frac{m}{m^*}}\right) \times \\ &\quad \theta\left(\left(1 - \frac{m}{m^*}\right)E_{F\downarrow} - \hbar\omega - E_{\downarrow}\right) \end{aligned} \quad (23)$$

This coherent part of the spectrum starts at the polaron ground state energy  $\hbar\omega = |E_{\downarrow}|$ , then grows like a square root and jumps to zero when  $\hbar\omega - |E_{\downarrow}| = (1 - \frac{m}{m^*})E_{F\downarrow}$ . On resonance, where  $m^* \approx 1.2$ , this occurs at  $\hbar\omega - |E_{\downarrow}| = 0.2x^{2/3}E_{F\downarrow} \approx 0.04E_{F\downarrow}$  for  $x = 0.1$ . This is still smaller than the Fourier width of the RF pulse used in the experiment of about  $0.1E_F$ . The size of the jump is given by  $2\pi\hbar\Omega_R^2 \frac{Z}{1 - \frac{m}{m^*}} \rho(E_{F\downarrow})$  and reflects the impurity Fermi surface in the RF spectrum. This behavior of the coherent part of the spectrum was found in [1] and was discussed recently in [4]. It is intriguing that the sharpness of the Fermi surface and its discontinuity should, at least in principle, be observable in the RF spectrum.

### Determination of $Z$ from experimental spectra

In order to extract the quasiparticle residue  $Z$ , we determine the area under the peak that is not matched by the environment's response and divide by the total area under the impurity spectrum (see spectrum in the inset of Fig. 4 in the main body of the paper). Due to the Fourier width of the probe pulse, the strong response of

the environment around zero RF offset (the resonance for

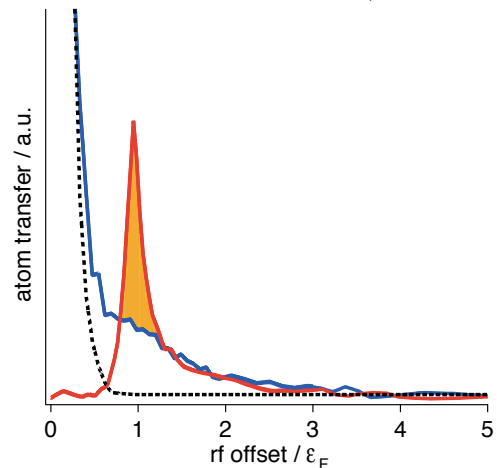


FIG. 1: Determination of the quasiparticle residue  $Z$ . Impurity spectrum (red), environment spectrum (blue) and spectral response of non-interacting atoms (black dashed), folded over from negative RF offsets.

non-interacting atoms) adds some weight to the environment background at the position of the polaron peak. To remove this effect in the determination of  $Z$ , the part of the environment's response at negative frequency offset is folded towards the positive side (dashed line in Fig. 1) and subtracted from the environment spectrum. As it turns out, this procedure changes the value for  $Z$  by less than 5% for all spectra in Fig. 2 of the main paper.

- 
- [1] M. Punk and W. Zwerger, Phys. Rev. Lett. **99**, 170404 (2007).
  - [2] P. Massignan, G. M. Bruun, and H. T. C. Stoof, Phys. Rev. A **78**, 031602 (2008).
  - [3] M. Veillette, E. G. Moon, A. Lamacraft, L. Radzihovsky, S. Sachdev, and D. E. Sheehy, Phys. Rev. A **78**, 033614 (2008).
  - [4] W. Schneider, V. B. Shenoy, and M. Randeria, preprint arXiv:0903.3006 (2009).
  - [5] W. Ketterle and M. Zwierlein, in *Ultracold Fermi Gases, Proceedings of the International School of Physics "Enrico Fermi", Course CLXIV, Varenna, 20 - 30 June 2006*, edited by M. Inguscio, W. Ketterle, and C. Salomon (IOS Press, Amsterdam, 2008).
  - [6] F. Chevy, Phys. Rev. A **74**, 063628 (2006).
  - [7] R. Combescot, A. Recati, C. Lobo, and F. Chevy, Phys. Rev. Lett. **98**, 180402 (2007).
  - [8] P. Nozières, *Theory of Interacting Fermi Systems*, Advanced Book Classics (Addison-Wesley, Reading, MA, 1997).
  - [9] A. Fetter and J. Walecka, *Quantum Theory of Many-Particle Systems* (McGraw-Hill, New York, 1971).

## Strongly interacting isotopic Bose-Fermi mixture immersed in a Fermi sea

Cheng-Hsun Wu, Ibon Santiago, Jee Woo Park, Peyman Ahmadi, and Martin W. Zwierlein

*Department of Physics, MIT–Harvard Center for Ultracold Atoms, and Research Laboratory of Electronics, Massachusetts Institute of Technology, Cambridge, Massachusetts 02139, USA*

(Received 23 March 2011; revised manuscript received 29 April 2011; published 13 July 2011)

We have created a triply quantum-degenerate mixture of bosonic  $^{41}\text{K}$  and two fermionic species  $^{40}\text{K}$  and  $^6\text{Li}$ . The boson is shown to be an efficient coolant for the two fermions, spurring hopes for the observation of fermionic superfluids with imbalanced masses. We observe multiple heteronuclear Feshbach resonances, in particular a wide  $s$ -wave resonance for the combination  $^{41}\text{K}$ - $^{40}\text{K}$ , opening up studies of strongly interacting *isotopic* Bose-Fermi mixtures. For large imbalance in the local densities of different species, we enter the polaronic regime of dressed impurities immersed in a bosonic or fermionic bath.

DOI: [10.1103/PhysRevA.84.011601](https://doi.org/10.1103/PhysRevA.84.011601)

PACS number(s): 03.75.Ss, 34.50.-s, 37.10.De, 67.60.Fp

Strongly interacting quantum mixtures of ultracold atoms provide an extremely rich platform for the study of many-body physics. They offer control over macroscopic quantum phenomena in and out of equilibrium, enabling a direct quantitative comparison to theoretical models [1]. Two-state mixtures of fermionic atoms near Feshbach resonances allow the creation of fermionic superfluids in the crossover between Bose-Einstein condensation and BCS superfluidity [2,3]. Combining different atomic species gives access to Bose-Bose [4,5], Bose-Fermi [6–12], Fermi-Fermi [13–15], and even triply degenerate Bose-Fermi-Fermi mixtures [13] that each connect to many different areas in condensed-matter, high-energy, or nuclear physics. Bose-Fermi mixtures may provide insight into, for example, boson-mediated Cooper pairing [16], QCD matter [17], and theoretical models of High- $T_c$  superconductivity [18]. A mixture of two different fermions might allow access to a superfluid of unlike fermions. In contrast to superconductors or neutron stars, superfluid pairing will occur between particles that are not related via time-reversal symmetry. Very recently, Fermi-Fermi mixtures of unlike fermionic species have been brought into the strongly interacting regime [19], offering prospects to observe universal physics in imbalanced mixtures, such as universal transport [20,21].

An important class of many-body problems involves the interaction of impurities with a Fermi sea or a bosonic bath, dressing them into quasiparticles known as polarons. For the Fermi polaron, an impurity interacting with a fermionic environment, the resulting energy shift has been experimentally measured [22] and calculated [23–25]. Due to the fermionic nature of the environment, the effective mass is only weakly enhanced [25–27] even for resonant interactions. However, if the impurity swims in a bosonic bath, there is no limit to the number of bosons that interact at close distance with the impurity, and the mass enhancement can be enormous [28].

In this work we present a rather ideal system to study strongly interacting quantum mixtures of different atomic species: a heavy, isotopic Bose-Fermi mixture of  $^{40}\text{K}$ - $^{41}\text{K}$  with widely tunable interactions coexisting with a light Fermi sea of  $^6\text{Li}$ . We show that  $^{41}\text{K}$  is an efficient sympathetic coolant for both  $^6\text{Li}$  and  $^{40}\text{K}$ , allowing us to reach a triply quantum degenerate mixture. In comparison to experiments employing  $^{87}\text{Rb}$  to cool the same fermionic species to triple degeneracy [13], we reach a significantly higher degree of degeneracy in  $^6\text{Li}$ . In the quest for optimized cooling schemes

of fermionic atoms, we thus establish  $^{41}\text{K}$  as a superior coolant that is available in all current experiments on fermionic  $^{40}\text{K}$ . For the potassium isotopes, we identify a strong  $p$ -wave Feshbach resonance, as well as a wide  $s$ -wave Feshbach resonance. There, at our lowest temperatures, the mixture is in a regime where theory predicts both Bose and Fermi polarons to exist [29,30]. The mass-imbalanced Bose-Fermi mixture  $^6\text{Li}$ - $^{41}\text{K}$  also allows for tunable interactions at several Feshbach resonances.

Predating our work, Feshbach resonances in nonisotopic Bose-Fermi mixtures were found in  $^{23}\text{Na}$ - $^6\text{Li}$ ,  $^{87}\text{Rb}$ - $^{40}\text{K}$ ,  $^{87}\text{Rb}$ - $^6\text{Li}$  [12], and  $^{85}\text{Rb}$ - $^6\text{Li}$  [31]. These systems are plagued by typically unequal trapping potentials and the large mass difference between unlike atoms, causing gravitational sag that has to be compensated. Predictions for Feshbach resonances in isotopic Bose-Fermi mixtures are available for  $^3\text{He}$ - $^4\text{He}$  [32] and for  $^6\text{Li}$ - $^7\text{Li}$  [33], with preliminary experimental findings reported in [34]. An atom-molecule mixture of  $^6\text{Li}$ - $^6\text{Li}_2$  allowed access to a part of the phase diagram of strongly interacting bosons and fermions [35]. However, for too strong an interaction the composite nature of the bosonic molecules becomes apparent. With  $^{40}\text{K}$ - $^{41}\text{K}$ , we have a Bose-Fermi mixture at our disposal with identical external potentials and essentially equal mass for bosons and fermions, so that the only relevant difference lies in quantum statistics.

The experimental setup, shown in Fig. 1, consists of two independent Zeeman slower for lithium and potassium, allowing us to simultaneously load large samples of each of the three atomic species directly into a UHV chamber. We trap  $3 \times 10^9$   $^{41}\text{K}$  atoms in 2 s and  $10^9$   $^6\text{Li}$  atoms in 1 s. Although the natural abundance of  $^{40}\text{K}$  is only 0.01%, the Zeeman slower with a typical flux of  $10^{11}$  atoms/s for abundant species still yields  $5 \times 10^7$   $^{40}\text{K}$  atoms loaded within 2 s into the magneto-optical trap.

To increase the initial atom density, a 40-ms compressed MOT phase and a 6-ms optical molasses stage compress and cool each gas before loading into the magnetic trap. For  $^{41}\text{K}$ , we follow closely the procedure laid out in [36].  $^{40}\text{K}$  and  $^6\text{Li}$  require less care, as we deliberately co-trap only a few  $10^5$  fermionic atoms with the coolant. The maximum number of fermions that can be brought into degeneracy by a given bosonic coolant is roughly given by the number of degenerate bosons the apparatus can provide. For  $^{41}\text{K}$ , this limits the

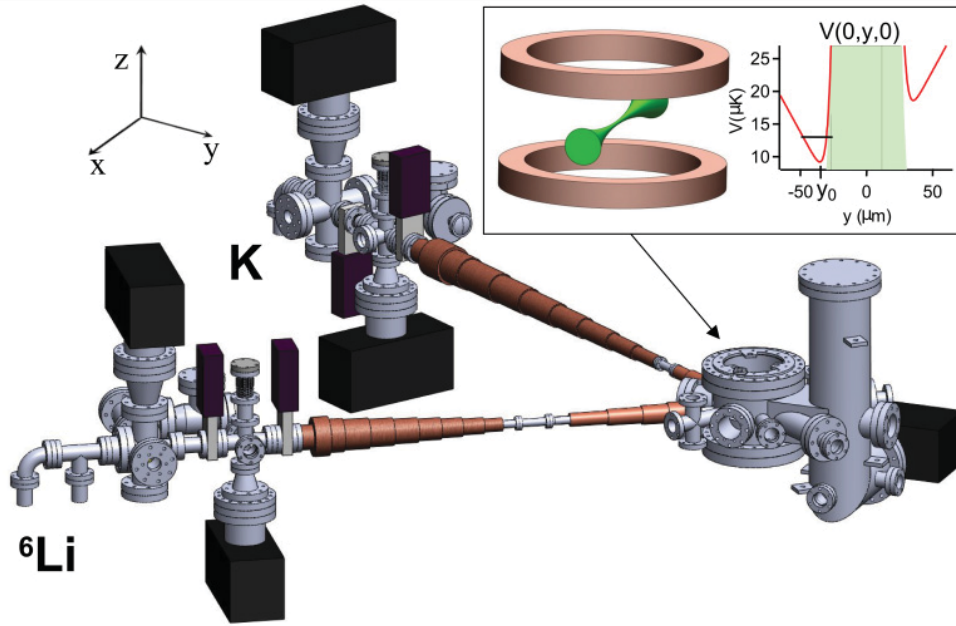


FIG. 1. (Color online) Schematic of the experimental setup. Two Zeeman slower yield optimized atom flux for  ${}^6\text{Li}$  and K, allowing a no-compromise approach to simultaneous magneto-optical trapping of  ${}^{41}\text{K}$ ,  ${}^{40}\text{K}$ , and  ${}^6\text{Li}$  in the main chamber. All species are subsequently loaded into an optically plugged magnetic trap (inset). rf evaporation of  ${}^{41}\text{K}$  sympathetically cools the fermionic species. The inset shows the trapping potential, essentially identical for all species, along the horizontal  $y$  axis perpendicular to the plug beam.

fermion number to about  $2 \times 10^5$ , while for  ${}^{23}\text{Na}$ , the number can be as large as  $7 \times 10^7$  [37].

After the molasses stage, atoms are prepared in the stretched hyperfine states of  $|F, m_F\rangle = |2, 2\rangle$  for  ${}^{41}\text{K}$ ,  $|9/2, 9/2\rangle$  for  ${}^{40}\text{K}$ , and  $|3/2, 3/2\rangle$  for  ${}^6\text{Li}$  via optical pumping. Evaporative cooling of  ${}^{41}\text{K}$  is performed in a quadrupole magnetic trap with a  $B'_z = 220$  G/cm ( $B'_\perp = 110$  G/cm) magnetic field gradient along the vertical (horizontal) direction. To avoid Majorana spin flips, the magnetic field zero is “plugged” by a repulsive laser beam (power 15 W, wavelength 532 nm) focused to a waist of  $20 \mu\text{m}$  [38]. Unwanted hyperfine states from imperfect optical pumping are removed by reducing  $B'_z$  for 200 ms to 15 G/cm, only supporting stretched states sufficiently against gravity. Without this cleaning procedure, spin-changing collisions would strongly reduce the atom number during evaporation. Evaporation is performed on  ${}^{41}\text{K}$  by driving  $|2, 2\rangle \rightarrow |1, 1\rangle$  rf transitions above the hyperfine transition of 254.0 MHz. For the last 2 s of evaporation, the trap is decompressed to  $B'_z = 110$  G/cm to suppress three-body losses. A well-centered plugged trap allows for two trap minima on each side of the plug laser (see Fig. 1). To obtain only a single trap minimum, in the final 2 s of evaporation a horizontal bias field is applied in the  $y$  direction, perpendicular to the plug beam, thus displacing the center of the magnetic trap by  $10 \mu\text{m}$ . The resulting trapping potential, shown in the inset of Fig. 1, is approximately harmonic for atoms at energies of  $\lesssim 2 \mu\text{K}$ . The effect of anharmonicities is strongest along the  $y$  direction, and most important for the light fermion  ${}^6\text{Li}$  at a typical Fermi energy of  $E_F = k_B \cdot 5 \mu\text{K}$  ( ${}^{40}\text{K}$  only has  $E_F \approx k_B \cdot 1.5 \mu\text{K}$ ).

Even for anharmonic traps, long time-of-flight expansion reveals the momentum distribution of the gas [2]. Time-of-flight images of triply quantum degenerate mixtures are shown

in Fig. 2. Condensation of  ${}^{41}\text{K}$  is observed at  $T_c = 1.2 \mu\text{K}$  with  $3 \times 10^5$  atoms. In the harmonic approximation, this translates into a geometric mean of the trapping frequencies of  $\bar{\omega}_{{}^{41}\text{K}} = 2\pi \cdot 380$  Hz. Observing a  ${}^{41}\text{K}$  Bose condensate in thermal contact with a cloud of  ${}^{40}\text{K}$  and  ${}^6\text{Li}$  fermions, each of

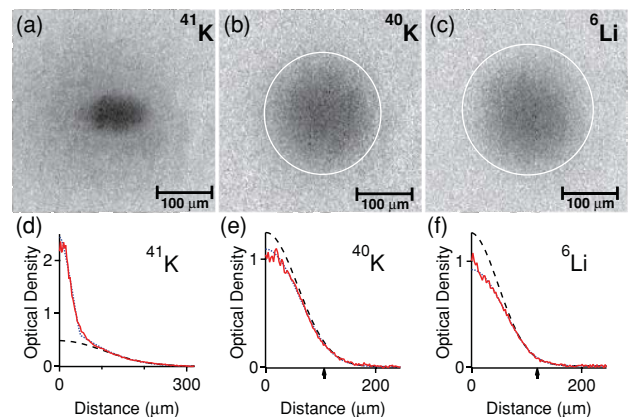


FIG. 2. (Color online) (a)–(c) Absorption images of triply degenerate quantum gases of  ${}^{41}\text{K}$ ,  ${}^{40}\text{K}$ , and  ${}^6\text{Li}$ , imaged after 8.12 ms, 4.06 ms, and 1 ms time-of-flight from the magnetic trap, respectively. The final rf-knife frequency was 500 kHz above the 254.0 MHz hyperfine transition of  ${}^{41}\text{K}$ . The white circles indicate the Fermi radius in time-of-flight  $t$ ,  $R_F = \sqrt{2E_F/m} t$ . (d)–(f) Azimuthally averaged column density. Solid dots: Gaussian fit to the wings of the column density. Solid black and blue lines are Gaussian and Fermi-Dirac fits to the entire profile. The deviation of the Gaussian fit from the data is more pronounced for the more deeply degenerate  ${}^6\text{Li}$  at  $T/T_F = 0.16$  than for  ${}^{40}\text{K}$  at  $T/T_F = 0.51$ . The arrows indicate the Fermi radii. The atom numbers for  ${}^6\text{Li}$ ,  ${}^{41}\text{K}$ , and  ${}^{40}\text{K}$  are  $1.6 \times 10^5$ ,  $1.1 \times 10^5$ , and  $2.0 \times 10^5$ , respectively.

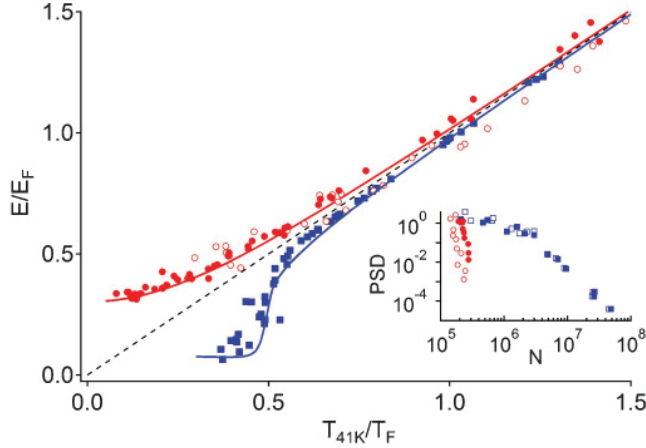


FIG. 3. (Color online) Observation of Pauli pressure and Bose condensation in a triply quantum degenerate mixture. Shown is the normalized release energy  $E/E_F$  of each cloud vs the normalized temperature  $T/T_F$ . Bose condensation of  $^{41}\text{K}$  occurs at  $T_c/T_F = 0.52$ , causing a sudden reduction in release energy below  $T_c$ . For fermions, in contrast, the release energy saturates due to Pauli pressure. Solid circles:  $^6\text{Li}$ ; open circles:  $^{40}\text{K}$ ; solid squares:  $^{41}\text{K}$ . Solid lines: theory for an interacting Bose gas and a noninteracting Fermi gas. Dashed line: Boltzmann gas. The inset shows the evolution of the phase space density (PSD) with atom number ( $N$ ) during evaporation of  $^{41}\text{K}$ . Open squares: Evaporation of  $^{41}\text{K}$  without  $^6\text{Li}$  and  $^{40}\text{K}$ .

roughly the same atom number, already implies degeneracy of the fermionic species. If  $T = T_{c,^{41}\text{K}}$ , then  $T/T_{F,^{40}\text{K}} = \frac{\bar{\omega}_{^{41}\text{K}}}{\bar{\omega}_{^{40}\text{K}}} \frac{1}{(6\zeta(3))^{1/3}} \approx 0.51$  and analogously,  $T/T_{F,^6\text{Li}} = 0.2$ . Taking into account anharmonicities along the  $y$  direction for  $10^5$   $^6\text{Li}$  atoms gives a small correction to the Fermi energy of  $-3.5\%$ . Consistent with this expectation, Thomas-Fermi fits to the time-of-flight distributions in Fig. 2 reveal  $T/T_{F,^6\text{Li}} = 0.16$  ( $N_{^6\text{Li}} = 2.0 \times 10^5$ ) and  $T/T_{F,^{40}\text{K}} = 0.51$  ( $N_{^{40}\text{K}} = 1.1 \times 10^4$ ), while  $T/T_{c,^{41}\text{K}} = 0.9$ . Evaporating further to obtain essentially pure condensates, we achieve  $T/T_{F,^6\text{Li}} = 0.08$  for  $^6\text{Li}$  and  $T/T_{F,^{40}\text{K}} = 0.35$  for  $^{40}\text{K}$ . For  $^6\text{Li}$ , the degree of degeneracy is about four times higher than what has been achieved in [13] with  $^{87}\text{Rb}$  as the coolant. For  $^{40}\text{K}$ , the performance is similar.

We directly observe Pauli pressure and Bose condensation in the triply quantum degenerate mixture. For this, we determine the  $1/e$  width  $R$  of a Gaussian fitted to the fermionic and bosonic distributions, and compare the release energy  $E \equiv \frac{1}{2}mR^2/t^2$  measured after time-of-flight  $t$  to the Fermi energy, defined for each species as  $E_F = k_B T_F = \hbar\bar{\omega}(6N)^{1/3}$ . In Fig. 3 we show  $E/E_F$  as a function of the reduced temperature  $T/T_F$ . Thermometry is provided by fitting Bose functions to the wings of the  $^{41}\text{K}$  distribution. At high temperatures,  $E/k_B$  simply equals the temperature of each gas. At low temperatures, the release energy of a trapped Fermi gas saturates due to Pauli pressure [6,7], while for a Bose cloud  $E$  is suddenly reduced as a condensate forms [38].

The inset in Fig. 3 shows the phase space density (PSD) of each atom cloud vs atom number  $N$  during sympathetic cooling. The efficiency of evaporation is measured by  $\Gamma \equiv -d \ln(\text{PSD})/d \ln(N)$ . Thanks to the small fermion number, the evaporation efficiency for  $^{41}\text{K}$  is similar with and without load,  $\Gamma \approx 3$  [36]. The near-vertical slope of PSD vs  $N$  for the

TABLE I. Observed interspecies Feshbach resonances between  $^6\text{Li}$ - $^{41}\text{K}$  and  $^{40}\text{K}$ - $^{41}\text{K}$  atoms. The width of the resonance,  $\Delta B_{\text{exp}}$ , is determined by a phenomenological Gaussian fit to the observed loss feature (see, e.g., Fig. 4). For the  $p$ -wave resonance, the width was measured at  $T = 8 \mu\text{K}$ .

Mixture	$B_0$ (G)	$\Delta B_{\text{exp}}$ (G)	Resonance Type
$^6\text{Li}   1/2, 1/2 \rangle ^{41}\text{K}   1, 1 \rangle$	31.9	0.2	$s$ wave [39]
$^6\text{Li}   1/2, 1/2 \rangle ^{41}\text{K}   1, 1 \rangle$	335.8	1.1	$s$ wave [39]
$^{40}\text{K}   9/2, 9/2 \rangle ^{41}\text{K}   1, 1 \rangle$	472.6	0.2	$s$ wave [40]
$^{40}\text{K}   9/2, 9/2 \rangle ^{41}\text{K}   1, 1 \rangle$	432.9	2.5	$p$ wave [40]
$^{40}\text{K}   9/2, 9/2 \rangle ^{41}\text{K}   1, 1 \rangle$	542.7	12	$s$ wave [40]

fermionic species demonstrates efficient sympathetic cooling by  $^{41}\text{K}$  with  $\Gamma = 12$  (15) for  $^6\text{Li}$  ( $^{40}\text{K}$ ).

We now turn to the creation of strongly interacting quantum mixtures. For this, atoms are loaded after evaporation into an optical dipole trap formed by two crossed laser beams of wavelength 1064 nm, each focused to a waist of  $100 \mu\text{m}$  at 7 W of power. For the study of  $^6\text{Li}$ - $^{41}\text{K}$  Feshbach resonances, atoms of both species are transferred into the hyperfine ground state via a Landau-Zener sweep of the bias magnetic field in the presence of 261.3 MHz and 234.2 MHz rf radiation. For  $^{40}\text{K}$ - $^{41}\text{K}$ , only  $^{41}\text{K}$  is transferred into the ground state. This mixture is stable against spin-changing collisions due to the inverted hyperfine structure and the large nuclear spin of  $^{40}\text{K}$ . Feshbach resonances are detected via atom loss from three-body collisions, after a fixed wait time, as a function of magnetic field. A list of observed resonances is given in Table I.

We observe a wide Feshbach resonance in collisions of  $^{40}\text{K}$  in state  $|9/2, 9/2\rangle$  with  $^{41}\text{K}$  in state  $|1, 1\rangle$  at 543 G

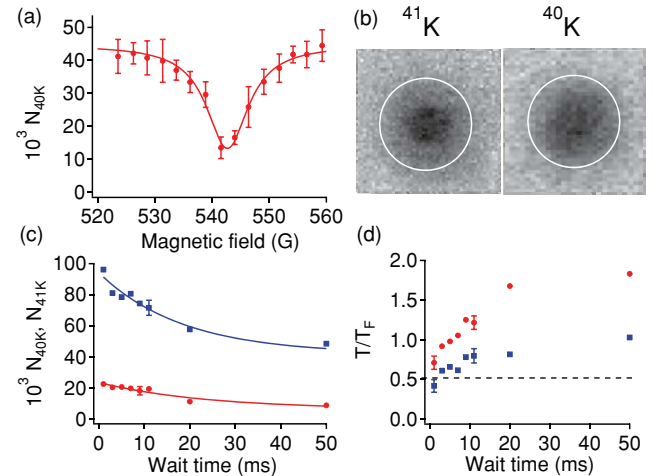


FIG. 4. (Color online) Observation of a wide Feshbach resonance in the isotopic Bose-Fermi mixture of  $^{41}\text{K}$ - $^{40}\text{K}$ . (a) The atom loss feature vs magnetic field is centered at  $B_0 = 542.7 \pm 0.5$  G. (b) Absorption images of the Bose and Fermi clouds after time of flight. The  $^{40}\text{K}$  image was scaled by the ratio of expansion factors of the Bose and Fermi cloud, the images thus approximately illustrate the in-trap density distribution. The white rim indicates the Fermi radius. (c) and (d) Atom number and reduced temperature  $T/T_F$  vs wait time at the Feshbach resonance. Circles:  $^{40}\text{K}$ ; squares:  $^{41}\text{K}$ . Dashed line: Bose-Einstein Condensate threshold  $T_c/T_F = 0.52$ .

[Fig. 4(a)]. This resonance is theoretically predicted [40] to occur at  $B_0 = 541.5$  G with a width of  $\Delta B = 52$  G, defined via the scattering length  $a = a_{\text{bg}}[1 - \Delta B/(B - B_0)]$ , where  $a_{\text{bg}} = 65a_0$  is the background scattering length in the vicinity of the resonance. This isotopic Bose-Fermi mixture with essentially no gravitational sag and wide tunability of its interaction strength is very promising for controlled many-body experiments, where the only relevant difference between the two atoms is that of quantum statistics. Figure 4(b) shows the immersion of a Bose-Einstein condensate of  $^{41}\text{K}$  into a Fermi sea of  $^{40}\text{K}$  with resonant interactions. The condensate survives for about 5 ms, and the remaining thermal atoms decay with a  $1/e$  lifetime of 25 ms at initial densities  $1(3) \times 10^{12} \text{ cm}^{-3}$  for  $^{40}\text{K}$  ( $^{41}\text{K}$ ). Our initial temperatures are low enough, and the condensate lifetime long enough so that polarons should form [29,30]. At the rim of the condensate, where bosons are the minority, bosons are dressed into Fermi polarons, possibly yielding a Fermi polaron condensate [30]. The formation time of such a dressed quasiparticle state should be on the order of  $\hbar/E_B \sim 1$  ms, where  $E_B = 0.6E_{F,^{40}\text{K}}$  is the polaron energy [22]. In the center of the gas, where fermions are the minority, they can be expected to be dressed by the Bose condensate. It will be intriguing to perform local rf spectroscopy on this unconventional state of polaronic matter and to directly demonstrate dressing of fermionic and bosonic impurities [22].

In conclusion, we have observed triply degenerate quantum gases of  $^{41}\text{K}$ ,  $^{40}\text{K}$ , and  $^6\text{Li}$ , through sympathetic cooling of the fermionic species by the boson  $^{41}\text{K}$ . In the Bose-Fermi mixtures of  $^6\text{Li}$ - $^{41}\text{K}$  and  $^{41}\text{K}$ - $^{40}\text{K}$ , five interspecies Feshbach resonances are detected, with  $s$ - and  $p$ -wave character. The isotopic potassium gas could become a pristine model system for strongly interacting Bose-Fermi mixtures, for example, for the study of polarons [22,27], observation of polaron condensation, and universal transport of mixtures with unlike statistics [20]. The doubly degenerate  $^{40}\text{K}$ - $^6\text{Li}$  Fermi-Fermi mixture holds promise for the observation of fermionic superfluidity and Cooper pairing between unlike fermions. Imposing species-dependent optical potentials on mixtures will allow the study of systems with mixed dimensionality [41] and impurity physics such as Anderson localization [42] and the interaction of localized impurities with fermionic superfluids [43].

We would like to acknowledge A. Simoni, T. Hanna, and E. Tiesinga for theoretical determinations of Feshbach resonances. We also thank S. Campbell, C. Clausen, C. Figgatt, K. Fisher, V. Ramasesh, and J. Sharpe for experimental assistance. This work was supported by NSF, AFOSR-MURI and YIP, ARO-MURI, ARO with funding from the DARPA OLE program, the Packard Foundation, and the Alfred P. Sloan Foundation.

- 
- [1] I. Bloch, J. Dalibard, and W. Zwerger, *Rev. Mod. Phys.* **80**, 885 (2008).
- [2] *Ultra-cold Fermi Gases*, edited by M. Inguscio, W. Ketterle, and C. Salomon, *Proceedings of the International School of Physics "Enrico Fermi," Course CLXIV, Varenna* (IOS Press, Amsterdam, 2008).
- [3] S. Giorgini, L. P. Pitaevskii, and S. Stringari, *Rev. Mod. Phys.* **80**, 1215 (2008).
- [4] I. Bloch *et al.*, *Phys. Rev. A* **64**, 021402 (2001).
- [5] G. Modugno *et al.*, *Science* **294**, 1320 (2001).
- [6] F. Schreck *et al.*, *Phys. Rev. Lett.* **87**, 080403 (2001).
- [7] A. G. Truscott *et al.*, *Science* **291**, 2570 (2001).
- [8] Z. Hadzibabic *et al.*, *Phys. Rev. Lett.* **88**, 160401 (2002).
- [9] G. Roati, F. Riboli, G. Modugno, and M. Inguscio, *Phys. Rev. Lett.* **89**, 150403 (2002).
- [10] C. Silber *et al.*, *Phys. Rev. Lett.* **95**, 170408 (2005).
- [11] J. M. McNamara *et al.*, *Phys. Rev. Lett.* **97**, 080404 (2006).
- [12] C. Chin *et al.*, *Rev. Mod. Phys.* **82**, 1225 (2010).
- [13] M. Taglieber *et al.*, *Phys. Rev. Lett.* **100**, 010401 (2008).
- [14] F. M. Spiegelhalter *et al.*, *Phys. Rev. Lett.* **103**, 223203 (2009).
- [15] T. G. Tiecke *et al.*, *Phys. Rev. Lett.* **104**, 053202 (2010).
- [16] H. Heiselberg, C. J. Pethick, H. Smith, and L. Viverit, *Phys. Rev. Lett.* **85**, 2418 (2000).
- [17] K. Maeda, G. Baym, and T. Hatsuda, *Phys. Rev. Lett.* **103**, 085301 (2009).
- [18] P. A. Lee, N. Nagaosa, and X.-G. Wen, *Rev. Mod. Phys.* **78**, 17 (2006).
- [19] A. Trenkwalder *et al.*, *Phys. Rev. Lett.* **106**, 115304 (2011).
- [20] A. Sommer, M. Ku, G. Roati, and M. W. Zwierlein, *Nature* **472**, 201 (2011).
- [21] A. Sommer, M. Ku, and M. W. Zwierlein, *New J. Phys.* **13**, 055009 (2011).
- [22] A. Schirotzek, C. H. Wu, A. Sommer, and M. W. Zwierlein, *Phys. Rev. Lett.* **102**, 230402 (2009).
- [23] F. Chevy, *Phys. Rev. A* **74**, 063628 (2006).
- [24] R. Combescot, A. Recati, C. Lobo, and F. Chevy, *Phys. Rev. Lett.* **98**, 180402 (2007).
- [25] N. Prokof'ev and B. Svistunov, *Phys. Rev. B* **77**, 020408 (2008).
- [26] Y. I. Shin, *Phys. Rev. A* **77**, 041603 (2008).
- [27] S. Nascimbène *et al.*, *Phys. Rev. Lett.* **103**, 170402 (2009).
- [28] R. P. Feynman, *Phys. Rev.* **97**, 660 (1955).
- [29] E. Fratini and P. Pieri, *Phys. Rev. A* **81**, 051605 (2010).
- [30] Z.-Q. Yu, S. Zhang, and H. Zhai, *Phys. Rev. A* **83**, 041603 (2011).
- [31] B. Deh *et al.*, *Phys. Rev. A* **82**, 020701 (2010).
- [32] M. R. Goosen, T. G. Tiecke, W. Vassen, and S. J. J. M. F. Kokkelmans, *Phys. Rev. A* **82**, 042713 (2010).
- [33] E. v. Kempen, B. Marcelis, and S. J. J. M. F. Kokkelmans, *Phys. Rev. A* **70**, 050701(R) (2004).
- [34] J. Zhang *et al.*, *AIP Conf. Proc.* **770**, 228 (2005).
- [35] Y. I. Shin, A. Schirotzek, C. H. Schunck, and W. Ketterle, *Phys. Rev. Lett.* **101**, 070404 (2008).
- [36] T. Kishimoto *et al.*, *Phys. Rev. A* **79**, 031602 (2009).
- [37] Z. Hadzibabic *et al.*, *Phys. Rev. Lett.* **91**, 160401 (2003).
- [38] K. B. Davis *et al.*, *Phys. Rev. Lett.* **75**, 3969 (1995).
- [39] T. Hanna and E. Tiesinga (private communication).
- [40] A. Simoni (private communication).
- [41] Y. Nishida and S. Tan, *Phys. Rev. Lett.* **101**, 170401 (2008).
- [42] U. Gavish and Y. Castin, *Phys. Rev. Lett.* **95**, 020401 (2005).
- [43] E. Vernier, D. Pekker, M. W. Zwierlein, and E. Demler, *Phys. Rev. A* **83**, 033619 (2011).

## Quantum degenerate Bose-Fermi mixture of chemically different atomic species with widely tunable interactions

Jee Woo Park,<sup>1,2</sup> Cheng-Hsun Wu,<sup>1,2</sup> Ibon Santiago,<sup>1,2</sup> Tobias G. Tiecke,<sup>1,3</sup> Sebastian Will,<sup>1,2</sup>  
Peyman Ahmadi,<sup>1,2</sup> and Martin W. Zwierlein<sup>1,2</sup>

<sup>1</sup>MIT-Harvard Center for Ultracold Atoms, and Research Laboratory of Electronics, Massachusetts Institute of Technology, Cambridge, Massachusetts 02139, USA

<sup>2</sup>Department of Physics, Massachusetts Institute of Technology, Cambridge, Massachusetts 02139, USA

<sup>3</sup>Department of Physics, Harvard University, Cambridge, Massachusetts 02138, USA

(Received 20 October 2011; published 9 May 2012)

We have created a quantum degenerate Bose-Fermi mixture of  $^{23}\text{Na}$  and  $^{40}\text{K}$  with widely tunable interactions via broad interspecies Feshbach resonances. Over 30 Feshbach resonances between  $^{23}\text{Na}$  and  $^{40}\text{K}$  were identified, including  $p$ -wave multiplet resonances. The large and negative triplet background scattering length between  $^{23}\text{Na}$  and  $^{40}\text{K}$  causes a sharp enhancement of the fermion density in the presence of a Bose condensate. As explained via the asymptotic bound-state model, this strong background scattering leads to wide Feshbach resonances observed at low magnetic fields. Our work opens up the prospect to create chemically stable, fermionic ground-state molecules of  $^{23}\text{Na}$ - $^{40}\text{K}$ , where strong, long-range dipolar interactions would set the dominant energy scale.

DOI: 10.1103/PhysRevA.85.051602

PACS number(s): 67.85.-d, 03.75.Ss, 34.50.-s, 37.10.De

Ultracold quantum gases realize paradigms of condensed-matter physics in pristine fashion, such as the superfluid to Mott insulator transition [1], the BEC-BCS crossover in fermionic superfluids [2,3], and the Berezinskii-Kosterlitz-Thouless transition in two-dimensional Bose gases [4]. A plethora of novel many-body systems may become accessible through the advent of quantum mixtures of different atomic species. In particular, Bose-Fermi mixtures with widely tunable interactions should reveal boson-mediated interactions between fermions and possibly boson-induced  $p$ -wave superfluidity [5,6]. The fate of impurities in a Fermi sea [7] or a Bose condensate [8–10] can be studied, and new quantum phases of matter are predicted in optical lattices [11]. Furthermore, the creation of fermionic ground-state molecules starting from a degenerate Bose-Fermi mixture opens up an intriguing avenue of research, as this results in a Fermi gas with long-range, anisotropic dipole-dipole interactions [12]. Since the first degenerate Bose-Fermi mixture of different atomic species,  $^{23}\text{Na}$  and  $^6\text{Li}$  [13], a variety of such systems has been realized [8,14–23]. However, so far only one mixture,  $^{87}\text{Rb}$ - $^{40}\text{K}$ , has allowed tunability of interspecies interactions with relative ease by means of a moderately wide ( $\Delta B \approx 3$  G) Feshbach resonance [24], and only in this case fermionic Feshbach molecules have successfully been produced [25,26].

In this Rapid Communication, we report on the experimental realization of a unique Bose-Fermi mixture of  $^{23}\text{Na}$  and  $^{40}\text{K}$  and the observation of over 30  $s$ - and  $p$ -wave Feshbach resonances at low magnetic fields. We demonstrate that  $^{23}\text{Na}$  is an efficient coolant for sympathetic cooling of  $^{40}\text{K}$ . A pattern of wide  $s$ -wave resonances exists for most of the energetically stable hyperfine combinations, the widest being located at 138 G with a width of about 30 G in the  $^{23}\text{Na}|F=1, m_F=1\rangle + ^{40}\text{K}|F=9/2, m_F=-5/2\rangle$  hyperfine configuration. We also observe  $p$ -wave multiplet resonances that are resolved thanks to their location at low magnetic fields.

In the singlet rovibrational ground state, the NaK molecule is known to have a large permanent electric dipole moment of

$2.72(6)$  D [27,28], five times larger than that of KRb [12], and is predicted to be chemically stable against atom-atom exchange reactions [29], in contrast to KRb [30]. An ultracold gas of fermionic ground-state molecules of NaK will thus be an ideal system for the study of Fermi gases with strong, long-range dipolar interactions. Indeed, the interaction energy here can be expected to be on the order of the Fermi energy.

The experimental setup is based on the apparatus presented in Ref. [8], which employs two independent Zeeman slowers capable of simultaneously loading sodium and potassium atoms directly into a UHV chamber. The potassium slower

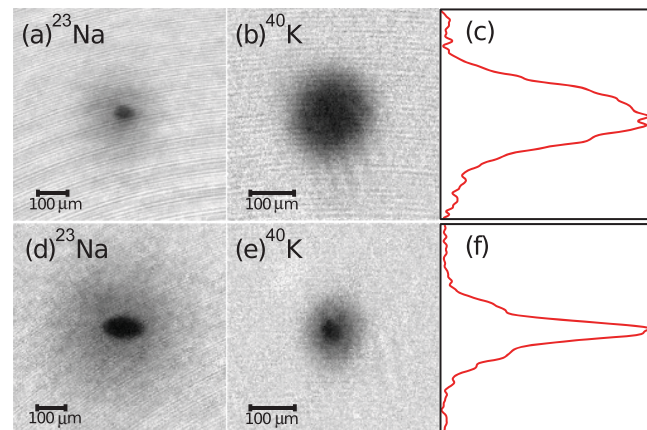


FIG. 1. (Color online) Simultaneous quantum degeneracy of  $^{23}\text{Na}$  and  $^{40}\text{K}$  atoms. (a) and (b), and (d) and (e) are pairs of time-of-flight (TOF) absorption images of a  $^{23}\text{Na}$  BEC and a  $^{40}\text{K}$  Fermi cloud with different atom number balance. A strong attractive interaction between the two species is observed in (e) as a sharp increase of the central density in the fermionic cloud in the presence of a Bose condensate. (c) and (f) are the center-sliced column density of the fermionic clouds of (b) and (e), respectively. TOF was (a) 11 ms, (b) 7 ms, (d) 17 ms, and (e) 5 ms. Atom numbers are (a)  $2.4 \times 10^5$ , (b)  $2 \times 10^5$ , (d)  $8.2 \times 10^5$ , and (e)  $6.7 \times 10^4$ .

selectively decelerates the  $^{40}\text{K}$  isotope, loading  $10^7$  atoms into a magneto-optical trap (MOT) in 10 s. For  $^{23}\text{Na}$ , we use a dark spot MOT [31], which allows us to load approximately  $10^9$  atoms in 2 s.

Multispecies experiments can suffer from atom losses due to light-assisted collisions in the MOT and spin-changing collisions in the magnetic trap. In order to minimize such losses, we developed a shelving technique where  $^{23}\text{Na}$  is first loaded into the MOT, optically pumped to the  $|2,2\rangle$  stretched state, and captured in the magnetic trap. Next, the trap gradient is reduced to 7.7 G/cm to only support the stretched state of  $^{23}\text{Na}$  against gravity. With this gradient left on, and the  $^{23}\text{Na}$  thus “shelved in the dark” in a purely magnetic trap, finally the MOT and slower beams for  $^{40}\text{K}$  are switched on to load the  $^{40}\text{K}$  MOT. This scheme guarantees that only  $^{23}\text{Na}$  atoms in the  $|2,2\rangle$  state are present in the magnetic trap before loading  $^{40}\text{K}$ , and it also potentially reduces light-assisted collisions that would be encountered in a double-species MOT.

Once both species are loaded into the optically plugged magnetic trap [8], the mixture is cooled for 7 s by rf-induced evaporation of  $^{23}\text{Na}$ , where thermally excited  $^{23}\text{Na}$  atoms in the  $|2,2\rangle$  state are removed from the trap by coupling to the high-field seeking state of  $|1,1\rangle$ . We decompress the initial magnetic gradient of 220 G/cm to 27.5 G/cm at the end of evaporation to reduce three-body losses. The 5- $\mu\text{K}$  cold mixture is then loaded into a crossed optical dipole trap (laser wavelength 1064 nm, maximum power 4.7 and 17 W, waist 73 and 135  $\mu\text{m}$ ).

At this stage, the  $1/e$  lifetime of the mixture, with  $^{23}\text{Na}$  and  $^{40}\text{K}$  still in their stretched states, is about  $\tau = 250$  ms, already signaling a strong attractive interaction increasing three-body losses and spin-changing dipolar losses. We thus immediately transfer  $^{23}\text{Na}$  atoms into their hyperfine ground state  $|1,1\rangle$  via a Landau-Zener sweep, and remove any remaining  $|2,2\rangle$  atoms via a resonant light pulse. In the  $^{23}\text{Na}|1,1\rangle + ^{40}\text{K}|9/2,9/2\rangle$  state, the mixture now lives for  $\tau = 20$  s. The gas is further evaporatively cooled in this spin mixture for 2 s by reducing the intensity of the dipole trap beams.

At the end of evaporation, a degenerate Fermi gas of  $^{40}\text{K}$  with  $2 \times 10^5$  atoms and  $T/T_F = 0.6$  coexists with a Bose-Einstein condensate of  $^{23}\text{Na}$ . Two sets of absorption images of the mixture for different values of  $^{23}\text{Na}$  and  $^{40}\text{K}$  atom numbers are shown in Fig. 1, where atom numbers are varied by changing the MOT loading times of the two species. The strong attractive interaction between  $^{23}\text{Na}$  and  $^{40}\text{K}$  in the  $^{23}\text{Na}|1,1\rangle + ^{40}\text{K}|9/2,9/2\rangle$  state is apparent. As the condensate grows, the fermionic cloud acquires a bimodal density distribution as it experiences the strong mean-field potential of the bosons [25]—see Fig. 1(e).

The evolution of the phase space densities (PSDs) and atom numbers  $N$  of both species during evaporation is shown in Fig. 2. Temperature is determined by fitting a thermal profile to the wings of the  $^{23}\text{Na}$  cloud. The cooling efficiency  $\Gamma = -d \ln(\text{PSD})/d \ln(N)$  for sodium in the magnetic trap is  $\Gamma_{\text{Na}} = 2.7$ , a rather high value thanks to the steep confinement in the plugged trap. This efficiency is not affected by the presence of the relatively small admixture of  $^{40}\text{K}$ . Sympathetic cooling is less efficient than in other mixtures [8,32] as  $^{40}\text{K}$  is seen to be lost due to three-body collisions in the magnetic trap. We

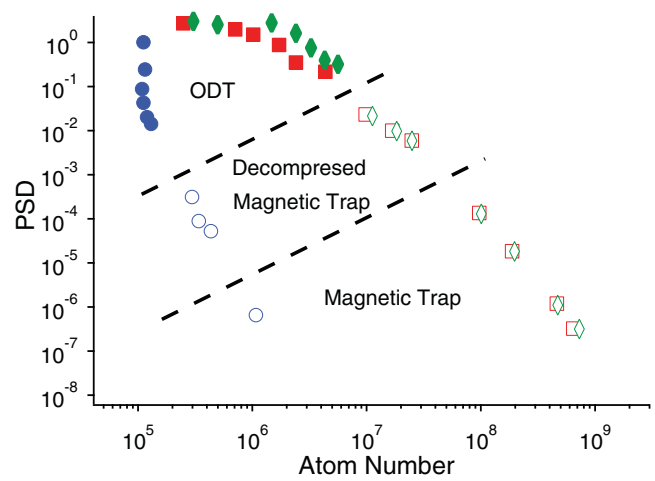


FIG. 2. (Color online) Evolution of the phase space density (PSD) with atom number ( $N$ ). Blue circles:  $^{40}\text{K}$ ; red squares:  $^{23}\text{Na}$  with  $^{40}\text{K}$ ; green diamonds:  $^{23}\text{Na}$  alone. Open and solid symbols represent the PSD in the magnetic trap and optical trap, respectively.

find  $\Gamma_K = 4.6$  for  $^{40}\text{K}$ . In the crossed optical dipole trap, with sodium in  $|1,1\rangle$ , the sodium cooling becomes less efficient due to the weaker confinement,  $\Gamma_{\text{Na}} = 0.9$ , but the  $^{40}\text{K}$  number is essentially conserved in this mixture so that sympathetic cooling is highly efficient, with  $\Gamma_K = 15.3$ . The lowest  $T/T_F$  achieved for  $^{40}\text{K}$  after evaporating all of  $^{23}\text{Na}$  is  $T/T_F = 0.35$  with  $3 \times 10^5$  atoms.

With this degenerate Bose-Fermi mixture at our disposal, the natural next step is to search for interspecies Feshbach resonances between  $^{23}\text{Na}$  and  $^{40}\text{K}$ . There have been theoretical indications for resonances below 100 G [34]. In addition, a large and negative triplet scattering length was predicted in Ref. [35], a value that has recently been refined to  $a_t = -575^{+191}_{-532}$  [34], indicating that the triplet potential has an almost bound, virtual state right above threshold. A large background scattering length is often a catalyst for wide Feshbach resonances [36], caused by strong coupling of molecular states to the almost resonant open channel. A famous example is the 300-G-wide Feshbach resonance in  $^6\text{Li}$  [37].

We performed Feshbach loss spectroscopy, mapping out atom losses of both species as a function of magnetic field. Over 30 Feshbach resonances were observed in four different spin state combinations of  $^{23}\text{Na}|1,1\rangle + ^{40}\text{K}|9/2,m_F\rangle$ , from the ground spin state  $m_F = -9/2$  up to  $m_F = -3/2$ . Spin states of  $^{40}\text{K}$  are prepared starting from  $m_F = +9/2$  by a single Landau-Zener sweep through the intermediate  $m_F$  states at 15 G. The experimentally observed resonance positions and widths are reported in Table I. Many wide  $s$ -wave Feshbach resonances at low magnetic fields are identified, the widest one at 138 G for collisions between  $^{23}\text{Na}|1,1\rangle + ^{40}\text{K}|9/2, -5/2\rangle$ , with a width of 30 G—see Fig. 3.

$p$ -wave Feshbach resonances are known to split into a doublet structure due to different projections of the orbital angular momentum onto the magnetic field axis [38]. In the NaK system, however, we observe triplet features for many  $p$ -wave resonances—see Fig. 4. These originate from the magnetic dipole-dipole interaction of constituent atoms,

TABLE I. Data summary on the Feshbach resonances between  $^{23}\text{Na}$  in  $|1,1\rangle$  and  $^{40}\text{K}$  in  $|9/2, m_F\rangle$ . The positions and widths of the resonances,  $B_0^{\text{expt}}$  and  $\Delta B_{\text{expt}}$ , are determined by phenomenological Gaussian fits ( $\propto e^{-(B-B_0^{\text{expt}})^2/\Delta B_{\text{expt}}^2}$ ) to the observed loss features. For  $p$ -wave resonances, we report the positions and widths of the resolved features, i.e., doublets and multiplets.  $B_0^{\text{th}}$  and  $\Delta B_{\text{th}}$  give the theoretical positions and widths from the ABM model.

Collision channel	$B_0^{\text{expt}}$ (G)	$\Delta B_{\text{expt}}$ (G)	$B_0^{\text{th}}$ (G)	$\Delta B_{\text{th}}$ (G)	Resonance type
$^{23}\text{Na} 1,1\rangle + ^{40}\text{K} 9/2, -9/2\rangle$	6.35, 6.41, 6.47, 6.68	0.02	7.2		$p$
	19.12, 19.18, 19.27	0.02	18.3		$p$
	78.3	1.1	75.5	1.1	$s$
	88.2	4.3	84.5	5.4	$s$
$^{23}\text{Na} 1,1\rangle + ^{40}\text{K} 9/2, -7/2\rangle$	7.32, 7.54	0.2, 0.03	8.7		$p$
	23.19, 23.29	0.05, 0.05	22.1		$p$
	81.6	0.2	82.1	0.04	$s$
	89.8	1.1	87.3	0.6	$s$
$^{23}\text{Na} 1,1\rangle + ^{40}\text{K} 9/2, -5/2\rangle$	108.6	6.6	105.7	13.1	$s$
	9.23, 9.60	0.14, 0.11	11.0		$p$
	29.19, 29.45, 29.52	0.04	27.8		$p$
	96.5	0.5	97.2	0.04	$s$
$^{23}\text{Na} 1,1\rangle + ^{40}\text{K} 9/2, -3/2\rangle$	106.9	1.8	103.8	0.45	$s$
	148 (138 <sup>a</sup> )	37 (30 <sup>a</sup> )	137.1	26	$s$
	12.51, 12.68	0.16, 0.06	14.8		$p$
	39.39, 39.86	0.15, 0.14	37.2		$p$
	116.9	0.5	118.3	0.07	$s$
	129.5	4.6	127.2	0.39	$s$
	175	20	187.8	50.5	$s$

<sup>a</sup>The resonance position and width have been refined by measuring the molecular binding energies via rf spectroscopy [33].

which couple molecular states with different total internal spin. The diagonal terms of the magnetic dipole-dipole interaction induce an energy shift that differs for the  $m_l = 0$  and  $|m_l| = 1$  quantum numbers, giving rise to the well-known doublet structures. The off-diagonal terms in the dipole-dipole interaction couple different values of  $m_l$  while conserving the total angular momentum  $m_l + M_F$ , where  $M_F = m_{F,K} + m_{F,Na}$ . These terms are in most mixtures negligible since molecular states with different values of  $M_F$  have to be nearly degenerate to result in a significant energy shift. However, due to the low-field nature of the NaK  $p$ -wave resonances, multiple molecular states are nearly degenerate with the open-channel spin state, allowing for the triplet structure to be resolved.

The assignment of  $s$ - and  $p$ -wave characters of the resonances follows from a simple, but powerful model of the molecular states involved. The singlet and triplet potentials of the interatomic potential allow for a variety of bound states. From the known scattering length [34] and the van der Waals coefficient  $C_6$  [39], the weakest  $s$ -wave bound states are expected at about  $E_s^s = -150(10)$  MHz and  $E_t^s = -1625(50)$  MHz for the singlet and triplet  $s$ -wave potentials, where the errors reflect uncertainties of the scattering lengths from Ref. [34]. The  $p$ -wave bound states follow from the  $s$ -wave bound states as in Ref. [40] and are slightly adjusted to fit the observed resonance positions. As described in Refs. [41,42], as a first guess for locations of Feshbach resonances one can neglect the part of the hyperfine interaction that couples singlet and triplet bound states. This already provides the pattern of Feshbach resonances as positions where these (uncoupled) molecular states cross the atomic

(open-channel) threshold. The analysis shows that the observed resonances are caused by the triplet bound states. Next, we use the asymptotic bound-state model (ABM) to include the singlet-triplet coupling of molecular states [43]. To couple the molecular states to the open channel, we follow Marcelis *et al.* [36] and only include the effect of the virtual state causing the large and negative triplet scattering length. The spin part of the coupling matrix element is obtained from the ABM Hamiltonian and the spatial part, i.e., the wave-function overlap between the respective bound state and the virtual state, is taken as one free fit parameter. For the background scattering length of the low-field resonances the effect of broad resonances is included. The virtual state causes strong coupling of several  $s$ -wave molecular states to the open channel, leading to wide, open-channel-dominated resonances as known from the case of  $^6\text{Li}$ . The theoretical values obtained with this model are shown in Table I. An exceptionally broad resonance for  $m_F = -3/2$  is predicted to be even wider and to be shifted further, possibly hinting at a shift between the loss maximum and the actual Feshbach resonance position. Our approach leads to a refined triplet bound-state energy of  $E_t^s = -1654(3)$  MHz and  $E_t^p = -1478(7)$  MHz, and using the long-range potential from Ref. [34], we obtain a refined value of the triplet scattering length of  $a_t = -830(70)a_0$ . The errors correspond to one standard deviation of a least-squares fit to the eight narrowest  $s$ -wave resonances that are least sensitive to the coupling to the scattering states and hence the error induced by the ABM is expected to be small [43].

In conclusion, we have produced a degenerate Bose-Fermi mixture of  $^{23}\text{Na}$  and  $^{40}\text{K}$ , and identified over 30  $s$ - and

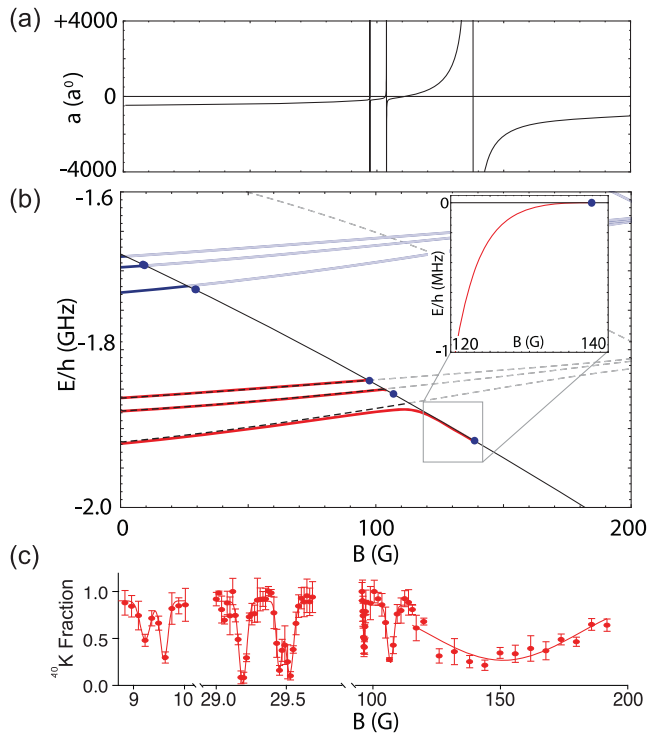


FIG. 3. (Color online) Feshbach resonances in  $^{23}\text{Na}$ - $^{40}\text{K}$ , here for  $^{23}\text{Na}|1, 1\rangle + ^{40}\text{K}|9/2, -5/2\rangle$  collisions. (a) Scattering length from the ABM model. (b) Open-channel threshold energy (black solid line), uncoupled ( $s$ -wave: dashed lines;  $p$ -wave: light blue/light gray lines) and coupled molecular states ( $s$ -wave: red/gray solid lines;  $p$ -wave: blue/dark gray solid lines). The blue dots denote experimentally measured resonances. The inset shows the energy, relative to threshold, of the molecular state at the wide  $s$ -wave resonance at 138 G [33]. (c) Experimental loss spectra of  $^{40}\text{K}$  in the presence of  $^{23}\text{Na}$ . Three  $s$ -wave resonances and two  $p$ -wave manifolds are found, the latter resolved in one doublet and one triplet.

$p$ -wave interspecies Feshbach resonances, including several exceptionally broad resonances. Remarkably, many  $p$ -wave Feshbach resonances are observed to be triplets or even

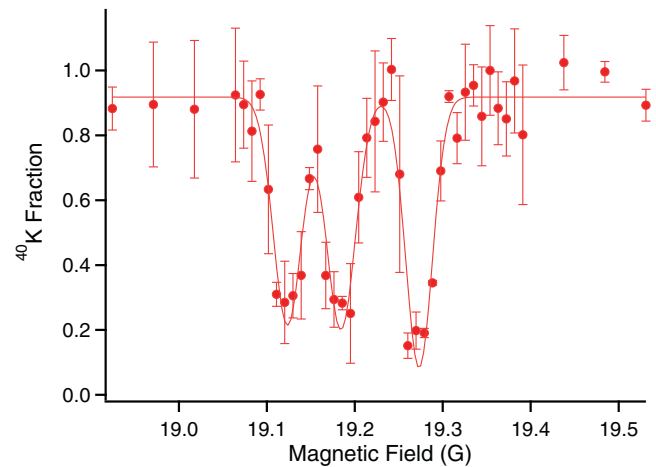


FIG. 4. (Color online) Triplet structure of the  $p$ -wave resonance at 19.1 G for the  $^{23}\text{Na}|1, 1\rangle + ^{40}\text{K}|9/2, -9/2\rangle$  spin configuration. A phenomenological triple Gaussian fit is applied as a guide to the eyes.

multiplets. Our strongly interacting  $^{23}\text{Na}$ - $^{40}\text{K}$  mixture near these Feshbach resonances should allow the study of Bose or Fermi polarons [7], of boson-mediated interactions between fermions, and possibly of unique states of matter in optical lattices. The formation of fermionic Feshbach molecules is within reach. In the rovibrational ground state, NaK molecules possess a large induced electric dipole moment and are stable against exchange reactions. One can thus hope to create a Fermi gas of polar molecules with strong dipole-dipole interactions that dominate the many-body physics of the gas, rather than being a small perturbative effect.

We thank Eberhard Tiemann for performing a coupled-channel calculation based on our results which stimulated us to further investigate the  $p$ -wave multiplet structures. We also thank Tout Wang for stimulating discussions. This work was supported by the NSF, AFOSR-MURI and -PECASE, ARO-MURI, ONR YIP, DARPA YFA, a grant from the Army Research Office with funding from the DARPA OLE program and the David and Lucille Packard Foundation.

[1] I. Bloch, J. Dalibard, and W. Zwerger, *Rev. Mod. Phys.* **80**, 885 (2008).  
 [2] *Ultracold Fermi Gases*, Proceedings of the International School of Physics “Enrico Fermi,” Course CLXIV, Varenna, 2006, edited by M. Inguscio, W. Ketterle, and C. Salomon (IOS, Amsterdam, 2008).  
 [3] W. Ketterle and M. Zwierlein, *Riv. Nuovo Cimento* **31**, 247 (2008).  
 [4] Z. Hadzibabic and J. Dalibard, *Riv. Nuovo Cimento* **34**, 389 (2011).  
 [5] M. J. Bijlsma, B. A. Heringa, and H. T. C. Stoof, *Phys. Rev. A* **61**, 053601 (2000).  
 [6] H. Heiselberg, C. J. Pethick, H. Smith, and L. Viverit, *Phys. Rev. Lett.* **85**, 2418 (2000).

[7] A. Schirotzek, C.-H. Wu, A. Sommer, and M. W. Zwierlein, *Phys. Rev. Lett.* **102**, 230402 (2009).  
 [8] C.-H. Wu, I. Santiago, J. W. Park, P. Ahmadi, and M. W. Zwierlein, *Phys. Rev. A* **84**, 011601 (2011).  
 [9] E. Fratini and P. Pieri, *Phys. Rev. A* **81**, 051605 (2010).  
 [10] Z.-Q. Yu, S. Zhang, and H. Zhai, *Phys. Rev. A* **83**, 041603 (2011).  
 [11] M. Lewenstein, L. Santos, M. A. Baranov, and H. Fehrmann, *Phys. Rev. Lett.* **92**, 050401 (2004).  
 [12] K. K. Ni, S. Ospelkaus, M. H. G. de Miranda, A. Pe’er, B. Neyenhuis, J. J. Zirbel, S. Kotochigova, P. S. Julienne, D. S. Jin, and J. Ye, *Science* **322**, 231 (2008).

- [13] Z. Hadzibabic, C. A. Stan, K. Dieckmann, S. Gupta, M. W. Zwierlein, A. Görlitz, and W. Ketterle, *Phys. Rev. Lett.* **88**, 160401 (2002).
- [14] G. Roati, F. Riboli, G. Modugno, and M. Inguscio, *Phys. Rev. Lett.* **89**, 150403 (2002).
- [15] J. Goldwin, S. Inouye, M. L. Olsen, B. Newman, B. D. DePaola, and D. S. Jin, *Phys. Rev. A* **70**, 021601 (2004).
- [16] C. Ospelkaus, S. Ospelkaus, K. Sengstock, and K. Bongs, *Phys. Rev. Lett.* **96**, 020401 (2006).
- [17] S. Aubin, M. H. T. Extavour, S. Myrskog, L. J. Leblanc, J. Estève, S. Singh, P. Scrutton, D. McKay, R. McKenzie, I. D. Leroux *et al.*, *J. Low Temp. Phys.* **140**, 377 (2005).
- [18] K. Günter, T. Stöferle, H. Moritz, M. Köhl, and T. Esslinger, *Phys. Rev. Lett.* **96**, 180402 (2006).
- [19] T. Best, S. Will, U. Schneider, L. Hackermüller, D. van Oosten, I. Bloch, and D. S. Lühmann, *Phys. Rev. Lett.* **102**, 030408 (2009).
- [20] C. Silber, S. Günther, C. Marzok, B. Deh, P. W. Courteille, and C. Zimmermann, *Phys. Rev. Lett.* **95**, 170408 (2005).
- [21] M. Taglieber, A. C. Voigt, T. Aoki, T. W. Hänsch, and K. Dieckmann, *Phys. Rev. Lett.* **100**, 010401 (2008).
- [22] H. Hara, Y. Takasu, Y. Yamaoka, J. M. Doyle, and Y. Takahashi, *Phys. Rev. Lett.* **106**, 205304 (2011).
- [23] A. H. Hansen, A. Khramov, W. H. Dowd, A. O. Jamison, V. V. Ivanov, and S. Gupta, *Phys. Rev. A* **84**, 011606 (2011).
- [24] F. Ferlaino, C. D'Errico, G. Roati, M. Zaccanti, M. Inguscio, G. Modugno, and A. Simoni, *Phys. Rev. A* **73**, 040702 (2006).
- [25] C. Ospelkaus, S. Ospelkaus, L. Humbert, P. Ernst, K. Sengstock, and K. Bongs, *Phys. Rev. Lett.* **97**, 120402 (2006).
- [26] J. J. Zirbel, K. K. Ni, S. Ospelkaus, J. P. D'Incao, C. E. Wieman, J. Ye, and D. S. Jin, *Phys. Rev. Lett.* **100**, 143201 (2008).
- [27] R. F. Wormsbecher, M. M. Hessel, and F. J. Lovas, *J. Chem. Phys.* **74**, 6983 (1981).
- [28] A. Gerdes, O. Dulieu, H. Knöckel, and E. Tiemann, *Eur. Phys. J. D* **65**, 105 (2011).
- [29] P. S. Zuchowski and J. M. Hutson, *Phys. Rev. A* **81**, 060703 (2010).
- [30] S. Ospelkaus, K.-K. Ni, D. Wang, M. H. G. de Miranda, B. Neyenhuis, G. Qumner, P. S. Julienne, J. L. Bohn, D. S. Jin, and J. Ye, *Science* **327**, 853 (2006).
- [31] W. Ketterle, K. B. Davis, M. A. Joffe, A. Martin, and D. E. Pritchard, *Phys. Rev. Lett.* **70**, 2253 (1993).
- [32] Z. Hadzibabic, S. Gupta, C. A. Stan, C. H. Schunck, M. W. Zwierlein, K. Dieckmann, and W. Ketterle, *Phys. Rev. Lett.* **91**, 160401 (2003).
- [33] C.-H. Wu *et al.* (unpublished).
- [34] A. Gerdes, M. Hobein, H. Knöckel, and E. Tiemann, *Eur. Phys. J. D* **49**, 67 (2008).
- [35] V. Venturi, M. Jamieson, and R. Côté, *J. Phys. B* **34**, 4339 (2001).
- [36] B. Marcellis, E. G. M. van Kempen, B. J. Verhaar, and S. J. J. M. F. Kokkelmans, *Phys. Rev. A* **70**, 012701 (2004).
- [37] K. Dieckmann, C. A. Stan, S. Gupta, Z. Hadzibabic, C. H. Schunck, and W. Ketterle, *Phys. Rev. Lett.* **89**, 203201 (2002).
- [38] C. Ticknor, C. A. Regal, D. S. Jin, and J. L. Bohn, *Phys. Rev. A* **69**, 042712 (2004).
- [39] A. Derevianko, J. F. Babb, and A. Dalgarno, *Phys. Rev. A* **63**, 052704 (2001).
- [40] T. G. Tiecke, M. R. Goosen, J. T. M. Walraven, and S. J. J. M. F. Kokkelmans, *Phys. Rev. A* **82**, 042712 (2010).
- [41] A. J. Moerdijk, B. J. Verhaar, and A. Axelsson, *Phys. Rev. A* **51**, 4852 (1995).
- [42] C. A. Stan, M. W. Zwierlein, C. H. Schunck, S. M. F. Raupach, and W. Ketterle, *Phys. Rev. Lett.* **93**, 143001 (2004).
- [43] E. Wille, F. M. Spiegelhalter, G. Kerner, D. Naik, A. Trenkwalder, G. Hendl, F. Schreck, R. Grimm, T. G. Tiecke, J. T. M. Walraven, S. J. J. M. F. Kokkelmans, E. Tiesinga, and P. S. Julienne, *Phys. Rev. Lett.* **100**, 053201 (2008).



## Ultracold Fermionic Feshbach Molecules of $^{23}\text{Na}^{40}\text{K}$

Cheng-Hsun Wu, Jee Woo Park, Peyman Ahmadi, Sebastian Will, and Martin W. Zwierlein

*MIT-Harvard Center for Ultracold Atoms, Research Laboratory of Electronics, and Department of Physics,  
Massachusetts Institute of Technology, Cambridge, Massachusetts 02139, USA*

(Received 22 June 2012; published 20 August 2012)

We report on the formation of ultracold weakly bound Feshbach molecules of  $^{23}\text{Na}^{40}\text{K}$ , the first fermionic molecule that is chemically stable in its absolute ground state. The lifetime of the nearly degenerate molecular gas exceeds 100 ms in the vicinity of the Feshbach resonance. The measured dependence of the molecular binding energy on the magnetic field demonstrates the open-channel character of the molecules over a wide field range and implies significant singlet admixture. This will enable efficient transfer into the singlet vibrational ground state, resulting in a stable molecular Fermi gas with strong dipolar interactions.

DOI: [10.1103/PhysRevLett.109.085301](https://doi.org/10.1103/PhysRevLett.109.085301)

PACS numbers: 67.85.-d, 03.75.Ss, 34.50.-s, 37.10.Mn

The quest for creating and manipulating ultracold molecules has seen spectacular advances over the past decade [1,2]. They include the production of cold molecules from laser cooled atoms [3], the formation of Feshbach molecules from ultracold atomic gases [4,5], the observation of Bose-Einstein condensates of bosonic Feshbach molecules [6–10], and the formation of ultracold dipolar ground state molecules [11]. Chemically stable, fermionic ground state molecules with large electric dipole moment would allow access to novel phases of matter in dipolar Fermi gases [2]. So far,  $^{40}\text{K}^{87}\text{Rb}$  is the only fermionic ground state molecule that has been produced at nearly degenerate temperatures [11]. However, the gas is unstable against the exchange reaction  $\text{KRb} + \text{KRb} \rightarrow \text{K}_2 + \text{Rb}_2$  [12].

Here we report on the production of ultracold weakly bound fermionic molecules of  $^{23}\text{Na}^{40}\text{K}$  near a broad Feshbach resonance [13]. The NaK molecule is chemically stable in its absolute ground state [14]. In addition, it possesses a large induced electric dipole moment of 2.72 Debye in its singlet ground state [15], compared to 0.57 Debye for KRb [11]. Therefore, fermionic ground state molecules of NaK can form a Fermi sea with strong, long-range anisotropic dipolar interactions, with an interaction energy greater than 30% of the Fermi energy. The Feshbach molecules we create provide an ideal starting point for the formation of ground state molecules. They are nearly degenerate and long-lived, with a lifetime exceeding 100 ms. We demonstrate their largely open-channel character in a wide magnetic field range. The open channel has significant admixture of the electronic spin singlet state, thus opening up a direct pathway towards the singlet rovibrational ground state using stimulated rapid adiabatic passage (STIRAP) via a singlet excited molecular state [1,11].

To form Feshbach molecules, we prepare a Bose-Fermi mixture of  $^{23}\text{Na}$  and  $^{40}\text{K}$  with  $150 \times 10^3$  atoms each in a crossed optical dipole trap as has been described previously [13,16,17]. Sodium is in its absolute hyperfine ground state  $|F, m_F\rangle = |1, 1\rangle$ , which forms a stable mixture

with any hyperfine state of  $^{40}\text{K}$  in the  $F = 9/2$  lower hyperfine manifold. Feshbach spectroscopy has revealed a rich pattern of interspecies Feshbach resonances [13]. One particular resonance stands out due to its exceptional width of 30 G at 140 G between  $|1, 1\rangle_{\text{Na}}$  and  $|9/2, -5/2\rangle_{\text{K}}$  atoms. Expecting open-channel dominated molecules with potentially long lifetimes, we use this resonance to form fermionic Feshbach molecules.

There are several established methods to associate Feshbach molecules [10]. For wide Feshbach resonances, where the molecular wave function can have a large extent and offer good overlap with two unbound atoms, a particularly clean way to form molecules is via radio frequency (rf) association [18–21]. Our approach is schematically shown in Fig. 1(a).

Here,  $^{23}\text{Na}$  and  $^{40}\text{K}$  atoms are initially prepared in the nonresonant hyperfine states  $|1, 1\rangle_{\text{Na}}$  and  $|9/2, -3/2\rangle_{\text{K}}$ . For optimized phase space overlap between the two species [20], we choose a temperature  $T$  of the mixture that is close to the critical temperature  $T_C$  for Bose-Einstein condensation of sodium, corresponding to  $T/T_F \approx 0.4$  for  $^{40}\text{K}$ . Via a radio frequency pulse [22] near the  $|9/2, -3/2\rangle_{\text{K}}$  to  $|9/2, -5/2\rangle_{\text{K}}$  hyperfine transition, we then transfer the unbound  $^{40}\text{K}$  atoms into the molecular bound state with sodium.

A typical rf spectrum at a magnetic field on the molecular side of the Feshbach resonance is shown in Fig. 1(a). Two features are observed: an atomic peak near the unperturbed hyperfine transition, and a molecular peak arising from  $^{40}\text{K}$  atoms that have been rf associated into NaK molecules. The distance between the atomic peak and the onset of the molecular feature yields the binding energy  $E_b$ . Direct absorption imaging of the large Feshbach molecules is possible using light resonant with the atomic transition [8,18–21]. We typically detect up to  $20 \times 10^3$  molecules, corresponding to a conversion efficiency of  $^{40}\text{K}$  atoms into molecules of about 15%.

The atomic feature at the hyperfine transition from  $|9/2, -3/2\rangle_{\text{K}}$  to  $|9/2, -5/2\rangle_{\text{K}}$  shows a strong mean-field

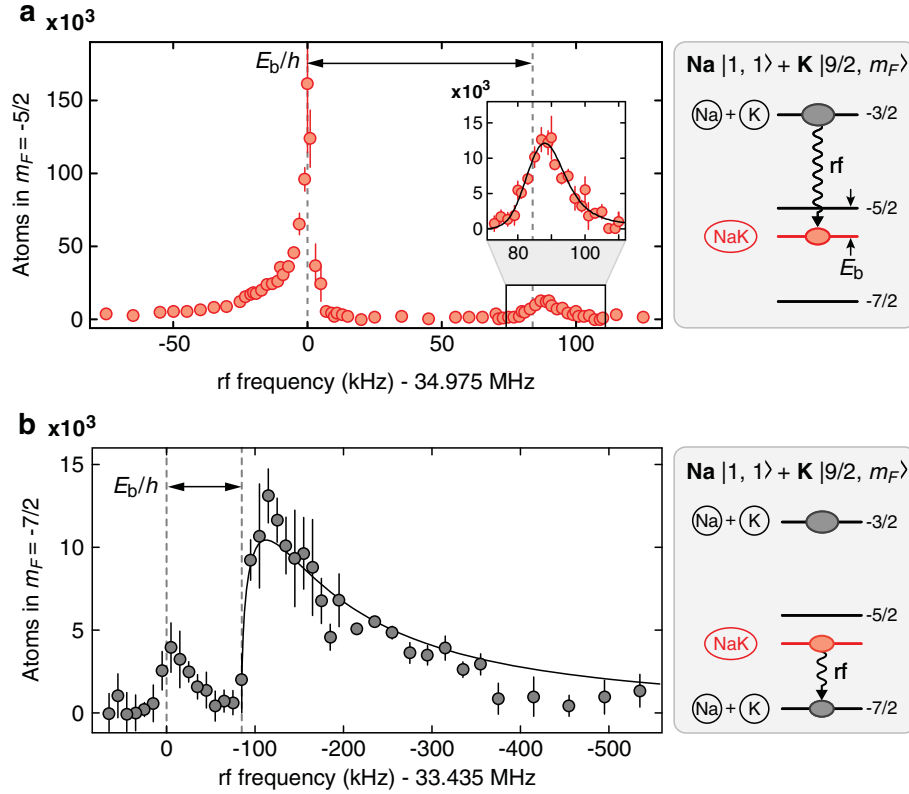


FIG. 1 (color online). (a) Association of fermionic Feshbach molecules. Starting with a mixture of  $|1, 1\rangle_{\text{Na}}$  and  $|9/2, -3/2\rangle_{\text{K}}$  atoms, rf spectroscopy near the  $|9/2, -3/2\rangle_{\text{K}}$  to  $|9/2, -5/2\rangle_{\text{K}}$  hyperfine transition reveals free  $^{40}\text{K}$  atoms repulsively interacting with the  $^{23}\text{Na}$  bath (near zero rf offset), as well as associated molecules (near 85 kHz rf offset). A fit to the molecular association spectrum yields a binding energy of  $E_b = h \times 84(6)$  kHz. The magnetic field corresponding to the atomic transition at 34.975 MHz was 129.4 G. (b) Dissociation of Feshbach molecules. Driving the  $|9/2, -5/2\rangle_{\text{K}}$  to  $|9/2, -7/2\rangle_{\text{K}}$  transition yields the molecular dissociation spectrum, showing a sharp onset at an rf frequency shifted by  $E_b/h$  from the atomic transition. The solid line shows the fit of a model  $\propto \theta(\nu - \nu_b)\sqrt{\nu - \nu_b}/\nu^2$  [10], yielding  $\nu_b = E_b/h = 85(8)$  kHz.

shift towards lower frequencies, which is a direct signature of the repulsive interactions between  $|1, 1\rangle_{\text{Na}}$  and  $|9/2, -5/2\rangle_{\text{K}}$  atoms on the repulsive branch of the Feshbach resonance. The free-free spectrum is directly proportional to the number of fermions that experience a given density of bosons. The long tail towards lower frequencies is caused by a small fraction of condensed bosons (about 10%) present in the mixture.

For accurate extraction of the molecular binding energy  $E_b$ , the functional form of the molecular association spectrum is required. The line shape can be modeled via Fermi's golden rule as

$$\Gamma_{\text{mol}}(\nu) \propto \mathcal{F}(h\nu - E_b)p(h\nu - E_b), \quad (1)$$

where  $\mathcal{F}(\epsilon) \propto (1 + \epsilon/E_b)^{-2}$  is the Franck-Condon factor between the wave functions of an unbound Na-K atom pair and a bound Feshbach molecule of binding energy  $E_b$  [24], and  $p(\epsilon)$  is the probability density to find a pair of potassium and sodium atoms with relative kinetic energy  $\epsilon$ . For thermal clouds,  $p(\epsilon) = \rho(\epsilon)\lambda_M^3 e^{-(\mu/M)(\epsilon/k_B T)}$ , where  $\rho(\epsilon)$  is the density of states with relative kinetic energy  $\epsilon$ ,  $\lambda_M = \sqrt{\frac{2\pi\hbar^2}{Mk_B T}}$  is the thermal de Broglie wavelength for an

atom pair, and  $M = m_{\text{Na}} + m_{\text{K}}$  and  $\mu = \frac{m_{\text{Na}}m_{\text{K}}}{m_{\text{Na}} + m_{\text{K}}}$  are the total and reduced mass, respectively. The inset in Fig. 1(a) shows a fit of this line shape, convoluted with the experimental resolution, to the molecular feature, giving a binding energy of  $E_b = h \times 84(6)$  kHz at a magnetic field of  $B = 129.4$  G. The width reflects the initial distribution of relative momenta between bosons and fermions and, indeed, is found to be compatible with the temperature of the sodium and potassium clouds.

A complementary demonstration of molecule formation is the observation of a dissociation spectrum [25], as shown in Fig. 1(b). To dissociate molecules, we drive the  $|9/2, -5/2\rangle_{\text{K}}$  to  $|9/2, -7/2\rangle_{\text{K}}$  transition after rf association of molecules. The onset of transfer is observed at  $E_b/h = 85(8)$  kHz, in good agreement with the association threshold in Fig. 1(a). We make use of molecule dissociation in the lifetime measurements discussed below to ensure the exclusive detection of molecules.

We have studied the molecular binding energies as a function of magnetic field [see Fig. 2(a)]. The approximately quadratic dependence of the binding energy on magnetic field reflects the open-channel character of the

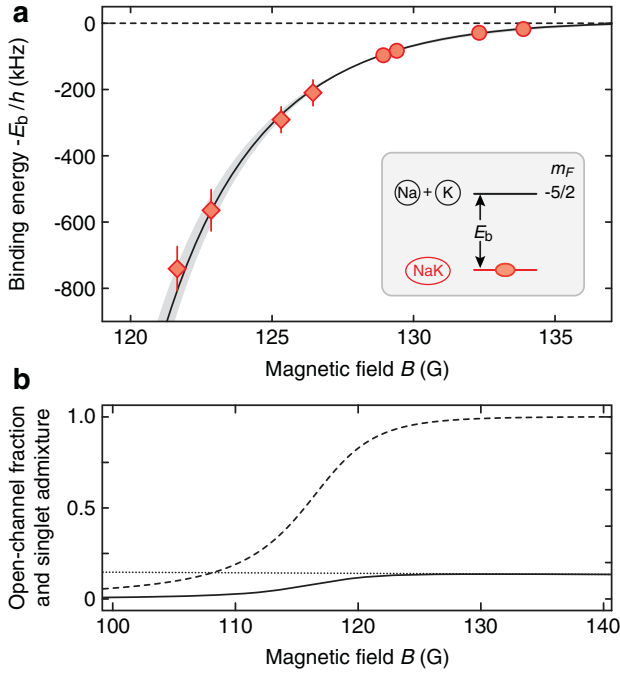


FIG. 2 (color online). (a) Binding energy of NaK Feshbach molecules at the wide Feshbach resonance between  $|1, 1\rangle_{\text{Na}}$  and  $|9/2, -5/2\rangle_{\text{K}}$ . Binding energies smaller than 200 kHz (circles) are obtained by direct detection of molecules [see Fig. 1(a)], while larger binding energies (diamonds) with weaker free-bound coupling are measured by detecting simultaneous atom loss in  $|1, 1\rangle_{\text{Na}}$  and  $|9/2, -3/2\rangle_{\text{K}}$ . The solid line is a one-parameter fit to the model described in the text, and the shaded region displays the uncertainty. (b) Open-channel fraction (dashed line) and singlet admixture of the molecular state (solid line), derived from the binding energy curve in (a), and singlet admixture of unbound pairs (dotted line).

molecular state over a wide field range, where the binding energy follows the law  $E_b \approx \frac{\hbar^2}{2\mu(a-\bar{a})^2}$ , with  $\bar{a} = 51a_0$  the mean scattering length for NaK and  $a(B) \approx a_{\text{bg}}(1 + \frac{\Delta B}{B-B_0})$  the dependence of the scattering length on magnetic field near the resonance [5]. Since the background scattering length  $a_{\text{bg}} = -690^{+90}_{-130}a_0$  is large and negative [13,26], the closed-channel molecular state is predominantly coupled to a virtual state [28,29] of energy  $E_{\text{vs}} = \frac{\hbar^2}{2\mu(a_{\text{bg}}-\bar{a})} = k_B \times 11(3) \mu\text{K}$ . In this case, the binding energy  $E_b$  is given by solving

$$E_b + E_c(B) - \frac{\frac{1}{2}A_{\text{vs}}}{E_{\text{vs}}(1 + \sqrt{\frac{E_b}{E_{\text{vs}}}})} = 0. \quad (2)$$

Here,  $E_c(B)$  is the magnetic field dependent energy of the closed-channel molecule relative to the scattering threshold, known from the asymptotic bound state model [13], and  $A_{\text{vs}}$  is the squared magnitude of the coupling matrix element between the closed-channel molecular state and the virtual state [28,29]. With  $A_{\text{vs}}$  as the only fit parameter,

we obtain excellent agreement with the data, finding  $A_{\text{vs}} = [h \times 5.2(6) \text{ MHz}]^2$ . The uncertainty in the background scattering length translates into the shaded uncertainty region in Fig. 2(a). The Feshbach resonance position is found to be  $B_0 = 139.7^{+2.1}_{-1.4} \text{ G}$ , its width (distance from resonance to the zero crossing of the scattering length) is  $\Delta B = 29(2) \text{ G}$ .

From the change of the binding energy with magnetic field we can directly deduce the closed-channel fraction  $Z = \frac{\partial E_b}{\partial E_c} \approx \frac{1}{\Delta\mu} \frac{\partial E_b}{\partial B}$  [5], where  $\Delta\mu = 2.4\mu_B$  is the difference between the magnetic moments of the closed-channel molecular state and the two free atoms near resonance. In Fig. 2(b), we show the open-channel fraction  $1 - Z$  along with the singlet admixture of the molecular state. Although the closed-channel molecular state is a bound state in the  $a(1)^3\Sigma^+$  triplet potential, the strong coupling to the entrance channel, which is 14% singlet, gives the Feshbach molecules a mixed singlet-triplet character. This will allow for direct two-photon coupling to the  $v = 0, X(1)^1\Sigma^+$  singlet rovibrational ground state via the singlet excited  $B(1)^1\Pi$  state.

To obtain an estimate for the temperature of the molecules we study their time-of-flight expansion right after association at  $E_b = h \times 84 \text{ kHz}$ . We measure an effective temperature (average kinetic energy) of 500 nK (see Fig. 3) for the molecules. From their number and trapping frequencies, this corresponds to a degeneracy factor of  $T/T_{\text{F,mol}} \approx 1.7$ . The molecular gas is more energetic than the sodium and potassium bath, which has a temperature of 220 nK. This partially reflects the broader momentum distribution of the  $^{40}\text{K}$  Fermi gas at  $T/T_{\text{F}} \approx 0.4$  due to Pauli pressure. Indeed, the momentum distribution of

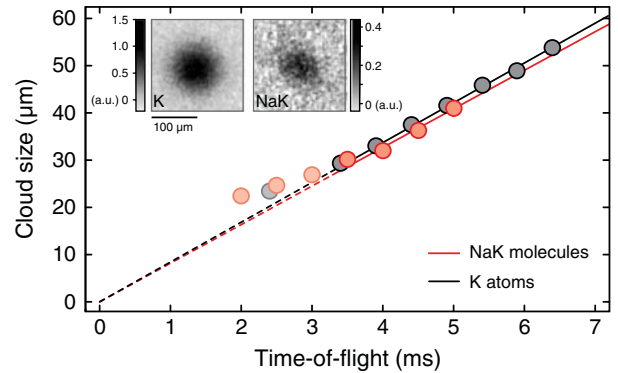


FIG. 3 (color online). Time-of-flight expansion of leftover  $^{40}\text{K}$  atoms and associated molecules at 129.4 G (binding energy  $h \times 84 \text{ kHz}$ ) right after rf association. Assuming a classical gas model, the width of the cloud corresponds to an average kinetic energy of 340 nK for the  $^{40}\text{K}$  cloud and 500 nK for the molecular cloud. Free atoms are transferred and detected in the  $m_F = -1/2$  state, while potassium atoms bound in NaK molecules are imaged in the  $m_F = -5/2$  state. The insets show an average of 20 absorption images for K atoms (NaK molecules) after 4.5 ms (4.0 ms) time of flight.

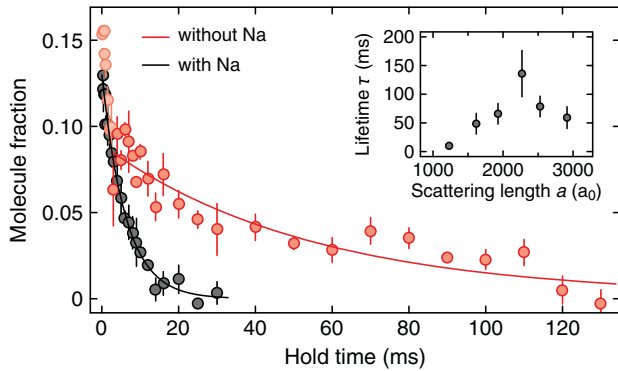


FIG. 4 (color online). Lifetime of fermionic Feshbach molecules. The measurement is performed at a magnetic field of 132.2 G, corresponding to a binding energy of 32 kHz. The red (black) data points show the number of molecules as a function of hold time with (without) removing sodium from the dipole trap directly after association. Solid lines correspond to exponential fits yielding a  $1/e$  time  $\tau$  of 54(13) ms and 8(1) ms, respectively. The inset shows the lifetime as a function of the scattering length between bosons and fermions. The maximum observed lifetime is 140(40) ms.

molecules after rf association is a convolution of the momentum distributions of the bosonic and fermionic clouds. At zero temperature, with bosons condensed and fermions fully occupying the Fermi sea, molecules would inherit the broad momentum distribution of the atomic Fermi gas. We also observe heating of the molecular cloud in the presence of sodium, likely due to three-body losses, that can occur already during the association pulse.

Figure 4 shows the lifetime of molecules close to the Feshbach resonance at a binding energy of  $h \times 32$  kHz. With the bosonic species still present, the lifetime is about 8 ms. Considering that the bosons can resonantly scatter with the fermions bound in the NaK molecules, this is already an impressive lifetime. However, the bosons can be selectively removed from the optical trap as its depth is species selective, being more confining for NaK molecules and  $^{40}\text{K}$  atoms than for  $^{23}\text{Na}$ . With bosons removed, the lifetime increases significantly to 54(13) ms, and further up to 140(40) ms at a binding energy of  $h \times 25$  kHz (see inset in Fig. 4). The lifetime  $\tau$  is likely limited by the presence of leftover  $^{40}\text{K}$  atoms in the  $|9/2, -3/2\rangle_{\text{K}}$  state. Their average density is  $n_A = \frac{1}{N} \int n^2 d^3r = 1 \times 10^{12} \text{ cm}^{-3}$ , yielding a loss rate of  $\beta = \frac{1}{n_A \tau} = 8(2) \times 10^{-12} \text{ cm}^3/\text{s}$ . As was studied in Ref. [19], the loss rate strongly depends on whether the collision partner is distinguishable or indistinguishable from the constituents of the molecule. For our case of distinguishable fermions as the collision partners, the above loss rate is 1 order of magnitude lower than the corresponding rate in KRb. In fact, it is still 3 times lower than the lowest rate measured in KRb for any collision partner [19]. Our loss rate even rivals that found for bosonic Feshbach molecules formed in a heteronuclear Fermi-Fermi mixture of LiK [30].

For collisions with distinguishable atoms, the molecular loss rate is expected to decrease like  $\beta \propto 1/a$  due to the reduced wave function overlap with lower-lying vibrational states [31]. While we observe a dramatic increase in the lifetime with scattering length for  $a \lesssim 2300a_0$  (binding energies  $E_b \gtrsim h \times 25$  kHz), the lifetime decreases again for even larger scattering lengths, possibly due to thermal dissociation when the binding energy becomes comparable to the temperature.

In conclusion, we have created ultracold fermionic Feshbach molecules of  $^{23}\text{Na}^{40}\text{K}$ , a molecule that is chemically stable in its absolute vibrational ground state. The molecular gas is formed close to degeneracy and is found to be long-lived near the Feshbach resonance. As revealed by the binding energy measurements, the Feshbach molecules are open-channel dominated over a wide magnetic field range, where they possess significant singlet character. These are ideal starting conditions for a two-photon transfer into the singlet rovibrational ground state [11]. Combined with the large induced dipole moment of 2.72 Debye, NaK presents us with a unique opportunity to create a stable, strongly dipolar Fermi gas with dominating long-range anisotropic interactions.

We would like to thank Tobias Tiecke for fruitful discussions and Ibon Santiago for experimental support in the early stages of the experiment. This work was supported by the NSF, AFOSR-MURI, AFOSR-PECASE, a grant from the Army Research Office with funding from the DARPA OLE program and the David and Lucile Packard Foundation.

- 
- [1] *Cold Molecules: Theory, Experiment, Applications*, edited by R. Krems, B. Friedrich, and W.C. Stwalley (CRC Press, Boca Raton, 2009).
  - [2] L.D. Carr, D. DeMille, R.V. Krems, and J. Ye, *New J. Phys.* **11**, 055049 (2009).
  - [3] K. Jones, E. Tiesinga, P. Lett, and P. Julienne, *Rev. Mod. Phys.* **78**, 483 (2006).
  - [4] T. Köhler, K. G'oral, and P.S. Julienne, *Rev. Mod. Phys.* **78**, 1311 (2006).
  - [5] C. Chin, R. Grimm, P. Julienne, and E. Tiesinga, *Rev. Mod. Phys.* **82**, 1225 (2010).
  - [6] S. Jochim, M. Bartenstein, A. Altmeyer, G. Hendl, S. Riedl, C. Chin, J. Hecker-Denschlag, and R. Grimm, *Science* **302**, 2101 (2003).
  - [7] M. Greiner, C.A. Regal, and D.S. Jin, *Nature (London)* **426**, 537 (2003).
  - [8] M.W. Zwierlein, C.A. Stan, C.H. Schunck, S.M.F. Raupach, S. Gupta, Z. Hadzibabic, and W. Ketterle, *Phys. Rev. Lett.* **91**, 250401 (2003).
  - [9] *Ultracold Fermi Gases*, Proceedings of the International School of Physics ‘‘Enrico Fermi,’’ Course CLXIV, edited by M. Inguscio, W. Ketterle, and C. Salomon (IOS Press, Amsterdam, 2008).
  - [10] W. Ketterle and M. Zwierlein, in *Ultracold Fermi Gases*, Proceedings of the International School of Physics ‘‘Enrico Fermi,’’ Course CLXIV, edited by M. Inguscio,

- W. Ketterle, and C. Salomon (IOS Press, Amsterdam, 2008); reprinted in *Riv. Nuovo Cimento* **31**, 247 (2008).
- [11] K. K. Ni, S. Ospelkaus, M. H. G. de Miranda, A. Pe'er, B. Neyenhuis, J. J. Zirbel, S. Kotochigova, P. S. Julienne, D. S. Jin, and J. Ye, *Science* **322**, 231 (2008).
- [12] S. Ospelkaus, K. K. Ni, D. Wang, M. H. G. de Miranda, B. Neyenhuis, G. Quemener, P. S. Julienne, J. L. Bohn, D. S. Jin, and J. Ye, *Science* **327**, 853 (2010).
- [13] J. W. Park, C.-H. Wu, I. Santiago, T. G. Tiecke, S. Will, P. Ahmadi, and M. W. Zwierlein, *Phys. Rev. A* **85**, 051602 (2012).
- [14] P. S. Zuchowski and J. M. Hutson, *Phys. Rev. A* **81**, 060703 (2010).
- [15] R. F. Wormsbecher, M. M. Hessel, and F. J. Lovas, *J. Chem. Phys.* **74**, 6983 (1981).
- [16] C.-H. Wu, I. Santiago, J. W. Park, P. Ahmadi, and M. W. Zwierlein, *Phys. Rev. A* **84**, 011601 (2011).
- [17] The trap frequencies for  $^{40}\text{K}$  [ $^{23}\text{Na}$ ] are  $\nu_x = 108(5)$  Hz [85(5) Hz],  $\nu_y = 127(5)$  Hz [101(6) Hz], and  $\nu_z = 187(4)$  Hz [148(3) Hz]. The differential gravitational sag is only  $4\ \mu\text{m}$ .
- [18] C. Ospelkaus, S. Ospelkaus, L. Humbert, P. Ernst, K. Sengstock, and K. Bongs, *Phys. Rev. Lett.* **97**, 120402 (2006).
- [19] J. J. Zirbel, K. K. Ni, S. Ospelkaus, J. P. D’Incao, C. E. Wieman, J. Ye, and D. S. Jin, *Phys. Rev. Lett.* **100**, 143201 (2008).
- [20] J. J. Zirbel, K.-K. Ni, S. Ospelkaus, T. L. Nicholson, M. L. Olsen, P. S. Julienne, C. E. Wieman, J. Ye, and D. S. Jin, *Phys. Rev. A* **78**, 013416 (2008).
- [21] C. Klempt, T. Henninger, O. Topic, M. Scherer, L. Kattner, E. Tiemann, W. Ertmer, and J. J. Arlt, *Phys. Rev. A* **78**, 061602 (2008).
- [22] A 1.2 ms long Blackman pulse [23] is used, allowing for Fourier-limited spectroscopy given the magnetic field stability of  $\pm 3$  mG that translates into about 3 kHz  $\sigma$ -width of transitions.
- [23] F. Harris, *Proc. IEEE* **66**, 51 (1978).
- [24] C. Chin and P. S. Julienne, *Phys. Rev. A* **71**, 012713 (2005).
- [25] C. A. Regal, C. Ticknor, J. L. Bohn, and D. S. Jin, *Nature (London)* **424**, 47 (2003).
- [26] From the potential in [27], modeled to yield the triplet binding energy found in [13], we obtain a triplet scattering length at  $a_t = -805_{-150}^{+100}a_0$ , where the error bar reflects not only the uncertainty in the triplet binding energy, as in [13], but also the uncertainty in the  $C_6$  coefficient [27].
- [27] A. Gerdes, M. Hobein, H. Knöckel, and E. Tiemann, *Eur. Phys. J. D* **49**, 67 (2008).
- [28] B. Marcellis, E. G. M. van Kempen, B. J. Verhaar, and S. J. J. M. F. Kokkelmans, *Phys. Rev. A* **70**, 012701 (2004).
- [29] E. G. M. v. Kempen, B. Marcellis, and S. J. J. M. F. Kokkelmans, *Phys. Rev. A* **70**, 050701(R) (2004).
- [30] A. C. Voigt, M. Taglieber, L. Costa, T. Aoki, W. Wieser, T. W. Hänsch, and K. Dieckmann, *Phys. Rev. Lett.* **102**, 020405 (2009).
- [31] J. P. D’Incao and B. D. Esry, *Phys. Rev. Lett.* **100**, 163201 (2008).

# Bibliography

- [1] M.H. Anderson, J.R. Ensher, M.R. Matthews, C.E. Wieman, and E.A. Cornell. Observation of Bose-Einstein condensation in a dilute atomic vapor. *Science*, 269:198–201, 1995.
- [2] K. B. Davis, M.-O. Mewes, M. R. Andrews, N. J. van Druten, D. S. Durfee, D. M. Kurn, and W. Ketterle. Bose-Einstein condensation in a gas of sodium atoms. *Physical Review Letters*, 75(22):3969–3973, 1995.
- [3] Cheng Chin, Rudolf Grimm, Paul Julienne, and Eite Tiesinga. Feshbach resonances in ultracold gases. *Reviews of Modern Physics*, 82(2):1225–1286, 2010.
- [4] A.J. Leggett. *Diatomic molecules and Cooper pairs*, pages 13–27. Springer-Verlag, Berlin, 1980.
- [5] W. Ketterle and M.W. Zwierlein. *Making, probing and understanding ultracold Fermi gases*. IOS Press, Amsterdam., 2008.
- [6] M Inguscio, W Ketterle, and C Salomon. *Ultracold Fermi Gases*. Proceedings of the International School of Physics ”Enrico Fermi”, Course CLXIV, Varenna, 20 - 30 June 2006. IOS Press, Amsterdam, 2008.
- [7] Stefano Giorgini, Lev P. Pitaevskii, and Sandro Stringari. Theory of ultracold atomic Fermi gases. *Reviews of Modern Physics*, 80(4):1215–60, 2008.
- [8] S. Nascimbene, N. Navon, K. J. Jiang, L. Tarruell, M. Teichmann, J. McKeever, F. Chevy, and C. Salomon. Collective oscillations of an imbalanced Fermi gas: Axial compression modes and polaron effective mass. *Physical Review Letters*, 103(17):170402–4, 2009.
- [9] Andre Schirotzek, Cheng-Hsun Wu, Ariel Sommer, and Martin W. Zwierlein. Observation of Fermi polarons in a tunable Fermi liquid of ultracold atoms. *Physical Review Letters*, 102(23):230402–4, 2009.
- [10] C. Kohstall, M. Zaccanti, M. Jag, A. Trenkwalder, P. Massignan, G. M. Bruun, F. Schreck, and R. Grimm. Metastability and coherence of repulsive polarons in a strongly interacting Fermi mixture. *Nature*, 485(7400):615–618, 2012.

- [11] K. K. Ni, S. Ospelkaus, M. H. G. de Miranda, A. Pe'er, B. Neyenhuis, J. J. Zirbel, S. Kotochigova, P. S. Julienne, D. S. Jin, and J. Ye. A high phase-space-density gas of polar molecules. *Science*, 322(5899):231–235, 2008.
- [12] M. A. Baranov, M. Dalmonte, G. Pupillo, and P. Zoller. Condensed matter theory of dipolar quantum gases. *Chemical Reviews*, 112(9):5012–5061, 2012.
- [13] V. Efimov. Energy levels arising from resonant two-body forces in a three-body system. *Physics Letters B*, 33(8):563–564, 1970.
- [14] T. et. al. Kraemer. Evidence for Efimov quantum states in an ultracold gas of caesium atoms. *Nature*, 440:315, 2006.
- [15] H. Metcalf and P. van der Straten. Cooling and trapping of neutral atoms. *Physics Reports*, 244(4 and 5):203, 1994.
- [16] W. Ketterle and N.J. van Druten. *Evaporative cooling of trapped atoms*, volume 37, pages 181–236. Academic Press, San Diego, 1996.
- [17] W. Ketterle, D.S. Durfee, and D.M. Stamper-Kurn. *Making, probing and understanding Bose-Einstein condensates*, pages 67–176. IOS Press, Amsterdam, 1999.
- [18] S.N. Bose. Plancks Gesetz und Lichtquantenhypothese. *Zeitschrift für Physik*, 26:178, 1924.
- [19] A. Einstein. Zur Quantentheorie des idealen Gases. *Sitzungsberichte der preussischen Akademie der Wissenschaften*, Bericht 3:18–25, 1925.
- [20] A. Griffin, D.W. Snoke, and S. Stringari. *Bose-Einstein Condensation*. Cambridge University Press, Cambridge, 1995.
- [21] D.G. Fried, T.C. Killian, L. Willmann, D. Landhuis, S.C. Moss, D. Kleppner, and T.J. Greytak. Bose-Einstein condensation of atomic hydrogen. *Physical Review Letters*, 81:3811–3814, 1998.
- [22] M. R. Andrews, C. G. Townsend, H. J. Miesner, D. S. Durfee, D. M. Kurn, and W. Ketterle. Observation of interference between two Bose-Einstein condensates. *Science*, 275(5300):637–641, 1997.
- [23] D.S. Jin, J.R. Ensher, M.R. Matthews, C.E. Wieman, and E.A. Cornell. Collective excitations of a Bose-Einstein condensate in a dilute gas. *Physical Review Letters*, 77:420, 1996.
- [24] E.A. Cornell, J.R. Ensher, and C.E. Wieman. *Experiments in Dilute Atomic Bose-Einstein Condensation*, pages 15–66. IOS Press, Amsterdam, 1999.
- [25] S. Inouye, M. R. Andrews, J. Stenger, H. J. Miesner, D. M. Stamper-Kurn, and W. Ketterle. Observation of Feshbach resonances in a Bose-Einstein condensate. *Nature*, 392(6672):151–154, 1998.

- [26] B. DeMarco and D.S. Jin. Onset of Fermi degeneracy in a trapped atomic gas. *Science*, 285:1703–1706, 1999.
- [27] M.W. Zwierlein, C.A. Stan, C.H. Schunck, S.M.F. Raupach, S. Gupta, Z. Hadzibabic, and W. Ketterle. Observation of Bose-Einstein condensation of molecules. *Physical Review Letters*, 91:250401, 2003.
- [28] Markus Greiner, Cindy A. Regal, and Deborah S. Jin. Emergence of a molecular Bose-Einstein condensate from a Fermi gas. *Nature*, 426:537, 2003.
- [29] S. Jochim, M. Bartenstein, A. Altmeyer, G. Hendl, S. Riedl, C. Chin, J. Hecker Denschlag, and R. Grimm. Bose-Einstein condensation of molecules. *Science*, 302(5653):2101–2103, 2003.
- [30] M.W. Zwierlein, C.A. Stan, C.H. Schunck, S.M.F. Raupach, A.J. Kerman, and W. Ketterle. Condensation of pairs of fermionic atoms near a Feshbach resonance. *Physical Review Letters*, 92:120403, 2004.
- [31] C. A. Regal, M. Greiner, and D. S. Jin. Observation of resonance condensation of fermionic atom pairs. *Physical Review Letters*, 92(4):040403, 2004.
- [32] M. W. Zwierlein, J. R. Abo-Shaeer, A. Schirotzek, C. H. Schunck, and W. Ketterle. Vortices and superfluidity in a strongly interacting Fermi gas. *Nature*, 435:1047–1051, 2005.
- [33] Markus Greiner, Olaf Mandel, Tilman Esslinger, Theodor W. Hänsch, and Immanuel Bloch. Quantum phase transition from a superfluid to a Mott insulator in a gas of ultracold atoms. *Nature*, 415:39–44, 2002.
- [34] Andrew G. Truscott, Kevin E. Strecker, William I. McAlexander, Guthrie B. Partridge, and Randall G. Hulet. Observation of Fermi pressure in a gas of trapped atoms. *Science*, 291:2570–2572, 2001.
- [35] F. Schreck, L. Khaykovich, K. L. Corwin, G. Ferrari, T. Bourdel, J. Cubizolles, and C. Salomon. Quasipure Bose-Einstein condensate immersed in a Fermi sea. *Physical Review Letters*, 87:080403, 2001.
- [36] J. Goldwin, S. B. Papp, B. DeMarco, and D. S. Jin. Two-species magneto-optical trap with  $^{40}\text{K}$  and  $^{87}\text{Rb}$ . *Physical Review A*, 65(2):021402, 2002.
- [37] Z. Hadzibabic, S. Gupta, C.A. Stan, C.H. Schunck, M.W. Zwierlein, K. Dieckmann, and W. Ketterle. Fifty-fold improvement in the number of quantum degenerate fermionic atoms. *Physical Review Letters*, 91:160401, 2003.
- [38] C. A. Stan, M. W. Zwierlein, C. H. Schunck, S. M. F. Raupach, and W. Ketterle. Observation of Feshbach resonances between two different atomic species. *Physical Review Letters*, 93:143001, 2004.

- [39] S. Inouye, J. Goldwin, M. L. Olsen, C. Ticknor, J. L. Bohn, and D. S. Jin. Observation of heteronuclear Feshbach resonances in a mixture of bosons and fermions. *Physical Review Letters*, 93:183201, 2004.
- [40] S. B. Papp and C. E. Wieman. Observation of heteronuclear Feshbach molecules from a  $^{85}\text{Rb}$ - $^{87}\text{Rb}$  gas. *Physical Review Letters*, 97(18):180404, 2006.
- [41] E. Wille, F.M. Spiegelhalder, G. Kerner, D. Naik, A. Trenkwalder, G. Hendl, F. Schreck, R. Grimm, T.G. Tiecke, J.T.M. Walraven, S.J.J.M.F. Kokkelmans, E. Tiesinga, and P.S. Julienne. Exploring an ultracold Fermi-Fermi mixture: Interspecies Feshbach resonances and scattering properties of  $^6\text{Li}$  and  $^{40}\text{K}$ . *Phys. Rev. Lett.*, 100:053201, 2008.
- [42] B. Deh, C. Marzok, C. Zimmermann, and Ph W. Courteille. Feshbach resonances in mixtures of ultracold  $^6\text{Li}$  and  $^{87}\text{Rb}$  gases. *Physical Review A*, 77(1):010701, 2008.
- [43] Andrea Simoni, Matteo Zaccanti, Chiara D’Errico, Marco Fattori, Giacomo Roati, Massimo Inguscio, and Giovanni Modugno. Near-threshold model for ultracold KRb dimers from interisotope Feshbach spectroscopy. *Physical Review A*, 77(5):052705, 2008.
- [44] G. Thalhammer, G. Barontini, L. De Sarlo, J. Catani, F. Minardi, and M. Inguscio. Double species Bose-Einstein condensate with tunable interspecies interactions. *Physical Review Letters*, 100(21):210402, 2008.
- [45] C. Marzok, B. Deh, C. Zimmermann, Ph. W. Courteille, E. Tiemann, Y. V. Vanne, and A. Saenz. Feshbach resonances in an ultracold  $^7\text{Li}$  and  $^{87}\text{Rb}$  mixture. *Physical Review A*, 79(1):012717, 2009.
- [46] Cheng-Hsun Wu, Ibon Santiago, Jee Woo Park, Peyman Ahmadi, and Martin W. Zwierlein. Strongly interacting isotopic Bose-Fermi mixture immersed in a Fermi sea. *Physical Review A*, 84(1):011601, 2011.
- [47] Cheng-Hsun Wu, Jee Woo Park, Peyman Ahmadi, Sebastian Will, and Martin W. Zwierlein. Ultracold fermionic Feshbach molecules of  $^{23}\text{Na}^{40}\text{K}$ . *Physical Review Letters*, 109(8):085301, 2012.
- [48] G. Modugno, G. Roati, F. Riboli, F. Ferlaino, R.J. Brecha, and M. Inguscio. Collapse of a degenerate Fermi gas. *Science*, 297:2240, 2002.
- [49] C. Ospelkaus, S. Ospelkaus, K. Sengstock, and K. Bongs. Interaction-driven dynamics of  $^{40}\text{K}$  -  $^{87}\text{Rb}$  Fermi-Bose gas mixtures in the large particle number limit. *Physical Review Letters*, 96:020401, 2006.
- [50] A. Trenkwalder, C. Kohstall, M. Zaccanti, D. Naik, A. I. Sidorov, F. Schreck, and R. Grimm. Hydrodynamic expansion of a strongly interacting Fermi-Fermi mixture. *Physical Review Letters*, 106:115304, 2011.

- [51] E. Abrahams. *50 Years of Anderson Localization*. World Scientific, 2010.
- [52] Yusuke Nishida. Phases of a bilayer Fermi gas. *Physical Review A*, 82(1):011605, 2010.
- [53] F. M. Cucchietti and E. Timmermans. Strong-coupling polarons in dilute gas Bose-Einstein condensates. *Physical Review Letters*, 96(21):210401, 2006.
- [54] Martin Bruderer, Alexander Klein, Stephen R. Clark, and Dieter Jaksch. Polaron physics in optical lattices. *Physical Review A*, 76(1):011605, 2007.
- [55] M Bruderer, A Klein, S R Clark, and D Jaksch. Transport of strong-coupling polarons in optical lattices. *New Journal of Physics*, 10(3):033015, 2008.
- [56] J. Tempere, W. Casteels, M. K. Oberthaler, S. Knoop, E. Timmermans, and J. T. Devreese. Feynman path-integral treatment of the BEC-impurity polaron. *Physical Review B*, 80(18):184504, 2009.
- [57] D H Santamore and Eddy Timmermans. Multi-impurity polarons in a dilute Bose-Einstein condensate. *New J. Phys.*, 13:103029, 2011.
- [58] H. Feshbach. A unified theory of nuclear reactions. *Annals of Physics*, 5:357–390, 1958.
- [59] H. Feshbach. A unified theory of nuclear reactions II. *Annals of Physics*, 19:287–313, 1962.
- [60] William C. Stwalley. Stability of spin-aligned hydrogen at low temperatures and high magnetic fields: New field-dependent scattering resonances and pre-dissociations. *Physical Review Letters*, 37:1628, 1976.
- [61] E. Tiesinga, B.J. Verhaar, and H.T.C. Stoof. Threshold and resonance phenomena in ultracold ground-state collisions. *Physical Review A*, 47:4114–4122, 1993.
- [62] Ananth Chikkatur. *Colliding and Moving Bose-Einstein Condensates: Studies of superfluidity and optical tweezers for condensate transport*. Ph.D. thesis, Massachusetts Institute of Technology, 2002.
- [63] W.D. Phillips. Laser cooling and trapping of neutral atoms. *Reviews of Modern Physics*, 70(3):721, 1998.
- [64] Rudolf Grimm, Matthias Weidemüller, and Yurii B. Ovchinnikov. Optical dipole traps for neutral atoms. *Advances in Atomic and Molecular Physics*, 42:95–170, 2000.
- [65] B. DeMarco and D. S. Jin. Exploring a quantum degenerate gas of fermionic atoms. *Physical Review A*, 58:R4267, 1998.

- [66] C.J. Myatt, E.A. Burt, R.W. Ghrist, E.A. Cornell, and C.E. Wieman. Production of two overlapping Bose-Einstein condensates by sympathetic cooling. *Physical Review Letters*, 78:586–589, 1997.
- [67] G. Modugno, G. Ferrari, G. Roati, R. J. Brecha, A. Simoni, and M. Inguscio. Bose-Einstein condensation of potassium atoms by sympathetic cooling. *Science*, 294:1320–1322, 2001.
- [68] M. J. Holland, B. DeMarco, and D. S. Jin. Evaporative cooling of a two-component degenerate Fermi gas. *Physical Review A*, 61:053610, 2000.
- [69] Peter Zarth. *Magneto-optical trapping of Potassium 40*. Diploma thesis, Massachusetts Institute of Technology, 2006.
- [70] NIST Atomic Weights and Isotopic. <http://www.nist.gov/pml/data/comp.cfm>.
- [71] C. A. Stan and W. Ketterle. Multiple species atom source for laser-cooling experiments. *The Review of Scientific Instruments*, 76:063113, 2005.
- [72] C. A. Stan. *Experiments with Interacting Bose and Fermi Gases*. Ph.D. thesis, Massachusetts Institute of Technology, 2005.
- [73] J. F. O’Hanlon. *A User’s Guide to Vacuum Technology*. John Wiley and Sons, 2003.
- [74] Michio Nagasaka and Toshiro Yamashina. Sorption of nitrogen at low pressures by titanium. *J. Vac. Sci. Technol.*, 9:543, 1972.
- [75] C Benvenuti and et al. Vacuum properties of TiZrV non-evaporable getter films. *Vacuum*, 60:57–65, 2001.
- [76] P. Costa Pinto P. Chiggiato. Ti-Zr-V non-evaporable getter films: From development to large scale production for the large hadron collider. *Thin Solid Films*, 515(2):382–338, 2006.
- [77] P. B. Johnson and R. W. Christy. Optical constants of transition metals: Ti, V, Cr, Mn, Fe, Co, Ni, and Pd. *Physical Review B*, 9(12):5056–5070, 1974.
- [78] A. P. Lanham and D. M. Terherne. *Proc. Phys. Soc.*, 83:1059, 1964.
- [79] David R. Lide. *CRC Handbook of Chemistry and Physics*. CRC Press, 92 edition, 2012.
- [80] W.D. Phillips. *Laser cooling and trapping of neutral atoms*, pages 289–343. North-Holland, Amsterdam, 1992.
- [81] W. Ketterle, K. B. Davis, M. A. Joffe, A. Martin, and D. E. Pritchard. High-densities of cold atoms in a dark spontaneous-force optical trap. *Physical Review Letters*, 70(15):2253–2256, 1993.

- [82] Christian Schunck. *Study of an ultracold cloud of fermionic  ${}^6\text{Li}$  atoms near a Feshbach resonance*. Diploma thesis, 2002.
- [83] Z. Hadzibabic, C. A. Stan, K. Dieckmann, S. Gupta, M.W. Zwierlein, A. Gøerlitz, and W. Ketterle. Two species mixture of quantum degenerate Bose and Fermi gases. *Physical Review Letters*, 88:160401, 2002.
- [84] Z. Hadzibabic. *Studies of a Quantum Degenerate Fermionic Lithium Gas*. Ph.D. thesis, 2003.
- [85] J. Catani, P. Maioli, L. De Sarlo, F. Minardi, and M. Inguscio. Intense slow beams of bosonic potassium isotopes. *Physical Review A*, 73(3):033415, 2006.
- [86] G. Roati, M. Zaccanti, C. D’Errico, J. Catani, M. Modugno, A. Simoni, M. Inguscio, and G. Modugno.  ${}^{39}\text{K}$  Bose-Einstein condensate with tunable interactions. *Physical Review Letters*, 99(1):010403, 2007.
- [87] L. De Sarlo, P. Maioli, G. Barontini, J. Catani, F. Minardi, and M. Inguscio. Collisional properties of sympathetically cooled  ${}^{39}\text{K}$ . *Physical Review A*, 75(2):022715, 2007.
- [88] M. Landini, S. Roy, L. Carcagnì, D. Trypogeorgos, M. Fattori, M. Inguscio, and G. Modugno. Sub-doppler laser cooling of potassium atoms. *Physical Review A*, 84(4):043432, 2011.
- [89] M. Landini, S. Roy, G. Roati, A. Simoni, M. Inguscio, G. Modugno, and M. Fattori. Direct evaporative cooling of  ${}^{39}\text{K}$  atoms to Bose-Einstein condensation. *Physical Review A*, 86(3):033421, 2012.
- [90] T. Kishimoto, J. Kobayashi, K. Noda, K. Aikawa, M. Ueda, and S. Inouye. Direct evaporative cooling of  ${}^{41}\text{K}$  into a Bose-Einstein condensate. *Physical Review A*, 79(3):031602, 2009.
- [91] D. S. Durfee. *Dynamic Properties of Dilute Bose-Einstein Condensates*. Ph.D. thesis, 1999.
- [92] G. S. Williams and A. Hazen. *Hydraulic tables: showing the loss of head due to the friction of water flowing in pipes, aqueducts, sewers, etc. and the discharge over weirs*. J. Wiley, 1905.
- [93] W. Lenth G. C. Bjorklund, M. D. Levenson and C. Ortiz. Frequency modulation (FM) spectroscopy. *Applied Physics B*, 32(3):145–152, 1983.
- [94] Ibon Santiago. *LiNaK: Multi-Species Apparatus for the Study of Ultracold Quantum Degenerate Mixtures*. M.S., Massachusetts Institute of Technology, 2012.
- [95] Immanuel Bloch, Markus Greiner, Olaf Mandel, Theodor W. Hänsch, and Tilman Esslinger. Sympathetic cooling of  ${}^{85}\text{Rb}$  and  ${}^{87}\text{Rb}$ . *Physical Review A*, 64:021402–4, 2001.

- [96] G. Roati, F. Riboli, G. Modugno, and M. Inguscio. Fermi-Bose quantum degenerate  $^{40}\text{K}$ - $^{87}\text{Rb}$  mixture with attractive interaction. *Physical Review Letters*, 89:150403, 2002.
- [97] C. Silber, S. Günther, C. Marzok, B. Deh, Ph. W. Courteille, and C. Zimmermann. Quantum-degenerate mixture of fermionic lithium and bosonic rubidium gases. *Physical Review Letters*, 95:170408, 2005.
- [98] J. M. McNamara, T. Jelten, A. S. Tychkov, W. Hogervorst, and W. Vassen. Degenerate Bose-Fermi mixture of metastable atoms. *Physical Review Letters*, 97(8):080404, 2006.
- [99] M. Taglieber, A.-C. Voigt, T. Aoki, T. W. Hänsch, and K. Dieckmann. Quantum degenerate two-species Fermi-Fermi mixture coexisting with a Bose-Einstein condensate. *Physical Review Letters*, 100(1):010401, 2008.
- [100] F. M. Spiegelhalder, A. Trenkwalder, D. Naik, G. Hendl, F. Schreck, and R. Grimm. Collisional stability of  $^{40}\text{K}$  immersed in a strongly interacting Fermi gas of  $^6\text{Li}$ . *Physical Review Letters*, 103(22):223203, 2009.
- [101] T. G. Tiecke, M. R. Goosen, A. Ludewig, S. D. Gensemer, S. Kraft, S. J. J. M. F. Kokkelmans, and J. T. M. Walraven. Broad Feshbach resonance in the  $^6\text{Li}$ - $^{40}\text{K}$  mixture. *Physical Review Letters*, 104(5):053202, 2010.
- [102] Francesca Ferlaino, Chiara D’Errico, Giacomo Roati, Matteo Zaccanti, Massimo Inguscio, Giovanni Modugno, and Andrea Simoni. Feshbach spectroscopy of a K-Rb atomic mixture. *Physical Review A*, 73(4):040702, 2006.
- [103] B. Deh, W. Gunton, B. G. Klappauf, Z. Li, M. Semczuk, J. Van Dongen, and K. W. Madison. Giant Feshbach resonances in  $^6\text{Li}$ - $^{85}\text{Rb}$  mixtures. *Physical Review A*, 82(2):020701, 2010.
- [104] J. Dalibard. *Collisional dynamics of ultra-cold atomic gases*. IOS Press, 1999.
- [105] C. C. Bradley, C. A. Sackett, and R. G. Hulet. Bose-Einstein condensation of lithium: Observation of limited condensate number. *Physical Review Letters*, 78(6):985–989, 1997.
- [106] Stephan Falke, Horst Knöckel, Jan Friebe, Matthias Riedmann, Eberhard Tieemann, and Christian Lisdat. Potassium ground-state scattering parameters and Born-Oppenheimer potentials from molecular spectroscopy. *Physical Review A*, 78(1):012503, 2008.
- [107] Myoung-Sun Heo, Jae-yoon Choi, and Yong-il Shin. Fast production of large  $^{23}\text{Na}$  Bose-Einstein condensates in an optically plugged magnetic quadrupole trap. *Physical Review A*, 83(1):013622, 2011.

- [108] Tobias G. Tiecke. *Feshbach resonances in ultracold mixtures of the fermionic quantum gases  ${}^6\text{Li}$  and  ${}^{40}\text{K}$* . Ph.D. thesis, Van der Waals-Zeeman Instituut of the University of Amsterdam, 2009.
- [109] A. Simoni. *private communication*, 2010.
- [110] T. Hanna and E. Tiesinga. *private communication*, 2010.
- [111] Elisa Fratini and Pierbiagio Pieri. Pairing and condensation in a resonant Bose-Fermi mixture. *Physical Review A*, 81(5):051605, 2010.
- [112] Zeng-Qiang Yu, Shizhong Zhang, and Hui Zhai. Stability condition of a strongly interacting boson-fermion mixture across an interspecies Feshbach resonance. *Physical Review A*, 83(4):041603, 2011.
- [113] R. P. Feynman. Slow electrons in a polar crystal. *Physical Review*, 97(3):660, 1955.
- [114] WAN Shao-Long Huang Bei-Bing. Polaron in Bose-Einstein-Condensation system. *Chin. Phys. Lett.*, 26(8):80302–080302, 2009.
- [115] Ariel Sommer, Mark Ku, Giacomo Roati, and Martin W. Zwierlein. Universal spin transport in a strongly interacting Fermi gas. *Nature*, 472(7342):201–204, 2011.
- [116] Yusuke Nishida and Shina Tan. Universal Fermi gases in mixed dimensions. *Physical Review Letters*, 101(17):170401, 2008.
- [117] Uri Gavish and Yvan Castin. Matter-wave localization in disordered cold atom lattices. *Physical Review Letters*, 95(2):020401, 2005.
- [118] Eric Vernier, David Pekker, Martin W. Zwierlein, and Eugene Demler. Bound states of a localized magnetic impurity in a superfluid of paired ultracold fermions. *Physical Review A*, 83(3):033619, 2011. Copyright (C) 2011 The American Physical Society Please report any problems to prola@aps.org PRA.
- [119] J. Goldwin, S. Inouye, M. L. Olsen, B. Newman, B. D. DePaola, and D. S. Jin. Measurement of the interaction strength in a Bose-Fermi mixture with  ${}^{87}\text{Rb}$  and  ${}^{40}\text{K}$ . *Physical Review A*, 70:021601, 2004.
- [120] S. Aubin, M. H. T. Extavour, S. Myrskog, L. J. Leblanc, J. Estève, S. Singh, P. Scrutton, D. McKay, R. McKenzie, I. D. Leroux, A. Stummer, and J. H. Thywissen. Trapping fermionic  ${}^{40}\text{K}$  and bosonic  ${}^{87}\text{Rb}$  on a chip. *Journal of Low Temperature Physics*, 140:377–396, 2005.
- [121] Kenneth Günter, Thilo Stöferle, Henning Moritz, Michael Köhl, and Tilman Esslinger. Bose-Fermi mixtures in a three-dimensional optical lattice. *Physical Review Letters*, 96(18):180402, 2006.

- [122] T. Best, S. Will, U. Schneider, L. Hackermüller, D. S. Lühmann, D. van Oosten, and I. Bloch. Role of interactions in  $^{87}\text{Rb}$ - $^{40}\text{K}$  Bose-Fermi mixtures in a 3D optical lattice. *Physical Review Letters*, 102(3):030408, 2009.
- [123] Hideaki Hara, Yosuke Takasu, Yoshifumi Yamaoka, John M. Doyle, and Yoshiro Takahashi. Quantum degenerate mixtures of alkali and alkaline-earth-like atoms. *Physical Review Letters*, 106(20):205304, 2011.
- [124] Anders H. Hansen, Alexander Khramov, William H. Dowd, Alan O. Jamison, Vladyslav V. Ivanov, and Subhadeep Gupta. Quantum degenerate mixture of ytterbium and lithium atoms. *Physical Review A*, 84(1):011606, 2011.
- [125] M. J. Bijlsma, B. A. Heringa, and H. T. C. Stoof. Phonon exchange in dilute Fermi-Bose mixtures: Tailoring the Fermi-Fermi interaction. *Physical Review A*, 61(5):053601, 2000.
- [126] H. Heiselberg, C. J. Pethick, H. Smith, and L. Viverit. Influence of induced interactions on the superfluid transition in dilute Fermi gases. *Physical Review Letters*, 85(12):2418, 2000.
- [127] M. Lewenstein, L. Santos, M. A. Baranov, and H. Fehrmann. Atomic Bose-Fermi mixtures in an optical lattice. *Physical Review Letters*, 92:050401, 2004.
- [128] A. Gerdes, M. Hobein, H. Knöckel, and E. Tiemann. Ground state potentials of the NaK molecule. *Eur. Phys. J. D*, 49(1):67–73, 2008.
- [129] C. Ospelkaus, S. Ospelkaus, L. Humbert, P. Ernst, K. Sengstock, and K. Bongs. Ultracold heteronuclear molecules in a 3D optical lattice. *Physical Review Letters*, 97(12):120402, 2006.
- [130] V. Venturi, M.J. Jamieson, and R. Côté. Scattering lengths for collisions between sodium and potassium atoms. *Journal of Physics B: Atomic, Molecular, and Optical Physics*, 34:4339–4347, 2001.
- [131] B. Marcelis, E.G.M. van Kempen, B.J. Verhaar, and S.J.J.M.F. Kokkelmans. Feshbach resonances with large background scattering length: Interplay with open-channel resonances. *Physical Review A*, 70:012701, 2004.
- [132] K. Dieckmann, C. A. Stan, S. Gupta, Z. Hadzibabic, C. Schunck, and W. Ketterle. Decay of an ultracold fermionic lithium gas near a Feshbach resonance. *Physical Review Letters*, 89:203201, 2002.
- [133] C. Ticknor, C. A. Regal, D. S. Jin, and J. L. Bohn. Multiplet structure of Feshbach resonances in nonzero partial waves. *Physical Review A*, 69:042712, 2004.
- [134] Christopher Carl Ticknor. *Controlling Cold Collisions of Polar Molecules with External Fields*. Ph.D. thesis, University of Colorado, 2005.

- [135] A. Derevianko, J. F. Babb, and A. Dalgarno. High-precision calculations of Van der Waals coefficients for heteronuclear alkali-metal dimers. *Physical Review A*, 63(5):052704, 2001.
- [136] A. J. Moerdijk, B. J. Verhaar, and A. Axelsson. Resonances in ultra-cold collisions of  ${}^6\text{Li}$ ,  ${}^7\text{Li}$  and  ${}^{23}\text{Na}$ . *Physical Review A*, 51:4852–4861, 1995.
- [137] R. F. Wormsbecher, M. M. Hessel, and F. J. Lovas. Microwave optical double resonance of  $X_1\Sigma^+$  of NaK. *J. Chem. Phys.*, 74(12):6983, 1981.
- [138] E.P. Gross. Structure of a quantized vortex in boson systems. *Nuovo Cimento*, 20:454–477, 1961.
- [139] L.P. Pitaevskii. Vortex lines in an imperfect Bose gas. *Soviet Physics JETP*, 13:451–454, 1961.
- [140] Y. Ohashi and A. Griffin. BCS-BEC crossover in a gas of Fermi atoms with a Feshbach resonance. *Physical Review Letters*, 89:130402, 2003.
- [141] T. Bourdel, L. Khaykovich, J. Cubizolles, J. Zhang, F. Chevy, M. Teichmann, L. Tarruell, S.J.J.M.F. Kokkelmans, and C. Salomon. Experimental study of the BEC-BCS crossover region in lithium-6. *Physical Review Letters*, 93:050401, 2004.
- [142] M. Bartenstein, A. Altmeyer, S. Riedl, S. Jochim, C. Chin, J. Hecker-Denschlag, and R. Grimm. Collective excitations of a degenerate gas at the BEC-BCS crossover. *Physical Review Letters*, 92:203201, 2004.
- [143] Markus Greiner, Cindy A. Regal, and Deborah S. Jin. Probing the excitation spectrum of a Fermi gas in the BCS-BEC crossover regime, 2004.
- [144] W. Zwerger. *The BCS-BEC Crossover and the Unitary Fermi Gas*. Springer, 2011.
- [145] K.W. Madison, F. Chevy, W. Wohlleben, and J. Dalibard. Vortex formation in a stirred Bose-Einstein condensate. *Physical Review Letters*, 84:806–809, 2000.
- [146] J.R. Abo-Shaeer, C. Raman, J.M. Vogels, and W. Ketterle. Observation of vortex lattices in Bose-Einstein condensates. *Science*, 292:476–479, 2001.
- [147] Immanuel Bloch, Jean Dalibard, and Wilhelm Zwerger. Many-body physics with ultracold gases. *Reviews of Modern Physics*, 80(3):885–80, 2008.
- [148] Nathan Gemelke, Xibo Zhang, Chen-Lung Hung, and Cheng Chin. In situ observation of incompressible Mott-insulating domains in ultracold atomic gases. *Nature*, 460(7258):995–998, 08 2009.
- [149] W. S. Bakr, A. Peng, M. E. Tai, R. Ma, J. Simon, J. I. Gillen, S. Fölling, L. Pollet, and M. Greiner. Probing the superfluid-to-Mott insulator transition at the single-atom level. *Science*, 329(5991):547–550, 2010.

- [150] D. Carr Lincoln, DeMille David, V. Krems Roman, and Ye Jun. Cold and ultracold molecules: science, technology and applications. *New Journal of Physics*, 11(5):055049, 2009.
- [151] S. Ospelkaus, K. K. Ni, D. Wang, M. H. G. de Miranda, B. Neyenhuis, G. Quéméner, P. S. Julienne, J. L. Bohn, D. S. Jin, and J. Ye. Quantum-state controlled chemical reactions of ultracold potassium-rubidium molecules. *Science*, 327(5967):853–857, 2010.
- [152] Jee Woo Park, Cheng-Hsun Wu, Ibon Santiago, Tobias G. Tiecke, Sebastian Will, Peyman Ahmadi, and Martin W. Zwierlein. Quantum degenerate Bose-Fermi mixture of chemically different atomic species with widely tunable interactions. *Physical Review A*, 85:051602, 2012.
- [153] Piotr S. Zuchowski and Jeremy M. Hutson. Reactions of ultracold alkali-metal dimers. *Physical Review A*, 81(6):060703, 2010.
- [154] A. Gerdes, O. Dulieu, H. Knöckel, and E. Tiemann. Stark effect measurements on the NaK molecule. *Eur. Phys. J. D*, 65:105, 2011.
- [155] Roman Krems, Bretislav Friedrich, and William C Stwalley. *Cold Molecules: Theory, Experiment, Applications*. CRC Press, Boca Raton, 2009.
- [156] M. Aymar and O. Dulieu. Calculation of accurate permanent dipole moments of the lowest  $1,3\Sigma^+$  states of heteronuclear alkali dimers using extended basis sets. *The Journal of Chemical Physics*, 122(20):204302–9, 2005.
- [157] Goulven Quéméner, John L. Bohn, Alexander Petrov, and Svetlana Kotochigova. Universalities in ultracold reactions of alkali-metal polar molecules. *Physical Review A*, 84(6):062703–, 12 2011.
- [158] FJ Harris. On the use of windows for harmonic analysis with the discrete Fourier transform. *Proceedings of the IEEE*, 66(1):51–83, 1978.
- [159] J. J. Zirbel, K. K. Ni, S. Ospelkaus, J. P. D’Incao, C. E. Wieman, J. Ye, and D. S. Jin. Collisional stability of fermionic Feshbach molecules. *Physical Review Letters*, 100(14):143201, 2008.
- [160] J. J. Zirbel, K.-K. Ni, S. Ospelkaus, T. L. Nicholson, M. L. Olsen, P. S. Julienne, C. E. Wieman, J. Ye, and D. S. Jin. Heteronuclear molecules in an optical dipole trap. *Physical Review A*, 78:013416, 2008.
- [161] C. Klempt, T. Henninger, O. Topic, M. Scherer, L. Kattner, E. Tiemann, W. Ertmer, and J. J. Arlt. Radio-frequency association of heteronuclear Feshbach molecules. *Physical Review A*, 78:061602, 2008.
- [162] Cindy A. Regal, Christopher Ticknor, John L. Bohn, and Deborah S. Jin. Creation of ultracold molecules from a Fermi gas of atoms. *Nature*, 424:47, 2003.

- [163] E.G.M. v. Kempen, B. Marcelis, and S.J.J.M.F. Kokkelmans. Formation of fermionic molecules via interisotope Feshbach resonances. *Physical Review A*, 70:050701(R), 2004.
- [164] J. P. D’Incao and B. D. Esry. Scattering length scaling laws for ultracold three-body collisions. *Physical Review Letters*, 94(21):213201, 2005.
- [165] A. C. Voigt, M. Taglieber, L. Costa, T. Aoki, W. Wieser, T. W. Hänsch, and K. Dieckmann. Ultracold heteronuclear Fermi-Fermi molecules. *Physical Review Letters*, 102(2):020405–4, 2009.
- [166] L.D. Landau. Über die bewegung der elektronen im kristallgitter. *Phys. Z. Sowjetunion*, 3:644–645, 1933.
- [167] S. I. Pekar. *Zh. Eksp. Teor. Fiz.*, 16:335, 1946.
- [168] H. Fröhlich. Electrons in lattice fields. *Adv. Phys.*, 3:325, 1954.
- [169] E. I. Rashba. *Optika i spektroskopiya*, 2(75), 1957.
- [170] J. Devreese, J. De Sitter, and M. Goovaerts. Optical absorption of polarons in the Feynman-Hellwarth-Iddings-Platzman approximation. *Physical Review B*, 5(6):2367–2381, 1972.
- [171] F. Chevy. Universal phase diagram of a strongly interacting Fermi gas with unbalanced spin populations. *Physical Review A*, 74(6):063628, 2006.
- [172] R. Combescot, A. Recati, C. Lobo, and F. Chevy. Normal state of highly polarized Fermi gases: Simple many-body approaches. *Physical Review Letters*, 98(18):180402, 2007.
- [173] Nikolay Prokofév and Boris Svistunov. Fermi-polaron problem: Diagrammatic monte carlo method for divergent sign-alternating series. *Physical Review B*, 77(2):020408, 2008.
- [174] N. N. Bogoliubov. On the theory of superfluidity. *J. Phys. (USSR)*, 11:23, 1947.
- [175] J. T. Devreese. Polarons. *Encyclopedia of Applied Physics*, 14:383, 1996.
- [176] Dmitry Abanin. *private communication*, 2012.
- [177] Michael Knap, Aditya Shashi, Yusuke Nishida, Adilet Imambekov, Dmitry A. Abanin, and Eugene Demler. Time-dependent impurity in ultracold fermions: Orthogonality catastrophe and beyond. *Physical Review X*, 2(4):041020–, 12 2012.
- [178] M. A. Baranov, M. S. Mar’enko, Val S. Rychkov, and G. V. Shlyapnikov. Superfluid pairing in a polarized dipolar Fermi gas. *Physical Review A*, 66(1):013606, 2002.

- [179] Shai Ronen and John L. Bohn. Zero sound in dipolar Fermi gases. *Physical Review A*, 81(3):033601, 2010.
- [180] Ching-Kit Chan, Congjun Wu, Wei-Cheng Lee, and S. Das Sarma. Anisotropic-Fermi-liquid theory of ultracold fermionic polar molecules: Landau parameters and collective modes. *Physical Review A*, 81(2):023602, 2010.
- [181] T. Shi, J. N. Zhang, C. P. Sun, and S. Yi. Singlet and triplet Bardeen-Cooper-Schrieffer pairs in a gas of two-species fermionic polar molecules. *Physical Review A*, 82(3):033623–, 09 2010.
- [182] N. R. Cooper and G. V. Shlyapnikov. Stable topological superfluid phase of ultracold polar fermionic molecules. *Physical Review Letters*, 103(15):155302, 2009.
- [183] J. Levinsen, N. R. Cooper, and G. V. Shlyapnikov. Topological  $p_x+ip_y$  superfluid phase of fermionic polar molecules. *Physical Review A*, 84(1):013603, 2011.
- [184] N. Read and Dmitry Green. Paired states of fermions in two dimensions with breaking of parity and time-reversal symmetries and the fractional quantum hall effect. *Physical Review B*, 61(15):10267–10297, 2000.
- [185] Ady Stern. Anyons and the quantum Hall effect—a pedagogical review. *Annals of Physics*, 323(1):204–249, 1 2008.
- [186] Chetan Nayak, Steven H. Simon, Ady Stern, Michael Freedman, and Sankar Das Sarma. Non-abelian anyons and topological quantum computation. *Reviews of Modern Physics*, 80(3):1083–1159, 09 2008.
- [187] A. Pikovski, M. Klawunn, G. V. Shlyapnikov, and L. Santos. Interlayer superfluidity in bilayer systems of fermionic polar molecules. *Physical Review Letters*, 105(21):215302, 2010.
- [188] N. T. Zinner, B. Wunsch, D. Pekker, and D. W. Wang. BCS-BEC crossover in bilayers of cold fermionic polar molecules. *Physical Review A*, 85(1):013603, 2012.
- [189] F. D. M. Haldane. Effective harmonic-fluid approach to low-energy properties of one-dimensional quantum fluids. *Physical Review Letters*, 47(25):1840–1843, 12 1981.
- [190] Y. Tsukamoto and N. Kawakami. *J. Phys. Soc. Jpn.*, 69:149, 2000.
- [191] H Inoue and K Nomura. Conformal field theory in the Tomonaga–Luttinger model with the  $1/r^\beta$  long-range interaction. *Journal of Physics A: Mathematical and General*, 39(22):7173, 2006.

- [192] J. M. Luttinger. An exactly soluble model of a many-fermion system. *J. Math. Phys.*, 4:1154, 1963.
- [193] T. Giamarchi. *Quantum Physics in One Dimension*. Clarendon Press, 2003.
- [194] Christopher Ticknor. Collisional control of ground state polar molecules and universal dipolar scattering. *Physical Review Letters*, 100(13):133202, 2008.
- [195] Vladimir Roudnev and Michael Cavagnero. Universal resonant ultracold molecular scattering. *Physical Review A*, 79(1):014701, 2009.
- [196] Paul S. Julienne, Thomas M. Hanna, and Zbigniew Idziaszek. Universal ultracold collision rates for polar molecules of two alkali-metal atoms. *Physical Chemistry Chemical Physics*, 13(42):19114–19124, 2011.
- [197] N. Yoshimura. *Vacuum Technology Practice for Scientific Instruments*. Springer, 2008.